# TaN thin films deposited by modulated pulsed power magnetron sputtering: Coating solutions for harsh environments

PhD THESIS

Presented by

Lucia Mendizabal Ortiz de Guzman

Supervisor

Javier Jesus Gonzalez Martinez

October 2016

eman ta zabal zazu

Universidad del País Vasco

Euskal Herriko Unibertsitatea

IK4 TEKNIKER

Research Alliance

*A l@s más importantes,*

*Mis abuelas, Aita, Ama, Maider y Gorka*

# AGRADECIMIENTOS

*Me hace especial ilusión poder escribir estas líneas. Primero, porque significa que en unos días depositaré mi tesis doctoral; y segundo, y más importante, porque me da la oportunidad de dedicar unas palabras a aquellas personas que directa o indirectamente también son parte de ella. He disfrutado mucho a lo largo de estos años, pero el último ha sido especialmente duro. El apoyo, técnico y emocional, de muchos de vosotros ha sido clave para que esta tesis sea hoy una realidad.*

*Lo primero, agradecer a mi director de tesis, Javier Jesus Gonzalez, haber aceptado dirigir esta tesis. Javier, gracias por tu apoyo, tus consejos y tu ayuda cada vez que lo he necesitado.*

*Quiero agradecer también a IK4-Tekniker y a la Fundación Centros Tecnológicos Iñaki Goenaga la beca que me ofrecieron hace 6 años para realizar esta tesis. Pero sobre todo, por brindarme la oportunidad de trabajar en un mundo, que aunque entonces no lo sabía, a día de hoy me apasiona.*

*A todas las personas que forman parte de las Unidades de Tribología y Física de Superficies. Es una suerte llegar a trabajar cada día a un ambiente de trabajo tan bueno. Todos sois parte de mi desarrollo profesional durante estos 6 años. Y además, muchos sois buenos amigos. Nada sería lo mismo sin vosotros.*

*Pero hay ciertas personas que se merecen unas palabras aparte. Javi, gracias por tu inmensa confianza en mí, por tu apoyo incondicional y por dejarme volar libre con cada una de mis ideas. También por haberte preocupado de que obtuviera la mejor formación posible en todo lo relacionado con el PVD.*

*Mis maravillosos y más cercanos compañeros del taller, Unai, Eneritz y Maite. Nunca olvidare los momentos que hemos pasado juntos, tanto buenos como malos, pero que han hecho posible el gran equipo que creo que formamos hoy. Unai, fuiste mi maestro en el PVD, me enseñaste, me formaste, me transmitiste tu pasión y me dejaste crecer al lado de mi inseparable 450. Siempre lo tendré presente. Ahora camino sola pero todo es más fácil cuando tu estas "around". Eneritz y Maite, vosotras completáis el grupo de COATERS que nos define en wassap. Vuestro apoyo moral, vuestra disposición a cubrir mi ausencia en el taller para que pudiera escribir esta tesis y vuestros ánimos, han contribuido enormemente a que hoy este donde estoy.*

*Eva, sin tus consejos y sin tu supervisión, esta tesis y las publicaciones que se incluyen en ella, quizá no estarían hoy acabadas, pero sobre todo, no tendrían la misma calidad. Gracias por haber*

*hecho el gran esfuerzo de corregir esta tesis durante tus vacaciones. No lo olvidare. Cris, gracias por todas las horas que has invertido en analizar la microestructura de las capas de TaN. Por nuestros momentos de alegría cuando detectábamos que no mostraban crecimiento columnar! Y por corregir, en detalle, la introducción de esta tesis. Nestor, sin tu ayuda, aun estaría dibujando las imágenes de esta tesis y peleándome con su formato. Gracias. No es fácil encontrar becarios como tú. Raquel, a ti te debo todo lo que sé sobre corrosión, que es parte fundamental de esta tesis. Te debo eso, y los grandes momentos que hemos compartido, tanto dentro como fuera de Tekniker. Gracias Rachel. Eres especial. Ainara, gracias por realizar los ensayos de tribocorrosion que se incluyen en el Capítulo 5 de esta tesis. Y por tu predisposición a ayudarme siempre.*

*También quiero dar las gracias a mis compañeros que han defendido la tesis a lo largo de este último año. Me hicisteis ver que era posible compaginar trabajo y tesis, cuando a veces ni yo misma lo creía ya. Fue el empujón que necesitaba para acabar la mía. Gracias Virginia, Cristina, Borja y Bihotz.*

*My special gratitude to the fantastic team at Sintef, up in Norway, with whom I have carried out the research about TaN films for bipolar plates in PEMFC that is included in Chapter 6 of this thesis. Anders, thanks for inviting me to Sintef for testing myself the TaN coatings in PEMFC environment when we didn't even know each other. I will never forget that. Thanks for introducing me to the fantastic world of hydrogen energy and for sharing with me your knowledge and passion on this field. Ole Edvard, I have learned so much about corrosion processes from you that I don't know how to thank you. Your willingness to teach and guide me is invaluable. Sigrid, thanks for testing the Ta_ITO coatings that are included in this thesis. Your help in analyzing the results related to bipolar plates has been enormous. But more specially, thanks for your friendship. Sharing COATELY project with all of you has meant much for me, both professionally and personally.*

*Agradecer a mis amigos el haberme soportado durante este último año. Vuestros animos, tan importantes, durante este largo camino. Y la alegría compartida de celebrar que se acerca el final de esta tesis.*

*Pero sobre todo, quiero compartir estas tesis con los que más quiero. Aita, Ama, Maider, esta tesis es tan mia como vuestra. La educación que me disteis fue la primera piedra de todo lo que he conseguido hasta hoy. Nunca olvidaré el gran esfuerzo que realizasteis para que pudiera estudiar lejos de casa, y mucho menos, el que un día, con 18 años, me animarais enormemente a hacerlo. Esas experiencias marcaron mi personalidad de hoy y mi desarrollo profesional. Aita, la inquietud*

*y la forma de ver la vida, el criterio propio y la cultura del esfuerzo los llevo grabados en mi ADN. Tú me los enseñaste y siempre los tendré presentes. Ama, tú me diste todo lo demás, el cariño, la simpatía, el saber escuchar y el apoyo incondicional. Y el ejemplo de mujer trabajadora. Mi sister, Maider, nada seria lo mismo sin ti. Mi pequeña mini-yo, mi otra mitad. Siempre estás, has estado y sé que estarás a mi lado. Te quiero.*

*A la persona que más me ha apoyado durante estos años, Gorka. Tú eres el que más ha sufrido que hoy este aquí. Soy consciente. Gracias por tu enorme paciencia, por estar SIEMPRE, SIEMPRE, cuando te he necesitado y porque me llena de alegría poder celebrar esta tesis y todo lo demás a tu lado. Haces todo más fácil. Haces todo especial. Maite zaitut kari.*

*Lucia*

# SUMMARY

Transition metal nitride (TMN) films deposited by dc magnetron sputtering (DCMS) technique are widely used today as protective hard coatings for different components in manifold industries. In spite of the numerous transition metals found in the periodic table, the current coating solutions are focused on a limited number of nitrides such as TiN, CrN, ZrN, TiAlN and CrAlN, while other attractive candidates are left behind. Furthermore, films deposited by DCMS generally fail in specific applications where coated components face severe corrosive operation conditions. Low ionization degree of sputtered material during DCMS (<5 %) promotes the development of low density and columnar microstructure films, which are responsible of these failures, enabling the corrosive solution penetration along the pores and defects of the films and hindering the substrate long-term protection against chemical attack. Corrosion phenomena is present in nearly all current high-tech applications, and hence, the development of advanced coating solutions capable to enhance the performance and durability of bulk materials is a must if these applications want to progress and become competitive.

The main objective of this thesis is the development of corrosion-resistant tantalum nitride (TaN) films by new emerging modulated pulsed power magnetron sputtering (MPPMS) technique. TaN thin films are promising candidates for corrosion applications owing to the exceptional electrochemical stability of tantalum (Ta), comparable to that of noble metals, but they have been barely explored for this purpose so far. The huge complexity of Ta-N system may have limited a more general knowledge attainment on this material. Ta-N shows many stable and metastable phases that motivate the exhibition of completely different properties depending on deposition conditions.

MPPMS belongs to the well-known high power pulsed magnetron sputtering (HPPMS) technologies, which also include high power impulsed magnetron sputtering (HiPIMS). HPPMS techniques generate a highly ionized metal plasma by the application of short pulses with low duty cycle and frequency leading to peak power target densities two orders of magnitude higher than in DCMS. Sputtered material ionizations up to 70 % have been reported during HPPMS, which enables the deposition of well-adherent, high density and low defect thin films. MPPMS was developed in 2006 in order to overcome the deposition rate loss found in HiPIMS process compared to DCMS, which has hindered the replacement of DCMS by HPPMS techniques worldwide.

In this thesis, the application of MPPMS for the industrial development of advanced TaN thin films to be used in corrosion facing applications was explored. For that purpose, an exhaustive study on TaN properties was accomplished.

Initially, the influence of $N_2$ flow on the composition, microstructure and properties of TaN films deposited by MPPMS was investigated, with special focus on corrosion resistance evaluation of these films. The industrial viability of MPPMS technique for the deposition of improved films at high production rates was also explored.

Once a general knowledge on electrochemical behaviour of TaN thin films deposited by MPPMS was obtained, the suitability of TaN coatings to protect metallic substrates in two real applications involving corrosion (namely, biomedical implants and polymer electrolyte membrane fuel cells) was addressed.

Multilayer TaN thin films were deposited by MPPMS to improve the performance and durability of pure titanium (Ti-cp) in biomedical implants. Implants are exposed to "tribocorrosion" phenomena, the synergistic effect of corrosion and wear taking place at the same time at the Ti-cp surface, which is subjected to mechanical loading in contact with body fluids. Tribocorrosion is one of the main failure mechanism of

biomedical implants. Ti-cp possesses excellent chemical stability and biocompatibility in the human body but it has poor mechanical properties which compromises the durability of Ti-cp implants. The evaluation of TaN coated Ti-cp and the comparison with uncoated Ti-cp performance was accomplished in this work.

A polymer electrolyte membrane fuel cell (PEMFC) converts hydrogen and oxygen gases into electricity with water as the only by-product and is considered as one of the most promising clean energy device beyond petroleum. Bipolar plate (BPP) is an important component within the PEMFC, since it provides the electrical connection from cell to cell, distributes gases and removes heat from the active areas. Stainless steel (SS) is the material of choice for the fabrication of BPP for transport applications, but its corrosion resistance and conductivity must be improved to ensure an adequate long-term operation performance. The deposition of TaN coatings by MPPMS for corrosion resistance and electrical properties enhancement was accomplished during this work. The electrochemical and electrical characteristics of TaN coated BPP were investigated in PEMFC simulated environment. A bi-layer coating made of tantalum (Ta) and indium-tin-oxide (ITO) layers was also explored as a coating solution for BPP's protection in PEMFC.

# RESUMEN

Los recubrimientos duros que se utilizan actualmente en la Industria para aumentar la vida útil de distintos componentes, están basados en nitruros metálicos de transición depositados por la técnica de magnetrón sputtering en corriente continua (DCMS por sus siglas en ingles). Sin embargo, y a pesar del elevado número de metales de transición existentes, la mayoría de recubrimientos están formados por uno o dos de los siguientes elementos: titanio, cromo, zirconio y aluminio.

Actualmente, los materiales se enfrentan a fenómenos de degradación por corrosión en multitud de aplicaciones. Las capas delgadas depositadas mediante magnetrón sputtering convencional, generalmente, no cumplen los requisitos necesarios para proteger al material base o substrato de la corrosión durante un periodo de tiempo largo. La microestructura de las capas depositadas por magnetrón sputtering tiende a ser poco densa y exhibe un crecimiento columnar, debido a la baja ionización del plasma generado durante la descarga, características que provocan la penetración de los medios corrosivos a través de los defectos de los recubrimientos, exponiendo el material base al ataque químico . Por ello, el aumento de la ionización del plasma durante el proceso de sputtering es uno de los principales objetivos que se persigue en este campo, con el fin de desarrollar recubrimientos con propiedades mejoradas, capaces de soportar condiciones de trabajo más severas.

El principal objetivo de esta tesis es el desarrollo de recubrimientos protectores frente a corrosión basados en nitruro de Tántalo (TaN) mediante la nueva tecnología conocida como *Modulated pulsed power magnetron sputtering (MPPMS).* Los recubrimientos de TaN tienen un gran potencial para aplicaciones con elevadas exigencias de resistencia a la corrosión, debido a la excelente estabilidad química del Tántalo, comparable a la de los metales nobles. Sin embargo, su comportamiento electroquímico en ambientes corrosivos ha sido poco explorado. La multitud de fases

cristalinas distintas que exhibe el TaN en forma de capa delgada, con sus correspondientes propiedades diferentes, puede ser una de las razones por la cual este recubrimiento sigue siendo un gran desconocido, a diferencia de los ampliamente estudiados TiN, CrN o ZrN.

La tecnología MPPMS es una variante del magnetrón sputtering convencional. Durante MPPMS, la potencia se aplica al blanco de sputtering mediante pulsos cortos de baja frecuencia dando lugar a potencias e intensidades de pico 2 órdenes de magnitud mayores que durante el sputtering convencional. Este fenómeno da lugar a la generación plasmas altamente ionizados, que incluyen un largo número de iones metálicos provenientes del blanco. La energía y la dirección de estos iones, pueden ser, por tanto, controlada mediante la aplicación de campos eléctricos en el portasubstratos, siendo una herramienta muy poderosa para la deposición de capas con propiedades mejoradas. De hecho, los recubrimientos depositados por MPPMS muestran una mayor adherencia, una microestructura más densa y un menor número de defectos que aquellos depositados por magnetrón sputtering convencional.

En esta tesis, se ha estudiado la utilización de la técnica de MPPMS para la deposición de capas de protectoras de TaN frente a corrosión en un sistema de sputtering industrial. Para ello, se llevó a cabo una evaluación exhaustiva de las propiedades de las capas de TaN desarrolladas.

Primeramente, se estudió la influencia del flujo de $N_2$ utilizado como gas reactivo durante el proceso de sputtering, en la composición, microestructura y propiedades de las capas de TaN. Se investigó de manera más profunda la resistencia a la corrosión de las distintas capas de TaN (caracterizadas por distintos contenidos de nitrógeno) en NaCl. Por último, se evaluó la viabilidad industrial de la tecnología de MPPMS para la deposición de recubrimientos.

Una vez adquirido un conocimiento general del comportamiento electroquímico de los recubrimientos de TaN producidos por MPPMS, se exploró la viabilidad de estos recubrimientos como capas protectoras para componentes en dos aplicaciones reales que están sometidas a fenómenos de corrosión: los implantes biomédicos y las pilas de combustible de membrana polimérica.

Se depositaron recubrimientos multicapa de TaN para mejorar el comportamiento y la durabilidad del titanio puro en implantes biomédicos. Los implantes están expuestos al fenómeno conocido como *tribocorrosion*, el cual se define como la degradación irreversible que sufren los materiales por la acción simultanea de procesos de corrosión y desgaste. Los implantes están sometidos a distintos tipos de cargas mecánicas una vez implantados en el cuerpo humano, que además, al ser un medio acuoso da lugar a la aparición de fenómenos corrosivos. La pérdida de material provocada por fenómenos de tribocorrosion es uno de los principales mecanismos de fallo de los implantes. El Titanio puro posee una excelente estabilidad química y biocompatibilidad, pero exhibe una baja estabilidad mecánica que compromete la durabilidad de los implantes fabricados con este material. En esta tesis se llevó a cabo la evaluación del comportamiento de recubrimientos de TaN multicapa sobre Titanio puro y se exploró su potencial para aumentar la durabilidad del mismo como material para la fabricación de implantes. Los resultados se compararon con Titanio puro sin recubrir.

Las pilas de combustible de membrana polimérica (PEMFC, por sus siglas en inglés) son dispositivos electroquímicos que convierten la energía química del hidrogeno en energía eléctrica, siendo el vapor de agua el único residuo generado. Las pilas PEMFC son consideradas una de las alternativas no contaminantes más prometedoras al petróleo para la generación de energía en un futuro próximo. La placa bipolar es uno de los componentes más importantes de la pila dado que conduce la electricidad generada dentro de la misma, distribuye los gases, disipa el

calor y dota de estabilidad mecánica a toda la celda. El acero inoxidable es el material seleccionado para la fabricación de placas bipolares en pilas PEMFC. Sin embargo, la resistencia a la corrosión y la conductividad del acero deben ser mejoradas para el correcto funcionamiento de las placas bipolares a largo plazo. En esta tesis, se desarrollaron recubrimientos TaN mediante MPPMS con el fin de mejorar las propiedades del acero y su durabilidad como material base de la placa bipolar. Se investigaron las propiedades electroquímicas y eléctricas de las placas de acero inoxidable recubiertas con TaN en ambiente simulados de pilas PEMFC. También se exploró el comportamiento de un recubrimiento bicapa formado por una capa de Tántalo (Ta) seguida de una capa de ITO (oxido de indio dopado con estaño) como posible solución para proteger las placas bipolares de acero.

# NOMENCLATURE

## CHAPTER 1

| | |
|---|---|
| PVD | Physical vapor deposition |
| TMN | Transition metal nitrides |
| TMC | Transition metal carbides |
| DCMS | Direct current magnetron sputtering |
| TaN | Tantalum nitride |
| Ta | Tantalum |
| HPPMS | High power pulsed magnetron sputtering |
| HiPIMS | High power impulse magnetron sputtering |
| MPPMS | Modulated pulsed power magnetron sputtering |
| Ti-cp | Pure titanium |
| PEMFC | Polymer electrolyte membrane fuel cell |
| SS | Stainless steel |
| BPP | Bipolar plate |

## CHAPTER 2

| | |
|---|---|
| $n_n$ | Neutral particle density |
| $f_n$ (E) | Energy distribution function of neutral particles |
| $n_e$ | Electron density |
| $f_e$ (E) | Energy distribution function of electrons |
| $n_i$ | Ion density |
| $f_i$ (E) | Energy distribution function of ions |

| | |
|---|---|
| $n_n$ | Plasma density |
| I | Ionization degree |
| $Ar^0$ | Argon atom |
| $Ar^+$ | Argon ion |
| $A^*$ | Excited argon atom |
| $e^-$ | Electron |
| γ | Sputter yield |
| E | Energy of the incident ion |
| $M_1$ | Mass of the incident ion |
| $M_2$ | Mass of target atom |
| $U_s$ | Surface binding energy |
| α | dimensionless parameter |
| $M^0$ | Metal atom |
| $M^+$ | Metal ion |
| $M^*$ | Excited metal atom |
| $G^0$ | Sputtering gas atom |
| $G^*$ | Excited sputtering gas atom |
| λ | Mean free path of an atom in a gas ambient |
| P | Working pressure |
| F | Lorentz force |
| q | charge |
| $\vec{E}$ | Electric field |
| $\vec{B}$ | Magnetic field |
| $\vec{V}$ | Velocity of the particle |
| $B_z$ | Magnetic field in the z-axis |
| $V_b$ | Bias voltaje |

| | |
|---|---|
| $\zeta_{on}$ | Voltaje “on” time of the micropulses (width of the micropulses) |
| $\zeta_{off}$ | Voltaje “off” time of the micropulses (distance between micropulses) |
| $E_{corr}$ | Corrosion potential |
| $I_{corr}$ | Corrosion current |
| F | Faraday’s constant |
| $I_A$ | Anodic current |
| $I_C$ | Cathodic current |
| N | moles involved in corrosion reaction |
| n | moles of electrons involved in corrosion reaction |

## CHAPTER 3

| | |
|---|---|
| CFUBMS | Closed field unbalanced magnetron sputtering |
| GD-OES | Glow discharge optical emission spectroscopy |
| SEM | Scanning electron microscope |
| TEM | Transmission electron microscope |
| FE-SEM | Field emission scanning electron microscope |
| XRD | X-ray diffraction |
| AES | Auger electron spectroscopy |
| NaCl | Sodium chloride |
| PBS | Phosphate buffer solution |
| $H_2SO_4$ | Sulfuric acid |
| CE | Counter electrode |
| RE | Reference electrode |
| WE | Working electrode |
| OCP | Open circuit potential |

| | |
|---|---|
| $E_{oc}$ | Open circuit potential |
| EIS | Electrochemical impedance spectroscopy |
| $E_{pit}$ | Pitting potential |
| $\beta_a$ | Anodic tafel constant |
| $\beta_c$ | Cathodic tafel constant |
| $R_p$ | Polarization resistance |
| M | Atomic weight |
| ρ | Density |
| R | Resistor |
| V | Voltage |
| I | Current |
| Z | Impedance |
| C | Capacitor |
| CPE | Constant phase element |
| Y | Admittance |
| $R_s$ | Solution resistance |
| $R_{ct}$ | Charge transfer resistance |
| $C_{dl}$ | Double layer capacitance |
| $C_c$ | Coating capacitance |
| $R_{pore}$ | Coating resistance through the pores |
| P | total applied load |
| $W_E$ | energy invested in the deformation and elastically recovered |
| $W_T$ | total energy invested in the deformation |
| $h_r$ | residual depth of the indentation |
| $h_t$ | maximum penetration depth |

## CHAPTER 4

| | |
|---|---|
| $P_{av}$ | Average power |
| $V_p$ | Peak voltage |
| $I_p$ | Peak current |
| $P_p$ | Peak power |
| F | Frequency |
| P | Porosity |

## CHAPTER 5

| | |
|---|---|
| $W_{tr}$ | Total material loss due to tribocorrosion |
| $W^m_{act}$ | Material loss due to mechanical loading in corrosion environment |
| $W^c_{act}$ | Material loss due to corrosion under wear processes |
| $R_{pass}$ | Polarization resistance of the passive material |
| $r_{pass}$ | Specific polarization of passive material |
| $A_0$ | Total surface area |
| $i_{pass}$ | Corrosion current of a passive material |
| B | Constant |
| $E_{oc}$ | Equilibrium potential |
| $E^s_{oc}$ | Potential during sliding |
| $A_{tr}$ | Surface area of the wear track |
| $A_{act}$ | Active surface area |
| $A_{pass}$ | Passive surface area |
| $t_{rot}$ | Rotation period |
| $t_{react}$ | Repassivation time |

| | |
|---|---|
| $R_{ps}$ | Polarization resistance during sliding |
| $R_{act}$ | Polarization resistance inside the wear track |
| $r_{act}$ | Specific polarization resistance of the active area |
| $t_{lat}$ | Period between two successive cycles |
| d | density |
| μ | Friction coefficient |
| FTT | Fast fourier transform |

## CHAPTER 6

| | |
|---|---|
| $W_{ele}$ | Electrical work |
| $Q_{heat}$ | Heat |
| MEA | Membrane electrode assembly |
| PTFE | Polytetrafluoroethylene |
| CL | Catalyst electrode layers |
| HOR | Hydrogen oxidation reaction |
| ORR | Oxygen evolution reaction |
| GDL | Gas diffusion layer |
| MPL | Micro-porous layer |
| ICR | Interfacial contact resistance |
| $V_{SHE}$ | Potential vs standard hydrogen electrode (SHE) |
| DoE | US Department of Energy |
| ITO | Indium-tin-oxide |

# LIST OF FIGURES

**Fig 2. 1:** The four states of matter: solid, liquid, gas and plasma (taken from [19]) ..... 62
**Fig 2. 2:** Schematic illustration of sputtering process ..... 63
**Fig 2. 3:** Voltage-current relationship in plasma discharges (taken from [18]) ..... 65
**Fig 2. 4:** Ionization of different sputtered materials with increasing electron density of plasma discharge (taken from [20]) ..... 66
**Fig 2. 5:** An example of planar magnetron conFiguration (taken from [24]) ..... 68
**Fig 2. 6:** The most common magnetron conFigurations in sputtering processes ..... 69
**Fig 2. 7:** Power vs time in DCMS, HiPIMS and MPPMS discharges ..... 72
**Fig 2. 8:** A comparison of the metal ionization vs pulse time during HiPIMS for different target materials (taken from [31]. ..... 73
**Fig 2. 9:** Voltage-current waveforms during HiPIMS discharge in MIDAS 450 system ..... 74
**Fig 2. 10:** Cross-sectional SEM images of CrN films deposited on Si by HPPMS at different peak target currents (taken from [38]) ..... 75
**Fig 2. 11:** Deposition rate for DCMS and HiPIMS discharges for different target materials (taken from [31]) ..... 76
**Fig 2. 12:** Voltage-current waveforms developed during MPPMS discharge in MIDAS 450 system ..... 78
**Fig 2. 13:** Schematic theoretical explanation of pulse shape generation during MPPMS ..... 79
**Fig 2. 14:** Ion energy distributions of Cr+, Ar+ and Cr2+ ions measured from MPP plasma with different peak currents and dc plasma during non-reactive sputtering of Cr (taken from [47]) ..... 81
**Fig 2. 15:** Cross-sectional SEM micrographs of the Ta coatings deposited at increasing negative substrate bias voltages, from 0V (a) to – 70V (d). Taken from [48]. ..... 82
**Fig 2. 16:** Normalized optical emission spectra recorded at d=1 cm from the Nb target powered by HiPIMS, MPPMS and DCMS in ArGON at p=1 Pa and at the average power P=300 W. (taken from [52]) ..... 83
**Fig 2. 17:** Average power-normalized deposition rate for NbOX coatings prepared by DCMS, HiPIMS and MPPMS as a function of oxygen flow (taken from [53]) ..... 84
**Fig 2. 18:** Naturally formed oxide layer on top of metallic materials exposed to moisture ..... 86

**Fig 2. 19:** Corrosion process taking place at iron metal surface (taken from [58]) ..... 88

**Fig 3. 1:** MIDAS 450 sputtering system ..... 106
**Fig 3. 2:** Zpulser SOLO and VESTA power supplies ..... 107
**Fig 3. 3:** ISO-TECH oscilloscope employed for V-I waveforms monitoring ..... 108
**Fig 3. 4:** Zpulser SOLO software employed for MPPMS discharge management ..... 109
**Fig 3. 5:** GD-OES equipment used for TaNx coatings composition analysis ..... 110
**Fig 3. 6:** FE-SEM microscope used for TaNx films analysis ..... 111
**Fig 3. 7:** Three-electrode electrochemical cell connected to a potentiostat ..... 116
**Fig 3. 8:** Potentiodynamic polarization plot including different active-passive regions ..... 120
**Fig 3. 9:** Sample Tafel plot from a potentiodynamic polarization scan ..... 121
**Fig 3. 10:** Impedance vector ..... 125
**Fig 3. 11:** Nyquist and Bode plots obtained from EIS analysis ..... 126
**Fig 3. 12:** Nyquist and Bode plots associated to Randles equivalent circuit ..... 128
**Fig 3. 13:** Randles circuit used to model an uncoated metallic substrate ..... 129
**Fig 3. 14:** Randles circuit used to model a coated metal with a non-porous thin film ..... 130
**Fig 3. 15:** Nyquist and Bode plots associated to two time constant equivalent circuit ..... 131
**Fig 3. 16:** Two time constant equivalent circuit used to model a coated metal with a porous thin film ..... 132
**Fig 3. 17:** Fischerscope H100VP nanoindenter ..... 133
**Fig 3. 18:** Schematic of a typical load – unload nanoindentation curve (taken from [20]) ..... 134
**Fig 3. 19:** Perthometer M2 profilometer of Mahr ..... 135

**Fig 4. 1** V-I characteristics of different MPPMS pulses employed for TaNx plasma discharge .. 146
**Fig 4. 2:** Deposition rate vs N2-to-Ar ratio ..... 149
**Fig 4. 3:** Chemical composition of TaNx films deposited at different N2-to-Ar ratios ..... 150
**Fig 4. 4:** XRD patterns of the TaNx films deposited at different N2-to-Ar ratios ..... 152
**Fig 4. 5:** Cross sectional and surface SEM micrographs of a), e) Ta; b), f) TaN_0.25; c), g) TaN_0.625 and d), h) TaN_1, respectively ..... 154
**Fig 4. 6:** Hardness and roughness values for TaNx films deposited at different N2-to-Ar ratios. 155
**Fig 4. 7:** Nyquist diagrams obtained for AISI 316L and TaNx films after EIS measurements at 4 h and 168 h of immersion ..... 157

**Fig 4. 8:** Bode plots obtained for AISI 316L and TaNx coatings from impedance measurements after 4 h and 168 h of immersion ..... 159
**Fig 4. 9:** Randles equivalent circuit used for fitting the EIS experimental data obtained for a) AISI 316L and b) Ta, TaN_0.25 and TaN_0.625 ..... 161
**Fig 4. 10:** Equivalent circuit used for fitting the EIS experimental data obtained for TaN_1 film 162
**Fig 4. 11:** Current vs applied potential for AISI 316L and TaNx films in NaCl 0.06 M after 192 h of immersion ..... 165
**Fig 4. 12:** Polarization resistance and porosity of AISI 316L and TaNx films deposited at different N2-to-Ar ratios..... 169

**Fig 5. 1:** Schematic representation of tribocorrosion phenomena, illustrating corrosion accelerated by friction and wear and abrasion accelerated by corrosion products ..... 189
**Fig 5. 2:** Voltage–current characteristics of different pulse shapes applied for TaN film deposition ..... 192
**Fig 5. 3:** Experimental set-up for tribocorrosion analysis used in this study ..... 194
**Fig 5. 4:** Schematic view of a circular tested sample before sliding (A0) and during sliding showing the wear track ..... 196
**Fig 5. 5:** Cross-sectional and top view of the wear track area generated during sliding ..... 198
**Fig 5. 6:** Schematic theoretical representation of TaN film microstructure..... 201
**Fig 5. 7:** Cross-sectional SEM micrographs of a) TaN monolayer, b) TaN multilayer_1, and c), TaN multilayer_2 films ..... 202
**Fig 5. 8**: Cross sectional TEM micrographs a) TaN monolayer, b) TaN multilayer_1, and c), TaN multilayer_2 films ..... 203
**Fig 5. 9:** Cross-sectional TEM micrographs a) TaN monolayer and b) TaN multilayer_2 films and corresponding FTTs for c) TaN monolayer and d)TaN multilayer_2 films at high magnification..... 205
**Fig 5. 10:** Bode plots obtained from EIS data at different immersion times for a) Ti-cp, b)TaN monolayer, c)TaN multilayer_1 and d)TaN multilayer_2 ..... 207
**Fig 5. 11:** Randles circuit applied for EIS data modeling ..... 209
**Fig 5. 12:** Evolution of corrosion resistance with time..... 211
**Fig 5. 13:** Potentiodynamic polarization curves obtained for uncoated Ti-cp and TaN films after 192 h of immersion in PBS+albumin solution..... 212

**Fig 5. 14:** Evolution of open circuit potential ($E_{oc}$) before, during and after sliding..... 213
**Fig 5. 15:** Nyquist plots obtained from EIS data a) before and b) during sliding ..... 215
**Fig 5. 16**: Bode plots obtained from EIS data before a), b) and during c), d) sliding..... 216
**Fig 5. 17:** Friction coefficient monitored during Wear test 2 (2600 cycles) ..... 218
**Fig 5. 18:** SEM images of wear tracks after tribocorrosion tests for a) Ti-cp, b) TaN monolayer, c) TaN multilayer_1 and d) TaN multilayer_2..... 220
**Fig 5. 19:** Determined total material loss ($W_{tr}$) from wear tracks volume after tribocorrosion tests ..... 221

**Fig 6. 1:** A schematic representation of operation principle of a PEMFC (taken from [6]) ..... 239
**Fig 6. 2:** Cross sectional overview of PEMFC components (taken from [7])..... 241
**Fig 6. 3:** Voltage-current characteristics of pulse 996 applied during TaNx coating deposition . 249
**Fig 6. 4:** Electrochemical set-up for ex-situ testing of TaNx coated SS316L in PEMFC environment..... 250
**Fig 6. 5:** Experimental set-up for ICR measurement between TaNx coated SS316L samples and GDL ..... 251
**Fig 6. 6:** Cross-sectional SEM micrographs of a) Ta, b)TaN_0.25, c) TaN_0.625 and d) TaN_1 coatings ..... 252
**Fig 6. 7:** Current-potential relation during potentiodynamic measurements at a) pH 3 and b) pH 6 ..... 254
**Fig 6. 8:** Potentiostatic tests (5 min) at 1 VSHE in pH 3 electrolyte of TaNX (N2-to-Ar ratio 0, 0.25, 0.625 and 1) coated on SS316L and non-coated SS316L..... 256
**Fig 6. 9:** Potentiostatic tests (5 min) at 1.4 VSHE in pH 3 electrolyte of TaNx (N2-to-Ar ratio 0, 0.25, 0.625 and 1) coated on SS316L and non-coated SS316L..... 256
**Fig 6. 10:** 11 ICR at 140 N cm-2 before and after polarization tests in pH 3 electrolyte (5 min) at different potentials for TaNx coated- and non-coated SS316L..... 257
**Fig 6. 11:** Potentiostatic tests (5 min) at 1.4 VSHE in pH 6 electrolyte of TaNx (N2-to-Ar ratio 0, 0.25, 0.625 and 1) coated SS316L and non-coated SS316L. ..... 258
**Fig 6. 12:** 11 ICR at 140 N cm-2 before and after polarization tests at 1.4 VSHE (5 min) in varying pH electrolytes (3 and 6) for TaNx coated- and non-coated SS316L..... 259
**Fig 6. 13:** Potentiostatic tests at 1.4 VSHE for 180 min in pH 3 electrolyte for TaNx coated and non-coated SS316L ..... 261

**Fig 6. 14:** ICR measurements at 140 N cm-2 for pre- and post-potentiostatic tests (1.4 VSHE, 180 min, pH 3 electrolyte) for TaNx coated and non-coated SS316L ..... 262
**Fig 6. 15:** AES results showing the change in barrier layer thickness and composition before and after polarization for each TaNx coating ..... 264
**Fig 6. 16:** Cross-sectional micrograph of bi-layer Ta_ITO coating..... 268
**Fig 6. 17:** Potentiostatic tests at 1.4 VSHE for 180 min in pH 3 electrolyte for metallic Ta and Ta_ITO films ..... 269
**Fig 6. 18:** ICR values at 140 N cm-2 measured for Ta and Ta_ITO films before and after polarization tests at 1.4 VSHE during 5 and 180 minutes ..... 270

# LIST OF TABLES

**Table 2. 1**: Comparative study between DCMS, HiPIMS and MPPMS discharges ..... 80

**Table 3. 1:** Elements used in equivalent circuit modelling ..... 127

**Table 4. 1:** Different MPPMS pulse shape employed for different plasma features generation during TaNx deposition discharge..... 144
**Table 4. 2:** Pulsing parameters for each pulse ..... 147
**Table 4. 3:** Deposition conditions for TaNx films. Thickness value: $\mathbf{X} = \mathbf{X} \pm \mathbf{2}\boldsymbol{\sigma}$ ..... 148
**Table 4. 4:** EIS data of AISI 316L and TaNx coatings obtained by equivalent circuit modelling at different immersion times..... 163
**Table 4. 5:** Tafel analysis from polarization curve data for TaNx films ..... 166
**Table 4. 6:** Experimental data for porosity calculation using equation [4.2]..... 168
**Table 4. 7:** Polarization resistance values obtained after electrochemical testing for AISI 316L and $TaN_x$ coatings in NaCl 0.06 M. ..... 171

**Table 5. 1:** Biomaterials application fields and type of implants ..... 180
**Table 5. 2:** Mechanical properties and toxic effects due to ion release shown by conventional biomaterial metallic alloys ..... 183
**Table 5. 3:** Pulse length, frequency and resulting peak power, voltage and current values during each pulse shape application..... 192
**Table 5. 4:** Pulse repeat duration, bilayer period and hardness of each TaN film ..... 193
**Table 5. 5**: EIS data of Ti-cp and TaN coatings obtained by equivalent circuit modelling using Randles circuit at different immersion times..... 210
**Table 5. 6:** EIS data of Ti-cp and TaN coatings before and during sliding obtained by equivalent circuit modeling using Randles Circuit ..... 217
**Table 5. 7:** Depth and width of the wear track of Ti-cp and TaN coatings after tribocorrosion tests ..... 219
**Table 5. 8:** Total material loss measured after tribocorrosion tests for Ti-cp and TaN coatings 220
**Table 5. 9:** Experimental parameters obtained during testing to calculate material loss due to corrosion mechanism..... 222

**Table 5. 10:** Intrinsic parameters of tested materials ..... 223
**Table 5. 11:** Total material loss (Wtr), material loss caused by electrochemical corrosion (Wc) and material loss caused by mechanical degradation (Wm) after tribocorrosion tests ..... 223
**Table 5. 12**: Electrochemical and mechanical features measured for TaN coatings and uncoated Ti-cp during tribocorrosion testing ..... 226

**Table 6. 1:** Pulsing parameters of MPPMS discharge during TaNx deposition ..... 249
**Table 6. 2:** Passive oxynitride layer thickness and composition of $TaN_X$ coatings after polarization at 1.4 $V_{SHE}$ for 180 min in pH 3 electrolyte ..... 265
**Table 6. 3:** Deposition parameters during Ta and ITO layers growth ..... 268
**Table 6. 4**: Corrosion current and ICR measured for different TaNx and Ta_ITO films in PEMFC simulated environment. ..... 273

# PUBLICATIONS

**Effect of $N_2$ flow rate on the microstructure and electrochemical behaviour of $TaN_X$ films deposited by modulated pulsed power magnetron sputtering**
*L. Mendizabal, R. Bayón, E. G-Berasategui, J. Barriga, J.J. Gonzalez*
Thin Solid Films 610 (2016) 1-6

**Tribocorrosion response in biological environments of multilayer TaN films deposited by HPPMS**
*L. Mendizabal, A. Lopez, R. Bayón, P. Herrero-Fernandez, J. Barriga, J.J. Gonzalez*
Surface & Coatings Technology 295 (2016) 60–69

**$TaN_x$ coatings deposited by HPPMS on SS316L bipolar plates for polymer electrolyte membrane fuel cells: Correlation between corrosion current, contact resistance and barrier oxide film formation**
*Lucia Mendizabal, Anders Oedegaard, Ole Edvard Kongstein, Sigrid Lædre, John Walmsley, Javier Barriga, Javier Jesus Gonzalez*
Accepted in International Journal of Hydrogen Energy

# Outline

**AGRADECIMIENTOS** ..... 2

**SUMMARY** ..... 6

**RESUMEN** ..... 10

**NOMENCLATURE** ..... 14

**LIST OF FIGURES** ..... 20

**LIST OF TABLES** ..... 26

**PUBLICATIONS** ..... 28

CHAPTER 1 ..... 34

INTRODUCTION ..... 34

**1. Thin films** ..... 36

**2. Challenges in thin films for harsh environments** ..... 37

**3. Tantalum nitride films** ..... 39

**4. Modulated pulsed power magnetron sputtering** ..... 40

**5. Motivation of this work** ..... 42

**6. Objectives** ..... 45

**7. Organization of the thesis** ..... 47

**7. References** ..... 50

CHAPTER 2 ..... 56

THEORETICAL BACKGROUND ..... 56

**1. Materials** ..... 58

**1.1 Tantalum** ..... 58

**1.2 Tantalum nitride** ..... 60

**2. Sputtering technologies** ..... 61

**2.1 Fundamentals** ..... 61

**2.1.1 The plasma** ..... 61

**2.1.2 Sputtering process** ..... 63

**2.1.3 Ionization processes** ..... 66

**2.2. DC Magnetron sputtering** ..... 67

**2.2.1 Definition** ..... 67

**2.2.2 Drawbacks** ..... 70

**2.3 HiPIMS** ..... 73

**2.4 MPPMS** ..... 77

**2.4.1 Principle** ... 77
**2.4.2 Advantages of MPPMS** ... 80
**3. Corrosion** ... 85
**3.1 Definition** ... 85
**3.2 Corrosion process** ... 86
**3.3 Corrosion modes** ... 91
**3.4 Advantages of HPPMS techniques for the deposition of corrosion protective coatings** ... 93
**4. References** ... 96
CHAPTER 3 ... 104
DEPOSITION SYSTEM & CHARACTERIZATION TECHNIQUES ... 104
**1. MIDAS 450 sputtering system** ... 106
**2. Characterization techniques** ... 108
**2.1. MPPMS discharge characteristics** ... 108
**2.2. Techniques for studying thin films microstructure and composition** ... 109
**2.2.1 Glow discharge – Optical Emission Spectroscopy (GD-OES)** ... 109
**2.2.2 Scanning electron microscope (SEM)** ... 111
**2.2.3 Transmission electron microscope (TEM)** ... 112
**2.2.4 X-Ray Diffraction (XRD)** ... 113
**2.2.5 Auger Electron Spectroscopy (AES)** ... 114
**2.3. Techniques for studying thin film properties** ... 115
**2.3.1 Techniques for studying corrosion** ... 115
*2.3.1.1 Open circuit potential (OCP) measurements* ... 117
*2.3.1.2 Polarization techniques* ... 117
*2.3.1.3 Electrochemical impedance spectroscopy* ... 123
**2.3.2 Hardness measurements** ... 133
**2.3.3 Roughness measurements** ... 135
**3. References** ... 137
CHAPTER 4 ... 140
GENERAL EVALUATION OF $TaN_X$ FILM PROPERTIES DEPOSITED BY MPPMS ... 140
**1. Introduction** ... 142
**2. Pulse shapes for $TaN_X$ deposition** ... 143
**3. Effect of $N_2$-to-Ar ratio on the $TaN_x$ films characteristics** ... 148
**3.1. $TaN_x$ coating deposition** ... 148

**3.2 $TaN_x$ coating characterization** ..... 149
**3.2.1. Deposition rate** ..... 149
**3.2.2. Film microstructure and composition** ..... 150
**3.2.3. Hardness and roughness** ..... 155
**3.2.4. Electrochemical behavior of $TaN_x$ films** ..... 156
*3.2.4.1 Electrochemical impedance spectroscopy (EIS)* ..... 156
*3.2.4.2 Potentiodynamic polarization* ..... 165
**4. Conclusions** ..... 169
**5. References** ..... 172
CHAPTER 5 ..... 178
MULTILAYER $TaN_X$ FILMS FOR TITANIUM IMPLANTS PROTECTION AGAINST TRIBOCORROSION ..... 178
**1. Introduction** ..... 180
**2. Corrosion and tribocorrosion phenomena in biomedical implants** ..... 185
**2.1. Corrosion** ..... 185
**2.2. Tribocorrosion** ..... 187
**3. Protection of Ti-cp by multilayer TaN films** ..... 190
**3.1. Multilayer TaN film deposition by MPPMS** ..... 190
**3.2. Simulated body fluid environment and testing protocol for tribocorrosion** ..... 193
**3.3. Multilayer TaN film characterization** ..... 200
**3.3.1. Microstructure characterization** ..... 200
**3.3.2 Hardness measurements** ..... 206
**3.3.3 Corrosion resistance evolution** ..... 206
**3.3.4. Tribocorrosion performance** ..... 213
**4. Conclusions** ..... 224
**5. References** ..... 227
CHAPTER 6 ..... 236
TANTALUM BASED FILMS FOR BIPOLAR PLATE PROTECTION IN PEMFC ..... 236
**1. Introduction** ..... 238
**2. PEMFC components** ..... 241
**3. Corrosion phenomena in bipolar plates** ..... 243
**4. Protective films for stainless steel bipolar plates** ..... 245
**4.1. Introduction** ..... 245

**4.2 Experimental development of $TaN_X$ films by MPPMS to protect SS bipolar plates in cathode side of PEMFC** ..... 248
**4.2.1 $TaN_X$ film deposition** ..... 248
**4.2.2 $TaN_X$ film characterization equipment in PEMFC simulated environment** ..... 250
**4.2.3 $TaN_x$ film performance in PEMFC environment** ..... 252
*4.2.3.1 Potentiodynamic measurements at different pH values.* ..... 253
*4.2.3.2 Potentiostatic measurements with different variable parameters* ..... 255
*4.2.3.3 AES measurements for barrier oxide features analysis* ..... 263
**4.3 Experimental development of bi-layer Ta_ITO coating to protect SS bipolar plates in cathode side of PEMFC** ..... 266
**4.3.1. Ta_ITO film deposition** ..... 267
**4.3.2. Ta_ITO film performance in PEMFC environment** ..... 268
**4.4. Conclusions** ..... 271
**6. References** ..... 274
CHAPTER 7 ..... 278
GENERAL CONCLUSIONS ..... 278
& PERSPECTIVES ..... 278
**1. Overall conclusions** ..... 280
**2. Future perspectives** ..... 283

# CHAPTER 1

# INTRODUCTION

# 1. Thin films

Thin films deposited by physical vapour deposition (PVD) technologies are widely applied today in a huge number of applications where specific surface properties of the materials are required [1-2]. Thin films are layers of material with a thickness ranging from a few atomic layers (~nm) to a few micrometers. The importance of thin films relies on the exhibition of completely different properties compared to those of bulk materials enabling the modification or enhancement of substrate functionality. They do not generally affect the properties of bulk material but they can, however, totally change the thermal, mechanical, electrochemical, magnetic, electrical and optical properties of the substrate surface.

Protective hard thin films based on transition metal nitrides (TMN) and carbides (TMC) [3] have been deposited on cutting tools deployed in machining or drilling for years, motivated by a huge increase of their service lifetime due to improved hardness, toughness and wear-, erosion- and oxidation/corrosion resistance compared with uncoated tools. Such properties are also required in automotive and aerospace applications, where the durability of many components is hindered by the harsh mechanical and environmental (corrosion, high temperature…) conditions they are subjected to.

Fine tuning of optical and electrical properties of tailored thin films has enabled a widespread utilization of thin films as mirrors, antireflective and low emissivity coatings in glass industry (eyewear, architectural and automotive windows), and transparent conductive oxide coatings in opto-electronic devices (solar cells, touch panels, LEDs and OLEDs), just to name a few applications [4]. Possibly, the main application of thin films is found in semiconductor devices and microelectronics where both conductive and dielectric thin films are crucial parts of integrated circuits [5].

It should be noticed, that the above-mentioned list of thin film applications is limited and by far not exhaustive. In fact, thin films are steadily extending their application domains.

Among PVD technologies, magnetron sputtering is considered the state-of-the-art technology attending to its reliability in terms of industrial production and its potential for the deposition of almost any material from those with high melting points to metal alloys and dielectric materials [2].

Nevertheless, the industry is continuously demanding thin films with improved properties and therefore, an active research is ongoing in the development of new structures, materials and deposition technologies capable to fulfill the special requirements and withstand the increasingly severe conditions present in current and future high-tech applications [6].

## 2. Challenges in thin films for harsh environments

Transition metal nitride films (TMN) deposited by magnetron sputtering are currently a general procedure in many applications owing to the increased performance and durability of coated components. However, nearly all the coating solutions are focused on a limited number of metals, namely, combinations of titanium (Ti), aluminum (Al), chromium (Cr) and zirconium (Zr) metals in binary and ternary nitride forms, while other potentially attractive compounds are overlooked. The same situation is found when it comes to scientific publications related to these materials. TiN, CrN, TiAlN, CrAlN, ZrN and ZrCN have been extensively studied during the last decades in terms of mechanical, tribological, electrical, corrosion and oxidation performance.

It is true that these “conventional” materials deposited by direct current magnetron sputtering (DCMS) as hard protective coatings can meet the established demands for tribological applications (including wear, erosion and abrasion resistance). These coatings can also enhance the corrosion and oxidation resistance of the uncoated substrate. Nevertheless, the main weakness of conventional magnetron sputtering techniques remains to be the development of highly corrosion resistance thin films. Even if great advantages have been made to improve this property in sputtered films (namely, development of amorphous films and fabrication of multilayer structure films), the typical columnar structure and the presence of defects, voids and pores along the coating thickness represent a direct pathway for the corrosive or oxidizing agents towards the substrate, jeopardizing corrosion protection after long time exposure [7]. The low ionization degree of sputtered particles (< 5%) during DCMS prevents the control of the direction and the energy of the material flux towards the substrate by external electric and/or magnetic fields [8-9]. This feature results in deposition of low density films containing pores and defects that are directly responsible for the not good enough corrosion resistance of the sputtered films [10-11].

Besides the importance of the microstructure on corrosion performance of a given thin film, the coating material itself represents an essential characteristic [12]. The metallic materials (including metallic based thin films) immersed in corrosive solutions tend to form an oxide barrier layer on top of their surfaces. This oxide is the first layer material facing the corrosive constituents in the solution. If this metal oxide layer is porous and electrochemically active, the corrosion resistance of the material will be low. Contrary, if the metal oxide is dense and stable, the corrosion resistance of the metallic material should be high unless protective oxide starts to break down.

Hence, two main features should be considered if a coating solution development for harsh environments is envisioned.

- Thin films should be made from one of the most electrochemically stable metallic materials available
- A strategy to deposit defect-free high density thin films should be addressed.

An electrochemically reliable coating deposited by magnetron sputtering capable to face satisfactorily corrosion phenomena has yet to become a reality.

## 3. Tantalum nitride films

Tantalum nitride (TaN) thin films belong to the TMN family group and have been studied rather extensively as structural elements in integrated circuits. At present, the principal use of TaN thin films is found in resistors and diffusion barriers in microelectronics industry [13-14].

As a transition metal nitride film, TaN owns exceptional features such as high melting point, high hardness, excellent mechanical properties and an extraordinary chemical stability. The tribological performance evaluation of TaN films has been reported by several authors [15-16]. Nevertheless, the electrochemical features evaluation of TaN coatings remains rather unexplored regardless of being Tantalum (Ta) one of the most inert metals in the periodic table.

Most metals are prone to corrosion in acids, while Ta is not attacked by acids or other strong chemicals. At temperatures below 150 ºC, Ta is completely stable in any aggressive environment except for hydrofluoric acid. Furthermore, Ta possess an outstanding biocompatibility and it neither reacts with body fluids nor generates adverse tissue reaction. The exceptional corrosion resistance of metal Ta to aggressive media is due to the spontaneous formation of an impervious stable and well-adherent tantalum pentoxide ($Ta_2O_5$) barrier layer on the metal surface [17].

The lack of information in TaN properties may be caused by the huge complexity of Ta-N system. While Ti-N and Cr-N systems are relatively simple with only two compounds such as tetragonal $Ti_2N$ and cubic TiN and hexagonal hcp-$Cr_2N$ and CrN, respectively, Ta-N exhibits many different stable and metastable phases [16, 18-19]. This complexity certainly gives rise to completely different mechanical, electrical and electrochemical features depending on composition, deposition technology and deposition process parameters and it is likely responsible for the absence of more general knowledge about TaN promising coating material.

## 4. Modulated pulsed power magnetron sputtering

Many attempts have been made in order to increase the sputtered material ionization during magnetron sputtering discharges that would promote a better control of material flux towards the substrate enabling a fine-tuning of film properties. Traditionally, the utilization of a hollow cathode or the application of a second discharge inside the chamber (by inductive coils, ion sources or microwaves applicator) have been employed for this purpose [20, 21]. However, these techniques never succeed in widespread industrialization due to the complexity of the deposition apparatus.

More recently, the so-called high power pulsed magnetron sputtering (HPPMS) technologies were developed including the initial high power impulse magnetron sputtering (HiPIMS) and the later modification known as modulated pulsed power magnetron sputtering (MPPMS). HPPMS techniques have gained increasing interest among both academia and industry, since they are considered as the best alternative for scalable solution in terms of enhanced ionization in magnetron sputtering based techniques [20, 22]. HPPMS discharge is created by simply exchanging DC power

supply with HPPMS power supply within the same deposition chamber, making easy the conversion of “conventional” sputtering system in new advanced HPPMS deposition equipment.

The basic idea behind HPPMS techniques is based on reaching a higher plasma ionization by increasing the power applied to the magnetron target. HPPMS generates a highly ionized metal plasma by the application of short pulses of low duty cycle and frequency leading to peak power target densities of kW $cm^{-2}$ (two orders of magnitude higher than DCMS). The pulses are repeated periodically to produce an average power that is comparable to that normally used in DCMS, to prevent target overheating [22]. Sputtered material ionization degrees from 20% to 70% depending on target material have been reported during HPPMS discharge [23-25]. The possibility to control the high flux of metal ions in HPPMS plasmas has turned into a new and unique tool to tailor the microstructure and properties of deposited films as demonstrated in both lab- and industrial-scale sputtering systems all over the world [22, 26-31].

HiPIMS was firstly introduced by Kouznetsov et al. in 1999 [32]. Henceforth, HiPIMS discharges have been theoretically studied thoroughly in lab scale sputtering systems. During the last decade, thin films deposited by HiPIMS at industrial scale have become a reality. However, the deposition rate for the HiPIMS films compared to films deposited by conventional DCMS at the same average power is much lower due to the “self-sputtering” effect [33-35]. Self-sputtering process occurs when ionized sputtered material is attracted back to the cathode and feeds the discharge (contributes to the sputtering process) instead of being deposited on the substrate, strongly decreasing the deposition rate of HiPIMS process. Besides, there is a great concern about the stability of HiPIMS process when such high peak current densities are generated and arcing continuously occurs.

In order to overcome these problems, the so-called modulated pulsed power magnetron sputtering (MPPMS) was developed in 2006 [36]. The main difference between HiPIMS and MPPMS is the magnitude, duration and shape of the pulses, which are created by different power supplies. A typical HiPIMS pulse is a short (50–200 μs) and unique pulse which develops very high peak power densities, whereas the MPPMS pulse is much longer (500–3000 μs) and can be modulated in different steps and generally exhibits lower peak power densities than HiPIMS [22]. Even though the peak power during MPPMS is not as high as in HiPIMS approach, it can still produce a high degree of ionization of sputtered particles [25]. More importantly, the deposition rate of MPPMS is not reduced compared to DCMS but even increased under certain conditions and sputtered materials as demonstrated in [37-39]

MPPMS generates a high density plasma by the superimposition of two or more (up to six) micropulses within one overall custom-shaped macropulse [40-41]. This versatility in pulse shape modification allows the development of different ionization stages during the macropulse to guarantee a stable highly ionized discharge regardless of sputtered material. Typically, a macropulse containing two micropulses is applied during film deposition discharge. The first micropulse is characterized by low peak current density to ignite the plasma in a stable manner followed by a high peak current density micropulse as the main ionization stage. Arcing phenomena has turned up easier to control when MPPMS technique is applied instead of HiPIMS.

## 5. Motivation of this work

At present, a vast number of technological applications involve corrosion degradation phenomena, which eventually limits material performance and is considered as one of the critical factors hindering new emerging technologies to step further. An

exhaustive evaluation of tantalum nitride (TaN) thin films deposited by MPPMS technique for corrosion protection of different metallic substrates in specific applications is the principal purpose of this thesis. The benefits of TaN material itself coupled with the utilization of MPPMS technique for the development of advanced corrosion-resistant thin films, briefly summarized above, are the main motivation for this work.

Corrosion processes are found in nearly all application sectors. Simply the humidity causes corrosion in materials expose to ambient atmosphere. Automotive internal combustion engines produce water vapour and exhaust gases, which condense in internal areas and lead to the degradation of metal parts. Implants face severe corrosive environment of the human body, including blood and body fluids. Metallic components used for the construction of nuclear plants, steam power plants, off-shore wind power and concentrated solar power deal with extremely harsh environments every day, where corrosion and oxidation phenomenon are critical. Plastic and food industry also encountered corrosion during processing.

It should be stressed, that the demand for better-performing and enhanced durability materials (i.e. high wear-corrosion-resistant and non-degradable materials) is ever-increasing to enable the production of more efficient and durable vehicles, aircrafts, implants and power plants, just to name a few representative products.

Clearly it is impossible to address all the applications mentioned above within this thesis, but the suitability of TaN thin films deposited by MPPMS to protect metallic substrates in two high-tech demanding applications is evaluated and serves as a driving force and motivation for the current work.

***Biomedical implants***

Pure titanium (Ti-cp) is commonly used today as an implant material owing to its low Young modulus (comparable to that of bone), superior biocompatibility and excellent

corrosion resistance. Nevertheless, Ti-cp exhibits poor wear resistance and high coefficient of friction. Biomedical implants are a general routine nowadays, and they exhibit excellent success rates for 10-15 years. However, they are not designed for serving properly much longer and the life expectancy increase is demanding long-term durability implants capable to work for much longer period of time without failure. Implants are exposed to which is known as “tribocorrosion”, the synergistic effect of wear and corrosion degradation processes together, because they are subjected to mechanical loading in body fluids aggressive environment. The main drawbacks to ensure longer lifetime for the implants are the lack of biocompatibility caused by the release of metal ions and the material loss due to tribocorrosion. Increasing Ti-cp biomaterial performance is explored by the application of multilayer TaN thin films by MPPMS.

***Polymer electrolyte membrane fuel cells***

Polymer electrolyte membrane fuel cells (PEMFC) are one of the most promising candidates as the next generation power sources using hydrogen as fuel to generate green electricity for transport applications. PEMFC electric vehicles are currently a technological reality but several components performance and durability must be enhanced for a widespread commercialization. The bipolar plate (BPP) is a crucial component in PEMFC since it acts as the current conductor between cells, provides conduits for reactant gases flow, removes heat and constitutes the backbone of a power cell stack. BPPs must be highly corrosion resistance in acidic environment and electrically conductive. Stainless steel (SS) is the material of choice for transport applications but its chemical stability in PEMFC environment needs to be improved for enhanced durability. Furthermore, the passive oxide film formed on top of SS bipolar plate during operation reduces its conductivity and hence, fuel cell efficiency. The evaluation of TaN coated SS bipolar plates is accomplished during this thesis in order to enhance PEMFC performance and lifetime.

Last but not least, the industrial viability demonstration of MPPMS technique for the production of high density corrosion-resistant thin films, using TaN coating as a proof of concept, encourages the attainment of this thesis. The low deposition rate and process stability problems found in HiPIMS discharges, have constrained this technology to stand in for DCMS as the new technology of choice for thin film deposition in Industry. As previously highlighted, MPPMS was developed to overcome these problems and to make HPPMS techniques industrially attractive and profitable. The demonstration of MPPMS capacity to fabricate low defect and high density coatings at high production rates would speed up extensive market penetration of these cutting-edge deposition technologies.

## 6. Objectives

The main objective of the present thesis is the development of advanced corrosion-resistant TaN thin films by new emerging MPPMS technology. The development of low defect and high density thin films by the application of highly ionized MPPMS discharge is pursued. The accomplishment of this objective would overcome the limitation currently found in sputtered films, i.e. the exhibition of a low corrosion resistance due to a low density and unsuitable microstructure architecture.

Furthermore, this thesis attempts to enhance the understanding of the electrochemical behaviour of TaN thin films deposited on different metallic substrates in several corrosive environments. The dependence of TaN film properties (with special focus on corrosion resistance) on process parameters during MPPMS deposition process is studied. Particularly, the nitrogen content effect on TaN microstructure and crystal phases and its correlation with corrosion resistance in NaCl solution is aimed.

Afterwards, the industrial validation of TaN coatings grown by MPPMS is addressed through the evaluation of these films as reliable coating solutions to protect metallic materials in two selected high-tech and demanding applications, i.e. biomedical implants and polymer electrolyte membrane fuel cells (PEMFC).

Pure titanium is commonly used for the fabrication of biomaterials. It possess an excellent biocompability and chemical stability, but suffers from poor mechanical properties. In biomedical implants, both mechanical and corrosion degradation phenomena take place at biomaterial surface and are subjected to the so-called "tribocorrosion". The development of different TaN films deposited by MPPMS with a multilayer structure architecture to enhance the performance and lifetime of uncoated Ti-cp is addressed. The evaluation of TaN as a coating solution to protect Ti-cp from tribocorrosion degradation in implants is the objective.

Stainless steel (SS316L) is generally used to manufacture the bipolar plates for PEMFC. It is necessary to improve the corrosion resistance of uncoated SS316L to ensure a longer service lifetime of the BPP and to minimize uttermost the power losses during cell operation. The development of highly corrosion resistant TaN films by MPPMS is proposed. Besides, the bipolar plates need to be conductive during operation to prevent cell efficiency reduction. Hence, developed TaN films must exhibit low interfacial contact resistance (ICR) with the gas diffusion layer (GDL) after corrosion testing. A correlation between oxide barrier film formation on top of TaN surface with corrosion current and ICR values needs to be made. The evaluation of TaN as a coating solution to protect SS316L bipolar plates from degradation during PEMFC operation is the goal.

Thus, specific objectives can be summarized as follows:

1. Develop high density and low-defect TaN thin films by MPPMS technique in an industrial size sputtering chamber.

2. Characterize the composition, microstructure and crystal phases of TaN films deposited by MPPMS under different process parameters (variable $N_2$-to-Ar ratio) and correlate them with TaN corrosion resistance.
3. Particularly analyse the corrosion and tribocorrosion performance of TaN coated Ti-cp in simulated body fluids. Evaluate TaN as a coating solution for biomedical implants.
4. Assess the corrosion resistance of TaN thin films in PEMFC simulated environment for SS316L bipolar plate protection. Measure the interfacial contact resistance value before and after corrosion testing. Evaluate TaN as a coating solution for BPP in PEMFC.
5. Elaborate a detailed study on modulated pulsed power magnetron sputtered TaN thin films performance in different application environments, being electrochemical behaviour the connecting feature.
6. Control the stability and reproducibility of the MPPMS process.

## 7. Organization of the thesis

The thesis is divided into 7 chapters.

In the next Chapter 2, the theoretical background needed to understand the thesis is given. The description of TaN coating material under investigation is displayed. The principles of sputtering, drawbacks of conventional DCMS and fundamentals and advantages of HiPIMS and more precisely, MPPMS are presented. Finally, a brief overview about corrosion degradation phenomena is given and the benefits of HPPMS technologies for the deposition of corrosion-resistant films are explained.

Chapter 3 details the features of the deposition system employed for the production of TaN coatings and the techniques used for TaN film characterization. Techniques

utilized for TaN films microstructure, composition and properties evaluation are described. Special emphasize is given to the electrochemical analysis of TaN films under polarization and electrochemical impedance spectroscopy methods.

The experimental work carried out and results obtained in this thesis are presented in Chapters 4, 5 and 6.

Chapter 4 is dedicated to a general investigation on TaN film microstructure and properties deposited by MPPMS. Monitoring of voltage-current characteristics during TaN discharge under different MPPMS pulse shapes is accomplished. The effect of nitrogen content on the TaN film microstructure and properties is accurately investigated.

In chapter 5, the TaN performance as protective coating for Ti-cp in biomedical implants is presented. An overview about metallic materials used for implants is given. Multilayer structure TaN films are developed in order to enhance tribocorrosion resistance of uncoated Ti-cp. Employed tribocorrosion testing procedure is described. Film microstructure and electrochemical, mechanical and tribocorrosion properties of multilayer TaN films are compared with monolayer TaN and uncoated Ti-cp.

In chapter 6, the TaN coatings are investigated as a coating solution to improve the performance and durability of PEMFC stainless steel bipolar plates. Corrosion and conductivity testing is performed on TaN coatings deposited at different $N_2$-to-Ar ratios. Special attention is given to the barrier oxide film formation on top of TaN coatings surface. Corrosion resistance and interfacial contact resistance values exhibited by TaN coatings are correlated with the thickness and the composition of the barrier oxide film. Finally, a novel and promising bi-layer coating made of tantalum and indium-tin-oxide (ITO) layers is also deposited by MPPMS and evaluated as protective coating for BPPs.

Finally, Chapter 7 presents overall conclusions of the work carried out in this thesis and future work.

# 7. References

[1] D.A. Glocker, S.I. Shah, Handbook of thin film process technology (2002)

[2] Handbook of Physical Vapor Deposition (PVD) Processing, 2nd edition; BOOK – 2010, DM Mattox, AUTHOR, Elsevier/ William Andrews; ISBN: 978-0-815-52037-5

[3] L. E. Toth, Transition Metal Carbides and Nitrides (Academic, New York, 1971)

[4] Rolf E. Hummel, Karl H. Guenther, Handbook of Optical Properties: Thin Films for Optical Coatings, Volumen 1, CRC Press (1995)

[5] Materials Science in Microelectronics I, The Relationships Between Thin Film Processing and Structure, E.S. Machlin, ISBN: 978-0-08-044640-0

[6] Research Perspectives on Functional Micro- and Nanoscale Coatings, Ana Zuzuarregui and Maria Carmen Morant-Miñana, 2016, DOI: 10.4018/978-1-5225-0066-7.

[7] S.H. Ahn, J.H. Lee, H.G. Kim, J.G. Kim, A study on the quantitative determination of through-coating porosity in PVD-grown coatings, Appl. Surf. Sci. 233 (2004) 105–114.

[8] C. Christou, Z.H. Barber, Ionization of sputtered material in a planar magnetron discharge, J. Vac. Sci. Technol. A 18 (2000) 2897.

[9] S. Konstantinidis, A. Ricard, M. Ganciu, J.P. Dauchot, C. Ranea, M. Hecq, Measurement of ionic and neutral densities in amplified magnetron discharges by pulsed absorption spectroscopy, J. Appl.Phys. 95 (2004) 2900.

[10] O. Auciello, R. Kelly, Ion Bombardment Modification of Surfaces: Fundamentals and Applications, Elsevier Science Ltd, Amsterdam, 1984.

[11] I. Petrov, P.B. Barna, L. Hultman, J.E. Greene, Microstructural evolution during film growth, J. Vac. Sci. Technol. A 21 (2003) S117.

[12] E. Bardal, Corrosion and Protection, Springer-Verlag, London (2004)

[13] M. Lane, R.H. Dauskardt, A. Vainchtein, H. Gao, Plasticity contributions to interface adhesion in thin-film interconnect structures, J. Mater. Res. 15 (2000) 203.

[14] T. Oku, E. Kawakami, M. Uekubo, M.Murakami, K. Takahiro, S. Yamaguchi, Diffusion barrier property of TaN between Si and Cu, Appl. Surf. Sci. 99 (1996) 265–272.

[15] S.K. Kim, B.C. Cha, Deposition of tantalum nitride thin films by D.C. magnetron sputtering, Thin Solid Films 475 (2005) 202–207.

[16] A. Aryasomayajula, K. Valleti, S. Aryasomayajula, D.G. Bhat, Pulsed DC magnetron sputtered tantalum nitride coatings for tribological applications, Surf. Coat. Technol. 201 (2006) 4401–4405.

[17] M. Schutze, R. Bender, K.G. Schutze, Corrosion Resistance of High-performance Materials, second ed. Wiley-VCH, Frankfurt, 2012.

[18] G.R. Lee, H. Kim, H.S. Choi, J.J. Lee, Superhard tantalum-nitride films formed by inductively coupled plasma-assisted sputtering, Surf. Coat. Technol. 201 (2007) 5207–5210.

[19] K. Valleti, A. Subrahmanyam, S.V. Joshi, A.R. Phani, M. Passacantando, S. Santucci, Studies on phase dependent mechanical properties of dc magnetron sputtered TaN thin films: evaluation of super hardness in orthorhombic Ta4N phase, Phys. D: Appl. Phys. 41 (2008) 045409.

[20] U. Helmersson, M. Lattemann, J. Bohlmark, A.P. Ehiasarian, J.T. Gudmundsson, Ionized Physical Vapor Deposition (IPVD): A Review of Technology and Applications, Thin Solid Films 513 (2006) 1-24

[21] H.R. Kaufman, Technology of ion beam sources used in sputteringJ. Vac. Sci. Technol. 15 (1978) 272.

[22] K. Sarakinos, J. Alami, S. Konstantinidis, High power pulsed magnetron sputtering: a review on scientific and engineering state of the art, Surf. Coat. Technol. 204 (2010) 1661–1684.

[23] A.P. Ehiasarian, R. New, W.-D. Münz, L. Hultman, U. Helmersson, V. Kouznetsov, Influence of high power densities on the composition of pulsed magnetron plasmas, Vacuum 65 (2002) 147.

[24] K. Macak, V. Kouznetsov, J.M. Schneider, U. Helmersson, I. Petrov, Ionized sputter deposition using an extremely high plasma density pulsed magnetron discharge, J. Vac. Sci.Technol. A 18 (2000) 1533.

[25] J. Lin, J.J.Moore,W.D. Sproul, B. Mishra, J.A. Rees, Z.L.Wu, R. Chistyakov, B. Abraham, Ion energy and mass distributions of the plasma during modulated pulse power magnetron sputtering, Surf. Coat. Technol. 203 (2009) 3676–3685.

[26] J. Alami, P.O.Å. Persson, J. Böhlmark, J.T. Gudmundsson, D. Music, and U. Helmersson, Ion-assisted physical vapor deposition for enhanced film properties on non-flat surfaces, J. Vac. Sci. Technol. A 23 (2005) 278.

[27] J. Alami, P. Eklund, J. M. Andersson, M. Lattemann, E. Wallin, J. Bolhmark, P. Persson, and U. Helmersson, Phase tailoring of Ta thin films by highly ionized pulsed magnetron sputtering, Thin Solid Films 515 (2007) 3434-3438.

[28] C. Reinhard, A.P. Ehiasarian, and P.E. Hovsepian, CrN/NbN superlattice structured coatings with enhanced corrosion resistance achieved by high power impulse magnetron sputtering interface pre-treatment, Thin Solid Films 515 (2007) 3685–3692

[29] P.E. Hovsepian, C. Reinhard, and A.P. Ehiasarian, CrAlYN/CrN superlattice coatings deposited by the combined high power impulse magnetron sputtering technique, Surf. Coat. Technol. 201 (2006) 4105-4110

[30] J. Lin, W.D. Sproul, J.J. Moore, B. Mishra, Z.L. Wu and J. Wang, "The structure and properties of chromium nitride coatings deposited using dc, pulsed dc and modulated pulse power magnetron sputtering", Surf. Coat. Technol. 204 (2010) 2230-2239.

[31] M. Hála, J. Čapek, O. Zabeida, J.E. Klemberg-Sapieha, L. Martinu, Hysteresis-free deposition of niobium oxide films by HiPIMS using different pulse management strategies J. Phys. D: Appl. Phys. 45 (2012) 055204

[32] V. Kouznetsov, K. Macak, J.M. Schneider, U. Helmersson, I. Petrov, A novel pulsed magnetron sputter technique utilizing very high target power densitiesSurf. Coat.Technol. 122 (1999) 290.

[33] K. Sarakinos, J. Alami, J. Dukwen, J. Wördenweber, M. Wuttig, A semi-quantitative model for the deposition rate in non-reactive high power pulsed magnetron sputteringJ. Phys. D: Appl. Phys. 41 (2008) 215301.

[34] S. Konstantinidis, J.P. Dauchot, M. Ganciu, A. Ricard, M. Hecq, Influence of pulse duration on the plasma characteristics in high-power pulsed magnetron discharges, J. Appl. Phys. 99 (2006) 013307.

[35] J. Alami, K. Sarakinos, G. Mark, M. Wuttig, On the deposition rate in a high power pulsed magnetron sputtering discharge Appl. Phys. Lett. 89 (2006) 154104.

[36] R. Chistyakov, U.S. Patent 7,147,759, "High-Power Pulsed Magnetron Sputtering,"December 12, 2006.

[37] J. Lin, W.D. Sproul, J.J. Moore, B. Mishra, Z.L. Wu and J. Wang, "The structure and properties of chromium nitride coatings deposited using dc, pulsed dc and modulated pulse power magnetron sputtering", Surf. Coat. Technol. 204 (2010) 2230-2239.

[38] J. Lin, J.J. Moore, W.D. Sproul, B. Mishra, J.A. Rees, Z. Wu, R. Chistyakov, B. Abraham, Ion energy and mass distributions of the plasma during modulated pulse power magnetron sputtering, Surf. Coat. Technol. 203 (2009) 3676.

[39] J. Lin, W. D. Sproul, J. J. Moore, S. Lee, S. Myers, High rate deposition of thick CrN and Cr2N coatings using modulated pulse power (MPP) magnetron sputtering, Surf. Coat. Technol 205 (2011) 3226–3234.

[40] R. Chistyakov, B. Abraham, W.D. Sproul, Advances in High Power Pulse Reactive Magnetron Sputtering, 49th Annual SVC Technical Conference, Washington, DC, April 23–27, 2006, 88–91.

[41] R. Chistyakov, B. Abraham, W. Sproul, J. Moore, J. Lin, Modulated Pulse Power Technology and Deposition for Protective and Tribological Coatings, Proceedings of the 50th Annual SVC Technical Conference, Louisville, KY, April 30–May 3, 2007, 139–143.

# CHAPTER 2

# THEORETICAL BACKGROUND

# 1. Materials

## 1.1 Tantalum

Tantalum was discovered by Anders Gustaf Ekenberg, a Swedish chemist, in 1802 in minerals obtained from Ytterby, Sweden. Many scientists believed that he had only discovered an allotrope of niobium, an element that is chemically similar to tantalum. The issue was finally settled in 1866 when, Jean Charles Galissard de Marignac, a Swiss chemist, proved that tantalum and niobium were two distinct elements. The first relatively pure samples of tantalum were first produced in 1907. Today, tantalum is primarily obtained from the minerals columbite ((Fe, Mn, Mg) $(Nb, Ta)_2O_6$), tantalite ((Fe, Mn)$(Ta, Nb)_2O_6$) and euxenite ((Y, Ca, Er, La, Ce, U, Th)$(Nb, Ta, Ti)_2O_6$ ).

Tantalum is a transition metal in Group 5 (VB) of the periodic table characterized by atomic number 73 and atomic weight of 180, 9479 g $mol^{-1}$. Tantalum's density is 16.4 $gcm^{-3}$. It is included within the refractory metals group, with high resistance to heat and wear. In fact, it has the third highest melting point (3020 ºC), surpassed only by rhenium and tungsten, yet it is highly conductive to heat and electricity [1].

Tantalum is dark, very hard, dense, ductile and malleable metal. Tantalum is renowned for its excellent corrosion resistance, being one of the most inert metals in the periodic table. Most metals tend to dissolve in acids but Ta is not affected by acids or other strong chemicals. In fact, at temperatures below 150 °C tantalum is almost completely immune to attack by the normally aggressive aqua regia. An exception here is the hydrofluoric acid which can causes severe corrosion [2]. Tantalum is an excellent biocompatible material, which does not react with body fluids or generate adverse tissue reaction.

Tantalum exists in two crystalline phases, alpha (α) and beta (β). The alpha phase is relatively ductile and soft; it has body-centered cubic (bcc) structure, a hardness of 8-12 GPa and electrical resistivity 15–80 μΩ cm. The beta phase is hard and brittle; its crystal symmetry is tetragonal, exhibits a hardness of 18-20 GPA and its electrical resistivity is relatively high at 170–210 μΩ cm. The β-phase is metastable and converts to the α-phase upon heating to 750–775 °C. Bulk tantalum is almost entirely α-phase, and the β-phase usually exists as thin films obtained by magnetron sputtering, chemical vapor deposition or electrochemical deposition techniques [3].

Tantalum forms oxides with oxidation states +5 ($Ta_2O_5$) and +4 ($TaO_2$). The most stable oxidation state is +5, which forms tantalum pentoxide ($Ta_2O_5$). $Ta_2O_5$ is an inert material characterized by an excellent chemical stability and resistance to acid attack which makes it insoluble in all solvents. However, it can be affected by strong bases and hydrofluoric acid. It is characterized by high refractive index and low absorption coefficient. It is an insulating material characterized by high dielectric constant. In fact, the outstanding resistance of metal Ta to aggressive media is attributable to the formation of an impervious stable and firmly adhering film of tantalum oxide ($Ta_2O_5$) on the metal surface [2].

The primary use of tantalum is in Electronic industry. Tantalum (Ta) thin films have been of importance since the early 1960s for their use in fabricating resistors and capacitors. Tantalum electrolytic capacitors exploit the tendency of tantalum to form a protective oxide surface layer, using tantalum thin film as one "plate" of the capacitor, the oxide thin layer as the dielectric, and an electrolytic solution or conductive solid as the other "plate". Because the dielectric layer can be very thin (thinner than the similar layer in, for instance, an aluminum electrolytic capacitor), a high capacitance can be achieved in a small volume. Because of the size and weight advantages, tantalum capacitors are attractive for portable telephones, personal computers, and automotive electronics.

Ta has a high melting point and is frequently used as a substitute for platinum, which is more expensive. Tantalum is used to make components for chemical plants, nuclear power plants, airplanes and missiles due to the high chemical stability previously mentioned. Tantalum does not react with bodily fluids and is used to make surgical equipment. Tantalum also does not irritate the body and is used to make surgical sutures as well as implants, such as artificial joints and cranial plates.

## 1.2 Tantalum nitride

Tantalum nitride (TaN) is a transition metal nitride rather unexplored compared to the well-known titanium nitride (TiN), chromium nitride (CrN) or zirconium nitride (ZrN).Transition metal nitrides exhibit remarkable physical properties including high hardness and mechanical strength, chemical inertness and high temperature stability. Due to its excellent properties, they have become technologically important in their thin film form for many industrial application areas [4-5].

TaN density is 14.3 g $cm^{-3}$ with a molecular weight of 194.955 g $mol^{-1}$. It has a high melting point of 3090 ºC and it is insoluble in water.

The properties of TaN thin films are determined by its composition and crystal phase structure. TaN thin films are complex since TaN exhibits many different phases and stoichiometry revealing different physical, chemical and mechanical properties. Both stable and metastable crystal phases have been reported for TaN system; including bcc α-Ta, tetragonal β-Ta, hexagonal $Ta_2N$, cubic TaN, hexagonal TaN, hexagonal $Ta_5N_6$, tetragonal $Ta_5N_6$, orthorhombic $Ta_3N_5$, orthorhombic $Ta_4N$… [6] Due to this complexity, TaN films with hardness ranging from 10 GPa up to 70 GPa have been reported [7-9]. Tribological performance and electrical properties of TaN films are also considerably variable upon TaN composition and crystal phases [10-12]. Thus, the TaN properties have been found to be strongly dependent on the deposition

technology, process parameters and growing conditions utilized during TaN films deposition.

TaN has been extensively studied for its application in microelectronic devices and as diffusion barrier in magneto resistive random access memory and resistors since it works as an excellent barrier against Cu diffusion, or as preferred barrier absorber material for EUV masks [13-14]. TaN has also been utilized as wear resistant layer and hard coating for cutting tools in tribological applications [15-16]. However, in spite of its well-known chemical inertness and corrosion resistance in harsh environments, there is a lack of consistency on its general performance against chemical attack. TaN is also highly biocompatible but there are not many research papers regarding its application in biomedical devices.

# 2. Sputtering technologies

## 2.1 Fundamentals

### 2.1.1 The plasma

Historically the term 'plasma' was introduced by Irving Langmuir in 1928 [17] when he investigated oscillations in an ionized gas. He used the word to describe a region containing balanced charges of ions and electrons.

Today, a plasma is defined as an ionized gas consisting of approximately equal numbers of positively charged ions and negatively charged electrons and a much larger number of gas neutrals that is in average electrically neutral but responds to a collective behavior [18]. We often refer to it as the "Fourth State of the Matter" because of its unique physical properties, distinct from solids, liquids and gases. In

fact, considering a temperature increase, a solid material will transform into a liquid, a gas, and eventually into a plasma if enough energy is supplied to ionize the atoms within the gas.

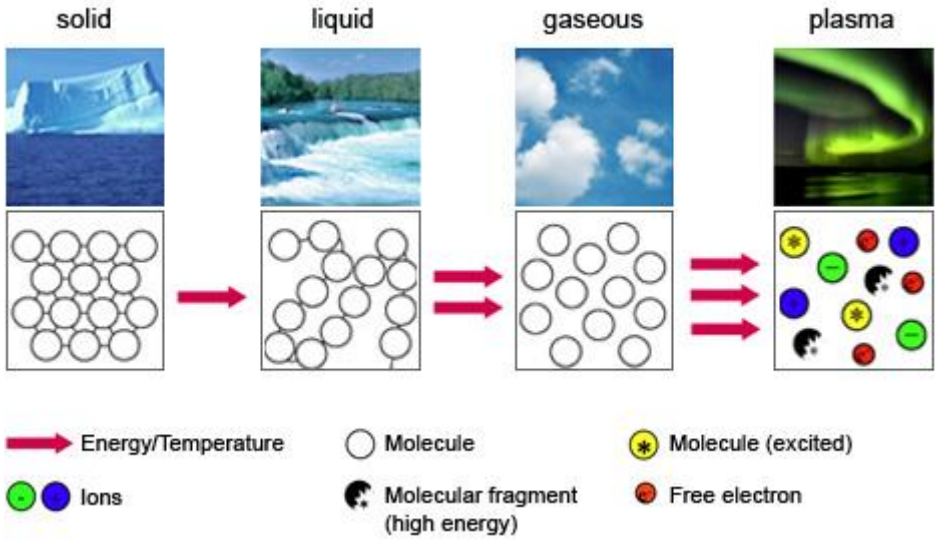


**Fig 2. 1: The four states of matter: solid, liquid, gas and plasma (taken from [19])**

Under the ordinary conditions on the Earth, plasma is rather a very rare phenomenon exclusively observed in lightning, fluorescent lights and neon signs, flames and auroras borealis. But in Universe, cold solid bodies are an exception. Most of the matter in the Universe is ionized and thus in the plasma state (about 99%). Plasma in the Universe is produced by various mechanisms. In the stars, the neutral atoms are ionized due to high temperature. Interstellar gases are ionized due to the ultraviolet radiation from the stars.

Currently, plasmas are artificially created in our laboratories and industries encompassing many areas ranging from the high-temperature plasmas of thermonuclear fusion to the low-temperature plasmas in material processing, and more specifically glow discharge plasmas that are the core of sputtering processes and will be further described in the next section 2.1.2.

The plasmas are characterized by their ionization state and charged particles density. This state is expressed in terms of the following parameters:

- The density of neutral particles, $n_n$
- The density of the electrons and the ions, $n_e$ and $n_i$, respectively
- The energy distribution function of the neutrals $f_n$ (E), ions $f_i$ (E), and electrons $f_e$ (E).
- The ionization degree

$$I = \frac{n_i}{n_i + n_n} \qquad [2.1]$$

Commonly, in the absence of negative ions, $n_e = n_i = n$, being n the plasma density.

### 2.1.2 Sputtering process

The basic principle in sputtering, relies on ejection (sputtering) of atoms from a solid source (target) by bombardment of gaseous ions (generally a noble gas such as argon) from a plasma. The ejected atoms are then transported to the substrate, where they condense to form a film. A schematic drawing of sputtering process is plotted in Fig 2.2.

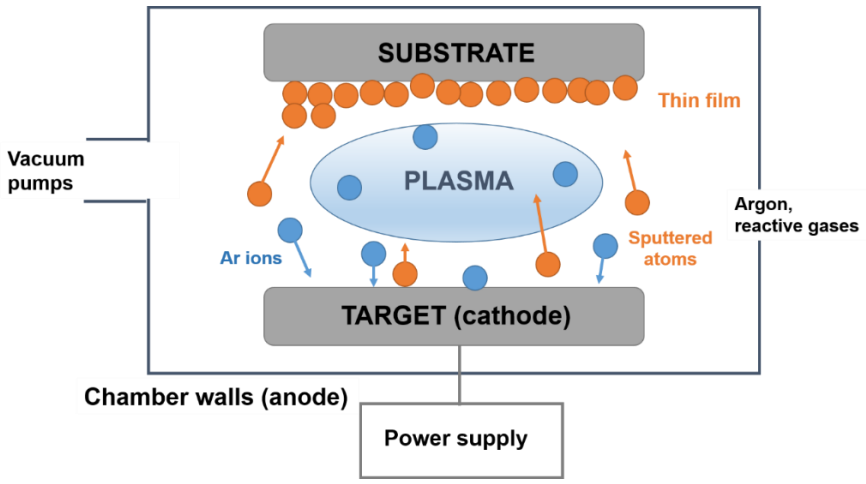


**Fig 2. 2: Schematic illustration of sputtering process**

A sputtering gas (normally argon) is introduced into a vacuum chamber. The plasma is created applying a voltage between the target (cathode) and the chamber walls (anode). The few free electrons initially presented in the gas will be accelerated away from the cathode, eventually hitting the gas atoms. If the electron energy is high enough, the gas atoms will be ionized and, hence, more electrons created, developing a small current inside the chamber through the following processes [20],

$$Ar^0 + e^- \rightarrow Ar^+ + 2\,e^- \quad [2.2]$$

$$Ar^* + e^- \rightarrow Ar^+ + 2\,e^- \quad [2.3]$$

The $Ar^+$ ions created during ionization processes will be accelerated towards the cathode, leading to an energetic bombardment against the target and ejecting target atoms and secondary electrons by momentum transfer mechanism. The cascade of ionizing collisions will ultimately result in a large current causing the gas to break down, and eventually the discharge becomes self-sustaining. This means that enough secondary electrons are generated to produce the required amount of $Ar^+$ ions to generate again, during the process of sputtering, enough secondary electrons to compensate the loss of charged particles through the diffusion to the chamber walls. The de-excitations of the particles during the whole process cause the emission of visible radiation and therefore, the discharge is called *glow discharge*. Depending on the applied potential and the resulting current, different regimes can be identified as shown in Fig 2.3. The sputtering process belongs to the glow discharge regime termed as *abnormal glow*, where the discharge voltage and current density increases with increasing applied power.

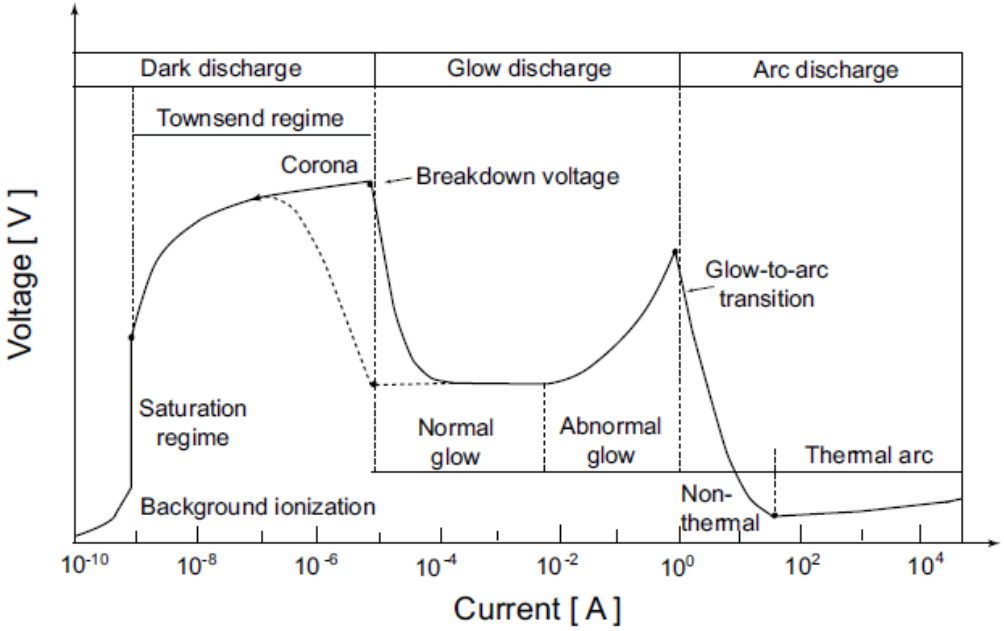


**Fig 2. 3: Voltage-current relationship in plasma discharges (taken from [18])**

The average number of atoms ejected from the target per incident ion is called the sputter yield (γ) and depends on the energy of the ion, the masses of the ion and target atoms, and the surface binding energy of atoms in the target. Thus, γ is a particular feature of the target material and deposition process. According to the theory of Sigmund, the sputter yield near threshold, i.e. at low ion energy, is given by [21]:

$$\gamma = \frac{3}{4\pi^2}\alpha\frac{4M_1M_2}{(M_1M_2)^2}\frac{E}{U_S} \qquad [2.4]$$

with E the energy of the incident ion, and $M_1$ and $M_2$ the masses of the incident ion and the target atom (in amu). $U_s$ is the surface binding energy and α dimensionless parameter depending on the mass ratio and the ion energy.

### 2.1.3 Ionization processes

In a sputtering plasma, the most common ionization process mechanisms for sputtered material are [20]:

- Direct electron impact ionization

$$M^0 + e^- \rightarrow M^+ + 2\,e^- \qquad [2.5]$$

- Electron impact ionization of excited sputtered atoms

$$M^* + e^- \rightarrow M^+ + 2\,e^- \qquad [2.6]$$

- Penning ionization

$$M^0 + G^* \rightarrow M^+ + G^0 + e^- \qquad [2.7]$$

being M and G sputtered atoms and sputtering gas atoms, respectively.

Plasma discharges with high values of $n_e$ are dominated by ionization processes of equations [2.5] and [2.6], while low $n_e$ discharges are dominated by Penning ionization (equation [2.7]. It is also known that ionization degree of the sputtered material is higher with increasing $n_e$ [20]. However, the ionization degree strongly varies between different materials, given material cross section for ionization by electron impact. This general trend is demonstrated in Fig 2.4.

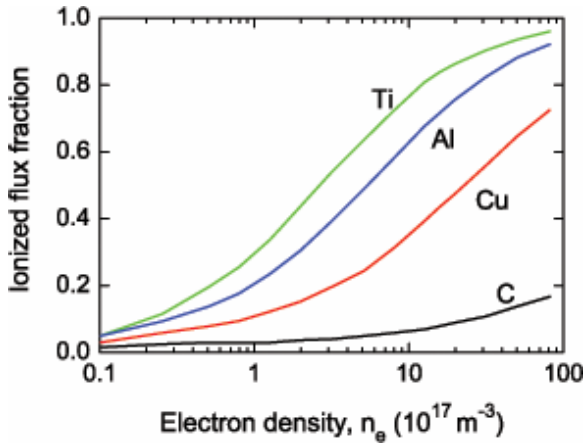


**Fig 2. 4: Ionization of different sputtered materials with increasing electron density of plasma discharge (taken from [20])**

## 2.2. DC Magnetron sputtering

### 2.2.1 Definition

The invention of the planar magnetron cathode by Chapin (patent issued in 1979) marked the beginning of a new era in vacuum coating technology.

In a basic sputtering process, the glow discharge is usually excited and sustained electrically by applying, through the gas and between two electrodes direct current (DC) power. Typically, the voltage applied is about 1-2 kV and the pressure is about a few Pa. In this set-up the electron trajectories are only defined by the electrical field between the cathode and the anode. The electrons are accelerated over the cathode sheath and move with high velocity towards the anode, leading to a rapid loss of electrons and reduction of plasma density in the vicinity of the cathode.

By applying a magnetic field during DC glow discharge sputter deposition (which is known as DC magnetron sputtering (DCMS)), one can trap the electrons in the discharge longer and, hence, produce more ions for the same electron density [23]. As the electron trajectory is elongated, the probability of ionizing a gas atom during their travel from cathode to anode increases, which enables a reduction in the discharge pressure (below 1 Pa) and cathode voltage (300-500 V) and increase of the *mean free path* (average distance traveled by a moving particle between successive collisions). Mean free path (λ) of an atom in a gas ambient is defined by the following equation:

$$\lambda = \frac{5\times10^{-3}}{P}\ (cm) \qquad [2.8]$$

being P the working pressure given in Torr.

In this way, the ions can reach the cathode with almost the full discharge voltage and the sputtered atoms can reach the substrate with only a few collisions. This is of great significance for the sputtering process efficiency in terms of thin films growth rate and quality compared to basic glow discharge sputtering process.

In a magnetron, magnets are placed directly behind the target creating a magnetic field of hundred Gauss. The electrons will then be trapped by the Lorentz force and will be driven around magnetic field lines in spiral-shaped orbits as shown in Fig 2.5. The Lorentz force is given by,

$$F = q\left(\vec{E} + \vec{v} \times \vec{B}\right) \quad [2.9]$$

where q is the charge, is the velocity of the particle and, and $\vec{E}$ and $\vec{B}$ the electric and magnetic fields, respectively.

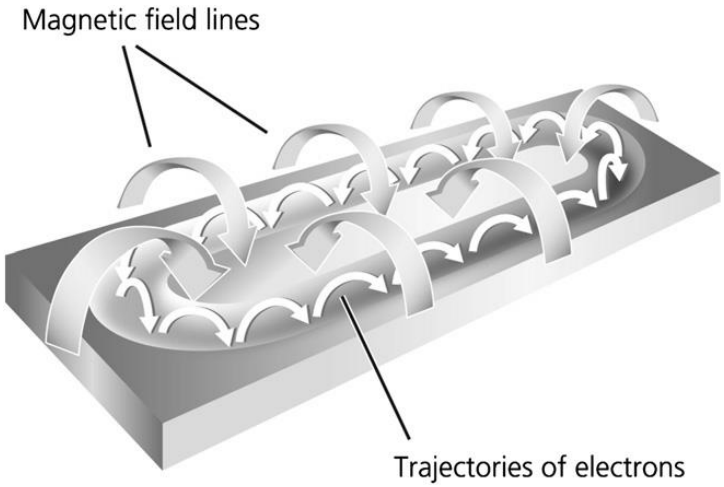


**Fig 2. 5: An example of planar magnetron conFiguration (taken from [24])**

Different magnetron configurations can be found today regarding geometry and electrical power, all depending on the application. The electrons in the magnetron plasma are highly sensitive to the magnetic fields over the target surface. This effect can be used to control the plasma properties and create different plasma effects to enhance the deposition process. Apart from magnetic field strength, the most influential aspect is the degree of magnetic balance or unbalance. The magnetic null

point where $B_z$ is zero in the middle of the target is the characteristic factor. The most common configurations (Fig 2.6.) are given below,

*Balanced magnetron sputtering*

The distance to $B_z$ is large. In this configuration, the inner and outer magnets of the magnetron balance each other. This configuration enhances the ionization degree on the vicinity of the target.

*Unbalanced magnetron sputtering*

In many cases, it is beneficial to avoid a too strong confinement of the plasma just close to the target, but also confining it close to the substrate. This is achieved by placing stronger outer magnets than the inner ones, forcing the plasma to extend further into the chamber toward the substrates. The null point $B_Z$ is closer to the target in this configuration. Unbalanced magnetron configuration improves both the ionization degree and the ion bombardment of the growing film, enhancing its physical properties. This is the most utilized type of magnetron in industrial systems.

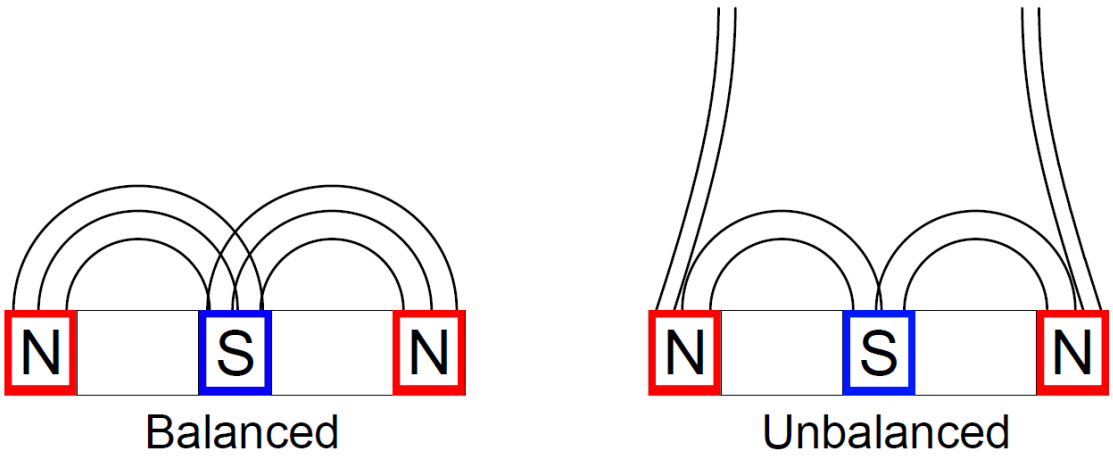


**Fig 2. 6: The most common magnetron configurations in sputtering processes**

## 2.2.2 Drawbacks

DC magnetron sputtering (DCMS) technique has found widespread use in many industrial sectors, and it is currently one of the main technologies for the deposition of thin films. However, the constant development of coating technology is driven by increasing commercial demands on existing coatings as well as a wish to replace traditional techniques with novel methods capable to offer thin films with tailored and enhanced properties.

In conventional DCMS discharge, only a small fraction of the sputtered atoms are ionized, roughly in the order of one or a few percentage. Thus, the sputtering process is, therefore, a line-of-sight process where the deposition flux towards the substrate cannot be easily controlled since it consist of mainly neutral atoms. In fact, the uniform deposition of thin films in a complex-shape substrates is rather difficult since there is no tool to modify the direction of sputtered atoms. Moreover, the ion bombardment of the growing film during synthesis has been shown to have favorable effects on film microstructure and properties [25]. To achieve this condition, in many cases bias voltage ($V_b$) values of several tenths or even hundreds of V are required in order to increase the average energy provided to the deposited atoms and significantly affect the film properties. However, the majority of available ions in DCMS for deposition process assistance come from the inert sputtering gas while ions of sputtered material are very rare. This fact in combination with the relatively high bias voltages may cause subplantation of the Ar atoms in the film, leading to a generation of lattice defects, high residual stresses, a deterioration of the quality of the film/substrate interface and poor film adhesion. Last but not least, the thin films deposited by DCMS tend to exhibit columnar microstructures due to the lack of sufficient energy to promote surface mobility of ad-atoms and densification of the growing films. A dense microstructure is one of the key characteristics for a well-

performing thin film in terms of corrosion protection. The voids and defects along the film enable the creation of a pathway for the electrolyte penetration towards the substrate, strongly jeopardizing its corrosion resistance. Thus, this is one of the main reasons why dc magnetron sputtered films are not commonly utilized for applications in severe corrosive conditions.

Thus, the increase of the fraction of the ionized sputtered species within DCMS discharge has been an objective of many research works during the recent decades. The enhancement of this feature would allow the deposition of improved coatings capable to withstand more severe conditions and be applied in not suitable substrates up to now.

The specific characteristics of DCMS processes depend on target material, gas type and pressure. Thus, it is difficult to make a general description for DCMS processes. However, DCMS often operates at a pressure of 0.1-1 Pa with a magnetic field strength between 100-1000 Gauss and at cathode potentials around 300-700 V. This leads to current densities below 0.1 A $cm^{-2}$ and power densities of a few W $cm^{-2}$ [26, 27]. This is the main reason why the ionization degree of sputtered particles is always very low (< 5%) in DCMS discharge. The given energy by the applied power in DCMS is not sufficiently high to ionize the target atoms.

Several sputtering systems have been designed to increase the plasma density of conventional DCMS. These include: inductively coupled plasma magnetron sputtering (ICP-MS), microwave amplified magnetron sputtering, hollow cathode magnetron sputtering and high power pulsed magnetron sputtering (HPPMS). This latter technique requires in principle only the sputtering power supply replacement and includes high power impulse magnetron sputtering (HiPIMS) and modulated power pulsed magnetron sputtering (MPPMS) depending on the power supply employed. During HPPMS discharges, the power is applied in pulses of low duty

cycle and frequency instead of in constant direct mode as in DCMS as illustrated in Fig 2.7. The HPPMS pulse mode allows the development of much higher peak power densities in the cathode at the same average power than during DCMS, which leads to much higher plasma density and ionization degree of sputtered particles. The main difference between HiPIMS and MPPMS arises from the duration and frequency of the pulse and the magnitude of the peak power density.

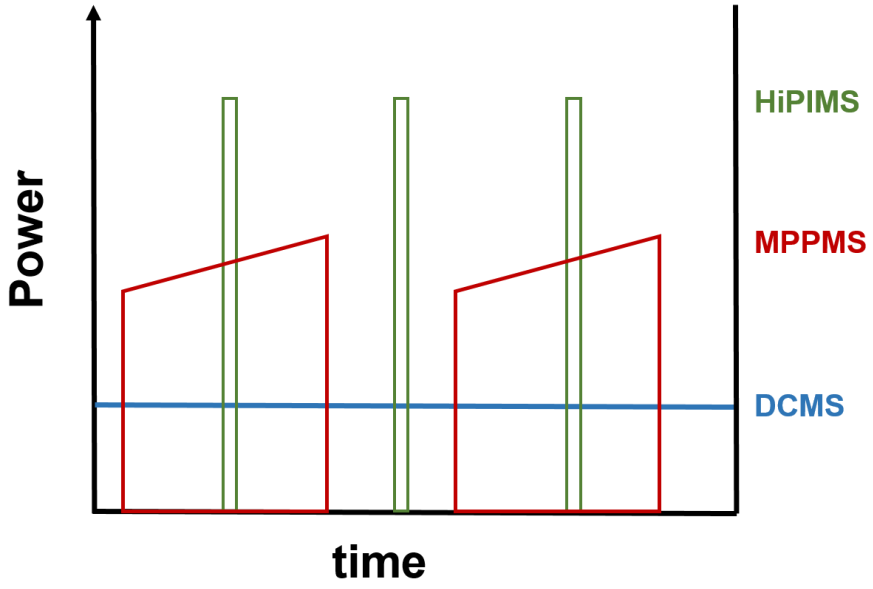


**Fig 2. 7: Power vs time in DCMS, HiPIMS and MPPMS discharges**

HiPIMS will be briefly introduced and MPPMS further described since it is the one employed for the deposition of TaN coatings in this thesis.

## 2.3 HiPIMS

High power pulsed magnetron sputtering (HiPIMS) was firstly introduced by Kouznetsov et al. [28] in the 1999 as a new promising ionized physical vapor deposition technique (I-PVD). In HiPIMS, a dense plasma is generated by applying high power unipolar pulses (1 - 3 kW $cm^{-2}$) to a cathode, for a short period of time (e.g. 10-200 μs), resulting in a high degree of ionization of the sputtered species [29, 30]. The amount of ionization depends mainly on the plasma discharge characteristics and the target material as shown in Fig 2.8 [31]. Values ranging from 5% for C [32] to 90% for Ti [33] have been reported.

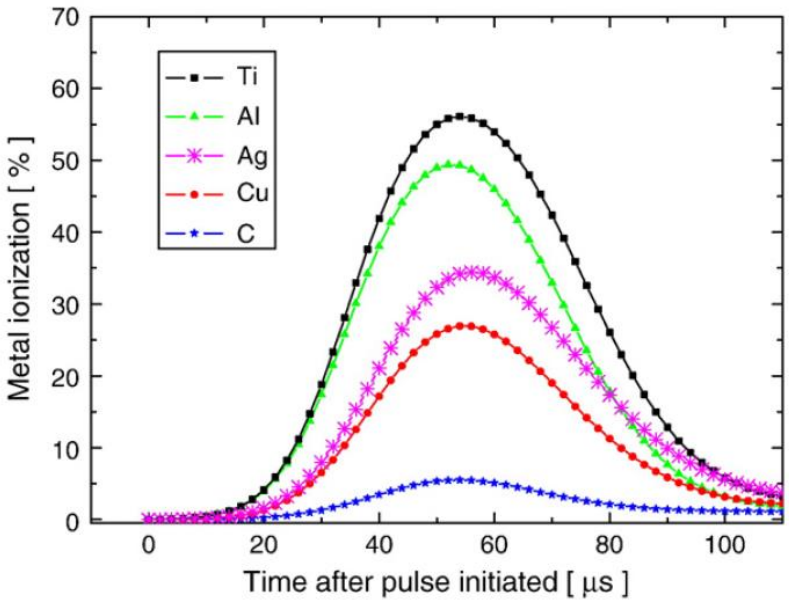


**Fig 2. 8: A comparison of the metal ionization vs pulse time during HiPIMS for different target materials (taken from [31].**

In order to avoid overheating of the target, the power is applied in very short pulses of low frequency and duty cycles of a few percentage. The typical V-I characteristics of HiPIMS discharge is shown in Fig 2.9.

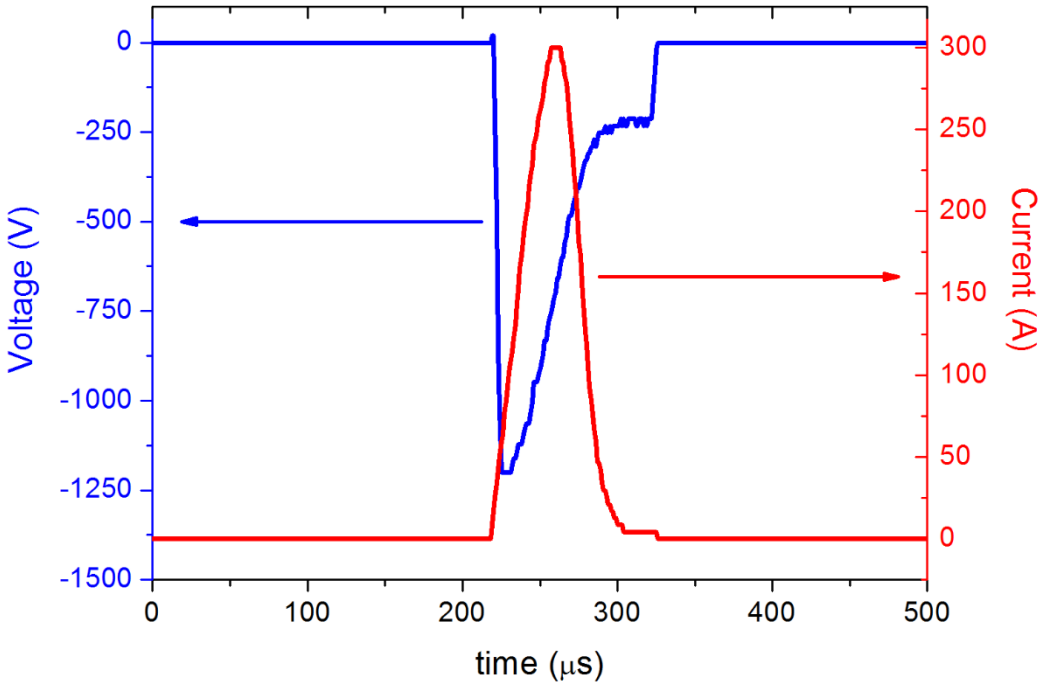


**Fig 2. 9: Voltage-current waveforms during HiPIMS discharge in MIDAS 450 system**

During the last decade, the high flux of metal ions generated in the HiPIMS discharges has been usefully utilized to tailor and enhance the properties of the growing films compared to those films deposited by conventional dc magnetron sputtering (DCMS) technique [34,35. Alami et al. have shown that Ta films deposited by HiPIMS exhibit a fully dense and a very smooth surface along with a less pronounced line-of-sight process as compared to DCMS [36]. The application of a negative bias voltage to the ionized metal flux allows an accurate control of the direction and energy of the arriving ions inducing a more homogeneous coating on complex-shape substrates. Besides, the possibility to tailor the phase composition of Ta films through the modification of process parameters was also reported by Alami et al [37]. The possibility to completely densify the CrN film microstructure by

increasing peak current density during HiPIMS process was also demonstrated [38] as shown in Fig 2.10.

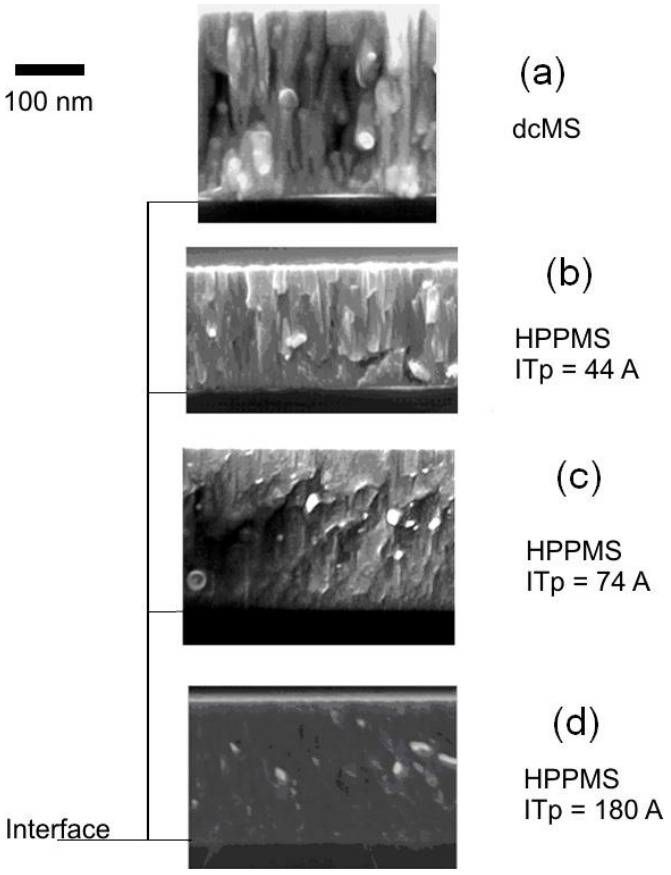


**Fig 2. 10: Cross-sectional SEM images of CrN films deposited on Si by HPPMS at different peak target currents (taken from [38])**

HiPIMS has been shown to be also beneficial in the development of protective coatings with enhanced corrosion resistance as demonstrated by C. Reinhard and co-workers [39]. The deposition of multilayer coatings by HiPIMS with excellent adhesion, oxidation and wear resistance was also demonstrated by P.E. Hovsepian et al. [40, 41].

The major drawback of HiPIMS technique is the drop in the deposition rate compared to DCMS technique for an equivalent amount of average power as shown in Fig 2.11. Deposition rate of deposited films is of great importance in coating preparation, alongside with their microstructure and properties, since it affects the profitability of

film production. The deposition rate reduction is caused by various physical reasons, being the most important one the loss of sputtered material via ionization and subsequent back-attraction towards the target, known as *self-sputtering* [42, 43]. Since high power pulsing greatly increases the probability of ionization of sputtered material, the quantity of metal ions created in the vicinity of the target considerably rises. These metal ions are then attracted back to the cathode by the electric field and participate in the sputtering process instead of contributing in thin film formation.

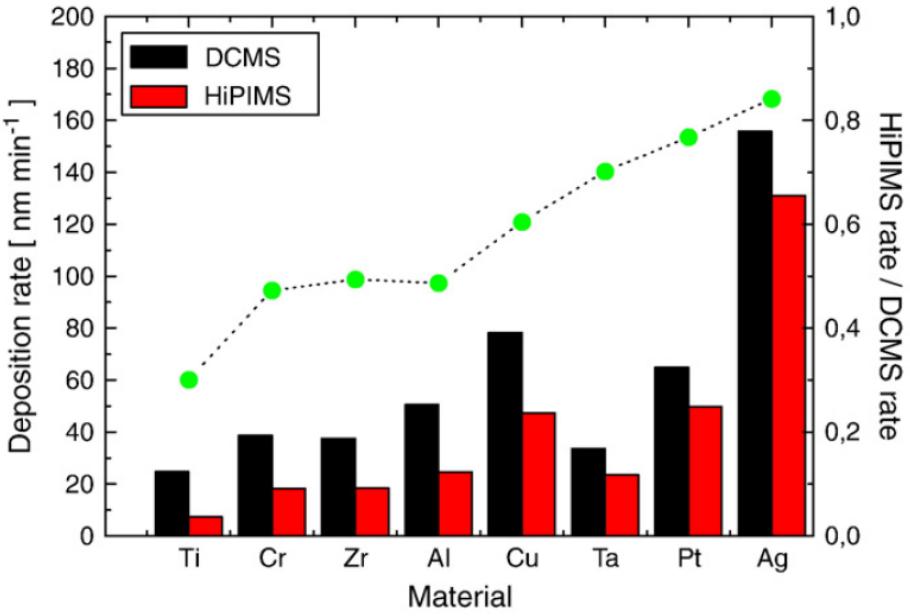


**Fig 2. 11: Deposition rate for DCMS and HiPIMS discharges for different target materials (taken from [31])**

## 2.4 MPPMS

### 2.4.1 Principle

Modulated Pulsed Power Magnetron Sputtering (MPPMS) technique was developed by R. Chistyakov and co-workers in 2006 [44-46] as a variation of originally introduced HiPIMS technique.

The differences between the originally introduced HiPIMS and MPPMS techniques are basically the magnitude, duration and shape of the high power pulses. With the MPPMS approach, the pulse length can be as long as 3000 μs whereas the peak power density is lower than in HiPIMS, typically up to 0.1-1.5 kW $cm^{-2}$. The duty cycle can be as high as 28% while during typical HiPIMS discharges it does not exceed the 5%. Unlike the simple one pulse shape in HiPIMS, MPPMS generates high density plasma by the superimposition of two or more micropulses within one overall pulse resulting in a complex step-like shape discharge waveform as shown in Fig 2.12.

The MPP generator's operation principle is based on the possibility to particularly design the pulse shape, including up to 6 different micropulses within one overall pulse. This mode of operation results in the development of stable discharges regardless off the type of deposited material. However, the typical MPP pulses generally contain two different micropulses. The first micropulse is characterized by low peak current values and ionization degrees in order to ignite and stabilize the plasma discharge. The second micropulse develops much higher peak current densities and it is known as the main ionization stage during the pulse. The peak current density achieved during MPPMS discharge is dependent on cathode voltage, target material, gas type, pressure and magnetron and deposition chamber configuration.

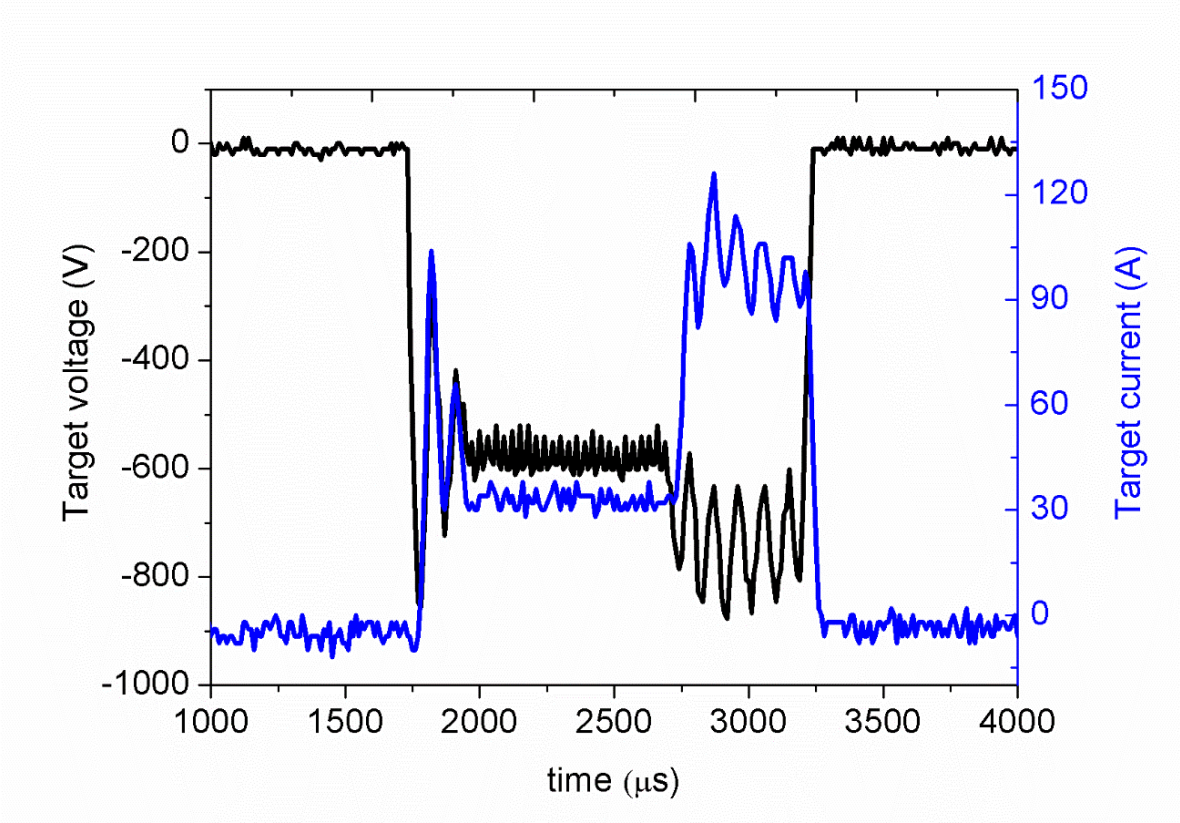


**Fig 2. 12: Voltage-current waveforms developed during MPPMS discharge in MIDAS 450 system**

MPP generator is a switching power supply that can control the voltage "on" time ($\zeta_{on}$) (the width of the micropulses) and the voltage "off" time ($\zeta_{off}$) (the distance between micro pulses) in the micropulses, offering the possibility to create low and/or high ionized micropulses. The higher the $\zeta_{on}$ / $\zeta_{off}$ ratio, the higher the peak current density. The operation principle of MPPMS is shown in Fig 2.13.

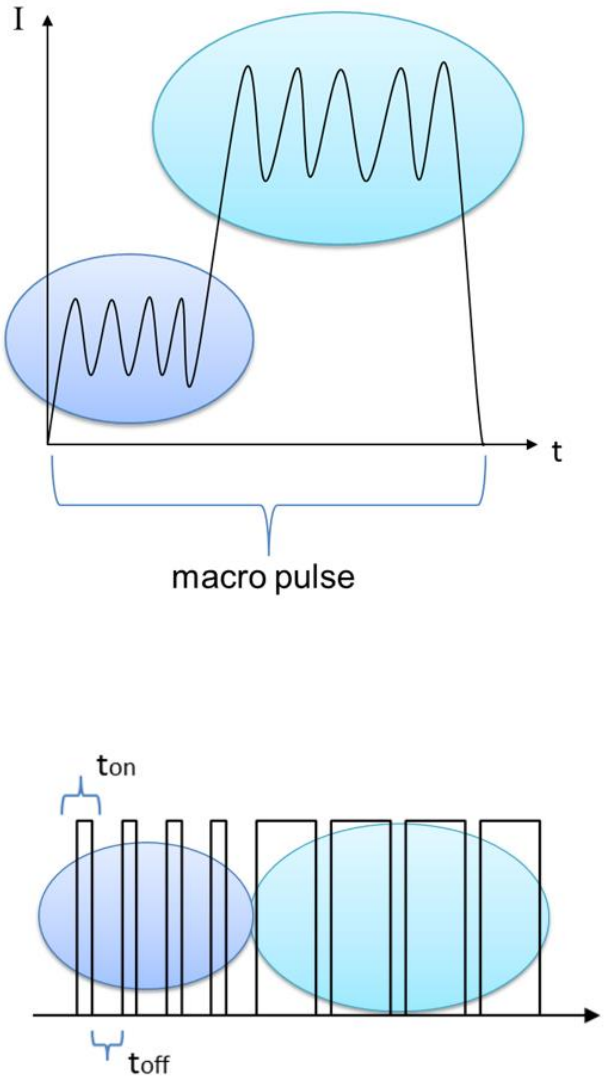


**Fig 2. 13: Schematic theoretical explanation of pulse shape generation during MPPMS**

The main differences between DCMS, HiPIMS and MPPMS techniques in terms of discharge and plasma parameters already described in this Chapter are summarized in Table 2.1.

| DISCHARGE PARAMETERS | | | |
|---|---|---|---|
| | **DCMS** | **HiPIMS** | **MPPMS** |
| **Average power** | 1-10 kW | 1-10 kW | 1-10 kW |
| **Peak power** | X | few MW | hundreds of kW |
| **Peak power density** | W $cm^{-2}$ | 1-3 kW $cm^{-2}$ | 0.1-1.5 kW $cm^{-2}$ |
| **Peak voltage** | 300-700 V * | 200-2000 V | 200-1200 V |
| **Peak current** | 1-20 A * | 10-1000 A | 10-550 A |
| **Pulse length** | X | 2-200 µs | 500-3000 µs |
| **Frequency** | X | 2-500 Hz | 10-400 Hz |
| **Duty cycle** | X | 5 % | 28 % |
| **PLASMA PARAMETERS** | | | |
| | **DCMS** | **HiPIMS & MPPMS** | |
| | *Weakly ionized plasma* | *Strongly ionized plasma* | |
| **Electron density** | $10^{14}$-$10^{15}$ $m^{-3}$ | $10^{16}$-$10^{20}$ $m^{-3}$ | |
| **Ionization degree of sputtered material** | < 0.05 | 0.05-0.90 depending on target material | |
| **DEPOSITION RATE** | | | |
| | **DCMS** | **HiPIMS** | **MPPMS** |
| | +++ | + | ++ |

**Table 2. 1: Comparative study between DCMS, HiPIMS and MPPMS discharges**

* in DCMS discharge, voltage and current are constant. There are no peak values like in HiPIMS and MPPMS pulsing discharges.

### 2.4.2 Advantages of MPPMS

The principal advantage of MPPMS technique is that ionization degree of the plasma discharge can be greatly increased compared to DCMS by simply changing the power supply to power the cathode in the sputtering system due to the increase of $n_e$ of the plasma discharge. Furthermore, MPPMS is known to deliver more stable plasma discharges characterized by lower arcing phenomena and higher deposition rate than during HiPIMS processes, which can accelerate a widespread industrial application of HPPMS techniques.

J.Lin and co-workers [47] showed that the amount of $Cr^+$ ions was considerably enhanced during MPPMS discharge as well as the energy of the ions as shown in Fig 2.14.

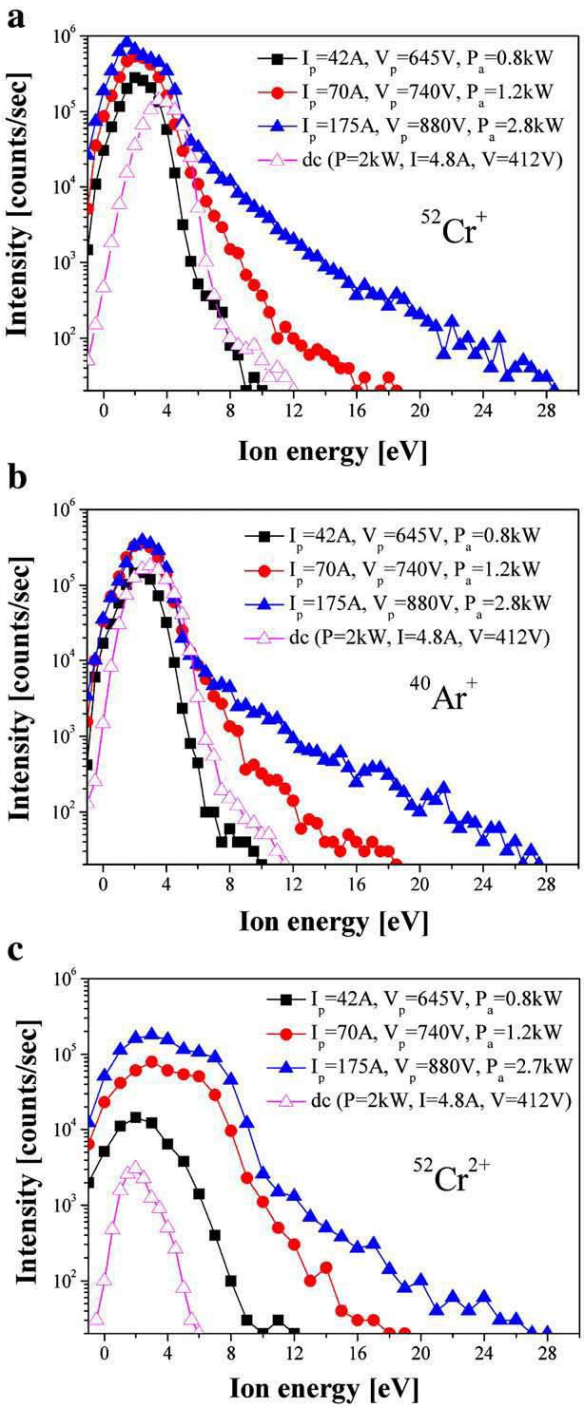


**Fig 2. 14: Ion energy distributions of Cr+, Ar+ and Cr2+ ions measured from MPP plasma with different peak currents and dc plasma during non-reactive sputtering of Cr (taken from [47])**

They also pointed out an increase on the quantity and the energy of the ions as the peak current density was increased by pulse shape adjustment, as it has been proved by many other researchers [33, 38]. It is also important to notice the huge increase on the amount of doubly charged $Cr^{2+}$ ions, which exceed in two-three (depending on peak current density) orders of magnitude the amount of $Cr^{2+}$ ions present during DCMS plasma.

An ionized deposition flux can be controlled in terms of direction and energy of the film forming species by electric and magnetic fields which allows for a complete control of the deposition process previously unfeasible during DCMS due to the high contribution from neutral atom deposition flux. The implications of this in the modification of thin film growth due to higher ion content present in the MPPMS process has been already demonstrated. The possibility to completely densify the Ta films along with phase transformation from β to α phase by the application of different bias voltages, and thus, different arriving ion energies was reported in [48] (Fig 2.15).

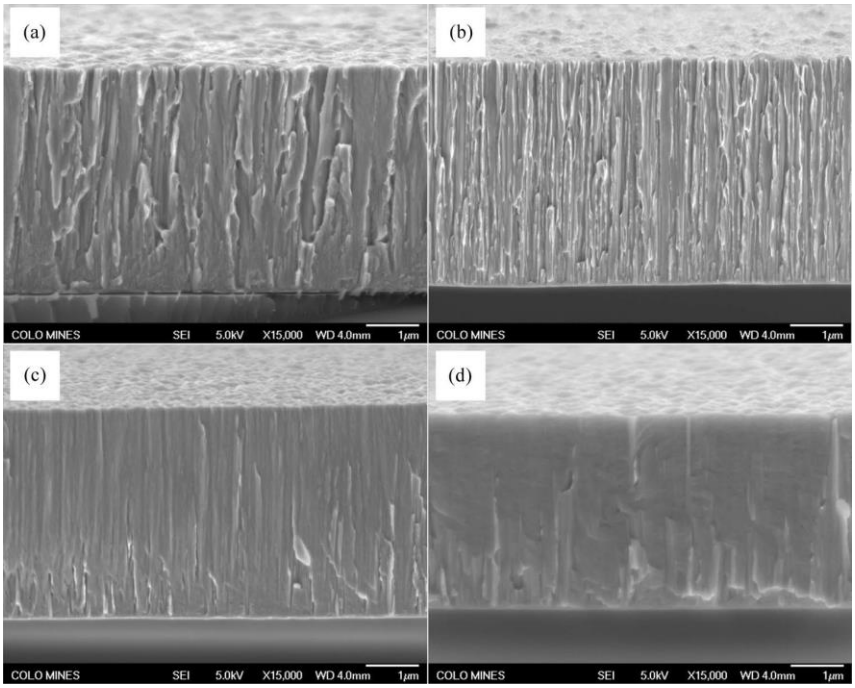


**Fig 2. 15: Cross-sectional SEM micrographs of the Ta coatings deposited at increasing negative substrate bias voltages, from 0V (a) to – 70V (d). Taken from [48].**

The enhancement of film properties by the possibility to accurately tune the arriving ion energies has been also demonstrated. The tribological properties enhancement of CrN films deposited by MPPMS technique including higher hardness, lower wear and better adhesion compared to DCMS deposited films was shown in [49] by J.Lin and co-workers. They measured the $Cr^+$, $N_2^+$ and $Ar^+$ ion flux in MPPMS and DCMS and observed 6 times higher $Cr^+$ ion content in the discharge, which is the parameter responsible for enhancement of films quality. The refinement of Cr film microstructure induced by MPPMS including finer grain size and higher density compared to DCMS grown Cr films was observed in [50]. Increasing the peak current density of MPPMS discharge led to the development of columnar grain-free Cr film structures. Hardness increase from 6 GPa to 16 GPa and corrosion resistance improvement of Cr films was seen by the application of MPPMS. The improvement of corrosion resistance of Cr-Si-N films deposited by MPPMS was observed in [51].

Compared to HIPIMS process, the MPPMS technique develops a lower ionized sputtering plasma under the same deposition conditions, as demonstrated by M. Hála et al [52] and shown in Fig 2.16.

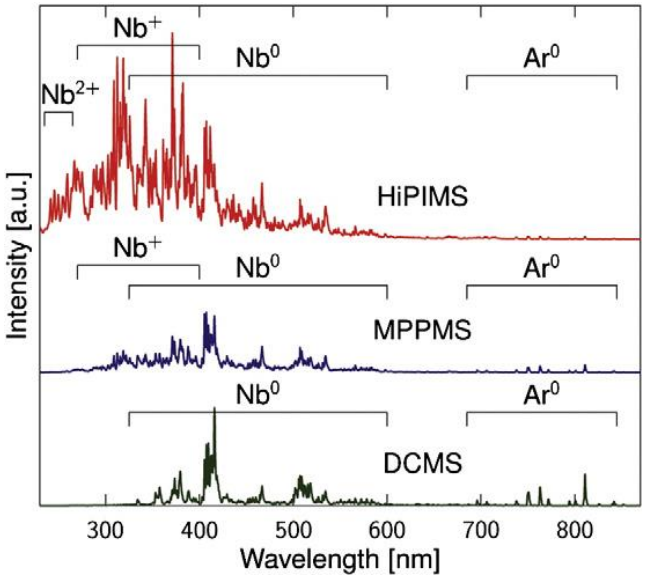


**Fig 2. 16: Normalized optical emission spectra recorded at d=1 cm from the Nb target powered by HiPIMS, MPPMS and DCMS in Argon at p=1 Pa and at the average power P=300 W. (taken from [52])**

The reason for this relies on the lower peak current densities achieved during MPPMS which prevents higher ionization degree of the plasma discharge and leads to lower self-sputtering effect. MPPMS pulses are much longer than HiPIMS pulses which leads to the development of lower peak power pulses in order to not exceed the upper limit for target overheating during sputtering process. However, this feature has a positive effect on the deposition rate of MPPMS process. Due to lower amount of metal ions during MPPMS, the self-sputtering effect is lower compared to HiPIMS discharge which in turns lead higher deposition flux towards the substrate. Moreover, the application of higher duty cycles during MPPMS promotes a higher deposition rate compared to HiPIMS process as observed in Fig 2.17 [53].

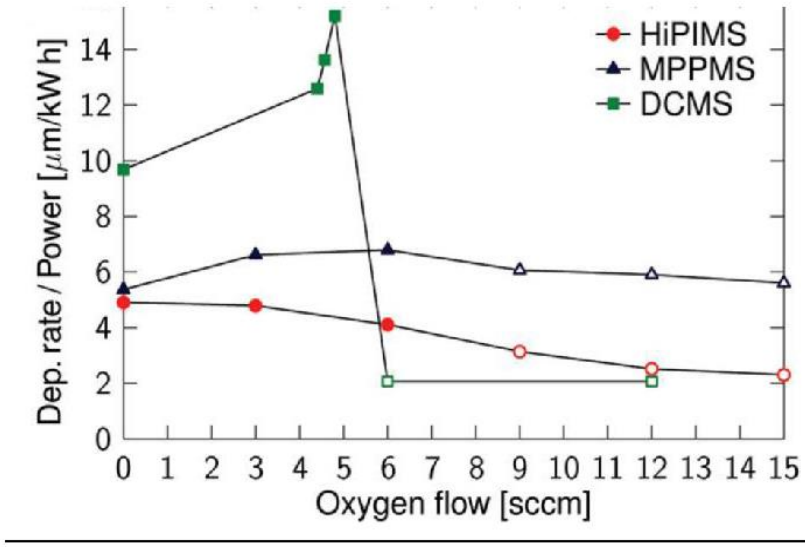


**Fig 2. 17: Average power-normalized deposition rate for $NbO_x$ coatings prepared by DCMS, HiPIMS and MPPMS as a function of oxygen flow (taken from [53])**

Therefore, the objective of this thesis is to enhance the understanding of MPPMS technique characteristics for the deposition of advanced TaN thin films at fast production rates. HiPIMS technique has been more accurately described and evaluated in the past few years, and many of these studies have being made public.

Nevertheless, MPPMS benefits for the deposition of tailored films are largely unknown. Several studies were performed on CrN film deposition by MPPMS [49-51] but many other promising coating materials have never been grown by this technique.

# 3. Corrosion

## 3.1 Definition

Corrosion is a naturally occurring process, which is defined as the degradation or deterioration of a substance and/or its properties by chemical or electrochemical interaction with their environment. The term corrosion is sometimes also applied to the degradation of plastics, concrete and wood, but generally refers to metals.

The environment to which metals are exposed to consists of the entire surrounding in contact with the metal. The major factors used to describe the environment are

- physical state of the environment either gas, liquid or solid;
- chemical composition which includes constituents and concentrations, pH
- temperature

In nature, almost all metals are found in their thermodynamically stable states which are ores that are comprised primarily of oxides, sulfides, and halides [54]. Energy must be given to extract the elemental metals from the ores. Hence, as soon as the elemental metals are extracted from their ores, they tend to revert back to their thermodynamically stable compounds. In most cases, metals will form oxides when exposed to moisture as shown in Fig 2.18. If the oxide is porous or does not have good adhesion to the substrate metal, the metal will actively corrode. If the oxide forms a compact impervious layer and has good adhesion, the metal will passivate,

resulting in excellent corrosion resistance. In environments that contain aggressive ions, however, the passive film can breakdown, resulting in localized corrosion and very high corrosion rates. Hence, coatings are very frequently needed to suppress corrosion in metals that do not naturally form protective passive films or for aggressive environments that can break down passivity [55].

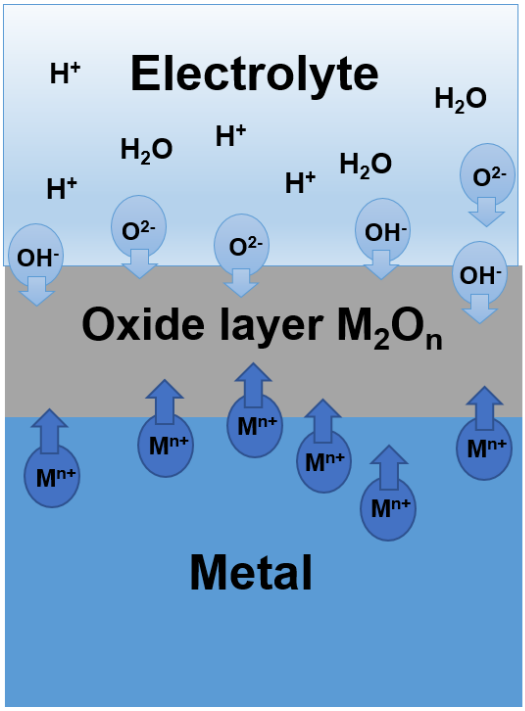


**Fig 2. 18: Naturally formed oxide layer on top of metallic materials exposed to moisture**

## 3.2 Corrosion process

The corrosion of metals can be divided into three groups [56]

- Wet corrosion where the corrosive environment is aqueous with dissolved species, normally the electrolyte is a liquid and the process is electrochemical.
- Corrosion in other fluids such as fused salts and/or molten salts.
- Dry corrosion where the corrosive environment is a high temperature dry gas.

This thesis will be focused exclusively on wet corrosion processes occurring in different real applications that degrade metallic components and on the application of TaN based coatings to reduce or inhibit these degradation mechanisms.

The wet corrosion process consists of three important elements which are necessary for the corrosion process to occur: anodic reaction, cathodic reaction and electrolyte solution or conducting liquid. The anodic reaction or oxidation of the metal results in dissolution of the metal, which is transferred to the solution as $M^{n+}$ ions. The cathodic reaction or reduction involves oxygen. Reduction of oxygen is the dominant cathodic reaction in natural environments (seawater, freshwater, soil and atmosphere). This process forms an electrical circuit without any accumulation of charge. The electrons are released by the anodic process and they are conducted through the metal to the cathode. The electrons released by the anodic process are consumed by the cathodic reaction [57]. This electrochemical process requires an ionically conducting liquid, the "electrolyte", which must be in contact with the metal. The electrochemical circuit is closed by ion conduction through the electrolyte. Typically the metal ions $M^{n+}$ are conducted towards $OH^-$ ions and together they normally produce a metal hydroxide, which is deposited on the surface of the metal. This process is illustrated in Fig 2.20.

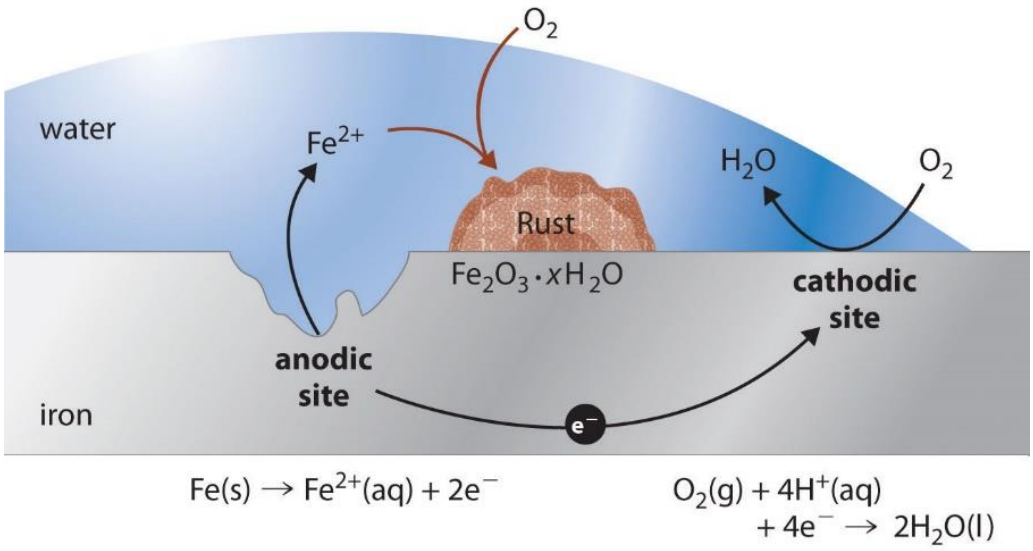


**Fig 2. 19: Corrosion process taking place at iron metal surface (taken from [58])**

Wet corrosion is an electrochemical process involving anodic (or oxidation) and cathodic (or reduction) reactions [57]. Dissolution and/or oxidation of a metal M, which is an anodic reaction, is represented by the following reactions

$$M \rightarrow M^{n+} + ne^- \quad [2.11]$$

$$M + nH_20 \rightarrow MO_n + 2\,nH^+ + 2\,ne^- \quad [2.12]$$

The electrons of the anodic reaction must be consumed by a cathodic reaction for corrosion to proceed. Two predominant cathodic reactions in aqueous corrosion are oxygen reduction and hydrogen evolution. Their half-cell reactions are represented as follows:

*Oxygen Reduction*

$$O_2 + 4e^- + 4H^+ \rightarrow 2H_2O \text{ (in acidic solutions)} \quad [2.13]$$

$$O_2 + 4e^- + 2H_2O \rightarrow 4OH^- \text{ (in basic solutions)} \quad [2.14]$$

*Hydrogen Evolution*

$2H^+ + 2e^- \rightarrow H_2$ *(in acidic solutions)* [2.15]

$2H_2O + 2e^- \rightarrow H_2 + 2OH^-$ *(in basic solutions)* [2.16]

Oxygen reduction can only occur in aerated solutions, which contain dissolved oxygen molecules. Hydrogen evolution can occur in both de-aerated and aerated solutions.

In the study of corrosion, polarization diagrams [59] are used to determine the rates of metal dissolution, metal oxidation, oxygen reduction, and hydrogen evolution and will be further described in Chapter 3. The thermodynamic driving force for the electrochemical reaction is measured in potential, E, on the vertical axis of the polarization diagram. The kinetics of the electrochemical reaction are measured in current, I, on the horizontal axis of the polarization diagram. Anodic and cathodic reactions involve the transfer of electrons, and, therefore, their rates are proportional to the current.

Based on Faraday's law, the moles, N, of species reacted is related to the current, I:

$$N = \frac{It}{nF} \quad [2.17]$$

where t is the duration of the current I, F is Faraday's constant (or charge on one mole of electrons), and n is the moles of electrons participating in the reaction.

Anodic reactions generate anodic currents, $I_A$, and cathodic reactions generate cathodic currents, $I_C$. The currents are often normalized with respect to the surface area, A, of the electrode:

$i_a = \frac{I_A}{A}$ (Anodic corrosion current density) [2.18]

$i_c = \frac{I_C}{A}$ (Cathodic corrosion current density) [2.19]

When corrosion occurs, the amount of electrons generated by metal dissolution is equal to that consumed by the cathodic reactions to conserve charge. Hence, the corroding material assumes the corrosion potential, $E_{corr}$, where the anodic, $i_a$, and cathodic, $i_c$, current densities have the same magnitude, called the corrosion current density, $i_{corr}$.

Depending on the metal and environment, metals may have active, passive, or active-passive electrochemical behavior. Active metals and alloys do not form protective passive films and show increasing anodic currents as the potential is increased above the corrosion potential ($E_{corr}$). Passive metals form protective passive films and have very low dissolution currents at potentials more positive than $E_{corr}$.

Most common coating solutions to prevent metal material degradation, provide one or more of the following characteristics to protect the metal substrate: (i) an impervious barrier to moisture and corrosive species, (ii) corrosion inhibition utilizing corrosion inhibitors, and (iii) cathodic protection. Barrier coatings are the ones evaluated during this thesis.

Barrier coatings ideally protect the substrate metal by providing an impervious barrier thin oxide layer to moisture and corrosive species. Corrosion cannot initiate if moisture is not present; hence, the substrate metal will be free of corrosion if the barrier coating is intact, but can initiate from coating defects or cracks in the presence of moisture and corrosive species. The electrical and electrochemical properties of the barrier coating can also affect the degree of corrosion that initiates at this breaches. Barrier coatings that are electrically conductive can accelerate corrosion at coating breaches, therefore, inorganic coatings such as oxides, nitrides, carbides, and so on, are generally preferable due to their often inherent insulating characteristics.

## 3.3 Corrosion modes

The wet corrosion processes can be divided in two main group, i.e. uniform corrosion and localized corrosion. Uniform corrosion (1), as the name suggests, occurs over the majority of the surface of a metal at a steady and often predictable rate and it accounts for the 30% materials failure. It is easily controllable due to its predictability, and the commonly employed strategy is to make the material thick enough to ensure the lifetime of the component. The second main group involves localized corrosion which represents the 70% of materials failure due to corrosion degradation mechanisms. The consequences of localized corrosion are massive compared to uniform corrosion, because the failure occurs without warning and the damage can be tremendous. Localized corrosion can occur in different forms [60], briefly described below:

(2) *Pitting corrosion* is a form of corrosion by which cavities or holes are generated in the material. Pitting is generally initiate by i) localized chemical or mechanical damage to the passive surface oxide film of the material, ii) breakdown of a protective coating and/or iii) non-uniformity present on material structure.

(3) *Crevice corrosion* refers to the localized attack on a metal surface at the gap or crevice between two joining surfaces. It is started by a difference in concentration of some metal constituents, generally oxygen, establishing an electrochemical concentration cell. Outside the gap, the two materials are corrosion resistant.

(4) *Galvanic corrosion* refers to corrosion damage induced when two dissimilar materials are coupled in a corrosive electrolyte. When two dissimilar metals are immersed in a conducting solution they usually develop different corrosion potentials. If the metals are in contact this potential difference provides the driving force for increased corrosion, the less noble of the two metals corroding more rapidly.

(5) *Erosion-corrosion* is the acceleration of the rate of deterioration of a metal resulting from relative movement between the corrosive fluid and the metal surface. It is characterized by the development of a surface profile of grooves, waves and rounded holes which usually exhibits a directional pattern.

(6) *Intergranular corrosion* is the preferential attack of the grain boundaries of the crystals that form the metal. Grain boundaries are somehow more reactive than the matrix of an alloy, but since the difference in reactivity is slight, grain boundary effects are usually of little consequence.

(7) *Environmentally assisted-cracking* includes stress-corrosion cracking, fatigue and hydrogen damage. All these modes of corrosion involve the combination of mechanical factors and corrosive environments. Stress-corrosion is based on the combined action of a static tensile stress and corrosion which forms cracks and eventually catastrophic failure of the component. During fatigue corrosion, the combined action of cyclic stresses and a corrosive environment reduce the life of components. Hydrogen, by various mechanisms, embrittles a metal especially in areas of high hardness causing blistering or cracking especially in the presence of tensile stresses.

The most common corrosion mechanisms when a coating-substrate system is immersed in an electrolyte are galvanic corrosion and pitting corrosion. When a coating is applied into a metal substrate and exposed to a corrosive electrolyte, it also tends to form a protective oxide layer on the top of its surface. However, if this oxide is not protective enough, it can allow the penetration of the corrosive medium along the coating thickness. If the microstructure of this coating presents voids, defects and/or pores, a diffusion pathway will be created towards the metal substrate. When corrosion potentials difference between the metal substrate and the coating is high, galvanic corrosion may occur at coating/substrate interface. This form of

corrosion can be observed when the coating corrosion resistance is lower than the bare metal substrate. When the chemical stability of the protective oxide layer is high, the material tends to be protected. However, the oxide layer may start to crack due to different factors, i.e. after a long time exposure, by the application of a potential, by the application of a mechanical load… In this situation, the fresh metal of the coating is exposed to direct contact with the electrolyte giving up electrons easily and initiating tiny pits formation which can cause severe corrosion. This form of corrosion is known as pitting corrosion. Eventually, pitting corrosion can end up as galvanic corrosion if the corrosion potentials of metal substrate and coating are different enough. Pitting commences when the electrode potential exceeds the critical value known as the pitting potential ($E_{pit}$) and its occurrence can be easily recognized by an abrupt increase on the corrosion current density in polarization diagrams.

## 3.4 Advantages of HPPMS techniques for the deposition of corrosion protective coatings

As already explained in sections 2.3 and 2.4 within this chapter, HPPMS plasma discharges are characterized by much higher ionization degree of sputtered material compared with DCMS discharges [29]. The ionized nature of sputtered material provides an added parameter to control the energy and direction of the ion flux towards the substrate. Superior coating properties can be obtained due to the unique high metal ion content in HPPMS plasmas, which allows the control by external electrical and magnetic fields of sputtered ion flux trajectory and acceleration supplying highly energetic material flux on the growing surface.

Despite of HPPMS technology was developed in the early 90's [28], HPPMS coatings ready for commercialization became a reality a few years ago. They were mainly developed for tribological applications [40, 61], where the better adhesion of coating-

to-substrate [34, 62-64], smoother surface [65] and more uniform coverage of the coated parts [36], did promote improved wear resistance and service lifetime of several components in cutting tools and automotive market.

Currently, there is a general belief about the great advantage HPPMS technology offers for the deposition of corrosion-resistant coatings. There is a general trend towards the possibility to use HPPMS coatings in real applications subjected to harsh environments where conventional sputtered coatings were unsuitable.

The corrosion resistance enhancement of sputtered films is promoted by the high ion-to-neutral ratio of sputtered particles during HPPMS plasma discharge, besides the features mentioned above. The two key characteristics to guarantee an adequate corrosion protection by a coating are:

- The formation of a well adherent and stable passive oxide film on the surface (which is dependent on coating material)
- The development of a defect-free and extremely dense microstructure film (which is influenced primarily by deposition technology)

Traditionally, the densification of coatings deposited by conventional magnetron sputtering techniques has been achieved by energy supply to the growing films through bias voltage and temperature application [66]. However, during DCMS, the majority of the ions available for thin film assistance are sputtering gas ions, $Ar^+$ ions, which coupled with very high bias voltages can induce argon incorporation into the film, lattice defects and high compressive stresses [67-69]. The high temperature application during film deposition limits the selection of substrate materials.

HPPMS technologies application for thin film growth adds a new powerful tool to tune the film microstructure and completely densify the coating, i.e. the high metal ion flux. It has been reported by several authors that the assistance of growing films by low energetic high ion flux irradiation is the most effective strategy for the development

of extremely dense films without increasing residual stresses and lattice defects [68, 70]. HPPMS techniques have well-proven capacity for the generation of highly ionized plasmas enabling complete densification and optimization of thin films microstructure [29, 30, 36, 38, 48, 71-73].

This increasing interest on corrosion applications is supported by the high amount of articles published recently related to the investigation of HPPMS coatings performance in harsh environments. T. Zhang et al. [74] synthesized Ti-Al-N films by HiPIMS from a compound $Ti_2AlN$ target and showed that densely packed nanocrystalline films could be obtained characterized by excellent oxidation and corrosion resistance compared to films grown by conventional pulsed DCMS. J.Lin and I. Dahan studied the performance of nanocrystalline Cr coatings on SS 304 samples prepared by MPPMS at different peak target current densities [50]. Cr films grown at peak current densities of 1.2 A $cm^{-2}$ exhibited extremely dense, columnar free and fine grain size microstructure with enhanced corrosion resistance compared to Cr films deposited by DCMS. P.Eh. Hovsepian and co-workers investigated the performance of CrN/NbN nanostructured films grown by HiPIMS in pure steam environment at 650 ºC [75]. CrN/NbN films with enhanced adhesion and very dense microstructure were deposited on P92 steel showing reliable protection in steam turbine simulated environment up to 2000 h operation. Y.X.Ou et al. [76] analyzed the structure, adhesion and corrosion resistance of CrN/TiN supperlatice films deposited by HPPMS on SS304L samples. They showed that films with dense microstructure, well-defined nanolayer interfaces and dense coating/substrate interface exhibited improved pitting and stress corrosion cracking compared to uncoated SS304L.

# 4. References

[1] Colakis, Marianthe; Masello, Mary Joan (2007-06-30). "Tantalum". Classical Mythology & More: A Reader Workbook"

[2] M. Schutze, R. Bender, K.G. Schutze, Corrosion Resistance of High-Performance Materials, second ed., Wiley-VCH, Frankfurt, 2012

[3] S.L. Lee, M. Doxbeck, J. Mueller, M. Cipollo, P. Cote, Texture, structure and phase transformation in sputter beta tantalumcoating Surf. Coat. Technol. 177–178 (2004) 44.

[4] L. E. Toth, Transition Metal Carbides and Nitrides (Academic, New York, 1971)

[5] W. Lengauer and A. Eder, 2006. Nitrides: Transition Metal Solid-State Chemistry. Encyclopedia of Inorganic Chemistry. .

[6] T.B. Massalski, H. Okamoto, ASM international, Binary Alloy Phase Diagrams, second ed., Materials Park, Ohio, 1990.

[7] R.Westergard, M. Bromark, M. Larsson, P. Hedenqvist, S. Hogmark, Mechanical and tribological characterization of DC magnetron sputtered tantalum nitride thin films. Surf. Coat. Technol 97 (1997) 779–784.

[8] G.R. Lee, H. Kim, H.S. Choi, J.J. Lee, Superhard tantalum-nitride films formed by inductively coupled plasma-assisted sputtering, Surf. Coat. Technol 20 (2007) 5207–5210.

[9] K. Valleti, A. Subrahmanyam, S. V Joshi, A.R. Phani, M. Passacantando, S Santucci, Studies on phase dependent mechanical properties of dc magnetron sputtered TaN thin films: evaluation of super hardness in orthorhombic Ta4N phase. Journal of Physics D: Applied Physics 41 (2008) 045409.

[10] D.-k. Kim, H. Lee, D. Kim, Y. K. Kim, Electrical and mechanical properties of tantalum nitride thin films deposited by reactive sputtering, Journal of Crystal Growth 283 (2005) 404–408

[11] S.K. Kim, B.C. Cha, Deposition of tantalum nitride thin films by D.C. magnetron sputtering, Thin Solid Films, 475 (2005) 202-207

[12] K-Y. Liu, J-W. Lee, F-B. Wu, Fabrication and tribological behavior of sputtering TaN coatings, Surf. Coat. Technol. 259 (2014) 123–128

[13] T. Riekkinen, J. Molarius, T.Laurila, A. Nurmela, I. Suni and J.K. Kivilauhti, Reactive sputter deposition and properties of $TaN_x$ thin films, Microelectron. Eng. 64 (2002) 289

[14] S.M. Rossnagel, Characteristics of ultrathin Ta and TaN filmsJ. Vac. Sci Technol. B 20 (2002) 2328

[15] T. Wada , K. Iwamoto, K. Tsukamoto, K. Hiro , Properties of TaN Coating Film Deposited on WC-Co-Based Cemented Carbide Using Magnetron Sputter Ion Plating, Applied Mechanics and Materials 87 (2011) 186-190

[16] M. Nordin, R. Sundström, T.I. Selinder, S. Hogmark, Wear and failure mechanisms of multilayered PVD TiN/TaN coated tools when milling austenitic stainless steel, Surf. Coat. Technol. 133-134 (2000) 240-246

[17] I. Langmuir, Oscillations in ionized gases, Proc. Nat. Acad. Sci. U.S. 14 (1928) 627-637

[18] J.R. Roth, Industrial Plasma Engineering Volume 1: Principles, Institute of Physics Publishing, Bristol, UK (1995)

[19] http://pixshark.com/states-of-matter-plasma.htm

[20] J.A. Hopwood, in: J.A. Hopwood (ed), Thin Films: Ionized Physical Vapour Deposition, Academic Press, San Diego, (2000), pp. 181.

[21] P. Sigmund, Theory of Sputtering. I. Sputtering Yield of Amorphous and Polycrystalline Targets, Phys. Rev. 184 (1969) 383–416.

[22] J. Hopwood, F. Qian, Mechanisms for highly ionized magnetron sputtering, J. Appl. Phys. 78 (1995) 758.

[23] D. Depla, S. Mahieu and J.E. Greene *"Sputter Deposition Processes"* in Handbook of Deposition Technologies for Films and Coatings (Third Edition), 3rd ed., P. M. Martin, Ed. Boston, MA: William Andrew Publishing, 2010, pp. 314- 363. Available online: http://www.sciencedirect.com/science/article/pii/B9780815520313000016#

[24] G. Brauer, B. Szyszka, M. Vergöhl, R. Bandorf, Magnetron sputtering – Milestones of 30 years, Vacuum 84 (2010)1354–1359

[25] B. Window, N. Savvides, Charged particle fluxes from planar magnetron sputtering sources, J. Vac. Sci.Technol. A 4 (1986) 196

[26] U. Helmersson, M. Lattemann, J. Bohlmark, A. P. Ehiasarian, J.T. Gudmundsson, Ionized Physical Vapor Deposition (IPVD): A Review of Technology and Applications, Thin Solid Films 513 (2006) 1-24

[27] R.K Waits, Planar magnetron sputteringJ. Vac. Sci. Technol. 15 (1978) 179

[28] V. Kouznetsov, K. Macák, J.M. Schneider, U. Helmersson, I. Petrov, A novel pulsed magnetron sputter technique utilizing very high target power densities, Surf. Coat.Technol. 122 (1999) 290-293.

[29] K. Sarakinos, J. Alami, S. Konstantinidis, High power pulsed magnetron sputtering: A review on scientific and engineering state of the art, Surf. Coat. Technol. 204 (2010) 1661-1684.

[30] J.T. Gudmundsson, N. Brenning, D. Lundin, U. Helmersson, High power impulse magnetron sputtering discharge, J. Vac. Sci. Technol. A 30 (2012) 030801.

[31] M. Samuelsson, D. Lundin, J. Jensen, M.A. Raadu, J.T. Gudmundsson, U. Helmersson, On the film density using high power impulse magnetron sputtering, Surf. Coat. Technol 205 (2010) 591–596

[32] B.M. DeKoven, P.R. Ward, R.E. Weiss, D.J. Christie, R.A. Scholl, W.D. Sproul, F. Tomasel and A. Anders 2003 Proc. 46th Annual Technical Conf. Proc. Society of Vacuum Coaters (2003) 158.

[33] J. Bohlmark, J. Alami, C. Christou, A.P. Ehiasarian, U. Helmersson, Ionization of sputtered metals in high power pulsed magnetron sputtering, J. Vac. Sci. Technol.A 23 (2005) 18

[34] A. Anders, Physics of plasma-based ion implantation & deposition (PBIID) and high power impulse magnetron sputtering (HIPIMS): A comparison, Phys. Status Solidi A, 205 (2008) 965–970

[35] J. Bohlmark, M. Lattemann , J.T. Gudmundsson, A.P. Ehiasarian, Y. Aranda Gonzalvo, N. Brenning, U. Helmersson, The ion energy distributions and plasma composition of a high power impulse magnetron sputtering discharge, Thin Solid Films 515 (2006) 1522–1526

[36] J. Alami, P.O.Å. Persson, J. Böhlmark, J.T. Gudmundsson, D. Music, and U. Helmersson, Ion-assisted physical vapor deposition for enhanced film properties on non-flat surfaces, J. Vac. Sci. Technol. A 23 (2005) 278.

[37] J. Alami, P. Eklund, J. M. Andersson, M. Lattemann, E. Wallin, J. Bolhmark, P. Persson, and U. Helmersson, Phase tailoring of Ta thin films by highly ionized pulsed magnetron sputtering, Thin Solid Films 515 (2007) 3434-3438.

[38] J Alami, K Sarakinos, F Uslu, C Klever, J. Dukwen, M Wuttig, On the phase formation of titanium oxide films grown by reactive high power pulsed magnetron sputteringJ. Phys. D: Appl. Phys. 42 (2009) 015304

[39] C. Reinhard, A.P. Ehiasarian, and P.E. Hovsepian, CrN/NbN superlattice structured coatings with enhanced corrosion resistance achieved by high power impulse magnetron sputtering interface pre-treatment, Thin Solid Films 515 (2007) 3685–3692

[40] P.E. Hovsepian, C. Reinhard, and A.P. Ehiasarian, CrAlYN/CrN superlattice coatings deposited by the combined high power impulse magnetron sputtering technique, Surf. Coat. Technol. 201 (2006) 4105-4110

[41] P.E. Hovsepian, A.P. Ehiasarian, A. Deeming, and C. Schimpf, Novel TiAlCN/VCN Nanoscale Multilayer PVD Coatings Deposited by the Combined High Power Impulse Magnetron Sputtering/Unbalanced Magnetron Sputtering, (HIPIMS/UBM), Vacuum 82 (2008) 1312-1317

[42] D.J. Christie, Target material pathways model for high power pulsed magnetron sputtering, J. Vac. Sci. Technol. A 23 (2005) 330

[43] D. Lundin, C. Huo, N. Brenning, M.A. Raadu, U. Helmersson, Deposition rate loss in High Power Impulse Magnetron Sputtering: Understanding trough computational modeling, Society of Vacuum Coaters 54th Annual Technical Conference Proceedings, Chicago, 2011

[44] R. Chistyakov, U.S. Patent 7,147,759, "High-Power Pulsed Magnetron Sputtering,"December 12, 2006.

[45] R. Chistyakov, B. Abraham, W.D. Sproul, Advances in High Power Pulse Reactive Magnetron Sputtering, 49th Annual SVC Technical Conference, Washington, DC, April 23–27, 2006, 88–91.

[46] R. Chistyakov, B. Abraham, W. Sproul, J. Moore, J. Lin, Modulated Pulse Power Technology and Deposition for Protective and Tribological Coatings, Proceedings of the 50th Annual SVC Technical Conference, Louisville, KY, April 30–May 3, 2007, 139–143.

[47] J. Lin, J.J. Moore, W.D. Sproul, B. Mishra, J.A. Rees, Z.Wu, R. Chistyakov, B. Abraham, Ion energy and mass distributions of the plasma during modulated pulse power magnetron sputtering, Surface & Coatings Technology 203 (2009) 3676–3685

[48] J.Lin, J. J. Moore, W. D. Sproul, S.L. Lee, and Jun Wang, Effect of Negative Substrate Bias on the Structure and Properties of Ta Coatings Deposited Using Modulated Pulse Power Magnetron SputteringIEEE TRANSACTIONS ON PLASMA SCIENCE, VOL. 38, NO. 11, NOVEMBER 2010

[49] J. Lin, W.D. Sproul, J.J. Moore, B. Mishra, Z.L. Wu and J. Wang, "The structure and properties of chromium nitride coatings deposited using dc, pulsed dc and modulated pulse power magnetron sputtering", Surf. Coat. Technol. 204 (2010) 2230-2239.

[50] J. Lin, I. Dahan, Nanostructured chromium coatings with enhanced mechanical properties and corrosion resistance, Surface & Coatings Technology 265 (2015) 154–159

[51] J. Lin, B. Wang, Y. Ou, W.D. Sproul, I. Dahan, J. J. Moore Structure and properties of CrSiN nanocomposite coatings deposited by hybrid modulated pulsed power and pulsed dc magnetron sputtering / Surface & Coatings Technology 216 (2013) 251–258

[52] M. Hála, J. Čapek, O. Zabeida, J.E. Klemberg-Sapieha, L. Martinu, Pulse management in high power pulsed magnetron sputtering of niobiumSurface & Coatings Technology 206 (2012) 4186–4193

[53] M. Hála, J. Čapek, O. Zabeida, J.E. Klemberg-Sapieha, L. Martinu, Hysteresis-free deposition of niobium oxide films by HiPIMS using different pulse management strategies J. Phys. D: Appl. Phys. 45 (2012) 055204

[54] Rosenqvist T. Principles of extractive metallurgy. 2nd ed. New York: McGraw-Hill Book Company; 1983.

[55] L.H. Hihara, "Chapter 1: Electrochemical Aspects of Corrosion-Control Coatings" in the book Intelligent Coatings for Corrosion Control, Butterworth Heinemann

[56] E. Bardal, Corrosion and Protection, Springer-Verlag, London (2004)

[57] P. ZARRAS and J. D. STENGER-SMITH , *"Corrosion processes and strategies for prevention: an introduction" in* Handbook of Smart Coatings for Materials Protection

[58] Martin Silberbeg,Principles of General Chemistry, 2nd edition, ISBN-13: 978-0077274320, ISBN-10: 0077274326

[59] Gellings PJ. Introduction to corrosion prevention and control for engineers. Rotterdam: Delft University Press; 1976.

[60] I. Gurrappa, I.V.S. Yashwanth *The Importance of Corrosion and the Necessity of Applying Intelligent Coatings for Its Control* in Intelligent Coatings for Corrosion Control book.

[61] K. D.Bakoglidis, I. Nedelcu, S. Schmidt, G. Greczynski, P. Ehret, L. Hultman, Rolling contact fatigue of bearing components coated with carbon nitride thin films, Tribology International 98 (2016) 100–107

[62] M. Lattemann, A.P. Ehiasarian, J. Bohlmark, P.Å.O. Persson, U. Helmersson, Investigation of high power impulse magnetron sputtering pretreated interfaces for adhesion enhancement of hard coatings on steel, Surface and coatings technology 200 (2006) 6495-6499

[63] A. P. Ehiasarian, J. G. Wen and I. Petrov, Interface microstructure engineering by high power impulse magnetron sputtering for the enhancement of adhesion, J. Appl. Phys. **101** (2007) 054301

[64] Martin Drábik, Vladimír Ballo, Martin Truchlý, Juraj Frkáň, Tomáš Roch, Lenka Kvetková, Leonid Satrapinskyy, Peter Kúš, Influence of plasma pretreatment on the performance of industrial tungsten carbide coatings deposited at low temperature on 100Cr6 bearing steel substrates, Surface & Coatings Technology 293 (2016) 2–9

[65] N. Bagcivan, K. Bobzin, S. Theiß, (Cr1−xAlx)N: A comparison of direct current, middle frequency pulsed and high power pulsed magnetron sputtering for injection molding components, Thin Solid Films 528 (2013) 180–186

[66] P. Patsalas , C. Charitidis, S. Logothetidis, The effect of substrate temperature and biasing on the mechanical properties and structure of sputtered titanium nitride thin films, Surface and Coatings Technology 125 (2000) 335-340

[67] I. Petrov, L. Hultman, J.-E. Sundgren and J. E. Greene, Polycrystalline TiN films deposited by reactive bias magnetron sputtering: Effects of ion bombardment on resputtering rates, film composition, and microstructure, J. Vac. Sci. Technol. A 10 (1992) 265 ç

[68] L. Hultman, J.E. Sundgren, J. E. Greene, D. B. Bergstrom, and I. Petrov, High flux low energy (20 eV) N+2 ion irradiation during TiN deposition by reactive magnetron sputtering: Effects on microstructure and preferred orientation, J. Appl. Phys. 78 (1995) 5395

[69] J. H. Kim, K. W. Chung, Microstructure and properties of silicon nitride thin films deposited by reactive bias magnetron sputtering, J. Appl. Phys. 83 (1998) 5831

[70] L. Hultman, W.-D. Münz, J. Musil, S. Kadlec, I. Petrov and J. E. Greene, Low-energy (∼100 eV) ion irradiation during growth of TiN deposited by reactive magnetron sputtering: Effects of ion flux on film microstructure, J. Vac. Sci. Technol. A 9 (1991) 434

[71] G. Greczynski, J. Jensen, J. Böhlmark, L. Hultman, Microstructure control of CrNx films during high power impulse magnetron sputtering, Surface and coatings technology 205 (2010)118-130

[72] G. Greczynski, J. Lu, J. Jensen, S. Bolz, W. Koelker, Ch. Schiffers, O. Lemmer, J. E. Greene, L. Hultman, A review of metal-ion-flux-controlled growth of metastable TiAlN by HIPIMS/DCMS co-sputtering, Surface and coatings technology 257 (2014) 15-25

[73] J. Lin, W.D. Sproul, J.J. Moore, Z.L. Wu, S.L. Lee, Effect of negative substrate bias voltage on the structure and properties of CrN films deposited by modulated pulsed power (MPP) magnetron sputtering, J. Phys. D: Appl. Phys. 44 (2011) 425305

[74] T. F. Zhang, Q.M. Wang, J. Lee, P. Ke, R. Nowak, K. H. Kim, Nanocrystalline thin films synthesized from a Ti2AlN compound target by high power impulse magnetron sputtering technique, Surf. Coat. Technol 212 (2012) 199–206

[75] P. Eh. Hovsepian, A.P. Ehiasarian, Y.P. Purandare, B. Biswas, F.J. Perez, M.I. Lasanta, M.T. de Miguel, A. Illana, M. Juez-Lorenzo, R. Muelas, A. Agüero, Performance of HIPIMS deposited CrN/NbN nanostructured coatings exposed to 650 C in pure steam environment, Materials Chemistry and Physics 179 (2016) 110-119

[76] Y.X. Ou, J. Lin, S. Tong, W.D. Sproul, M.K. Lei, Structure, adhesion and corrosion behavior of CrN/TiN superlattice coatings deposited by the combined deep oscillation magnetron sputtering and pulsed dc magnetron sputtering, Surface & Coatings Technology 293 (2016) 21–27

# CHAPTER 3

# DEPOSITION SYSTEM &

# CHARACTERIZATION TECHNIQUES

# 1. MIDAS 450 sputtering system

The Ta and $TaN_x$ films were synthetized in the MIDAS 450 closed field unbalanced magnetron sputtering (CFUBMS) system designed and mounted at IK4-TEKNIKER (Fig 3.1.). The maximum coating area is 500 mm in height and 400 mm in diameter. It is pumped to a base pressure of 1 x $10^{-5}$ mbar using a primary mechanical pump and a diffusion pump connected in series.

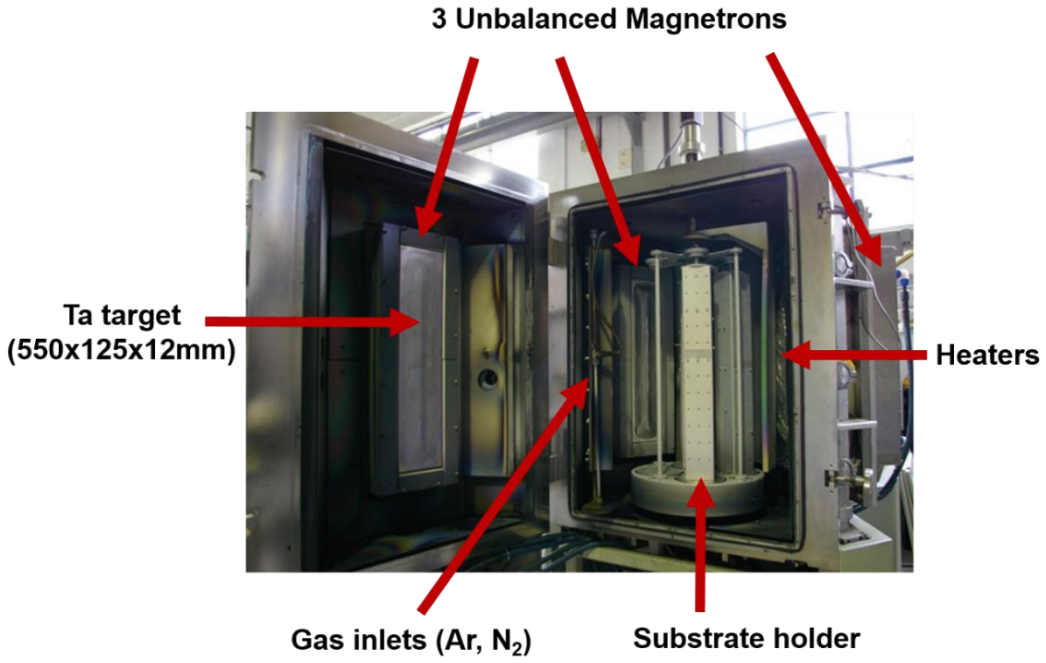


**Fig 3. 1: MIDAS 450 sputtering system**

The system is equipped with three rectangular magnetrons manufactured by Gencoa Ltd. with a target size of 550x125 $mm^2$. During this thesis, a unique Ta target (99.99% purity supplied by GfE, Gesellschaft für Elektrometallurgie mbH) was employed for $TaN_x$ films deposition. Metallic Ta and nitride TaN films were grown in Ar and $Ar/N_2$ mixture atmospheres, respectively. Ar and $N_2$ gases are introduced into the chamber through separate mass flow controllers from the gas inlet shown in Fig 3.1.

The system incorporates a twofold rotation substrate holder which can be negatively biased up to -600 V. The target-to-substrate distance is 70 mm. The substrate holder can be heated up to 350 ºC.

The magnetrons can be powered by DC, pulsed DC and MPP power supplies. During this thesis MPP power supply and dedicated bias power supply were employed for $TaN_x$ thin film synthesis and are described below and shown in Fig 3.2.

The power supply employed for MPPMS plasma discharge generation is the so-called SOLO/AXIS - 180™ Pulsed DC Plasma Generator manufactured by Zpulser LLC, USA. It is a 20 kW average power supply which can deliver a maximum peak power of 300 kW with 550 A maxium peak current and 1100 V maximum peak voltage. Zpulser Vesta is a 10 kW DC bias supply solution for high-power pulsed plasma magnetron that comes with a built-in arc suppression circuit to prevent the loss or significant drop of bias voltage during high power pulsing.

**Fig 3. 2: Zpulser SOLO and VESTA power supplies**

The cleaning procedure realized on substrate samples before all $TaN_x$ coating deposition processes that will be described in Chapter 4, 5 and 6 is explained hereafter.

The substrates were ultrasonically cleaned in ethanol for 10 min, followed by drying in warm air. Once the substrates were introduced into the chamber and base pressure of $10^{-5}$ mbar was reached, the substrates were sputter etched in $Ar+H_2$ plasma for 10 min at – 300 V DC bias voltage for adhesion enhancement between the substrate and the coating and native oxide layer removal from metal substrate surfaces.

# 2. Characterization techniques

## 2.1. MPPMS discharge characteristics

During the Ta and $TaN_x$ deposition processes, the voltage and current waveforms at the cathode for each pulse shape were monitored and recorded from an oscilloscope (ISO-TECH, IDS 8064, Fig 3.3) connected to the magnetron.


**Fig 3. 3: ISO-TECH oscilloscope employed for V-I waveforms monitoring**

Furthermore, the Zpulser SOLO software registers the evolution of peak and average voltage, peak and average current, peak and average power and frequency during the whole MPPMS process as shown in Fig 3.4.

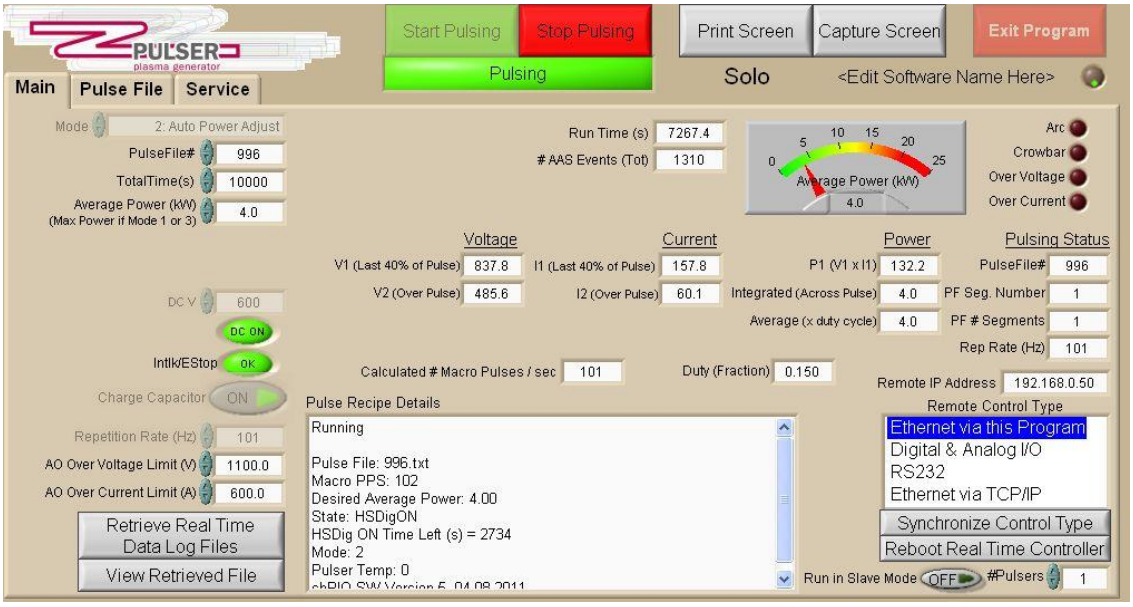


**Fig 3. 4: Zpulser SOLO software employed for MPPMS discharge management**

## 2.2. Techniques for studying thin films microstructure and composition

### 2.2.1 Glow discharge – Optical Emission Spectroscopy (GD-OES)

Glow discharge optical emission spectroscopy (GD-OES) is an efficient method for the analysis of the elemental composition of a material. It provides rapid depth profiling analysis of composition and thickness of solid materials.

The operational principle of GD-OES is briefly described [1]. In a glow discharge, cathodic sputtering using Ar ions is used to remove material layer by layer from the tested sample starting from the surface. The removed atoms migrate into the plasma where they are excited and ionized through collisions with electrons or Ar gas atoms. The characteristic spectrum emitted by these excited atoms or ions is measured by a spectrometer. The intensities are recorded as function of time. Based on a

calibration method, establish beforehand, these qualitative results can be transformed in a quantitative content depth profile.

In this thesis, a GDPROFILER 2 manufactured by Horiba Jobin Yvon shown in Fig 3.5 was employed.


**Fig 3. 5: GD-OES equipment used for TaNx coatings composition analysis**

The compositional analysis of $TaN_x$ coatings obtained during experimental work within this thesis is considered qualitative. Quantified profiles can be obtained after calibration. Calibration procedure is based on the comparison between measured intensities of the unknown sample with those measured using a standard material of known composition. An adequate calibration would need different elemental composition TaN reference sample measurements to compare with the unknown sample. In this study, just Ta reference samples of known composition were used to establish a relationship between emission intensities and elemental composition of $TaN_x$ coatings. Hence, the given elemental composition values of $TaN_x$ are relative.

### 2.2.2 Scanning electron microscope (SEM)

Scanning electron microscope (SEM) is a high-resolution microscope that uses a focused beam of high-energy electrons to produce a variety of signals at the surface of solid materials [2]. The SEM uses electrons for imaging, like optical microscope uses visible light. The advantages of SEM are much higher magnification (>100000X) and greater depth of field (100 times higher) compared to optical microscope. The signals obtained after electron-solid material interactions reveal information about the surface of tested material including morphology, composition, surface topography… The SEM column and chamber are at vacuum to enable the electrons to travel freely from the beam source to the tested material and then to the detectors.

In this thesis, a high resolution field emission scanning electron microscope (FE-SEM) Ultra Plus manufactured by Carl Zeiss shown in Fig 3.6 was employed.


**Fig 3. 6: FE-SEM microscope used for TaNx films analysis**

In this thesis, different analysis on $TaN_x$ coated samples were carried out. The microstructure of all $TaN_x$ coatings was analyses by cross-sectional micrographs

using silicon wafers. The thickness of the $TaN_x$ coated silicon wafers was measured by the following procedure. 3 different zones along the cross-section were selected and 5 thickness measurements were made/per zone, obtaining 15 thickness values/per sample to calculate the average thickness of each $TaN_x$ coating. The starting and ending points of the $TaN_x$ films to measure the thickness were determined from perpendicular lines drawn using FESEM software at 90 º angle with respect to the substrate.

Surface morphology of $TaN_x$ films characterized by different N/Ta ratios was investigated in Chapter 5. Surface topography of as-deposited and worn surfaces (Chapter 5) of the samples was evaluated.

### 2.2.3 Transmission electron microscope (TEM)

The transmission electron microscope (TEM) is a very powerful tool for material analysis. A high energy beam of electrons is throw through a very thin sample, and the interactions between the electrons and the atoms are detected enabling the investigation of material features such as the crystal structure and features in the structure like dislocations and grain boundaries. Chemical analysis can also be performed. TEM can be used to study the growth of layers, their composition and defects. High resolution TEM can be employed to study the quality, shape, size and density of quantum wells, wires and dots. The resolution of TEM is much higher than SEM.

In this thesis, TEM was used for $TaN_x$ multilayer microstructure analysis (Chapter 5), since no differences were detected between monolayer and multilayer TaN films using SEM. Cross-sectional samples deposited onto Si substrates were prepared for transmission electron microscopy (TEM), by dimple-grinding with a Gatan 656

dimpler and Ar ion-milling with a Fischione 1010 model until an electron transparent area was obtained at the center of the sample. The procedure is fully described in reference [4]. Transmission electron microscopy studies were done using a JEOL 3010 F microscope with a field-emission gun, 300 kV acceleration voltage and 0.17 nm of structural resolution. Image processing of the high-resolution images was carried out using Gatan Digital Micrograph and Image J software packages.

### 2.2.4 X-Ray Diffraction (XRD)

X-ray diffraction (XRD) is a common technique for the study of crystal structures and atomic spacing of materials [5]. XRD is based on constructive interference of monochromatic X-rays and a crystalline sample. These X-rays are generated by a cathode ray tube, filtered to produce monochromatic radiation, collimated to concentrate, and directed toward the sample. The interaction of the incident rays with the tested sample produces constructive interference when conditions satisfy Bragg's Law ($n\lambda=2d \sin\theta$). This law relates the wavelength of electromagnetic radiation to the diffraction angle and the lattice spacing in a crystalline sample. These diffracted X-rays are then detected, processed and counted.

In this thesis, the crystal structure of the $TaN_x$ films depending on $N_2$-to-Ar ratio was determined by X – ray diffraction (XRD) using grazing incidence (Chapter 4). A Bruker AXS D8 Advance diffractometer operated in θ–2 θ mode was employed using Cu Kα radiation.

### 2.2.5 Auger Electron Spectroscopy (AES)

Auger Electron Spectroscopy (AES) is one of the most sensitive methods of surface analysis and is widely employed due to its relative simplicity compared to other techniques [6].

AES operational procedure is based on the excitation of sample surface with a finely focused electron beam which causes Auger electrons to be emitted from the surface. An electron energy analyser is used to measure the energy of the emitted Auger electrons. Using the measured kinetic energy and intensity of an Auger peak, the elemental identity and quantity of a detected element can be determined. The average depth of analysis for an AES measurement is approximately 5 nm and the lateral spatial resolution as small as 8 nm. Spatial distribution information is obtained by scanning the micro focused electron beam across the sample surface.

In this thesis, AES technique has been utilized to measure the elemental composition of barrier oxide film formation (very few nanometres thick) before and after polarization tests on $TaN_x$ film surface. The sensitivity of AES technique allows the thickness and composition measurement of such a thin oxide layer (Chapter 6). Auger analysis was conducted using a JEOL 9500F AES microprobe. This was operated at 10 kV electron beam energy. Composition depth profiles were achieved by sputtering with Ar ions with an accelerating voltage of 500 V. The depth scale is defined by the sputtering rate calibrated using a thermal $SiO_2$ standard sample.

## 2.3. Techniques for studying thin film properties

One of the main objectives of this thesis is the evaluation of $TaN_x$ films corrosion resistance in different corrosive environments. The electrochemical characterization of $TaN_x$ films is carried out in all the studies completed for this thesis. Summarizing,

- Electrochemical features of different composition $TaN_x$ films in NaCl solution are investigated in Chapter 4.
- Corrosion and tribocorrosion performance of TaN multilayer films in PBS solution is examined in Chapter 5.
- Electrochemical and electrical properties of different composition $TaN_x$ films in simulated PEM fuel cell environment ($H_2SO_4$ solution) are investigated in Chapter 6.

Hence, the techniques employed for electrochemical and corrosion resistance analysis are deeply described in the following section 2.3.1., which special emphasize in their application for coating performance assessment.

Tribocorrosion characterization procedure and set-up, and interfacial contact resistance measurement method and set-up, are uniquely employed within Chapter 5 and 6, respectively, and thus, they will be individually explained in the corresponding chapter.

Hardness and roughness characterization set-ups are described in the next sections 2.3.2 and 2.3.3.

### 2.3.1 Techniques for studying corrosion

Since corrosion is an electrochemical process, it follows that electrochemical techniques and electrochemical instrumentation can be used to study the corrosion

process. Indeed, a number of electrochemical techniques have been developed over the years especially for the measurement of corrosion processes [7]. The reasons for the popularity of electrochemical techniques for corrosion resistance evaluation of materials are based on the following characteristics:

- *They are fast*. Corrosion is a slow process. Real-time weight loss measurements need days or even weeks to make a reliable measurement of corrosion rate. Electrochemical techniques enable the measurement of corrosion rate in minutes or hours.
- *They are sensitive* and can measure very low corrosion rates.
- *They are accurate*
- *They are versatile.* Electrochemical techniques can be used to study a wide range of corrosion-related phenomena. The rate of uniform corrosion can be measured. The tendency of a metal to exhibit localized (pitting or crevice) corrosion can be measured. The passivation behavior of a corroding system can be studied. Galvanic corrosion can be quantitated.

Three-electrode electrochemical cell (Fig 3.7) set up connected to a potentiostat has been utilized for corrosion testing [8].

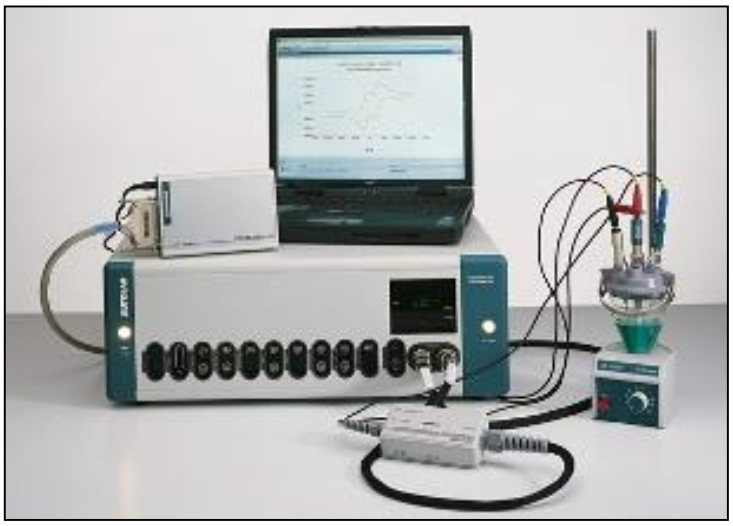

**Fig 3. 7: Three-electrode electrochemical cell connected to a potentiostat**

This set up is composed of three electrodes, the counter electrode (CE), the reference electrode (RE) and the working electrode (WE). The *counter electrode*, is an electrode which is used to close the current circuit in the electrochemical cell. It is usually made of an inert material (e.g. Pt, Au, graphite, glassy carbon) and usually it does not participate in the electrochemical reaction. The *reference electrode* is an electrode which has a stable and well-known electrode potential and it is used as a point of reference in the electrochemical cell for the potential control and measurement. The *working electrode* is the electrode in an electrochemical system on which the reaction of interest is occurring. Hence, the coated samples act as WE in this set-up.

In this section, only the electrochemical techniques employed during the study of TaN coatings corrosion performance within this thesis will be described; i.e. open circuit potential (OCP) measurements, polarization techniques and electrochemical impedance spectroscopy (EIS).

*2.3.1.1 Open circuit potential (OCP) measurements*

Open circuit potential, named commonly as $E_{oc}$, is the potential in a working electrode comparative to the reference electrode when there is no current or potential existing in the cell. When $E_{oc}$ reaches a stable value, polarization and EIS techniques are applied to the samples to evaluate electrochemical response of the tested materials.

*2.3.1.2 Polarization techniques*

Polarization methods involve changing the open circuit potential, $E_{oc}$, (equilibrium potential at which there is no current) of the working electrode and monitoring the current which is produced as a function of time or potential.

## Potentiodynamic polarization

Potentiodynamic polarization is a technique where the potential of the electrode is varied at a selected rate by application of a current through the electrolyte. It is probably the most commonly used polarization testing method for measuring corrosion resistance. Measurements of current-potential relations under carefully controlled conditions can yield information on corrosion rates, coatings and films, passivity, pitting tendencies and other important data [9,10].

When a metal coated or uncoated sample is immersed in a corrosive medium, both reduction and oxidation processes occur on its surface. Typically, the sample oxidizes (corrodes) and the medium (solvent) is reduced. In acidic media, hydrogen ions are reduced. The sample must function as both anode and cathode and both anodic and cathodic currents occur on the sample surface. Any corrosion processes that occur are usually a result of anodic currents. When a sample is in contact with a corrosive liquid and the sample is not connected to any instrumentation – as it would be "in service" – the sample assumes a potential (relative to a reference electrode) termed the corrosion potential, $E_{corr}$. A sample at $E_{corr}$ has both anodic and cathodic currents present on its surface. However, these currents are exactly equal in magnitude so there is no net current to be measured. The sample is at equilibrium with the environment. $E_{corr}$ can be defined as the potential at which the rate of oxidation is exactly equal to the rate of reduction. It is important to stress that when a sample is at $E_{corr}$ both polarities of current are present. If the sample is polarized slightly more positive than $E_{corr}$, then the anodic current predominates at the expense of the cathodic current. As the sample potential is driven further positive, the cathodic current component becomes negligible with respect to the anodic component. Clearly, if the sample is polarized in the negative direction, the cathodic current predominates and the anodic component becomes negligible [11].

Potentiodynamic anodic polarization employed within different chapters of this thesis is the characterization of a metal coated or uncoated sample by its current-potential relationship. The sample potential is scanned slowly in the positive going direction and therefore acts as an anode such that it corrodes or forms a passive oxide film on sample surface. These measurements are used to determine corrosion characteristics of metallic samples in aqueous environments. Investigation such as passivation tendencies of the tested sample is easily performed with this technique.

Experimentally, one measures polarization characteristics by plotting the current response as a function of the applied potential. Since the measured current can vary over several orders of magnitude, usually the log current function is plotted vs. potential on a semi-log chart. This plot is termed a potentiodynamic polarization plot. The potential-current relationship characteristics in a potentiodynamic anodic polarization plot can yield important information such as:

- The ability of the material to spontaneously passivate in the particular medium.
- The potential region over which the specimen remains passive.
- The corrosion rate in the passive region.
- The potential at which the passivating film of the specimen starts to break
- The pitting potential
- The transpassive region

The different regions that can be identified in a potentiodynamic polarization plot are shown in Fig 3.9.

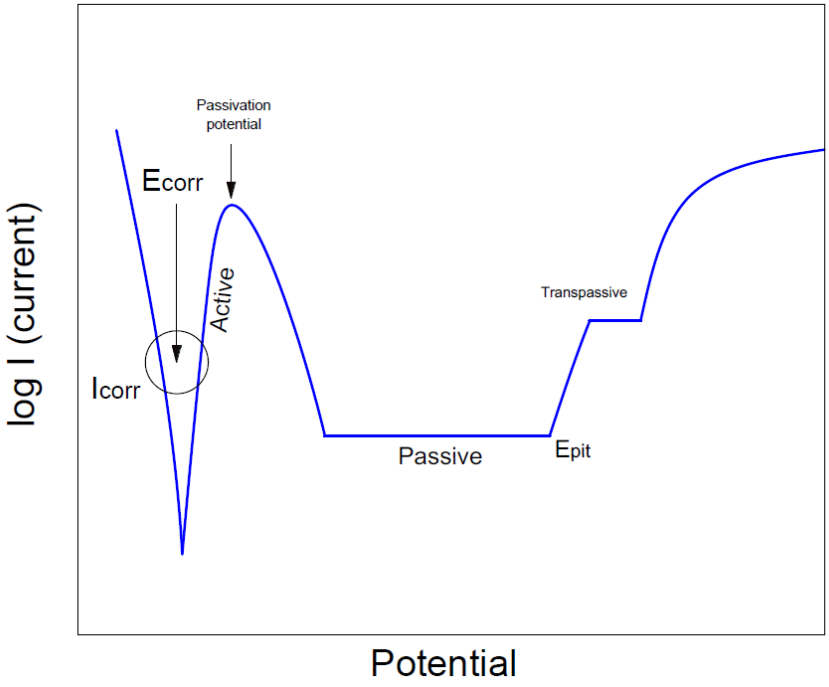


**Fig 3. 8: Potentiodynamic polarization plot including different active-passive regions**

**Tafel extrapolation method** uses data obtained from cathodic and anodic polarization measurements to calculate corrosion current density, polarization resistance and corrosion rate [12]. To determine these factors from such polarization measurements, the Tafel region is extrapolated to the corrosion potential. For an electrochemical reaction under activation control, polarization curves exhibit linear behavior in the E Vs log (i) plots called Tafel behavior [13].

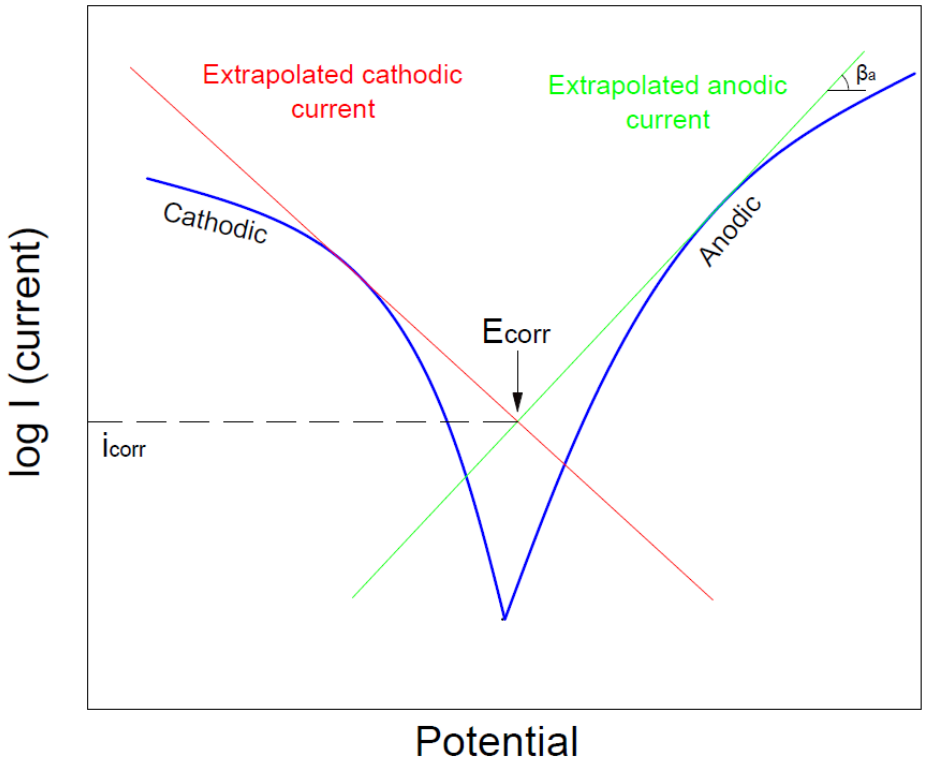


**Fig 3. 9: Sample Tafel plot from a potentiodynamic polarization scan**

$E_{corr}$ and $I_{corr}$ values can be directly determined from the cross-over point, as shown in Fig 3.10. At the corrosion potential, rate of cathodic reduction is equal to rate of anodic reaction (metal corrosion). Tafel constants ($\beta_a$ and $\beta_c$) are calculated from the anodic and cathodic slopes.

For potentials close to corrosion potential the following relation can be established between corrosion current density $i_{corr}$ and polarization resistance $R_p$ [8]:

$$R_p = 2.303 \frac{\beta_a \beta_c}{\beta_a + \beta_c} \left(\frac{1}{i_{corr}}\right) \quad [3.1]$$

According to Faraday's law, there is a linear relationship between the metal dissolution rate or corrosion rate (C.R.) and the corrosion current $i_{corr}$ [8] established according to the following equation [3.2]:

$$C.R. = \frac{M}{nF\rho} i_{corr} \quad [3.2]$$

Where M is the atomic weight of the metal, ρ is the density, n is the charge number which indicates the number of electrons exchanged in the dissolution reaction and F is the Faraday constant, (96.485 C/mol).

**Potentiostatic polarization**

Potentiostatic polarization experiments allow the controlled polarization of a metal surface in an electrolyte. It is used to observe anodic and cathodic behaviors. Measurements of current vs time relationship under a constant applied potential are obtained.

*Anodic polarization:* the potential is changed in the anodic (or more positive) direction causing the working electrode to become the anode and causing the electrons to withdrawn to be withdrawn from it.

*Cathodic polarization:* the potential shifts in the negative direction (below $E_{corr}$), forcing the working electrode to become more negative and adding electrons to the sample surface.

*2.3.1.3 Electrochemical impedance spectroscopy*

**EIS definition**

Electrochemical impedance spectroscopy (EIS) is a recent and more sophisticated tool than conventional dc polarization techniques for the analysis of electrochemical response of material systems in the study of corrosion, batteries, fuel cells and electro-organic systems. EIS is also called AC Impedance. EIS can give accurate, error-free kinetic and mechanistic information about electrochemical systems and it is capable to distinguish between the dielectric and electric properties of individual contributions of different components within the electrochemical system under investigation [14].

The concept of electrical resistance is well known and is defined by Ohm's law in DC mode. Resistance is the ability of a circuit to resist the flow of current, mathematically expressed as:

$$R = \frac{V}{I} \qquad [3.3]$$

where R is resistance in ohms, V is voltage in volts, and I is current in amperes. However, this relationship is limited to one circuit element, the resistor. In the real world, many systems exhibit a much more complex behavior and we are forced to abandon the simple concept of resistance. In its place we use impedance, Z, which is a measure of a circuit's tendency to resist (or impede) the flow of an alternating (AC) electrical current [11].

In AC theory, where the frequency is non-zero, the analogous equation is:

$$Z = \frac{E(t)}{I(t)} = \frac{E_0 \sin(\omega t)}{I_0 \sin(\omega t + \varphi)} = Z_0 \frac{\sin(\omega t)}{\sin(\omega t + \varphi)} \qquad [3.4]$$

Where E (t) and I (t) are instantaneous voltage and current, $E_0$ and $I_0$ maximum voltage and current amplitudes, ω is frequency, t is time and φ is the phase angle between the voltage and the current.

In an electrochemical cell, slow electrode kinetics, slow preceding chemical reactions, and diffusion can all impede electron flow, and can be considered analogous to the resistors, capacitors, and inductors that impede the flow of electrons in an AC circuit. Z is defined as impedance, the ac equivalent of resistance. The term *impedance* refers to the frequency dependent resistance to current flow of a circuit element, which includes resistors, capacitors, inductors… Thus, the EIS analysis can considered more exhaustive and complete than conventional dc polarization techniques.

The main advantages of EIS compared to DC polarization techniques are summarized below:

- More information can be obtained
- EIS can distinguish between two or more electrochemical reactions taking place
- EIS can identify diffusion occurring through a passive film
- EIS provides information on the capacitive behaviour of the system
- EIS gives information about the electron transfer rate

During EIS acquisition data, the same three-electrode electrochemical cell connected to a potentiostat utilized during polarization methods is employed. However, for EIS analysis a small sinusoidal voltage (5-10 mV) is applied to the working electrode (coated sample) over a wide frequency range.

Impedance Z can be easily represented by vector analysis which provides a convenient method of characterizing an AC waveform, since it allows the description of the wave in terms of its amplitude and phase characteristics. Impedance vector

can be defined according to the following equations and may be plotted in the plane with either rectangular or polar coordinates as shown in Fig 3.11 [15].

$$Z(\omega) = Z' + jZ'' \quad [3.5]$$

The two rectangular coordinates are

$$Z' = Re(Z) = |Z| \cos \varphi \quad [3.6]$$

$$Z'' = Im(Z) = |Z| \sin \varphi \quad [3.7]$$

With the phase angle and modulus being

$$\varphi = \tan^{-1}\left(\frac{Z''}{Z'}\right) \quad [3.8]$$

$$|Z| = [(Z')^2 + (Z'')^2]^{1/2} \quad [3.9]$$

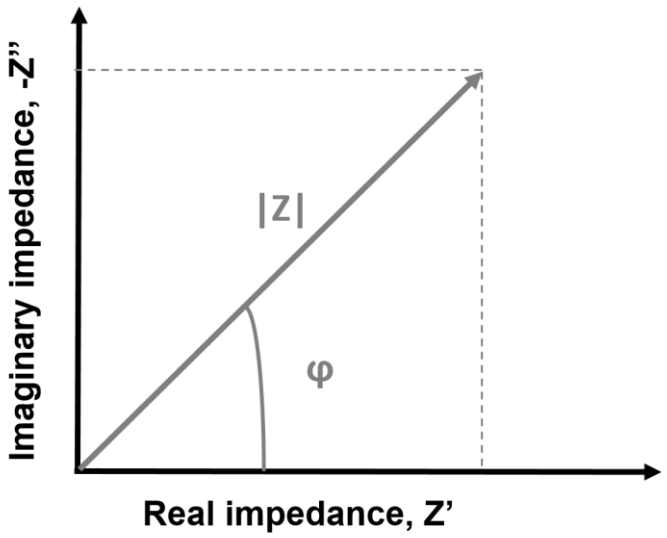


**Fig 3. 10: Impedance vector**

## Nyquist and Bode plots

Once an EIS experiment is complete, the data is generally plotted in terms of Nyquist and Bode plots (Fig 3.12). The expression for Z (ω) is composed of a real and an imaginary part. If the real part is plotted on the X axis and the imaginary part on the Y axis of a chart, the *Nyquist plot* is obtained. In Bode plots, the impedance is plotted with log frequency (log f) on the X-axis and both the absolute value of the impedance (|Z| =$Z_0$) and phase-shift φ on the Y-axis. Unlike the Nyquist plot, the Bode plot explicitly shows frequency information.

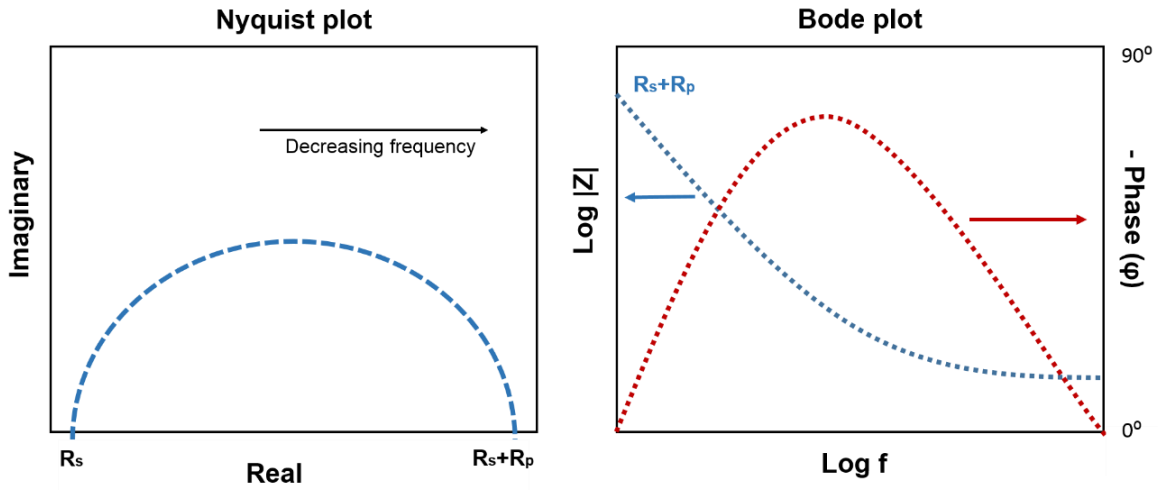


**Fig 3. 11: Nyquist and Bode plots obtained from EIS analysis**

## Equivalent circuit modelling

The main advantage of EIS is the possibility to use a pure electronic model to represent an electrochemical system. An electrode interface being subjected to an electrochemical reaction is typically analogous to an electronic circuit consisting of a specific combination of resistors and capacitors. Using well-established AC circuit theory, this analogy can be employed to characterize the electrochemical system in

terms of its equivalent circuit. Experimentally, the information obtained from Nyquist and Bode plots for a given electrochemical system can be correlated with one or more equivalent circuits. Once a particular model is chosen, physical or chemical properties can be correlated with circuit elements and numerical values can be given by fitting the data to the circuit model.

The most common elements employed in equivalent circuit models for electrochemical system interpretations are summarized in Table 3.1.

| Element | Symbol | Impedance | Description |
|---|---|---|---|
| Resistor | R | R | Impedance is independent of frequency. It has only real component. |
| Inductor | I | iwL | Impedance increases as frequency increases. It has only imaginary component. |
| Capacitor | C | 1/iwC | Impedance decreases as frequency raises. It has only imaginary component. |
| Constant phase element | CPE | $1/Y_0 (iw)^n$ | Non-ideal capacitor. $Y_0$ is proportional to the capacitance of pure capacitive electrodes. n indicates the deviated degree of the capacitance from ideal C ($0 < n < 1$) |
| Warburg impedance | W | $1/Y_0 (iw)^{-1/2}$ | Describes diffusion processes occurring at coating/substrate system. |

**Table 3. 1: Elements used in equivalent circuit modelling**

There are many equivalent circuit models to interpret the electrochemical reactions occurring in metallic materials immerse in corrosive medium. However, in this thesis, two different equivalent circuits have been employed for fitting the data obtained from impedance plots of each material tested, i.e. different uncoated metallic substrates, and $TaN_x$ coated metallic substrates.

## Circuit 1: Randles circuit

The Randles cell equivalent circuit [16] is a simple model composed of a capacitor and two resistor characterized by a semi-circle featured Nyquist plot and one time constant in Bode plot as shown in Fig 3.13.

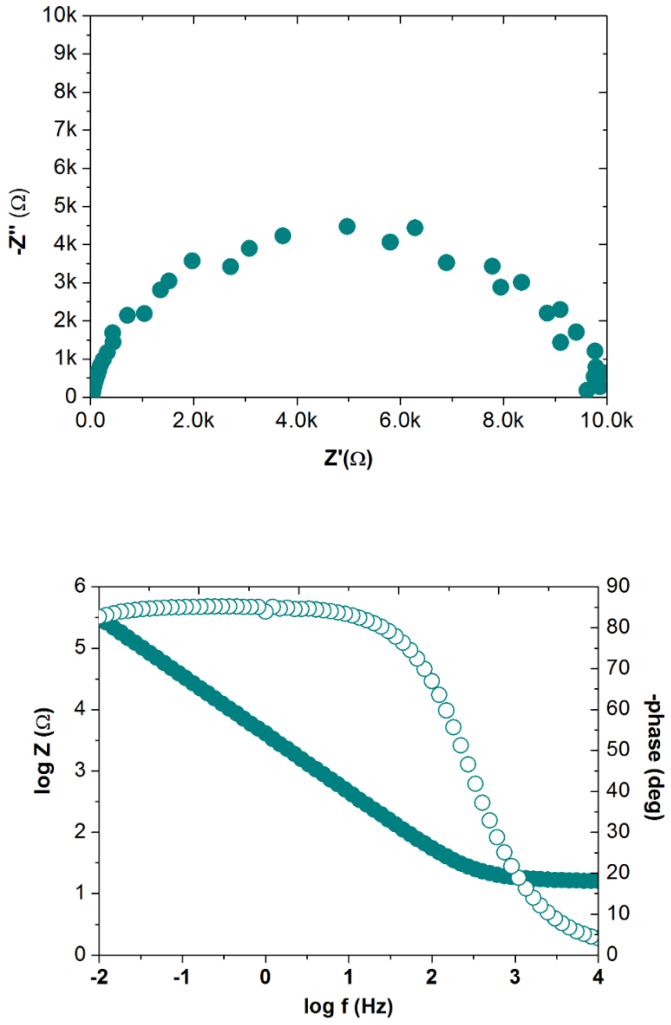


**Fig 3. 12: Nyquist and Bode plots associated to Randles equivalent circuit**

This electrical circuit is utilized for representing two type of electrochemical systems immersed in an electrolyte; uncoated metal substrate and coated metal with a non-porous thin film. However, the values and meanings of the components are different [17].

$R_s$, solution resistance, is the same for both systems and it is associated with the electrolyte resistance.

When Randles circuit is applied to model **an uncoated metal** (Fig 3.14), the capacitor, C, is associated with the double layer capacitance ($C_{dl}$) of the metal/electrolyte interface. The resistance, R, is associated with the charge transfer resistance $R_{ct}$ which gives information about the kinetics of a surface in a corrosive medium. This $R_{ct}$ can be generally named as polarization resistance $R_p$ of the uncoated metal.

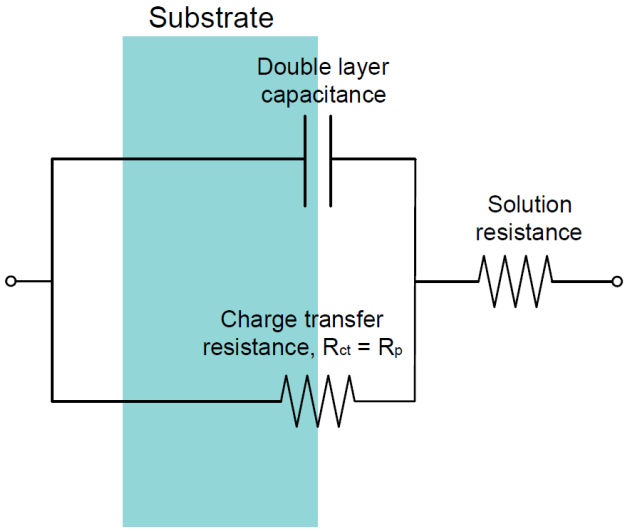


**Fig 3. 13: Randles circuit used to model an uncoated metallic substrate**

When Randles circuit is applied to model **a coated metal with a dense film** (Fig 3.15), the capacitor, C, represents the coating capacitance ($C_c$) and can be characterized by the thickness and dielectric constant of the coating material. The resistance is associated with the polarization resistance of the coating and is known as $R_p$. It is also a property of the material of the coating and varies with the thickness and composition of the coating.

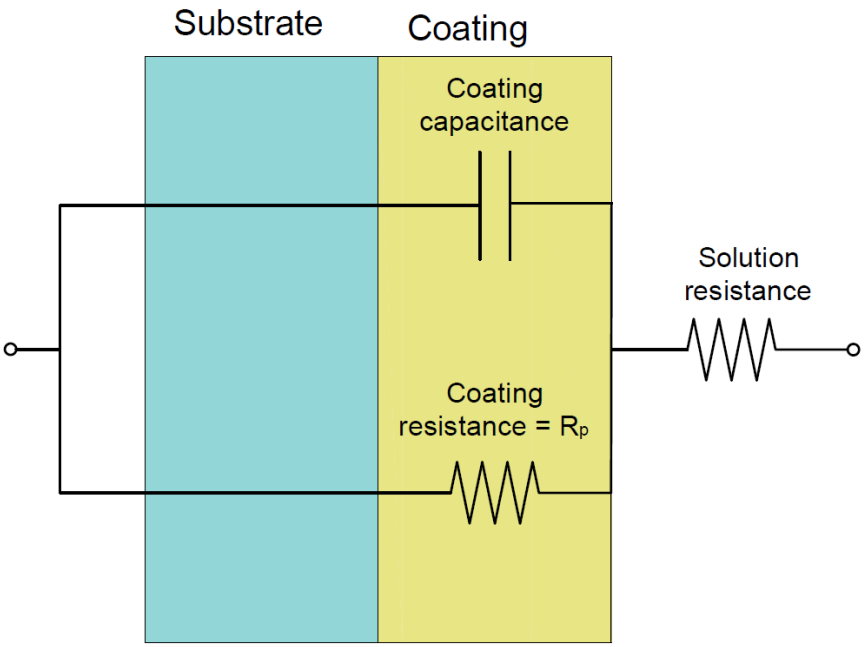


**Fig 3. 14: Randles circuit used to model a coated metal with a non-porous thin film**

## *Circuit 2*

The second equivalent circuit used in this thesis is composed of two pairs of capacitor and resistor elements combined in parallel. It is commonly utilized for describing the electrochemical characteristics of **a metal coated with a porous coating**, which suggests the presence of two electrochemical interfaces: electrolyte/coating and electrolyte/metal substrate [18]. When a coating is not completely stable and dense, after a certain amount of time, the electrolyte penetrates into the coating through the pores and forms a new electrolyte/substrate interface under the coating. Corrosion phenomena can occur at this new interface.

The corresponding Nyquist plot diagram is characterized by the exhibition of two semi-circles, and the Bode plot shows two time constants as illustrated in Fig 3.16.

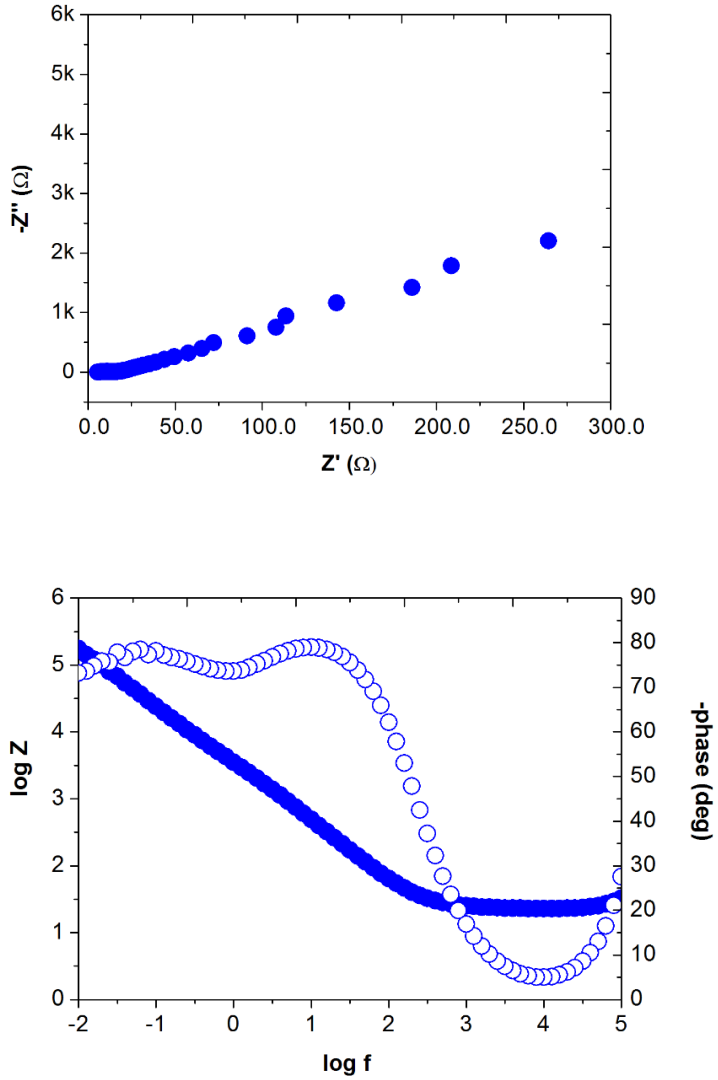


**Fig 3. 15: Nyquist and Bode plots associated to two time constant equivalent circuit**

In this equivalent circuit $R_s$ is again related to electrolyte resistance. The semi-circle at high frequency (left side) in Nyquist plot is due to the coating capacitance ($C_c$) and the semi-circle at lower frequency is due to the double Layer capacitance ($C_{dl}$). In Bode plot, the maximum at higher frequencies represents the $C_c$, and the second maximum at lower frequencies $C_{dl}$. $R_{pore}$ is pore resistance which is an indicative of the number of pinholes in the thickness and their resistance to conducting flow and $R_{ct}$ is associated with the charge transfer at the electrolyte/substrate interface. $R_p$ is the sum of $R_{pore}$ and $R_{ct}$.

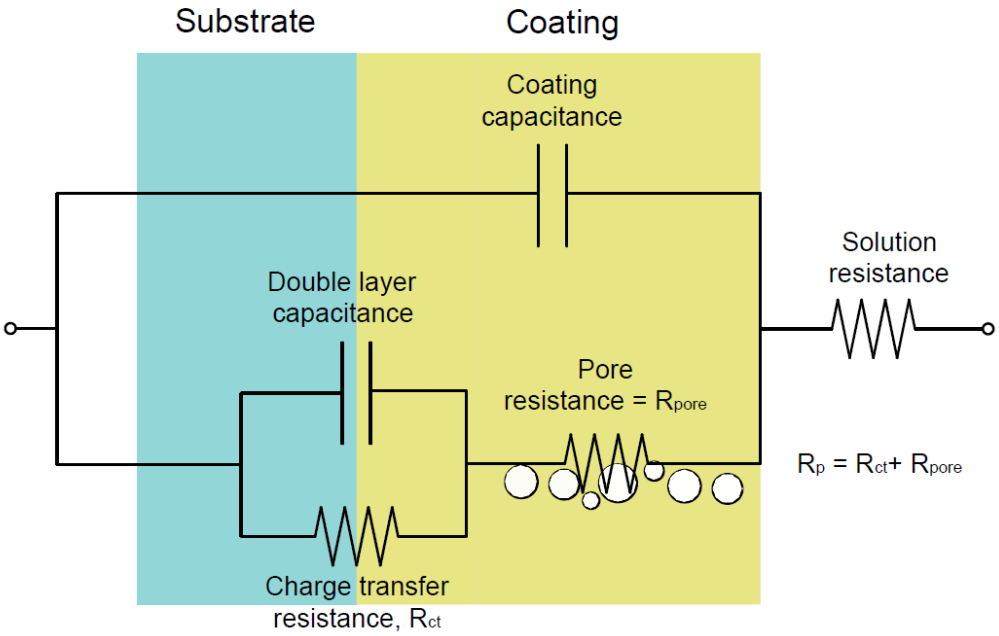


**Fig 3. 16: Two time constant equivalent circuit used to model a coated metal with a porous thin film**

The development of a coating with a purely capacitive behavior is the ideal feature for a protective coating. Upon initial exposure to an electrolyte, a high performance coating with excellent barrier properties will act as an almost-perfect capacitor. At this stage, R is extremely high. The Bode plot shows a straight line of slope –1 with high impedance at low frequency and a phase angle of –90° throughout the entire frequency range, characteristic of a pure capacitor. However, as any ideal behavior it does not generally occur in real world applications. Thus, instead of a capacitor, a constant phase element (CPE) will be introduced for modelling the coating/metal systems. A CPE has been described as a "non-ideal capacitor" and is commonly utilized because it gives better fit with a model. CPE is defined by admittance Y and power index number n, given by:

$$Y = Y_0(jw)^n \qquad [3.10]$$

This is a general dispersion formula; for n=0 it stands for resistance, while it is capacitance if n=1.

The impedance of the CPE constant phase element can be defined in terms of the admittance $Y_0$ and n parmeter as follows [99]:

$$Z_{CPE} = \frac{1}{Y_0}(iw)^{-n} \quad [3.11]$$

where $Y_0$ is proportional to the capacitance of pure capacitive electrodes and it is measured experimentally from EIS data. The parameter n ranging between 0 and 1 is defined as the phenomenological coefficient which indicates the deviated degree of the capacitance from the ideal condition and ω is the angular frequency.

### 2.3.2 Hardness measurements

The hardness measurements of thin films were performed using the nanoindenter Fischerscope H100VP equipped with a Vickers indentation tip plotted in Fig 3.18.

**Fig 3. 17 Fischerscope H100VP nanoindenter**

This equipment uses the method developed by Oliver and Pharr to estimate hardness, H, and Young Modulus, E, of thin films using load-unload curves shown in Fig 3.19 [19].

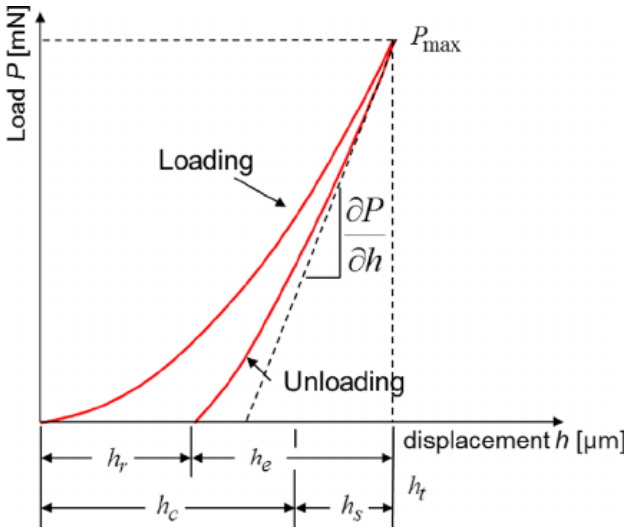


**Fig 3. 18 Schematic of a typical load – unload nanoindentation curve (taken from [20])**

The Fischerscope equipment uses a dedicated software for the calculation of the hardness from data obtained through 6 to 10 indentation tests and corresponding load-penetration parameters. From this data, plastic and elastic properties of the thin film material can be measured.

Indentation tests are performed in different points over the sample surface and the following parameters can be calculated: plastic and elastic coefficients, differential hardness, plastic hardness, Young modulus and penetration values depending on applied loads. In the Fischerscope equipment, the penetration depth under indenter load is measured; in contrast to the Vickers hardness test, where the diagonal of the indentation trace is measured. The equivalence with Vickers hardness (expressed in GPa) is obtained by applying the next conversion formula from the curves penetration depth versus applied load:

$$HV = \frac{378{,}5}{102} \times \frac{P \times h_r}{h_t^3\left(1-\frac{W_E}{W_T}\right)} \qquad \text{given in GPa} \qquad [3.12]$$

Being

- P total applied load
- $W_E$ energy invested in the deformation and elastically recovered
- $W_T$ total energy invested in the deformation
- $h_r$ residual depth of the indentation
- $h_t$ maximum penetration depth

Total indentation load can range between 4 and 1000 mN; the minimum indentation load is 0.4 mN. The sample surface has to be flat and the indentation depth must not be higher than 10 % of the coating total thickness to consider the test valid.

### 2.3.3 Roughness measurements

Surface roughness is a component of the surface texture. In this thesis, the Perthometer M2 profilometer of Mahr is employed to calculate the surface roughness of $TaN_X$ films.

**Fig 3. 19 Perthometer M2 profilometer of Mahr**

The Tracing method is an inspection method for the two-dimensional tracing of the surface. It requires a surface pick-up to be traversed horizontally across the surface at constant speed. The Traced profile is the surface profile traced by the pick-up stylus. It is quantified by the vertical deviations of a real surface from its ideal form.

Different roughness parameters can be obtained during testing. However, the most commonly given value is the mean roughness, known as $R_a$, which is the arithmetic average of the absolute values of the roughness profile coordinates and it is defined as follows:

$$R_a = \frac{1}{L}\int_0^L |Z\ (x)|\ dx \qquad [3.13]$$

To calculate the $R_a$ values, the equipment has followed the DIN EN ISO 4288 and DIN EN ISO 4287 standards.

# 3. References

[1] Johann Angeli, Arne Bengtson, Annemie Bogaerts, Volker Hoffmann, Vasile-Dan Hodoroaba and Edward Steers, Glow discharge optical emission spectrometry: moving towards reliable thin film analysis–a short review, J. Anal. At. Spectrom., 2003, 18, 670–679

[2] C.W. Oatley, W.C. Nixon, R.F.W. Pease, Scanning Electron Microscopy, Advances in Electronics and Electron Physics 21 (1966) 181-247

[3] L. Reimer, H. Kohl, In book, Transmission Electron Microscopy: Physics of Image Formation, 5th Ed. Edited by Springer series in Optical Science (2008)

[4] M. Manso Silvan, M. Langlet, J.M. Martinez Duart, P. Herrero, Nucl. Instr. and Meth. in Phys. Res. B 257 (2007) 623–626

[5] Harold P. Klug, Leroy E. Alexander, X-Ray Diffraction Procedures: For Polycrystalline and Amorphous Materials, 2nd Edition. Harold P. Klug, Leroy E. Alexander. ISBN: 978-0-471-49369-3.

[6] Chuan C. Chang, Auger electron spectroscopy, Surface Science 25 (1971) 53 – 79

[7] http://www.gamry.com/

[8] http://www.ecochemie.nl/

[9] S.H. Ahn et al. / Surface and Coatings Technology 162 (2003) 212–221

[10] E. Cerro Prada et al. / Construction and Building Materials 80 (2015) 48–55

[11] Web: www.princetonappliedresearch.com

[12] Lecture 10: Polarization Techniques – Corrosion Rate Determination http://nptel.ac.in/

[13] E. Barsoukov, J.R. Macdonald, Impedance Spectroscopy, Theory, Experiment, and Applications, Wiley-Intersience 2005

[14] R. Cottis, S. Turgoose, Electrochemical Impedance, NACE International 1999. ISBN 1-57590-093-9.

[15] E. Barsoukov, J.R. Macdonald, Impedance Spectroscopy, Theory, Experiment, and Applications, Wiley-Intersience 2005

[16] Randles, J. E. B. (1947). "Kinetics of rapid electrode reactions". Discussions of the Faraday Society 1: 11.

[17] David Loveday, Pete Peterson, and Bob Rodgers—Gamry Instruments, Evaluation of Organic Coatings with Electrochemical Impedance Spectroscopy. Part 1

[18] David Loveday, Pete Peterson, and Bob Rodgers—Gamry Instruments, Evaluation of Organic Coatings with Electrochemical Impedance Spectroscopy. Part 2

[19] W.C. Oliver, G.M. Pharr, An improved technique for determining hardness and elastic modulus using load and displacement sensing indentation experiments, J.Mater. Res. 7 (1992) 1564.

[20] J. Lee, K. Polychronopoulou, A. N. Cloud, J. R. Abelson, A. A. Polycarpou, Shear strength measurements of hafnium diboride thin solid films, Wear 318 (2014) 168-176

# CHAPTER 4

# GENERAL EVALUATION OF $TaN_X$ FILM PROPERTIES DEPOSITED BY MPPMS

# 1. Introduction

Ta–N system is rather complex system, containing a variety of different compounds. In addition to the equilibrium phases, a lot of metastable phases have been reported [1-2]. Unlike the well-known TiN and CrN coating materials that exhibit only two compounds, tetragonal $Ti_2N$ and cubic TiN [3] and hexagonal $Cr_2N$ and cubic CrN [4], respectively, the Ta-N system has manifold compounds and has not been exhaustively investigated. Ta-N system includes both equilibrium and metastable phases such as bcc α-Ta, tetragonal β-Ta, hexagonal $Ta_2N$, cubic TaN, hexagonal TaN, hexagonal $Ta_5N_6$, tetragonal $Ta_5N_6$, orthorhombic $Ta_3N_5$, and orthorhombic $Ta_4N$ [5-7].

Due to this complexity, the chemical and phase composition of as-deposited $TaN_x$ layers have been found to be critically dependent on growth conditions, primarily on nitrogen content, for all deposition techniques utilized. K. Valleti et al. [7] and D. Bernoulli et al. [8] investigated the relationship between the crystal phases of $TaN_x$ coatings grown at different $N_2$-to-Ar ratio and film hardness. S.K. Kim et al. [9], A. Aryasomayajula et al. [10] and K.-Y. Liu et al. [11] analyzed the tribological behavior of $TaN_x$ films deposited at different $N_2$-to-Ar ratios by DC, pulsed DC and RF magnetron sputtering, respectively. M. Cheviot el al. [12] monitored the influence of process parameters on $TaN_x$ films structure, confirming the $N_2$ partial pressure as a key parameter to optimize $TaN_x$ performance. Electrical resistivity of $TaN_x$ films has been also studied by several researchers with special focus on $N_2$ influence [13, 14]. Corrosion resistance and mechanical properties of TaN coated Ti have been recently investigated for dental application [15], but nitrogen content influence on $TaN_x$ films corrosion response is not provided. All these studies demonstrate the importance of nitrogen effect on $TaN_x$ thin film characteristics.

Conventional dc magnetron sputtering is one of the state-of-art techniques for the depositions of hard coating materials, including TaN. However, when it comes to corrosion resistance evaluation, the large amount of defects typically present on sputtered films strongly jeopardizes their performance. To overcome this problem, the application of recently developed modulated pulsed power magnetron sputtering technology (MPPMS) is analyzed [16] in this thesis. The possibility to deposit very dense and columnar-free microstructure Ta coatings by MPPMS technique has been demonstrated [17], but the influence of the microstructure on its corrosion response remains unknown.

Hence, in this chapter, an exhaustive investigation on $TaN_x$ coating performance deposited at different $N_2$-to-Ar ratios by MPPMS is accomplished. Firstly, the fundamentals of MPPMS technique in terms of pulse shape definition are explained and particularly studied for $TaN_x$ coating deposition. Secondly, the effect of nitrogen flow on the microstructure, crystal phases and properties of $TaN_x$ films deposited by MPPMS, with special focus on $TaN_x$ electrochemical behavior, is addressed.

## 2. Pulse shapes for $TaN_X$ deposition

MPPMS technique is characterized for the development of highly ionized plasmas by the application of complex step-like pulse shapes as previously described in Chapter 2. The pulse shape eventually defines the voltage-current (V-I) characteristics of the plasma discharge, and hence, the ionization degree of the plasma species. The pulsing parameters during MPPMS plasma discharge are also highly dependent on process parameters and target material.

Three different MPPMS pulses have been used to analyze plasma discharge characteristics during $TaN_x$ coating process under the same process parameter conditions. Pulse shape and V-I features during each $TaN_x$ coating deposition are

monitored using the oscilloscope already described in Chapter 3. The correlation between the pulse shape and pulsing parameters (peak voltage, peak current and peak power) developed during MPPMS discharge is investigated. The characteristics of each pulse are shown in Table 4.1. Pulse 200 and Pulse 914 have the same macropulse length (1000 µs) but contained 2 and 3 micropulses, respectively, within the overall macropulse. Pulse 996 contains 2 micropulses within one overall longer macropulse (1500 µs). Voltage "on" time and voltage "off" time ratios ($\zeta_{on}/\zeta_{off}$) of the capacitors are different per micropulse, which are responsible for different peak voltage and current values along and per macropulse.

| Pulse | Macro pulse length (µs) | 1st micropulse | | | 2nd micropulse | | | 3rd micropulse | | |
|---|---|---|---|---|---|---|---|---|---|---|
| | | Length (µs) | $\zeta_{on}$ (µs) | $\zeta_{off}$ (µs) | Length (µs) | $\zeta_{on}$ (µs) | $\zeta_{off}$ (µs) | Length (µs) | $\zeta_{on}$ (µs) | $\zeta_{off}$ (µs) |
| P200 | 1000 | 500 | 10 | 30 | 500 | 10 | 15 | - | - | - |
| P914 | 1000 | 200 | 10 | 30 | 500 | 10 | 20 | 300 | 16 | 6 |
| P996 | 1500 | 1000 | 10 | 20 | 500 | 12 | 10 | - | - | - |

**Table 4. 1: Different MPPMS pulse shape employed for different plasma features generation during $TaN_x$ deposition discharge**

The following process parameters have been employed for monitoring (V-I) characteristics of each MPPMS pulse through an oscilloscope connected to SOLO power supply.

<u>$TaN_x$ coating deposition</u>

- Pressure: 1 Pa
- Ar flow: 48 sccm
- $N_2$ flow: 12 sccm
- Average power: 4 kW
- Capacitor voltage: 575 V
- Temperature: 350 ºC

Voltage and peak current evolution with time during each pulse are shown in Fig 1. All pulses exhibit the typical MPPMS curves. A current rise is observed at the beginning of the pulse to ignite the plasma, followed by a low and stable ionization stage (voltage and current values are relatively low) and a final step characterized by high peak voltage and current values recognized as the main ionization stage. All pulses show similar current values (~ 30A) during the first micropulse segment. The 1st and 2nd micropulse of Pulse 914 are indistinguishable due to similar and low $\zeta_{on}/\zeta_{off}$ ratios than are not capable to generate considerable differences in current. The main difference between pulses is observed during the main ionization stage (2nd micropulse for P200 and P996 and 3rd micropulse for P914) caused by substantially different $\zeta_{on}/\zeta_{off}$ ratios in these pulse segments.

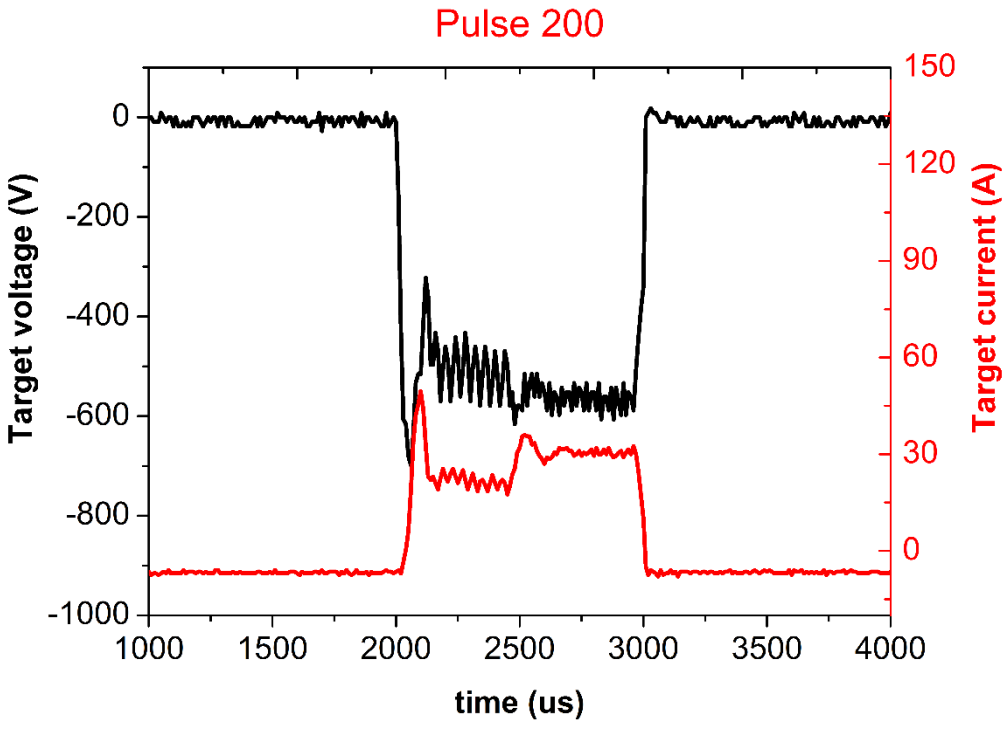

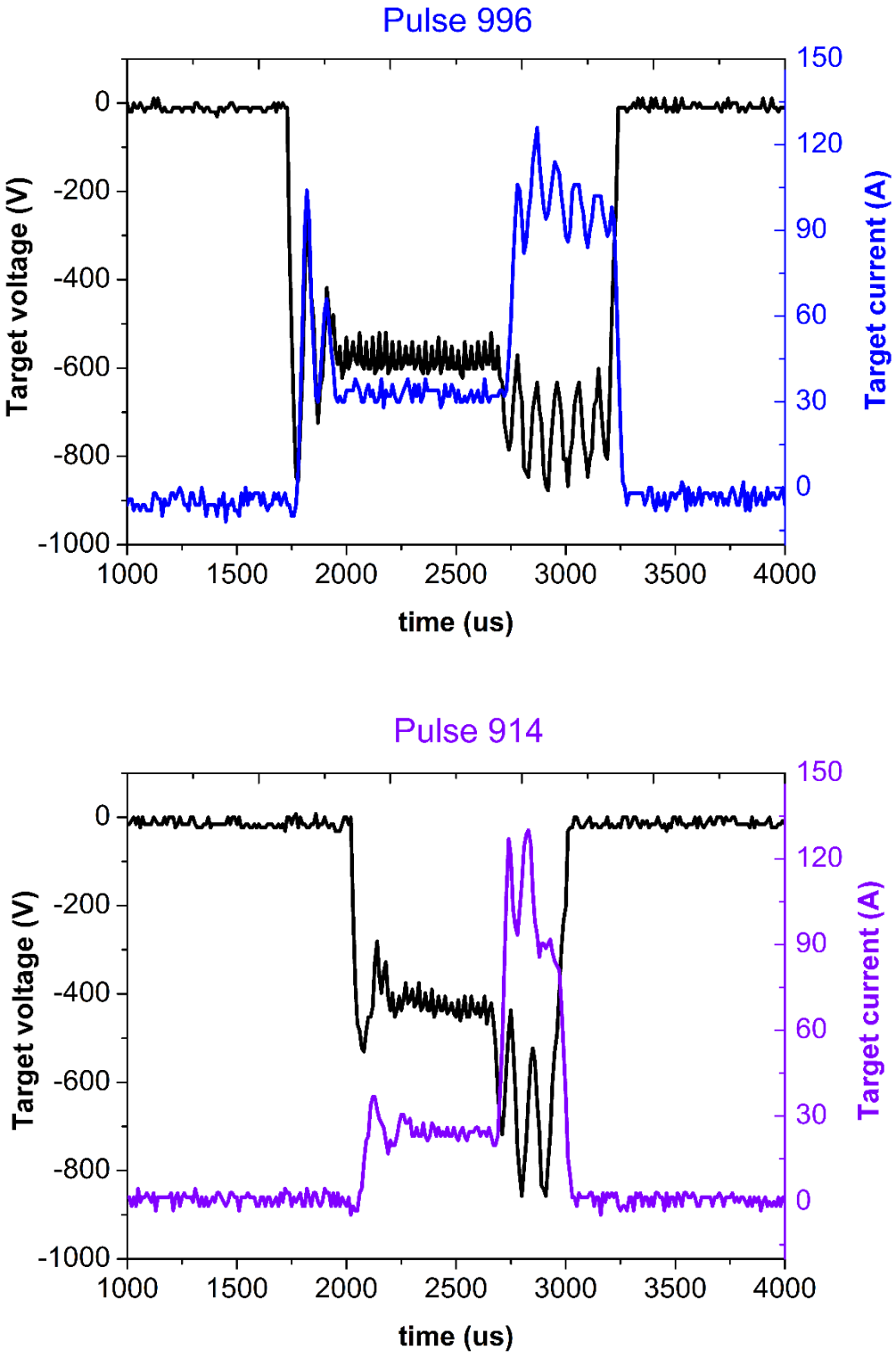


**Fig 4. 1 V-I characteristics of different MPPMS pulses employed for $TaN_x$ plasma discharge**

The detailed pulsing parameters measured for each pulse shape are plotted in Table 4.2.

| Pulse | Capacitor voltage (V) | Average power $P_{av}$ (kW) | Peak voltage $V_p$ (V) | Peak current $I_p$ (A) | Peak power $P_p$ (kW) | Frequency F (Hz) |
|---|---|---|---|---|---|---|
| P200 | 575 | 4 | 590 | 40 | 24 | 290 |
| P914 | 575 | 4 | 800 | 110 | 88 | 190 |
| P996 | 575 | 4 | 866 | 100 | 86 | 113 |

**Table 4. 2: Pulsing parameters for each pulse**

As shown in Table 2, the pulse design plays an important role on plasma discharge features tuning. Pulse 914 and Pulse 996 exhibit double peak current values than Pulse 200 due to much higher $\zeta_{on}/\zeta_{off}$ ratios in the high ionization micropulse segment. Peak current density during HPPMS discharges is recognized as the main parameter influencing ionization degree of the sputtering plasma [18, 19]. Peak current density has been usefully utilized to tailor the density [20], geometry [21], texture and crystal phases [22, 23] and tribological properties [24-26] of thin films, among others. Absolute peak current value is higher for P914; but during P996, high ionization stage is maintained for longer time (1500 μs instead of 1000 μs per pulse) than in P914. Hence, P996 is selected as the best alternative in terms of higher ionization degree of $TaN_x$ sputtering plasma. P996 is employed for further analysis on $TaN_x$ film properties deposited by MPPMS in this chapter.

# 3. Effect of $N_2$-to-Ar ratio on the $TaN_x$ films characteristics

## 3.1. $TaN_x$ coating deposition

$TaN_x$ films were deposited by MPPMS in the MIDAS 450 sputtering system previously described in Chapter 3.

AISI 316L coupons, silicon wafers and high speed steel disks were used as substrates. The substrates underwent the cleaning procedure explained in Chapter 3 before $TaN_x$ coating deposition. During the depositions, the working pressure was maintained at 0.7 Pa. The average power was set at 4 kW and the bias voltage was constant at -50 V. The substrate temperature was 350 ºC. Prior to $TaN_x$ coatings growth, a thin Ta interlayer film of 100 nm thickness was deposited for better adhesion between the substrate and the coating. Four different $TaN_x$ deposition processes were carried out, characterized by different $N_2$-to-Ar ratio of 0, 0.25, 0.625 and 1.

The same MPPMS pulse, P996 (Fig 4.1), was used for all deposition processes. P996 pulse features were described in Section 2. The detailed V-I characteristics during each $TaN_x$ coating deposition were monitored by an oscilloscope and are summarized in Table 4.3.

| | $N_2$/Ar ratio | Peak target voltage (V) | Peak target current (A) | Peak target power (kW) | Frequency (Hz) | Thickness (µm) |
|---|---|---|---|---|---|---|
| Ta | 0 | 720 | 85 | 61.2 | 150 | 2.61±0.03 |
| TaN_0.25 | 0.25 | 740 | 93 | 68.8 | 140 | 2.48±0.02 |
| TaN_0.625 | 0.625 | 700 | 75 | 52.5 | 162 | 2.29±0.02 |
| TaN_1 | 1 | 700 | 66 | 46.2 | 169 | 2.09±0.02 |

**Table 4. 3: Deposition conditions for $TaN_x$ films. Thickness value: $\mathbf{X} = \overline{\mathbf{X}} \pm \mathbf{2}\boldsymbol{\sigma}$**

## 3.2 $TaN_x$ coating characterization

### 3.2.1. Deposition rate

The thickness of the $TaN_x$ films calculated by SEM is plotted in Table 4.3. From thickness measurements, the deposition rate of each $TaN_x$ film was calculated. The deposition rate decreases as $N_2$-to-Ar ratio increases as shown in Fig. 4.2. Two factors are responsible for this tendency, namely 1) TaN formation on the surface of the sputtering target which leads to lower deposition rates (target poisoning) and 2) lower sputtering yield of the $N_2$ gas with respect to Ar.

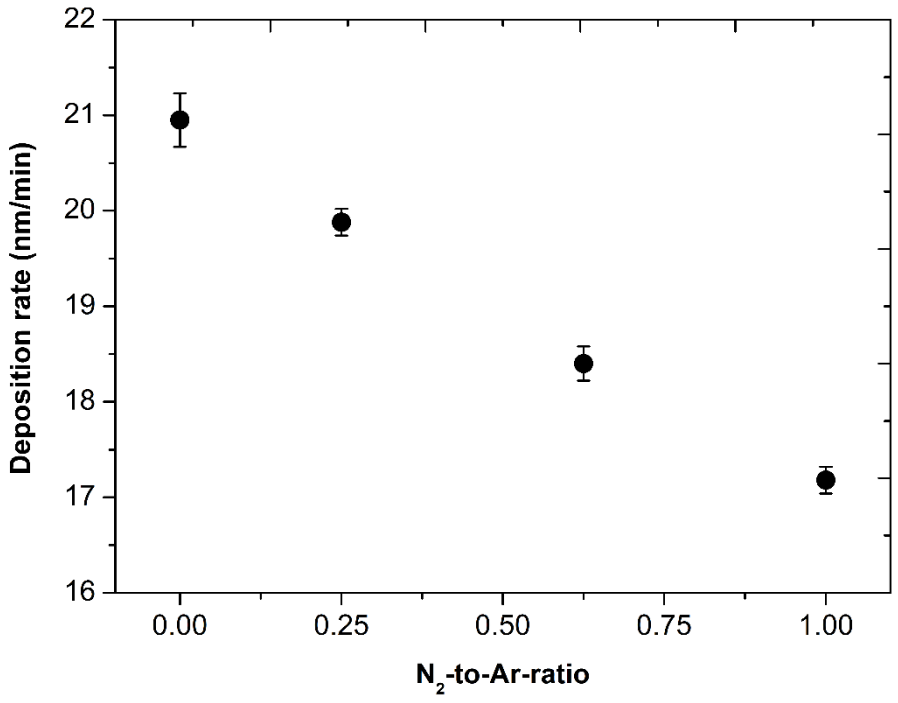


**Fig 4. 2: Deposition rate vs $N_2$-to-Ar ratio**

The deposition rate of $TaN_x$ films grown by MPPMS varies from 17 nm $min^{-1}$ to 21 $nm^{-1}$ as $N_2$-to-Ar ratio increases, corresponding to a mean value around 1.12 μm $h^{-1}$.

This deposition rate is considered adequate in terms of industrial productivity of MPPMS technique for the deposition of $TaN_x$ films.

### 3.2.2. Film microstructure and composition

The film composition determined from GD-OES is shown in Fig. 4.3. The $TaN_x$ film deposited in argon atmosphere (i.e. $N_2$-to-Ar ratio is 0) is certainly characterized by 100 at. % of Ta. The films deposited at 0.25 and 0.625 $N_2$-to-Ar ratios exhibit 10 at. % and 25 at. % nitrogen content on the growing films, respectively. The TaN film deposited at 1 $N_2$-to-Ar ratio shows a 45 at. % N content. This slight under stoichiometry can be ascribed to the high flux of metal Ta and Ar ions commonly observed in MPPMS plasmas which can be responsible for a preferential re-sputtering effect of light nitrogen instead of tantalum [27]. Large momentum transfer from $Ta^+$ and $Ar^+$ ions to the atoms on the film surface is expected during MPPMS discharges, contributing to the lightweight N atoms deficiency with respect to heavier Ta atoms.

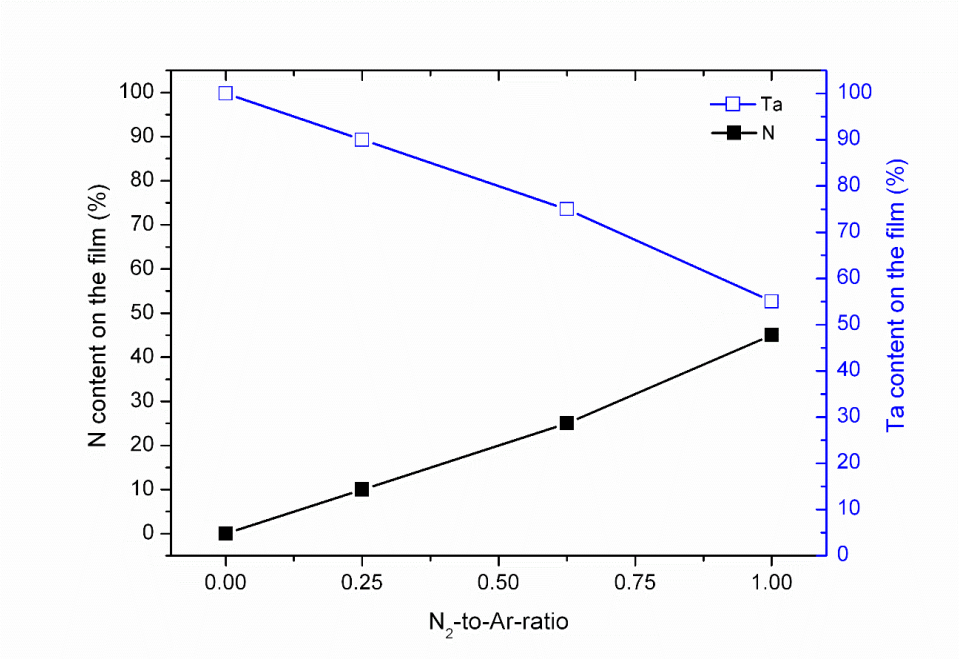


**Fig 4. 3: Chemical composition of $TaN_x$ films deposited at different $N_2$-to-Ar ratios**

The crystal phases present in the $TaN_x$ coatings where characterized by means of 2θ XRD scans performed at glancing angle incidence. The XRD scans are plotted in Fig. 4.4. Tantalum metallic films exhibit two crystalline phases, Alpha-Tantalum (α-Ta), which is body-centered cubic and Beta-Tantalum (β-Ta), which is metastable-tetragonal [1]. α-Ta is generally preferred for wear and corrosion protection applications. The spectrum of Ta film deposited during this study exhibits a unique peak at 38.4 º, which corresponds to the (110) α-Ta reflection. There are two different factors promoting the growth of α-Ta phase in this study, i.e. the application of external substrate heating and the utilization of MPPMS deposition technology. Substrate temperature reached 350 ºC during $TaN_x$ deposition processes. Myers et al. [1] and Knepper et al. [28] have reported that the β to α phase transformation occurs at temperatures around 365 ºC and 350 ºC, respectively. The high ion bombardment and bias voltage application during $TaN_x$ MPPMS discharge induce a greater rise in substrate temperature, promoting better adatom mobility onto the growing films. In fact, Jin et al. [17] and J. Alami et al. [29] have demonstrated the possibility to control the α-Ta phase formation by ion energy modification using different bias voltage values.

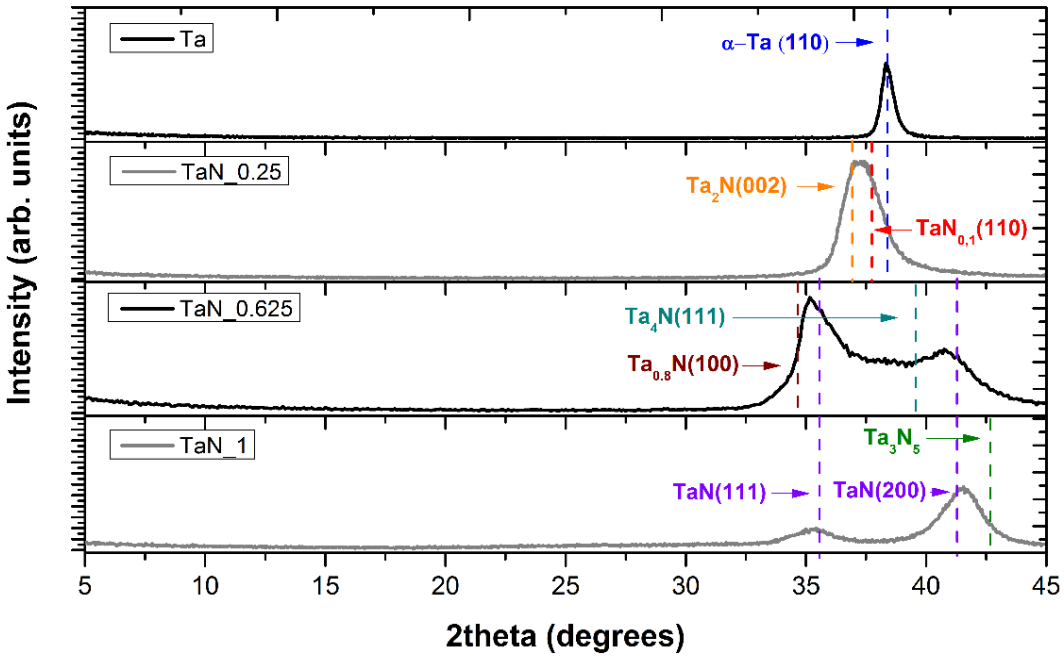


**Fig 4. 4: XRD patterns of the TaNx films deposited at different $N_2$-to-Ar ratios**

The $TaN_x$ films grown at different $N_2$-to-Ar ratio give rise to many different crystal phases [5, 7, and 10]. Fig. 4.4 indicates the presence of multiple phases in all TaN samples deposited in $N_2$/Ar gas mixture. The TaN_0.25 film shows a prominent broad peak between 36.5 º-38.5 º diffraction angles. Contributions from sub-stoichiometric TaN phases, such as α-Ta (110), cubic $TaN_{0.1}$ (110) and hexagonal $Ta_2N$ (002), are observed in its spectrum. The TaN_0.625 film exhibits two prominent peaks at diffraction angles 35 º and 41 º. A strong cubic TaN phase is observed through the (111) and (200) reflections. Contribution from hexagonal $TaN_{0.8}$ and orthorhombic $Ta_4N$ phases is also considered due to the presence of (100) and (111) reflections, respectively. TaN_1 film spectrum exhibits predominant contribution from cubic TaN and a smaller contribution from hexagonal $Ta_3N_5$. The predominant peak at 41 º corresponds to TaN (200) reflection and $Ta_3N_5$ crystal phase while the smaller peak at 35 º includes the TaN (111) reflection.

The microstructure of the films was analyzed by SEM, since the corrosion characteristics of thin films are highly dependent on the microstructure. The development of columnar-free and low-defect film structure has a positive effect on corrosion resistance [30]. Fig. 4.5 shows the cross-sectional and surface topography SEM micrographs of $TaN_x$ films.

The pure metallic Ta film (Fig 4.5.a) exhibits a columnar structure with a typical signature of competitive growth and a rough surface. Ta surface morphology (Fig 4.5.e) correlates well with the crystallographic predominant α-Ta phase surface appearance, which is characterized by dense regularly spaced grain facets [31]. The addition of nitrogen into the gas mixture during $TaN_x$ deposition processes leads to radical changes in coating microstructure. The TaN film deposited at 0.25 $N_2$-to-Ar ratio (Fig 4.5.b and 4.5.f), corresponding to 10 at. % N in the film, exhibits a completely dense and featureless microstructure, with no signs of columnar growth and granular surface topography. At 0.625 $N_2$-to-Ar ratios, similar dense microstructures are developed although some indications of columnar growth start to appear. Increasing nitrogen flow, brings back the signature of a columnar growth that can be appreciated in the TaN film deposited at 1 $N_2$-to-Ar ratio (45 at. % N in the film). The decrease in the peak current value during this deposition process (see Table 4.3) also promotes the development of columnar structure since it is indicative of lower amount of ions capable to induce densification of the films. In fact, surface topography of TaN_0.625 (Fig 4.5.g) and TaN_1 (Fig 4.5.h) exhibits a "cauliflower-shaped" microstructure, commonly related to columnar structure films [32]. Therefore, feature-free microstructure development is not only dependent on the application of MPPMS technique characterized by highly ionized plasma. For $TaN_x$ films deposited in this study the suppression of columnar growth is restricted to the films containing 10% of nitrogen in the film. The influence of the microstructure on the corrosion resistance of these films will be further analyzed in section 3.2.3.

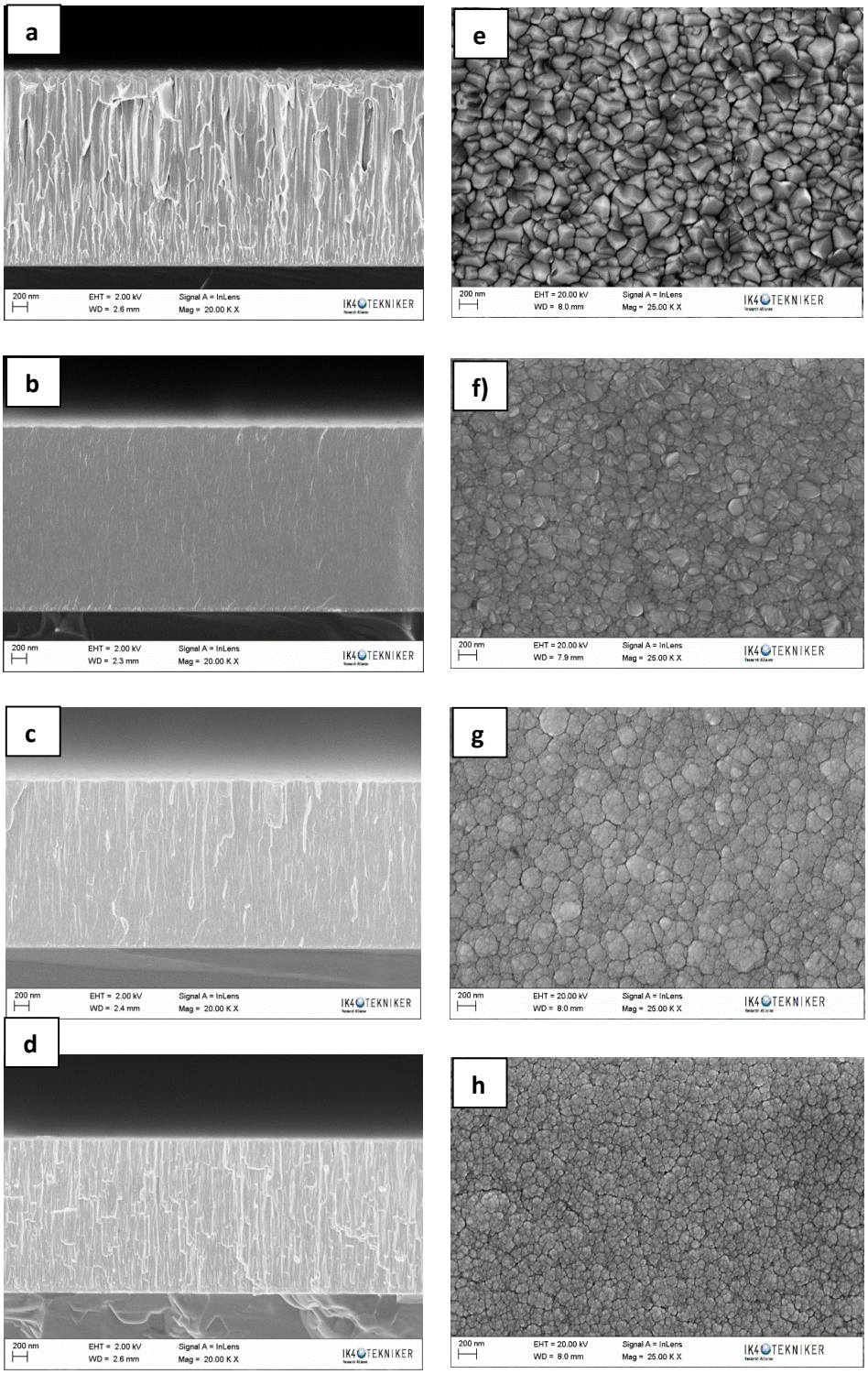


**Fig 4. 5: Cross sectional and surface SEM micrographs of a), e) Ta; b), f) TaN_0.25; c), g) TaN_0.625 and d), h) TaN_1, respectively**

### 3.2.3. Hardness and roughness

Fig. 4.6 shows the hardness and roughness values of $TaN_x$ films deposited at different $N_2$-to-Ar ratios. Hardness was calculated using the method of Oliver and Pharr [33]. The roughness measurements were performed using the Mahr Perthometer M2 equipment. The metallic Ta film shows hardness values of 8 GPa, confirming the α-Ta crystalline phase presence [1] and high roughness values of 0.5 µm. As the nitrogen increases, the hardness also increases up to 25 GPa for the TaN_0.625 film, containing 25 at. % N in the film. This great hardness increase can be attributed to the small presence of $Ta_4N$ phase in this film which was given a superhardness value of 51.2 GPa by Valleti et al. [7]. Contrary, a huge decrease on the roughness is observed when nitrogen is added to $TaN_x$ films deposition processes. The hardness of the films decreases significantly at $N_2$-to-Ar gas ratio of 1, due to the disappearance of $Ta_4N$ phase and the formation of softer $Ta_3N_5$ phase [17].

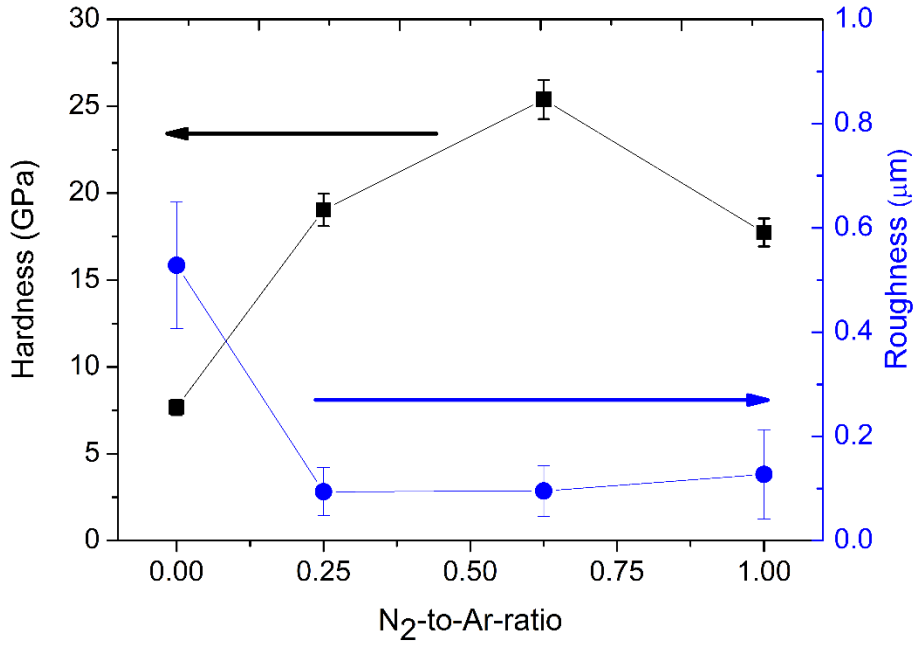


**Fig 4. 6: Hardness and roughness values for $TaN_x$ films deposited at different $N_2$-to-Ar ratios.**

### 3.2.4. Electrochemical behavior of $TaN_x$ films

#### *3.2.4.1 Electrochemical impedance spectroscopy (EIS)*

The corrosion performance was analyzed using a potentiostat PGSTAT 30N Autolab-Metrohm connected to a three-electrode electrochemical cell already described in Chapter 3 (Fig 3.7). The reference electrode was an Ag/AgCl (KCl 3 M) with a potential of 0.207 V versus standard hydrogen electrode. Tests were carried out at room temperature and under aerated conditions.

Electrochemical impedance spectroscopy (EIS) analysis was performed on coated AISI 316L substrates to investigate the electrochemical response of $TaN_x$ films in NaCl 0.06 M media. A sinusoidal AC perturbation of 10 mV was applied to the electrode at a frequency range from 100 kHz to 10 mHz. EIS measurements were registered at Open Circuit Potential ($E_{oc}$) after 4 h and 168 h of immersion time to assess the corrosion resistance evolution with time for each $TaN_x$ coating. The interpretation of the Impedance experimental data was based on the equivalent circuit modeling using Autolab software.

Nyquist diagrams registered are plotted in Fig. 4.7 for AISI 316L substrate and $TaN_x$ films.

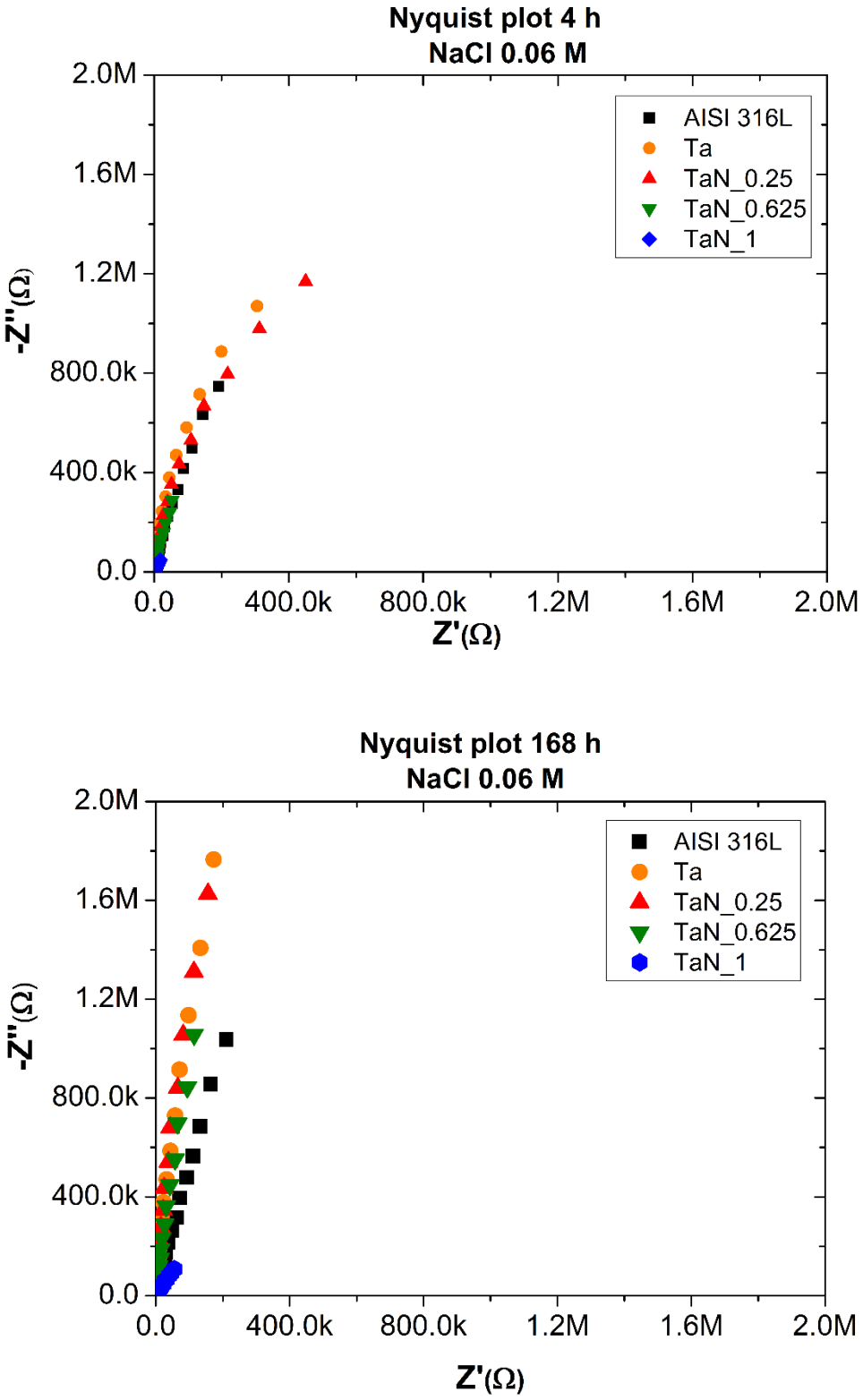


**Fig 4. 7: Nyquist diagrams obtained for AISI 316L and $TaN_x$ films after EIS measurements at 4 h and 168 h of immersion**

The Nyquist diagrams at 4 h and 168 h immersion times (Fig 4.7.a and Fig 4.7.b, respectively) presented depressed semi-circles which are characteristic of a capacitive behavior. The semi-circles are incomplete for both immersion times registered due to high impedance values exhibited by AISI 316L and $TaN_x$ films. The semi-circle diameters registered at 168 h are higher than those obtained at 4 h, indicating an increase in corrosion resistance with immersion time. This behavior is observed for the AISI 316L and all $TaN_x$ films. This corrosion resistance improvement with time is due to the formation of a protective oxide layer on the top of the surfaces that occurs spontaneously when metallic passive materials are exposed to oxygen. The stability of the oxide layer is higher after 168 h time exposure, demonstrating the passive behavior of $TaN_x$ films. The Ta and TaN_0.25 films exhibit the highest corrosion resistance values. This difference will be quantified in the following paragraphs by equivalent circuit (EC) analysis [34]. The Nyquist plot of TaN_1 cannot be clearly observed since higher scale is needed to plot remaining $TaN_x$ coatings electrochemical response.

Fig. 4.8 shows the Bode plots diagrams obtained at 4 h and 168 h of immersion time in NaCl 0.06 M. Bode plots bring additional information about the electrochemical properties of $TaN_x$ films and in these diagrams the corrosion characteristics of the $TaN_x$ films are readily distinguished from each other.

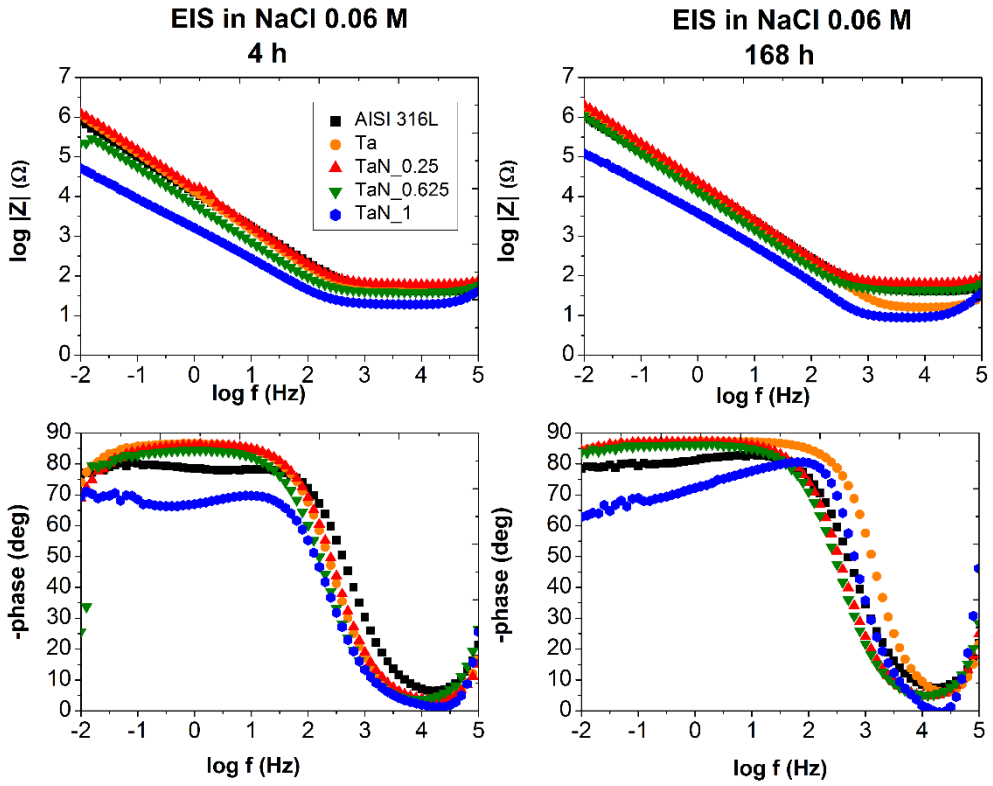


**Fig 4. 8: Bode plots obtained for AISI 316L and TaNx coatings from impedance measurements after 4 h and 168 h of immersion**

Bode plots are used to characterize the impedance of the electrolyte/coating/substrate system. The logarithmic impedance modulus |Z| and phase angle vs logarithmic frequency are represented. The point where log |Z| curve crosses the Y-axis is related to the polarization resistance of the coating. In the phase angle vs log f diagram, if the phase angle is equal to -90 °, the coating behaves like an ideal capacitor which implies the presence of a stable dielectric film. If the phase angle equals 0 °, the coating behaves like a resistor. The broader the range of frequencies is in which the phase angle remains around -90 °, the more stable the material is [35, 36]. The appearance of two maximums or time constants in the phase angle diagram reveals the existence of substrate contribution through the pores and defects of the coating. At medium frequencies, the electric current is distributed over

the entire surface of the coated area, presenting the behavior of $TaN_x$ coating. At low frequencies, the electric current is concentrated at the defects of the coating, exhibiting the response of the substrate along the pores [34].

EIS spectrum for SS316L shows a unique time constant in phase angle vs log f diagram, indicating the passive behavior of the bare substrate. SS316L is best fitted using Randles Circuit shown in Fig 4.9a and already described in Chapter 3.

EIS spectrum for Ta, TaN_0.25 and TaN_0.625 shows one time constant in phase angle vs log f diagram. The absence of substrate contribution in the electrochemical response of these systems indicates a low defect microstructure. Therefore, the equivalent circuit used to model electrochemical behavior of these films is the Circuit 1, Randles circuit. When Randles Circuit is applied to fit electrochemical behavior of a coating, it indicates that the coating is extremely dense allowing the complete isolation of bare metal with the corrosive medium It is important to mention that the constant phase element (CPE) and resistance (R) have different meanings when Randles is applied to an uncoated metal or to a dense coating as shown in Fig 4.9.

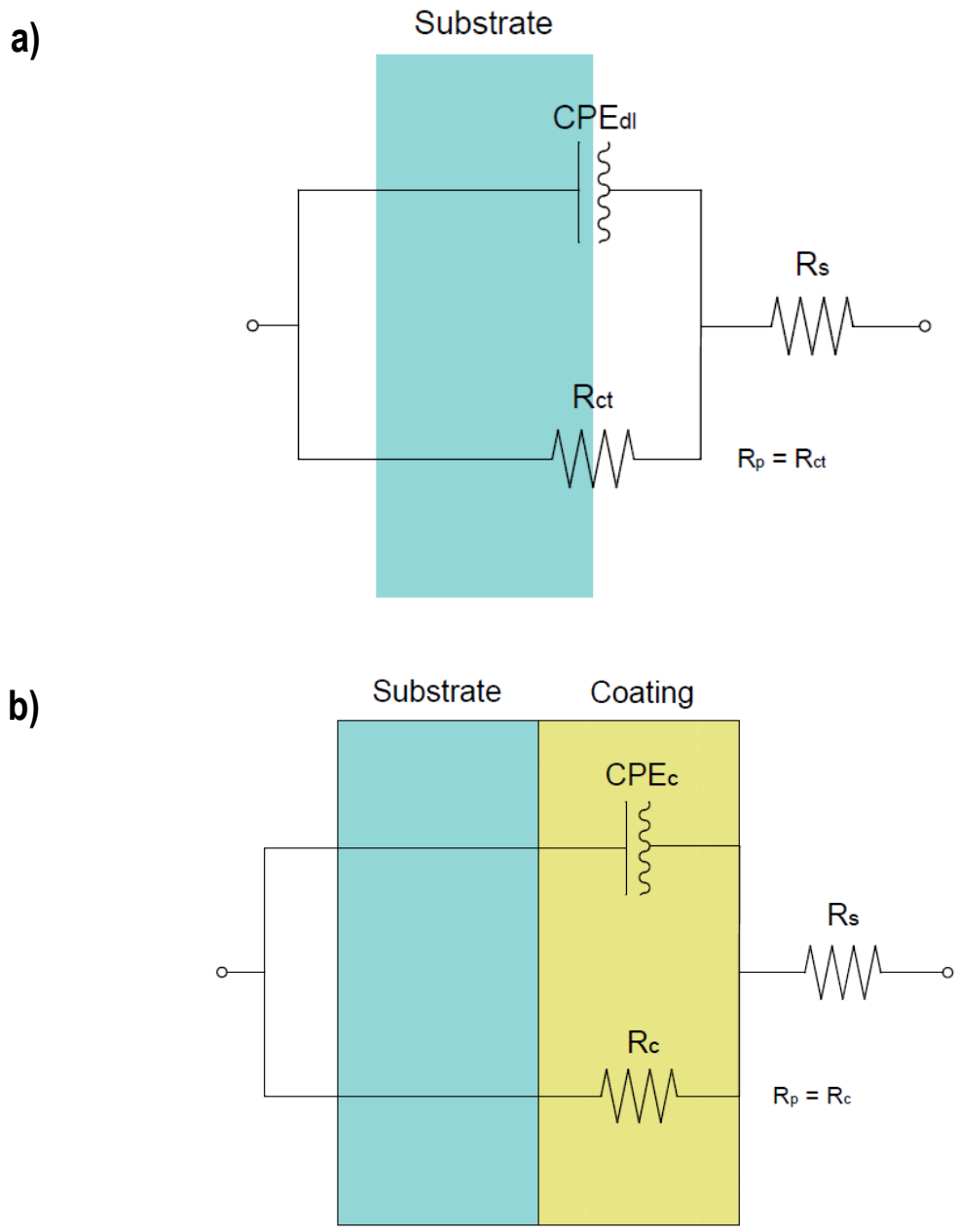


**Fig 4. 9: Randles equivalent circuit used for fitting the EIS experimental data obtained for a) AISI 316L and b) Ta, TaN_0.25 and TaN_0.625**

TaN_1 spectrum exhibits two time constants which is ascribed to the presence of two-electrochemical interfaces in the system i) electrolyte/coating interface and ii) electrolyte/substrate interface. TaN_1 presents higher pore/defect density than the other coatings. The TaN_1 coating is fitted by the equivalent circuit shown in Fig. 4.10, corresponding to Circuit 2 already described in Chapter 3.

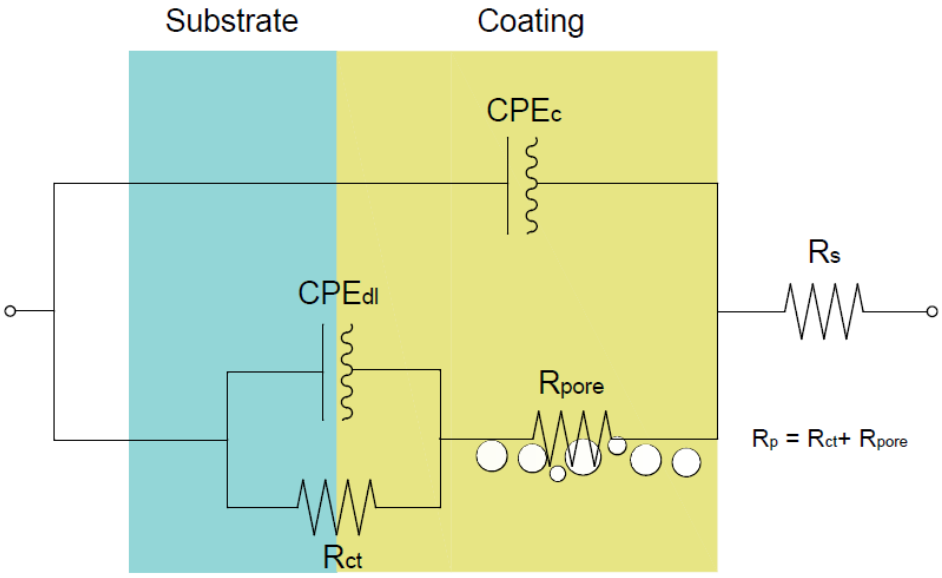


**Fig 4. 10: Equivalent circuit used for fitting the EIS experimental data obtained for TaN_1 film**

As it is revealed in Fig. 4.8., this coating exhibits two time constants in the phase angle vs. log f curves, suggesting the presence of two electrochemical interfaces simulated by two pairs of CPE/R elements combined in parallel. When this equivalent circuit is used to model a coating, it indicates that the coating is porous and it cannot prevent the electrolyte penetration towards the metal substrate. The electrolyte penetrates through pores and pinholes of the coating and makes contact with the metallic substrate [31, 37].

Experimental parameters obtained after fitting are displayed in Table 4.4. AISI 316L substrate exhibits similar behavior at both registered immersion times, showing elevated corrosion resistances (10 MΩ $cm^2$) and rather capacitive behavior represented by a shift near to -90 º phase angles in Bode plot (Fig 4.8.), low $Y_0$ values and n values between 0.88-0.91 at 4 h and 168 h, respectively. The high corrosion resistance of SS316L is due to the formation of a protective $Cr_2O_3$ stable oxide on the top of its surface [38].

| | | $R_s$ (Ω) | $R_{ct}$ (MΩ cm²) | $Y_0$-$CPE_{dl}$ (μF cm⁻²) | n | | | | $R_p$ (MΩ cm²) |
|---|---|---|---|---|---|---|---|---|---|
| **AISI 316L** | 4h | 40.40 | 11.70 | 15.10 | 0.88 | | | | 11.70 |
| | 168h | 41.10 | 10.80 | 10.50 | 0.91 | | | | 10.80 |
| | | $R_s$ (Ω) | $R_c$ (MΩ cm²) | $Y_0$-$CPE_c$ (μF cm⁻²) | n | | | | $R_p$ (MΩ cm²) |
| **Ta** | 4h | 57.28 | 5.32 | 12.40 | 0.96 | | | | 5.32 |
| | 168h | 16.37 | 22.90 | 8.04 | 0.97 | | | | 22.90 |
| **TaN_0.25** | 4h | 61.54 | 4.04 | 10.40 | 0.96 | | | | 4.04 |
| | 168h | 65.90 | 34.20 | 7.06 | 0.97 | | | | 34.20 |
| **TaN_0.625** | 4h | 40.12 | 1.21 | 27.50 | 0.95 | | | | 1.21 |
| | 168h | 44.52 | 18.90 | 13.00 | 0.96 | | | | 18.90 |
| | | $R_s$ (Ω) | $R_{pore}$ (MΩ cm²) | $Y_0$-$CPE_c$ (μF cm⁻²) | n | $R_{ct}$ (MΩ cm²) | $Y_0$-$CPE_{dl}$ (μF cm⁻²) | n | $R_p$ (MΩ cm²) |
| **TaN_1** | 4h | 20.30 | $2.9x10^{-3}$ | 87.90 | 0.89 | 0.55 | 87.00 | 0.76 | 0.55 |
| | 168h | 8.99 | $2.1x10^{-3}$ | 26.90 | 0.80 | 1.03 | 38.00 | 0.69 | 1.03 |

**Table 4. 4: EIS data of AISI 316L and $TaN_x$ coatings obtained by equivalent circuit modelling at different immersion times**

All $TaN_x$ coatings exhibit lower polarization resistances than the bare substrate after 4 h of immersion. However, Ta, TaN_0.25 and TaN_0.625 coatings greatly increase their polarization resistances (18-32 MΩ cm²) after 168 h showing better resistances than the uncoated AISI 316L. The low values of $Y_0$-$CPE_c$ element as well as n values very close to 1 are indicative of almost perfect capacitors. The reason for this behavior is the formation of an extremely stable tantalum pentoxide ($Ta_2O_5$) protective film on the top of their surfaces [39]. The lower polarization resistance of the films at 4 h may indicate slower formation of this tantalum oxide compared to $Cr_2O_3$ formation on the SS316L substrate surface. In fact, these $TaN_x$ coatings exhibit much better capacitive behavior after 168 h of immersion than the substrate. The high capacitive behavior of $TaN_x$ coatings is represented by a single maximum at -90 º for all medium-low frequencies range. Among them, the broadest range of frequencies where phase angle remains at -90 º is observed for Ta coating, suggesting higher chemical stability, which is in accordance with the corrosion

response expected for this material in NaCl [4]. Nevertheless, the highest polarization resistance value is obtained for TaN_0.25 film as shown in Table 4.4. This fact is surprising, since such a high corrosion protection is devoted to the tantalum metal (Ta) itself and better protection could be expected for Ta coating. The film microstructure analysis in Fig. 4.5 reveals a columnar-free microstructure and flat surface for TaN_0.25. The suppression of columnar growth in this film promotes longer prevention against corrosive medium penetration towards the substrate. The lowest roughness observed for TaN_0.25 coating leads to lower area exposure to corrosive media which decreases corrosion degradation phenomena. The high amount of tantalum (90 at. %) in the nitride film and the presence of corrosion-resistant α-Ta phase further enhance TaN_0.25 corrosion resistance. It is demonstrated that besides electrochemical characteristics of the coating material itself, the microstructure of the film plays an important role on the final corrosion resistance of a film. The TaN_1 film is the only one showing worse performance than the uncoated AISI 316L at both immersion times registered. Contribution from the substrate is distinguished from Bode plots. The high content of nitrogen in the film (45 at. %) is diminishing its polarization resistance compared to the films containing lower amount of nitrogen and higher of tantalum, i.e. Ta, TaN_0.25 and TaN_0.625. In fact, the polarization resistance value in the range of the MΩ $cm^{-2}$ is due to the passive behavior of the SS316L substrate itself, not due to coating resistance, since $R_{pore}$ is negligible compared with $R_{ct.}$ The highly corrosion resistance α-Ta phase is not detected on TaN_1 XRD spectrum (Fig. 4.4.) and the presence of high nitrogen content $Ta_3N_5$ may be detrimental in terms of corrosion protection. The exhibition of high corrosion resistance and protective character in NaCl 0.06 M is restricted to the $TaN_x$ films containing at least 75 at. % Ta in the film in this study. The suppression of columnar growth and the development of smooth surface on TaN_0.25 positively influences the corrosion resistance of this film.

### *3.2.4.2 Potentiodynamic polarization*

Potentiodynamic polarization was performed on $TaN_x$ samples after 192 h immersion time in NaCl 0.06 M to accurately evaluate the passive behavior of $TaN_x$ films. The potential was varied from $E_{oc}$ – 0.4 V to $E_{oc}$ + 1.4 V with a scan rate of 0.5 mV/s. Corrosion potential, corrosion current and polarization resistance values were obtained by means of Tafel's extrapolation using Autolab software. The porosity of the coatings was also calculated from the experimental results obtained after the tests [40, 41].

The corrosion currents and polarization resistances were calculated from Tafel analysis of the polarization curves (Fig 4.10.) and are displayed in Table 4.5.

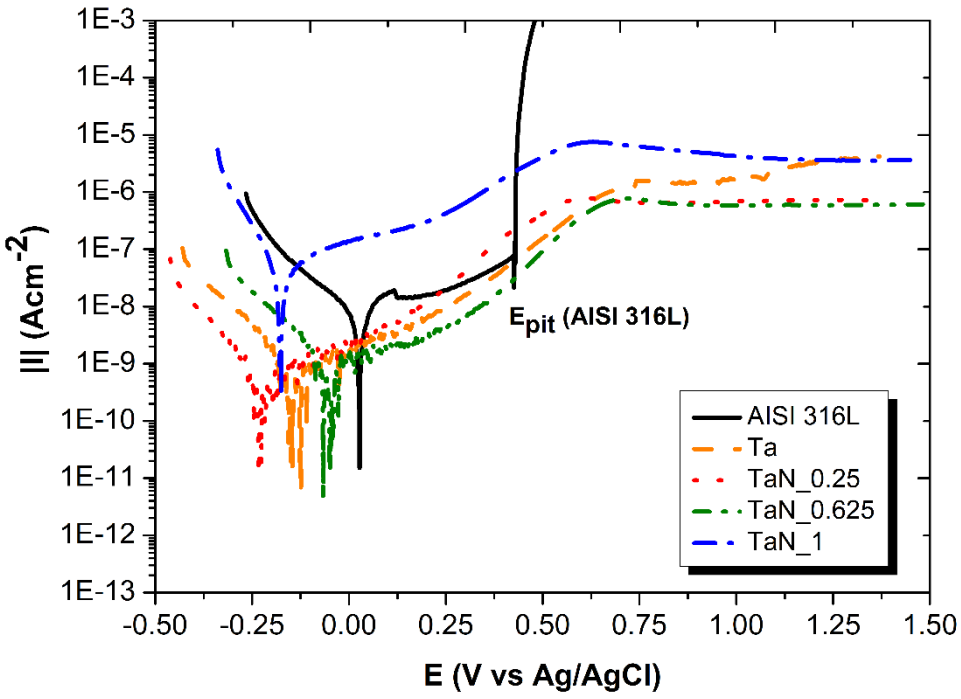


**Fig 4. 11: Current vs applied potential for AISI 316L and TaNx films in NaCl 0.06 M after 192 h of immersion**

| | $E_{CORR}$ (V) | $I_{CORR}$ (ηA $cm^{-2}$) | $R_P$ (MΩ $cm^2$) |
|---|---|---|---|
| **AISI 316L** | 0.027 | 5.40 | 6.10 |
| **Ta** | -0.14 | 0.55 | 65.61 |
| **TaN_0.25** | -0.21 | 0.28 | 103.53 |
| **TaN_0.625** | -0.05 | 0.90 | 55.50 |
| **TaN_1** | -0.17 | 32.10 | 0.81 |

**Table 4. 5: Tafel analysis from polarization curve data for TaNx films**

The corrosion current values for Ta, TaN_0.25 and TaN_0.625 are one order of magnitude lower than the current values for the bare substrate. They exhibit corrosion resistance values one order of magnitude higher than the substrate, supporting the better performance of these coatings already reported after EIS analysis and quantified in table 4.2. The analysis does not show big differences between these three coatings, which confirms that passive and stable tantalum oxide barrier film [5] is formed on the top of all these coating surfaces. It is demonstrated that tantalum oxide owns better chemical stability than $Cr_2O_3$-based oxide film grown on the top of the AISI 316L. This analysis evidences that TaN_0.25 presents the best corrosion resistance as indicated by the lowest corrosion current (0.28 nA $cm^{-2}$) and the highest corrosion resistance values (103.53 MΩ $cm^2$) shown in table 4.3. This behavior is in accordance with the results obtained during EIS analysis, confirming the selection of TaN_0.25 coating as the best candidate to protect AISI 316L against corrosive attack in NaCl. Contrary, the TaN_1 film exhibits corrosion currents and corrosion resistance values worse than the bare substrate indicating that the barrier oxide layer cannot block the corrosive medium penetration towards the substrate. The high nitrogen content (Fig. 4.3.) on this film may induce lower chemical stability surface barrier oxynitride layer formation instead of greatly protective tantalum oxide. The composition and crystal phases of the $TaN_x$ coatings determines the type of

barrier oxide surface layer that will grow which eventually protects or not the coating from corrosion phenomena.

The pitting potential represents the critical potential at which pits start to grow on the protective oxide layer when transpassive region is reached at anodic potentials leading to a complete removal of the oxide layer and exposing the fresh metal to corrosive medium. The pitting potential is detected at +0.45 V for AISI 316L substrate [42]. At this potential, an abrupt increase of the corrosion current is observed in polarization diagram (Fig 4.11.), indicating the fast dissolution of the passive film. No pitting corrosion is detected for $TaN_x$ films in Fig 4.11, and no pits were observed on $TaN_x$ sample surfaces when removed from the electrochemical cell after polarization. The $TaN_x$ films reach a passive state at potentials between 0.5 – 0.75 V, which is an indication of tantalum barrier oxide layer growth and do not undergo any change up to 1.5 V. They are remarkably chemically stable, showing corrosion currents $i_{corr}$ < 1 μA $cm^{-2}$ during the whole polarization test. The corrosion current showed by TaN_1 is higher than currents exhibited by the other coatings, confirming again the worst corrosion resistance of this film compared with other $TaN_x$ films.

Porosity is a key feature influencing corrosion response of the coatings, since high pore and defect microstructure film is prone to corrosion. Porosity can be estimated from electrochemical values obtained after polarization curves analysis. Matthews et al. [40] established an empirical equation to estimate the porosity (P) of the coating:

$$P = \frac{R_{pm\,(substrate)}}{R_{p(coating)}} \times 10^{-\left|\Delta E_{corr}/\beta_a\right|} \quad [4.1]$$

where P is the total coating porosity, $R_{pm}$ the polarization resistance of the bare substrate, $R_p$ the polarization resistance of the coating, $\Delta E_{corr}$ the difference of corrosion potential between coating and substrate, and $\beta_a$ the anodic Tafel slope of the bare substrate. Experimental parameters used to calculate porosity for each $TaN_x$ coating are shown in Table 4.6.

| | $R_{pm}$ ($M\Omega\ cm^2$) | $R_p$ ($M\Omega\ cm^2$) | $R_{pm}/R_p$ | $\Delta E_{corr}$ (mV) | $\beta_a$ (mV) | P |
|---|---|---|---|---|---|---|
| **Ta** | 6.09 | 65.61 | 9.2 E-02 | 168 | 157.85 | 8.0E-03 |
| **TaN_0.25** | 6.09 | 103.53 | 5.8 E-02 | 246 | 157.85 | 1.6E-03 |
| **TaN_0.625** | 6.09 | 55.50 | 1.1 E-01 | 73 | 157.85 | 3.7E-02 |
| **TaN_1** | 6.09 | 0.81 | 7.5 E+00 | 199 | 157.85 | 4.1E-01 |

**Table 4. 6: Experimental data for porosity calculation using equation [4.2]**

The porosity and polarization resistance values of $TaN_x$ coatings are plotted in Fig 4.11. The diagram reveals a significant correlation between these two parameters illustrating that polarization resistance of the $TaN_x$ films is inversely proportional to the estimated porosity. The lowest porosity is observed for TaN_0.25 coating which indicates that thin films characterized by columnar-free microstructure lead to defect and pore density reduction. Pore and defect density is directly related to the peak current density developed during MPPMS discharge (Table 4.3). Higher peak current density implies higher metal ion content during the discharge. Larger number of ions increases the surface adatom mobility into the growing film surface. This effective movement will fill the voids, create more nucleation sites and stop the columnar growth, thereby increasing the density of the films and reducing the porosity.

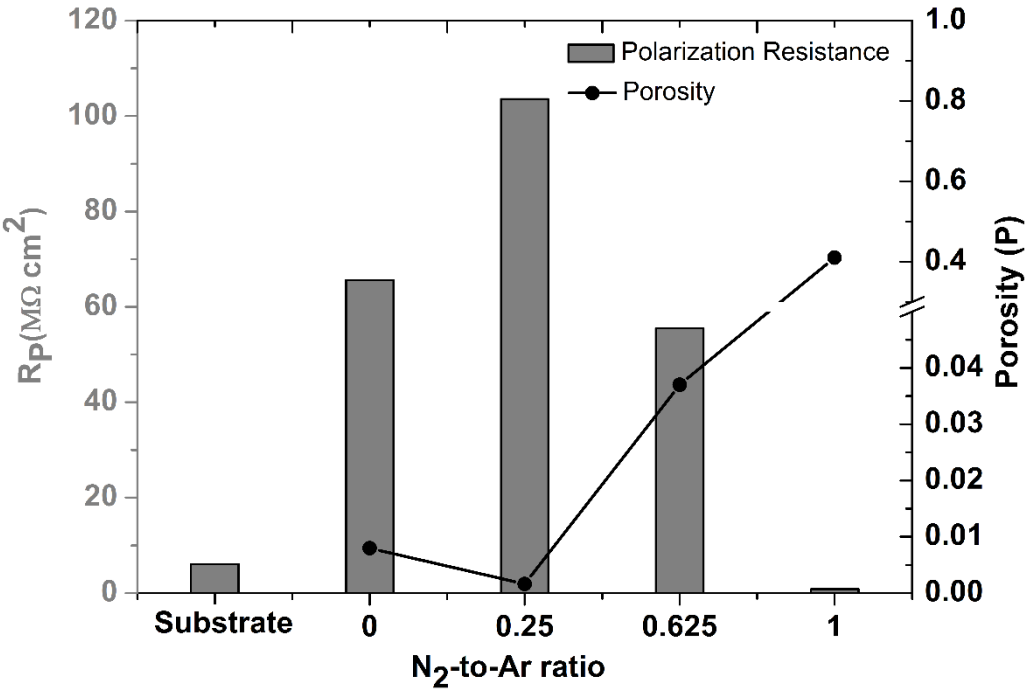


**Fig 4. 12: Polarization resistance and porosity of AISI 316L and $TaN_x$ films deposited at different $N_2$-to-Ar ratios**

# 4. Conclusions

Highly corrosion-resistant $TaN_x$ films have been obtained by MPPMS technique after an appropriate selection of optimized MPPMS pulse shape. The composition, microstructure, surface topography, hardness and corrosion resistance of $TaN_x$ films have been correlated with $N_2$-to-Ar ratio during film deposition processes. Deposition rate mean values around 1.12 μm $h^{-1}$ have been obtained, demonstrating the industrial viability of MPPMS technique for the deposition of high corrosion resistance $TaN_x$ coatings.

The development of different crystal phases has been observed depending on the atomic %. of nitrogen on the films. The SEM analysis reveals a dense microstructure for all $TaN_x$ films. However, the suppression of columnar growth is restricted to

TaN_0.25 characterized by 10 at. % of nitrogen and corresponding to the higher peak current density during MPPMS discharge. The hardness increases from 8-25 GPa as nitrogen content on the film increases. The maximum value of hardness is observed in case of TaN_0.625 film, characterized by 25 at. % on the film and exhibiting the contribution from the super-hard $Ta_4N$ crystal phase. The roughness is much lower for $TaN_x$ films containing nitrogen compared to metallic Ta.

Corrosion resistance of $TaN_x$ films has been analyzed in terms of $N_2$-to-Ar ratio and correlated with composition, microstructure and surface topography of the films. High corrosion resistance values ($10^7$-$10^8$ Ω $cm^2$) are observed for metallic Ta and low nitrogen content $TaN_x$ films (lower than 30 at. %). The excellent corrosion resistant of these films is attributable to the growth of a spontaneous, chemical inert and extremely stable tantalum oxide surface barrier layer. Pitting corrosion phenomena observed on AISI 316L at +0.45 V in NaCl 0.06 M is not detected for $TaN_x$ films. Films deposited at 0.25 $N_2$-to-Ar ratio present the best corrosion performance. The presence of highly corrosion resistant α-Ta phase, the suppression of columnar growth, the lowest porosity and the extremely smooth surface topography of TaN_0.25 will lead to the formation of a more compact, well-adherent and impervious tantalum oxide surface layer that is responsible for better electrochemical behavior of this film. The much lower corrosion resistance observed for TaN_1 is due to the formation of an oxynitride tantalum surface layer derivable from an excessive amount of nitrogen on the film. This oxynitride Ta layer does not own the inertness and chemical stability exhibited by tantalum oxide.

To summarize the corrosion resistance evaluation of different $TaN_x$ films accomplished in this work, the polarization resistance values obtained after EIS and polarization analysis are shown in Table 4.7.

| EIS analysis | | |
|---|---|---|
| **Samples** | **Time of immersion** | **Polarization resistance, $R_p$ (MΩ cm$^2$)** |
| AISI 316L | 4 h | 11.70 |
| | 168 h | 10.80 |
| Ta | 4 h | 5.32 |
| | 168 h | 22.90 |
| TaN_0.25 | 4 h | 4.04 |
| | 168 h | 34.20 |
| TaN_0.625 | 4 h | 1.21 |
| | 168 h | 18.90 |
| TaN_1 | 4 h | 0.55 |
| | 168 h | 1.03 |
| **Polarization, Tafel analysis** | | |
| **Samples** | **Time of immersion** | **Polarization resistance, $R_p$ (MΩ cm$^2$)** |
| AISI 316L | 192 h | 6.10 |
| Ta | 192 h | 65.61 |
| TaN_0.25 | 192 h | 103.53 |
| TaN_0.625 | 192 h | 55.50 |
| TaN_1 | 192 h | 0.81 |

**Table 4. 7 Polarization resistance values obtained after electrochemical testing for AISI 316L and $TaN_X$ coatings in NaCl 0.06 M.**

# 5. References

[1] S. Myers, J. Lin, R. Martins Souza, W.D. Sproul, J.J. Moore, The β to α phase transition of tantalum coatings deposited by modulated pulsed power magnetron sputtering, Surf. Coat. Technol., 214 (2013) 38-45

[2] T.B. Massalski, H. Okamoto, ASM international, *Binary Alloy Phase Diagrams*, second ed., Materials Park, Ohio, 1990.

[3] J.-E. Sundgren, B.-O. Johansson, A. Rockett, S.A. Barnett, J.E. Greene, in: J.E. Greene, W.D. Sproul, J.A. Thornton (Eds.), Physics and Chemistry of Protective Coatings, vol. 149, American Institute of Physics, New York, 1986, p. 95.

[4] A.E. McHale, Phase Equilibria Diagrams: Borides, Carbides, and Nitrides, vol. X, The American Ceramic Society, Westerville, USA, 1994.

[5] G.R. Lee, H. Kim, H.S. Choi, J.J. Lee, Superhard tantalum-nitride films formed by inductively coupled plasma-assisted sputtering. Surf. Coat. Technol., 201 (2007) 5207-5210

[6] R. Sreenivasan, T. Sugawara, K.C. Saraswat, P.C. Mcintyre, High temperature phase transformation of tantalum nitride films deposited by plasma enhanced atomic layer deposition for gate electrode applications, Appl. Phys. Lett. 90 (2007) 102101

[7] K. Valleti, A. Subrahmanyam, S.V. Joshi, A.R. Phani, M. Passacantando, S. Santucci, Studies on phase dependent mechanical properties of dc magnetron sputtered TaN thin films: evaluation of super hardness in orthorhombic Ta4N phase, Phys. D: Appl. Phys., 41 (2008) 045409

[8] D. Bernoulli, U. Müller, M. Schwarzenberger, R. Hauert, R. Spolenak, Magnetron sputter deposited tantalum and tantalum nitride thin films: An analysis of phase, hardness and composition, Thin Solid Films 548 (2013) 157–161

[9] S.K. Kim, B.C. Cha, Deposition of tantalum nitride thin films by D.C. magnetron sputtering, Thin Solid Films, 475 (2005) 202-207

[10] A. Aryasomayajula, K. Valleti, S. Aryasomayajula, D.G. Bhat, Pulsed DC magnetron sputtered tantalum nitride coatings for tribological applications, Surf. Coat. Technol., 201 (2006) 4401-4405

[11] K-Y. Liu, J-W. Lee, F-B. Wu, Fabrication and tribological behavior of sputtering TaN coatings, Surface & Coatings Technology 259 (2014) 123–128

[12] M. Cheviot, M. Gouné, A. Poulon-Quintin, Monitoring tantalum nitride thin film structure by reactive RF magnetron sputtering: Influence of processing parameters, Surface & Coatings Technology 284 (2015) 192–197

[13] Y.M. Lu, R.J. Weng, W.S. Hwang, Y.S. Yang, Study of phase transition and electrical resistivity of tantalum nitride films prepared by DC magnetron sputtering with OES detection system, Thin Solid Films 398 –399 (2001) 356–360

[14] Nishat Arshi, Junqing Lu, Yun Kon Joo, Jae Hong Yoon, Bon Heun Koo, Effects of nitrogen composition on the resistivity of reactively sputtered TaN thin films, Surf. Interface Anal. 47 (2015) 154–160

[15] Y. Zhang, Y. Zheng, Y. Li, L. Wang, Y. Bai, Q. Zhao, X. Xiong, Y. Cheng, Z. Tang, Y. Deng, S. Wei, Tantalum Nitride-Decorated Titanium with Enhanced Resistance to Microbiologically Induced Corrosion and Mechanical Property for Dental Application, PLOS ONE | DOI:10.1371/journal.pone.0130774 June 24, 2015

[16] J. Lin, W.D. Sproul, J.J. Moore, Z. Wu, S.Lee, R. Chistyakov, B. Abraham, Recent advances in modulated pulsed power magnetron sputtering for surface engineering, JOM 63 (2011) 48-58

[17] J. Lin, J.J. Moore, W.D. Sproul, S.L. Lee, J. Wang, Effect of negative substrate bias on the structure and properties of Ta coatings deposited using modulated pulse power magnetron sputtering, IEEE Trans. Plasma Sci., 38 (2010) 3071-3078

[18] U. Helmersson, M. Lattemann, J. Bohlmark, A. P. Ehiasarian, J. T. Gudmundsson, Ionized physical vapor deposition (IPVD): A review of technology and applications, Thin Solid Films 513 (2006) 1-24

[19] J. Alami, Kostas Sarakinos, G. Mark and M. Wuttig, On the deposition rate in a high power pulsed magnetron sputtering discharge, Applied Physics Letters 89 (2006) 154104

[20] J Alami, K Sarakinos, F Uslu, M Wuttig, On the relationship between the peak target current and the morphology of chromium nitride thin films deposited by reactive high power pulsed magnetron sputtering, J. Phys. D: Appl. Phys. 42 (2009) 015304

[21] G. Greczynski, J. Jensen, L. Hultman, Mitigating the geometrical limitations of conventional sputtering by controlling the ion-to-neutral ratio during high power pulsed magnetron sputtering, Thin Solid Films 519 (2011) 6354–6361

[22] Montri Aiempanakit, Ulf Helmersson, Asim Aijaz, Petter Larsson, Roger Magnusson Jens Jensen, Tomáš Kubart, Effect of peak power in reactive high power impulse magnetron sputtering of titanium dioxide, Surface & Coatings Technology 205 (2011) 4828–4831

[23] A. P. Ehiasarian, A. Vetushka, Y. Aranda Gonzalvo, G. Sáfrán, L. Székely, P. B. Barna, Influence of high power impulse magnetron sputtering plasma ionization on the microstructure of TiN thin films, J. Appl. Phys. 109 (2011) 104314

[24] P. Eh. Hovsepian, A.P. Ehiasarian, I. Petrov, Structure evolution and properties of TiAlCN/VCN coatings deposited by reactive HIPIMS, Surface & Coatings Technology 257 (2014) 38–47

[25] K. Bobzin , N. Bagcivan , P. Immich , S. Bolz , J. Alami and R. J. Cremer, Advantages of nanocomposite coatings deposited by high power pulse magnetron sputtering technology", J. Mater. Process. Technol. 209, (2009) 165-170

[26] M. Lattemann, A. P. Ehiasarian , J. Bohlmark , P. A. O. Persson and U. Helmersson, Investigation of high power impulse magnetron sputtering pretreated interfaces for adhesion enhancement of hard coatings on steel, Surf. Coat. Technol. 200 (2006) 6495-6499

[27] G. Greczynski, J. Jensen, J. Bohlmark, L. Hultman, Microstructure control of CrNx films during high power impulse magnetron sputtering, Surf. Coat. Technol., 205 (2011) 118-130

[28] R. Knepper, B. Stevens and S.P. Baker, Effect of oxygen on the thermomechanical behavior of tantalum thin films during the β-α phase transformation J. Appl. Phys., 100 (2006) 123508

[29] J. Alami, P. Eklund, J.M. Andersson, M. Lattemann, E. Wallin, J. Bohlmark, P. Persson, U. Helmersson, Phase tailoring of Ta thin films by highly ionized pulsed magnetron sputtering, Thin Solid Films, 515 (2007) 3434

[30] Y.P. Purandare, A.P. Ehiasarian, M.M. Stack, P.Eh. Hovsepian, CrN/NbN coatings deposited by HIPIMS: A preliminary study of erosion-corrosion performance Surf. Coat. Technol., 204 (2010) 1158-1162

[31] H. Ren, M. Sosnowski, Tantalum thin films deposited by ion assisted magnetron sputtering Thin Solid Films, 516 (2008) 1898-1905

[32] J. Nazon, J. Sarradin,V. Flaud, J.C. Tedenac, N. Frety, Effects of processing parameters on the properties of tantalum nitride thin films deposited by reactive sputtering, J. Alloys and Compounds, 464 (2008) 526-531

[33] W.C. Oliver and G.M. Pharr, An improved technique for determining hardness and elastic modulus using load and displacement sensing indentation experiments, J. Mater. Res., 7 (1992) 1564

[34] C. Liu, Q. Bi, A. Leyland, A. Matthews, An electrochemical impedance spectroscopy study of the corrosion behaviour of PVD coated steels in 0.5 N NaCl aqueous solution: Part I. Establishment of equivalent circuits for EIS data modelling, Corrosion Science, 45 (2003) 1243-1256

[35] C.A. Della Rovere, J.H. Alano, R. Silva, P.A.P Nascente, J. Otubo, S.E. Kuri, Characterization of passive films on shape memory stainless steels, Corrosion Science, 57 (2012) 154-161

[36] S. Kumar, T.S.N. Narayanan, S.G.S Raman, S.K. Seshadri, Thermal oxidation of Ti6Al4V alloy: Microstructural and electrochemical characterizationMater.Chem. Phys., 119 (2010) 337-346

[37] D. Loveday, P. Peterson, B. Rodgers, JCT Coatings Tech, Gamry Instruments EIS part II (2004)

[38] A. Pardo, M.C. Merino, A.E. Coy, F. Viejo, R. Arrabal, E. Matykina, Pitting corrosion behaviour of austenitic stainless steels – combining effects of Mn and Mo additionsCorrosion Science, 50 (2008) 1796-1806

[39] M. Schutze, R. Bender, K.G. Schutze, Corrosion Resistance of High-Performance Materials, second ed., Wiley-VCH, Frankfurt, 2012

[40] B. Matthews, E. Broszeit, J. Aromaa, H. Ronkainen, S.P. Hannula, A. Leyland, A. Matthews, Corrosion performance of some titanium-based hard coatings, Surf. Coat. Technol., 49 (1991) 489-495

[41] S.H. Ahn, J.H. Lee, J.G. Kim and J.G. Han, Localized corrosion mechanisms of the multilayered coatings related to growth defects, Surf. Coat. Technol. 177 (2004) 638-644

[42] K.V.S. Ramana, T. Anita, S. Mandal, S. Kapliappan, H. Shaikh, P.V. Sivaprasad, R.K. Dayal, H.S. Khatak, Effect of different environmental parameters on pitting behavior of AISI type 316L stainless steel: Experimental studies and neural network modeling Materials and Design, 30 (2009) 3770-377

# CHAPTER 5

# MULTILAYER $TaN_X$ FILMS FOR TITANIUM IMPLANTS PROTECTION AGAINST TRIBOCORROSION

# 1. Introduction

Materials used for biomedical applications are huge and can be divided in five groups based on their physicochemical nature: metallic materials, ceramic materials, polymeric materials, composite materials and biodegradable polymers [1-2].

Currently, biomedical implants and medical devices are commonly employed to replace and/or restore the function of traumatized or degenerated tissues or organs, and thus improve the quality of life of the patients. This includes a broad range of medical solutions [3-4] as summarized in Table 5.1.

| Division | Type of implants |
|---|---|
| Cardiovascular implantable devices | Stents, vascular grafts, heart valves, pacemakers… |
| Neural devices | Neuronal implants and prostheses, cochlear and retinal applications… |
| Orthopaedic prostheses | Bone fixation (plate, screw, pin)<br>Artificial joints (knee, hip, shoulder, ankle…) |
| Dentistry | Orthodontic wire, Filling<br>Dental implants |
| Craniofacial | Plates, screw… |

**Table 5. 1: Biomaterials application fields and type of implants**

Around 70-80% of implants are made today of metallic biomaterials [5-6]. The high strength and resistance to fracture that this class of material can provide, gives reliable implant performance in major load-bearing situations. Coupled with a relative ease of fabrication of both simple and complex shapes using well-established and widely available fabrication techniques (e.g., casting, forging, machining). Therefore, for load-bearing implants; namely, hip and knee prostheses, fracture fixation wires, pins, screws, plates and dental implants, metals have been used almost exclusively. Despite the large number of metals and alloys available to be produced in industry,

only a few are biocompatible and capable of relatively long-term success as an implant material [5, 7-8].

To be considered suitable, metal implants should exhibit some essential features such as:

1. Excellent biocompatibility
2. High corrosion resistance
3. Adequate mechanical properties
4. High wear resistance

Due to all these requirements, three main groups dominate the biomedical metal implant market [9]:

- **Stainless Steel SS316L** (Fe-alloy with 16-18 % Cr, 10-14 % Ni, 2 % Mo, 2 % Mn, small amount of other elements and an extremely low carbon content to prevent chromium depletion, hence the suffix L [10-13]).
- **Cobalt chromium (CoCr) alloys** which are classified into two types: CoCrMo alloys [Cr (27-30 %), Mo (5-7 %), Ni (2.5 %)] and CoNiCrMo alloys [Cr (19-21 %), Ni (33-37 %) and Mo (9-11 %)] [15].
- **Titanium (Ti) and its alloys** which are divided in three categories [16-21]:
    - *Pure Ti (Ti-cp):* The commercially available Ti-cp is classified into 4 grades depending on their oxygen content. Grade 4 is characterized by highest oxygen content (0.4 %), whereas grade 1 has the lowest (0.18 %). The hardness of Ti-cp increases with increasing oxygen content.
    - *$Ti_6Al_4V$:* Known as titanium grade 5, which is composed of Ti alloyed with 6 % of Aluminum and 4 % of Vanadium to enhance mechanical properties of Ti-cp.

- *β alloys:* Al- and V-free new Ti alloys. Different alloys can be found including mainly the following alloying elements: Mo, Nb, Ta and Zr.

Currently, all these metallic biomaterials are commonly used in different parts of the human body, being the number of implants applied for spinal, hip, knee and dental replacements extremely high. Increase in life expectancy has led to a considerable increase of aged people population and it is estimated to continuously grow in the following years. Consequently, the need for biomedical implants has tremendously increased, demanding primarily long-lasting implants capable to serve for much longer period of time without failure or revision surgery. Unfortunately, stainless steel, Co-Cr and Ti alloys have exhibited tendencies to fail after long-time exposure coming from different degradation mechanisms for each material [5]. Stainless steel and CoCr alloys have shown problems of biocompatibility once Ni, Co and Cr are released into the human body [22]. Ni is widely recognized as a high risk element due to incompatibility problems with the human body and skin related diseases [23-24]. Numerous animal studies have demonstrated carcinogenicity due to the presence of Co [25]. Moreover, the higher Young modulus of these materials compared with bone can lead to bone atrophy and loosening of implants after some years of implantation [26-27]. Lately, titanium and its alloys are gaining special attention due to their excellent corrosion resistance, highest biocompatibility and low Young modulus comparable to that of bone [16, 28]. In spite of these outstanding features, mostly used $Ti_6Al_4V$ alloy has been found to release V and Al ions due to corrosion after long time exposure to body environment which are connected with toxicity and Alzheimer's diseases, respectively [29-30]. Ti-cp does not show biocompatibility problems, but it suffers for poor mechanical properties that prevent its use in loaded joints where high wear can occur [31]. New β- alloys have not yet shown biocompatibility problems and own superior mechanical properties than Ti-cp. Nevertheless, mechanically reliable titanium implant alloy has yet to become a reality.

Mechanical properties and effects of release ions due to corrosion into the human body of conventional materials used for biomedical implants fabrication are summarize in Table 5.2.

| Materials | Young's Modulus (GPa) | Ultimate Tensile strength (MPa) | Release ions | Effects |
|---|---|---|---|---|
| 316L | 200 | 500-1350 | Cr<br>Ni | Ulcers, central nervous syst. disturbances<br>Affects skin – Dermatitis |
| CoCr alloys | 240 | 900-1800 | Co<br>Cr<br>Ni<br>Mo | Anemia B, carcinogenicity<br>Ulcers, central nervous syst. disturbances<br>Affects skin – Dermatitis<br>No toxic effect reported |
| Ti-cp | 115 | 240-550 | Ti | No toxic effect |
| $Ti_6Al_4V$ | 110 | 930 | Ti<br>Al<br>V | No toxic effect<br>Alzheimer's disease and epileptic effects<br>Toxic in the elementary state |
| Ti β-alloys | 40-100 | 350-1100 | Ti<br>Nb, Mo, Ta, Zr | No toxic effect<br>Considered relatively safe today |
| Cortical Bone | 15-30 | 70-150 | - | - |

**Table 5. 2: Mechanical properties and toxic effects due to ion release shown by conventional biomaterial metallic alloys**

Therefore, there is a great concern for the development of appropriate strategies to increase implants service lifetime. The main drawbacks to ensure a longer lifetime for the implants include both the biocompatibility decrease due to the release of metal ions into the body [5, 32-33] and the material loss caused by tribocorrosion mechanism which involves the synergistic effect of wear and corrosion processes simultaneously [34-35]. Different strategies addressed so far to increase implants durability, include the development of new metallic alloys [36-39], biodegradable materials [40], surface modification processes [41], advanced coating deposition [42], micro/nano engineering methods [4]… One of the most frequent strategies to

enhance tribocorrosion behaviour of biomedical alloys is the deposition of corrosion-wear resistant protective coatings [43-47].

This chapter describes the corrosion and tribocorrosion phenomenon in current biomedical implants. It is well-known that surface characteristics of biomaterials have significant impact on their daily performance and hence, in this thesis, the deposition of multilayer tantalum nitride (TaN) coatings grown by MPPMS for Ti-cp tribocorrosion resistance enhancement is performed and evaluated. Ti and Ta are considered amongst the most biocompatible materials and their non-toxicity has been already demonstrated [48]. However, Ti-cp wear resistance and mechanical properties need to be improved to open up the application fields of this material to loaded implant components. A testing protocol for tribocorrosion evaluation of passivating materials is deeply described which has been used for addressing$TaN_x$ coatings performance as protective film for Ti-cp. Apart from the coating material characteristics itself, the development of multilayer structure is investigated for further enhancing TaN coating properties.

# 2. Corrosion and tribocorrosion phenomena in biomedical implants

## 2.1. Corrosion

Corrosion is a great concern when metallic biomaterials are implanted in the hostile aggressive environment of the human body. Implants face severe corrosion environment including blood and body fluids that contain different constituents like water, sodium, chlorine, proteins, plasma, amino acids [49]. Moreover, the pH of the human body is generally maintained at 7.0, but this value can undergo changes from 3.0 to 9.0 due to several causes such as accidents, infections, surgery…

Corrosion resistance of typically used materials; i.e., stainless steel, CoCr alloys and Ti alloys, is attributable to the protective oxide film formed on top of their surfaces.

Surface oxide film plays an important role as an inhibitor for the release of metallic ions. The composition, porosity and structure of this surface oxide film will determine the corrosion resistance of the biomaterial [50, 51]. The composition of the oxide layer depends on the biomaterial composition itself and on the reactions occurring between the material surface and surrounding living tissue and constituents [52].

However, it has been thoroughly demonstrated that even advanced materials used today, are prone to corrosion to a certain extent after long time exposures. This means that protective surface oxide layer cannot completely block the release of metallic ions with time.

In addition, it is necessary to remember that apart from corrosion, biomedical implants are subjected to different wear and fretting processes which will induce the rupture of the protective oxide layer [53-54]. This synergistic effect of wear and corrosion is known as tribocorrosion and will be deeply described in section 2.2.

When the surface oxide film is disrupted, corrosion rapidly starts and metal ions are continuously released unless the protective film is re-build. The time taken for re-passivation is of sum importance since it conditions the quantity of released metal ions. Repassivation time for AISI 316L is higher than for Co-Cr alloys and much higher than for titanium alloys [55].

It is also of sum importance the type of metal ions that are exposed to living tissue, since adverse effects of several ions present on most common biomaterials have been already reported (Table 5.2).

AISI 316L alloy owns good corrosion resistance due to the formation of a protective oxide layer consisting mainly of chromium and iron oxides [56]. However, it doesn't retain adequate corrosion resistance for long-term biomedical implants. Studies on retrieved implants show that more than 90% of AISI 316L implant failures result from pitting and crevice corrosion attack.

CoCr alloys have superior corrosion resistance than stainless steel. The high chromium content on its composition leads to the quick and spontaneous formation of passive $Cr_2O_3$ layer within the human body environment. Cobalt oxides are also present on the passive film [57]. Mo and Ni alloy elements further increase CoCr alloy's corrosion resistance [58]. The main problem with CoCr alloys arises from the allergic reactions due to Ni and Co release.

Compared with stainless steel and CoCr alloys, Ti alloys have higher biocompatibility resulting from their superior corrosion resistance. Corrosion resistance of Ti-alloys come from the formation of highly stable, well-adherent and dense $TiO_2$ protective layer [59]. Besides, titanium does not play any known biological role into the human body and is non-toxic even in large doses [60]. Surface oxide grown on $Ti_6Al_4V$ consist of $TiO_2$ with a small amount of aluminium oxide [61]. Protective layer formed

on β-alloys surface is a mixture of $TiO_2$ with highly stable niobium, tantalum and/or zirconium oxide, depending on the alloy type [62-63].

In terms of corrosion, Ti-alloys are considered superior materials of choice for biomedical implants.

## 2.2. Tribocorrosion

Apart from corrosion itself, biomedical implants are articulating systems that operate under sliding, rotation, vibration and loading conditions [64]. Hence, biomedical implants are exposed to degradation by different wear processes. When corrosion and wear occur simultaneously, these two processes lead to what is commonly known as "tribocorrosion" [65-67]. Tribocorrosion in biomedical implants is defined as a degradation phenomena of biomaterial surfaces (wear, cracking, corrosion…) subjected to the combined action of mechanical loading (friction, abrasion, erosion) and corrosion attack caused by human body environment (chemical and/or electrochemical interactions) [64, 68].

The coupling of the mechanical loading and chemical reactions taking place at the interface between the biomaterial and body fluids often results in accelerated degradation and implant damage than the one which would be expected by simply adding the degradation caused by individual processes [69-71].

Tribocorrosion is essentially a surface process, but it can negatively affect bulk mechanical properties of the whole material which have considerable impact on implants lifetime.

The effect of tribocorrosion on the wear rate of passivating biomaterials used for biomedical implants is directly related to some properties of the surface passive film. Tribocorrosion phenomena is illustrated in Fig 5.1. Generally, when biomaterials are

implanted in the human body, they tend to form a passive film (consisting mainly on oxides) that protect themselves from corrosion in the absence of mechanical loading. However, once wear processes take place, the protective film is considered to be snatched in the contact area, exposing the bare biomaterial alloy to corrosion attack. In this situation, the corrosion resistance of biomaterial is considerably reduced by wear. After mechanical loading removal, the biomaterial surface undergoes which is known as re-passivation phenomena, the re-building of passive protective film. The time taken for repassivation particularly in biomedical implants is crucial, since it limits the release of metal ions to the human body. Certain constituents of biomaterials (Ni, Co, Al, V…) have been found toxic and high ion release can cause adverse tissue reaction and loss of biocompatibility of implant material. Corrosion products generated during wear and repassivation processes are usually hard oxide particles that promote abrasive wear on the contact area. Thus, tribological resistance of the biomaterial can be diminished due to three-body wear mechanism induced by corrosion products.

It is hence demonstrated that friction and wear affect corrosion resistance of biomaterials and alternatively, corrosion enhance wear degradation of implants. Corrosion and wear are widely studied modes of degradation of materials. However, in the majority of real life applications two degradation mechanisms take part at the same time and cannot be evaluated separately, since one directly affects the other. Particularly in biomedical implants, the analysis and control of synergistic effect of corrosion and wear is of sum importance, since the implant damage induced by tribocorrosion involves the metallic ion release to the human body which has been proven to produce important health problems [5, 48, and 51]. Therefore, a dedicated testing protocol for tribocorrosion evaluation is crucial.

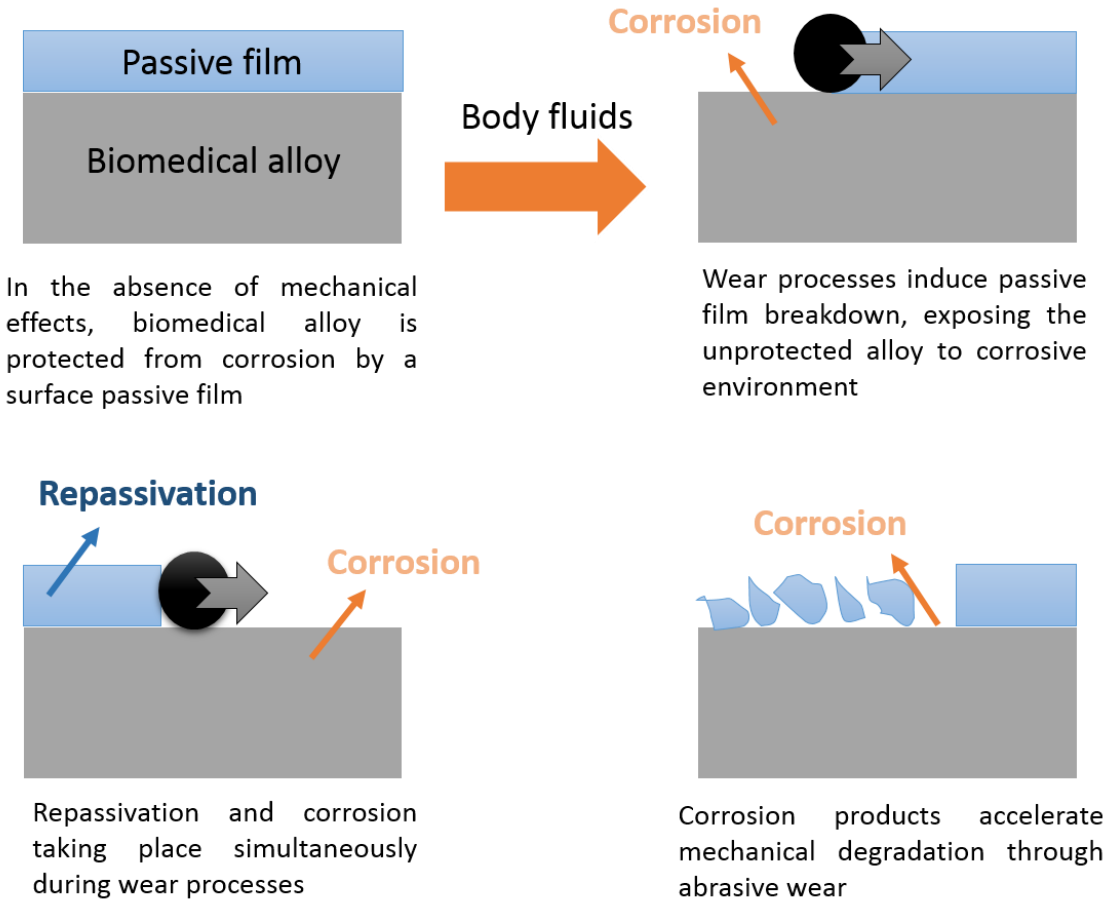


**Fig 5. 1: Schematic representation of tribocorrosion phenomena, illustrating corrosion accelerated by friction and wear and abrasion accelerated by corrosion products**

# 3. Protection of Ti-cp by multilayer TaN films

## 3.1. Multilayer TaN film deposition by MPPMS

$TaN_x$ films were deposited by MPPMS in MIDAS 450 sputtering system. The $TaN_x$ films were deposited on Ti-cp (grade 2) disks of 24mm in diameter and silicon wafers. Prior to deposition, the substrates were submitted to a cleaning procedure already described in Chapter 3.

The multilayer structure development approach used in this thesis is new and relies on the possibilities offered by the SOLO MPPMS plasma generator. In general, a multilayer film is made from two or more heterogeneous phase materials that are arranged in a laminated structure with an optimized modulation period. In this thesis, the multilayer structure is made from a unique material, TaN, that is composed of nanolayers with different composition, hardness and crystal phases.

The MPPMS generator offers the possibility to develop structurally laminated multilayer films by alternately switch between different pulse shapes in the same target within one overall process [72]. This mode of operation has been defined by j. Lin and co-workers as multi pulse MPPMS technique [73]. Each pulse is applied to the target for a certain duration (t) which mainly determines the thickness of each nanolayer and the bilayer period of the multilayer film. The application of different pulse shapes leads to the development of different plasma discharge characteristics defined by distinct peak power ($P_p$), peak current ($I_p$) and peak voltage ($V_p$) values. It is well-known that plasma features strongly influence the properties of the growing films. Hence, the application of different pulse shapes along the deposition process creates alternate TaN nanolayers featured by different microstructures and properties leading to structurally laminated TaN multilayer films. Multilayer films commonly exhibit better wear and corrosion resistance than monolayer ones. The

presence of a higher number of interfaces preventing the movement of dislocations and the propagation of micro-cracks increases wear resistance [74]. The re-nucleation process present in multilayer structures reduces the amount of pores, thereby resulting in better corrosion resistance compared to monolayer films [75].

In the current study, three different TaN systems have been analyzed. Two different multilayer TaN films, characterized by different bilayer periods deposited by multi pulse MPPMS using two pulse shapes with different pulse repeat durations and a monolayer TaN film deposited by a single MPPMS pulse.

The selected process parameters for $TaN_x$ films deposition were already optimized in the experimental work carried out in Chapter 4, and those applied for the deposition of columnar-free and most corrosion-resistant TaN monolayer film are used in this study, corresponding to TaN_0.25 coating. The working pressure was 0.6 Pa with a constant Ar-to-$N_2$ ratio of 0.25.

For all coatings, a thin Ta interlayer of 100 nm was applied for enhancing the adhesion. The average power was set to 4kW during all TaN deposition processes. Two fold substrate rotation and 350 ºC substrate temperature were used during depositions, while a bias potential of −50 V was applied on the substrate. The deposition time was established at 125 min.

The voltage-current characteristics of the two pulse shapes (P996 and P200, already described in Chapter 4) employed for $TaN_x$ multilayer depositions are shown in Fig. 5.2. The pulse 996 was also utilized for the deposition of TaN monolayer film. The pulse length, frequency, discharge parameters and deposition rate for each pulse shape are summarized in Table 5.3. Two pulses with high variation on peak current density were selected to obtained nanolayers with different hardness, density and microstructure.

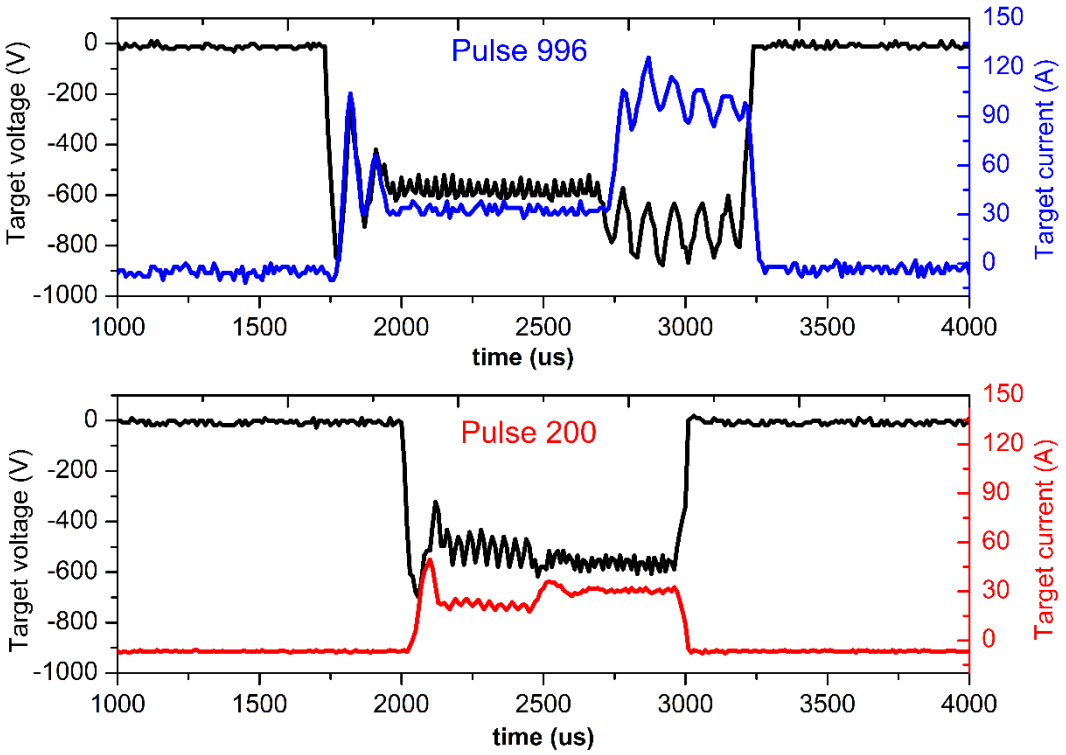


**Fig 5. 2: Voltage–current characteristics of different pulse shapes applied for TaN film deposition**

| | Pulse length (µs) | Frequency (Hz) | Peak target power (kW) | Peak target voltage (V) | Peak target current (A) | Deposition rate (nm/min) |
|---|---|---|---|---|---|---|
| P996 | 1500 | 113 | 86.2 | 866.5 | 99.4 | 18.48 |
| P200 | 1000 | 286 | 27.1 | 591.7 | 45.9 | 21.51 |

**Table 5. 3: Pulse length, frequency and resulting peak power, voltage and current values during each pulse shape application**

The time during which a given pulse shape was applied, i.e pulse repeat duration (t), was 5 and 2 minutes for TaN multilayer_1 and TaN multilayer_2, respectively, which leads to different bilayer periods for each coating as shown in Table 5.4.

| | Film structure | Pulse repeat duration (s) | Thickness (µm) | Bilayer period (nm) | Hardness (GPa) |
|---|---|---|---|---|---|
| **TaN monolayer** | Monolayer | - | 2.311 | - | 16.7 |
| **TaN multilayer_1** | Multilayer | 300 | 2.44 | ~200 | 15.81 |
| **TaN multilayer_2** | Multilayer | 120 | 2.5 | ~80 | 15.27 |

**Table 5. 4: Pulse repeat duration, bilayer period and hardness of each TaN film**

## 3.2. Simulated body fluid environment and testing protocol for tribocorrosion

The natural physiological environment contains not only inorganic species but also organic molecules such as serum proteins [76]. Thus, a Phosphate Buffered Solution (0.14M NaCl, 1mM $KH_2PO_4$, 3 mM KCl, 10 mM $Na_2HPO_4$) plus 1 gram of albumin (PBS+albumin) was chosen as experimental electrolyte for this study in order to accurately reproduce the human body fluid environment [77, 78]. Corrosion and tribocorrosion tests were performed on this electrolyte.

Tribocorrosion tests were done by using a uni-directional rotatory tribometer under ball-on-disc conFiguration. The electrochemical cell was placed on a rotatory plate in order to perform the electrochemical measurements during the tribological process as shown in Fig 5.3.

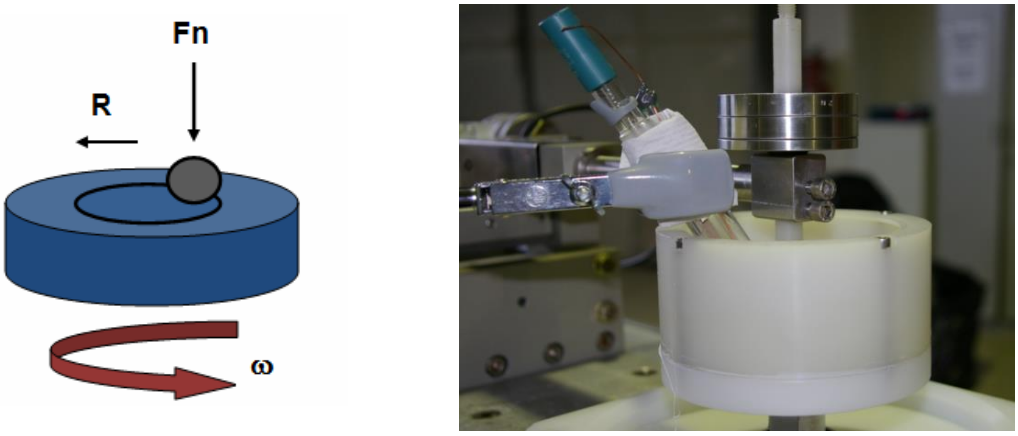


**Fig 5. 3: Experimental set-up for tribocorrosion analysis used in this study**

For analyzing tribocorrosion performance of Ti-cp and TaN coated samples, a new protocol introduced by N. Diomidis, J.-P. Celis, P. Ponthiaux and F. Wenger [79-81] and specifically designed for testing passivating materials (metallic biomaterials are included in this classification) was employed. The testing procedure is divided into four experiments and allows the quantification of the total material loss ($W_{tr}$), the material loss due to mechanical loading in the presence of a corrosive environment ($W^m_{act}$) and the material loss due to corrosion under wear processes ($W^c_{act}$). Four experiments and their purpose are described hereafter.

*Experiment 1: Electrochemical impedance spectroscopy (EIS) measurement at open circuit potential ($E_{oc}$) without any sliding*

This experiment is performed to gather information of the surface characteristics of the passive film of the biomaterial in the absence of sliding. For that purpose, the tested sample is immersed in the electrolyte and open circuit potential is monitored until it reaches a steady value, which is an indicative of passivation of the surface. After achieving a long-term stable $E_{oc}$, the polarization resistance of the passive material, $R_p$, is measured by EIS. From this measurement, the specific polarization of passive material, $r_{pass}$, can be calculated using the total surface area $A_0$, as:

$$r_{pass} = R_p A_0 \quad [5.1]$$

The corrosion current density of the material covered by a passive surface film, $i_{pass}$, can be calculated as follows:

$$i_{pass} = \frac{B}{r_{pass}} \quad [5.2]$$

with B a constant. B depends on the nature of the material and the surrounding environment and normally varies between 13 and 35 mV for metallic biomaterials. This current $i_{pass}$ corresponds to the dissolution current of the biomaterial through the passive film in a steady-state.

*Experiment 2: Evolution of open circuit potential in the electrolyte before, during and after sliding generating an active material surface*

This experiment is performed in order to get information about passive-active characteristics of the material in the rubbed area. A wear test is carried out while $E_{oc}$ is recorded before, during and after the test. The $E_{oc}$ before sliding represents the passive state of the surface. The $E^s_{oc}$ value recorded during sliding corresponds to a mixed potential from the galvanic coupling of two material surface features; namely, the active material inside the wear track ($A_{tr}$) and the passive material outside the wear track ($A_0$-$A_{tr}$). Assuming that during continuous sliding the wear track is always in an active state and no-repassivation phenomena occurs ($t_{lat}$, latency time, in tribological tests known as the time between two successive contact events, is very small). Hence, wear track area $A_{tr}$ and active area $A_{act}$ are equal and the remaining area ($A_0$-$A_{act}$) can be considered in a passive state as shown in Fig 5.4. Summarizing,

$$A_{act} = A_{tr} \quad [5.3]$$

$$A_{pass} = A_0 - A_{tr} \quad [5.4]$$

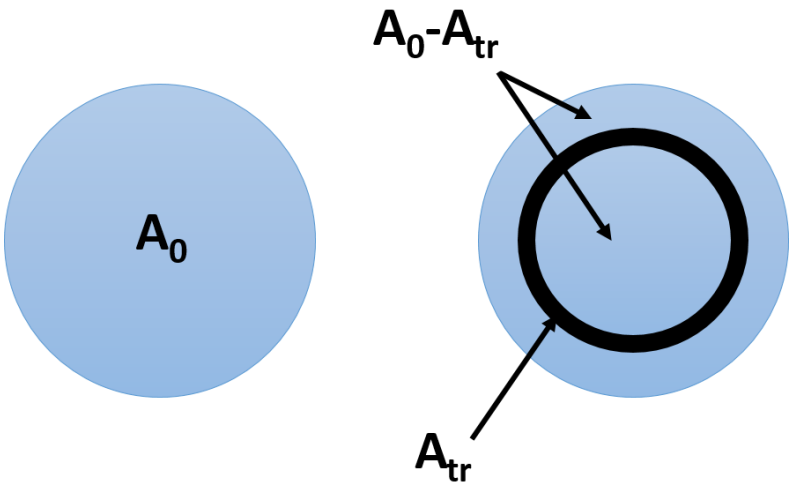


**Fig 5. 4: Schematic view of a circular tested sample before sliding (A0) and during sliding showing the wear track**

The $E_{oc}$ after sliding represents the surface characteristics after mechanical loading removal and gives information about the re-passivated surface of the tested material. If $E_{oc}$ before and after sliding is equal, it means that the repassivated surface film is identical to the initial passive surface.

*Experiment 3: Electrochemical impedance spectroscopy under sliding at a fixed potential corresponding to $E^s_{oc}$*

This experiment allows the determination of the corrosion rate of depassivated material. For that purpose, a second wear test is carried out under a rotation period ($t_{rot}$) much smaller to the time needed for the passive film to re-grow ($t_{react}$). Generally, $t_{rot}$ is taken as:

$$t_{rot} = \frac{t_{react}}{10000} \quad [5.5]$$

Before the wear test starts, the sample is polarized at $E^s_{oc}$. Then, during sliding, EIS measurements are performed to obtain the polarization resistance of the sample surface during sliding, $R_{ps}$. $R_{ps}$ includes two different polarization resistances; i.e. $R_{act}$

related to the active area of $A_{act}$ (resistance of the material inside the wear track) and $R_{pass}$ related to the remaining unworn area $A_0$-$A_{act}$:

$$\frac{1}{R_{ps}} = \frac{1}{R_{act}} + \frac{1}{R_{pass}} \quad [5.6]$$

where,

$$R_{act} = \frac{r_{act}}{A_{act}} \quad [5.7]$$

$$R_{pass} = \frac{r_{pass}}{(A_0 - A_{act})} \quad [5.8]$$

Since, $r_{pass}$ is known from Equation 5.1, it is possible to calculate specific polarization resistance of the active surface, $r_{act}$, and corrosion current density of the active material, $i_{act}$, using the following equations:

$$r_{act} = \frac{A_{tr} R_{ps} r_{pass}}{r_{pass} - R_{ps}(A_0 - A_{tr})} \quad [5.9]$$

$$i_{act} = \frac{B}{r_{act}} \quad [5.10]$$

During this test, the coefficient of friction is also monitored.

*Experiment 4: Determination of sliding wear track area and profile after testing in the electrolyte*

This last experiment enables the quantification of the material loss due to tribocorrosion phenomena.

The sliding track area ($A_{tr}$) can be measured using a profilometer, an optical microscope and/or a scanning electron microscope. The sliding track area ($A_{tr}$) is equal to the active area ($A_{act}$), taking into account that there is no time for repassivation in this approach. $A_{tr}$ is obtained following the next equation:

$$A_{tr} = A_{act} = a \times L \quad [5.11]$$

The total material loss ($W_{tr}$) for uni-directional sliding tests can be estimated from the cross section area and the length of the wear track using the expression:

$$W_{tr} = S \times L \quad [5.12]$$

being,

$$S = \frac{\pi ab}{4} \quad [5.13]$$

$$L = 2\pi r \quad [5.14]$$

Values a and b are calculated for experimental measurements of the wear track and r is defined before tribocorrosion tests as illustrated in Fig 5.5.

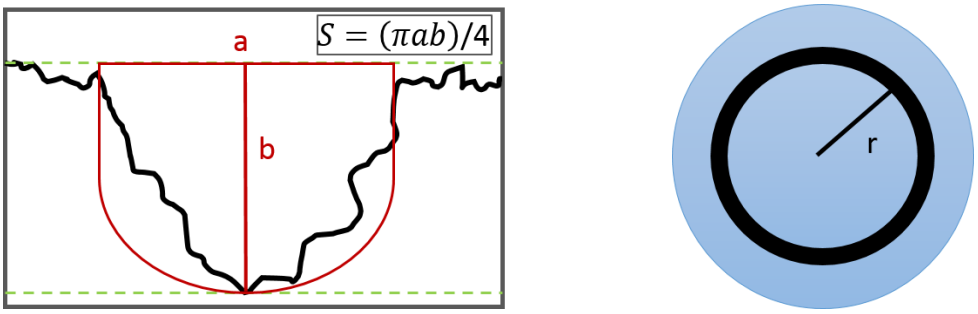


**Fig 5. 5: Cross-sectional and top view of the wear track area generated during sliding**

For simplicity, it is supposed that total material loss due to tribocorrosion ($W_{tr}$) is the sum of material loss due to mechanical loading in the presence of a corrosive environment ($W^m_{act}$) and the material loss due to corrosion under wear processes ($W^c_{act}$) as stated in the following equation:

$$W_{tr} = W^m_{act} + W^c_{act} \quad [5.15]$$

This approach does not take into account the material loss due to pure electrochemical or mechanical degradation.

The electrochemical contribution to the total material loss can be calculated from EIS data using the following equation:

$$W_{act}^{c} = i_{act} A_{act} \frac{M}{nFd} N t_{lat} \quad [5.16]$$

where $i_{act}$ is the activation current density due to corrosion, $A_{act}$ is active area of the wear track, N the number of cycles performed, $t_{lat}$ the period between two successive cycles, F is the Faraday constant (96485 A/mol), d is the density, M the molecular weight of the material and n the number of electrons involved in the electrochemical process. While $i_{act}$, $A_{act}$, N and $t_{lat}$ are obtained from the experimental EIS measurements and testing conditions; d, M and n are intrinsic properties of tested materials.

The mechanical contribution to the total material loss ($W^{m}_{act}$) is then calculated by:

$$W_{act}^{m} = W_{tr} - W_{act}^{c} \quad [5.17]$$

Particularly, the following tests and testing conditions were applied for $TaN_x$ coatings analysis:

1. Open Circuit Potential measurement was performed during 1 hour of immersion. Mean value of the open circuit potential ($E_{oc}$) after stabilization period was calculated for each sample.

2. Then, a first EIS measurement was recorded at $E_{oc}$. EIS conditions were the same as the ones used for corrosion tests.

3. First sliding process (Wear test 1) was carried out under the following tribological conditions:

- Counterbody: Alumina ball - Ø 10 mm
- Normal load: 3 N
- Radius track: 5 mm
- Rotation speed: 100 rpm
- Number of cycles: 400

Simultaneously to wear process, the evolution of the open circuit potential was monitored and registered. $E_{oc}$ registration starts two minutes before sliding and ends 10 minutes after the sliding process ends. Mean value of the open circuit potential during sliding ($E^s_{oc}$) is calculated for each sample.

4. A second sliding process (Wear test 2) was performed under the same tribological conditions described above but for a total number of cycles of 2600. In this case, samples are polarized at $E^s_{oc}$ value and a second EIS measurement is performed under potentiostatic control during this second wear process. Friction coefficient was also simultaneously monitored.

5. Determination of the total material loss due to tribocorrosion ($W_{tr}$) by calculating the volume of material loss in the wear track.

## 3.3. Multilayer TaN film characterization

### 3.3.1. Microstructure characterization

The microstructure of TaN films is theoretically explained in Fig 5.6. The TaN monolayer film microstructure is composed of a continuous thick layer developed during single MPP pulse utilization. The TaN multilayer_1 film microstructure incorporates 25 thin nanolayers which are a consequence of different MPP pulse

shape application every 5 minutes as stated in Table 5.4. In the case of TaN multilayer_2, the number of nanolayers is higher, up to 63, due to the pulse shape alternation every 2 minutes. The thickness of the nanolayers is theoretically calculated from the deposition rate of each pulse shown in Table 5.3.

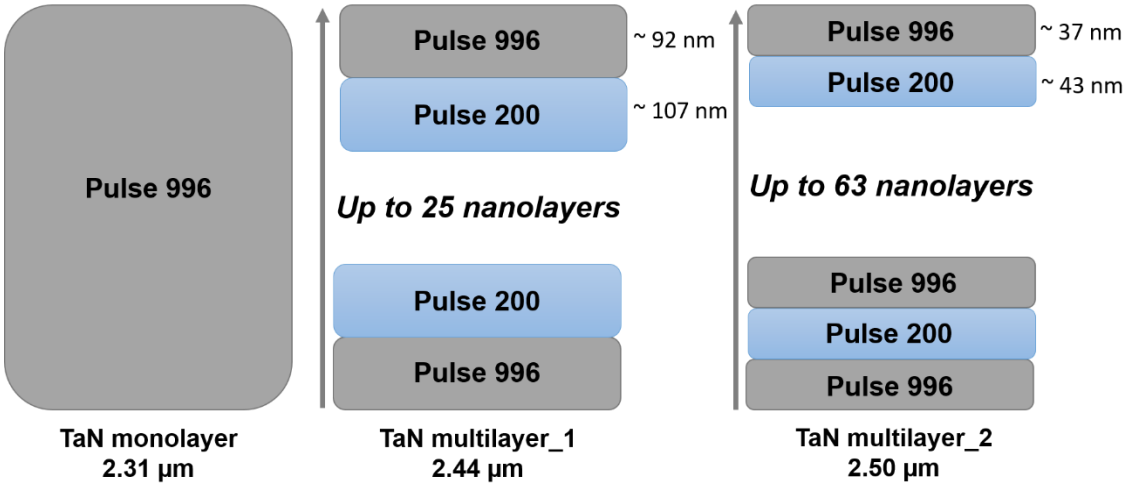


**Fig 5. 6: Schematic theoretical representation of TaN film microstructure**

The chemical composition of the TaN coatings was measured by GD-OES. All TaN film composition analysis reveal around 80 at. % of Ta and 20 at. % of N. Fig 5.7 shows the cross-sectional SEM micrographs of the deposited TaN films. Suppression of columnar growth is observed for all TaN coatings. In order to get a more accurate analysis, TEM micrographs were taken and are shown in Fig 5.8. The breaking down of columnar grains and the grain refinement became more pronounced in the multi pulse MPP films (Fig 5.8b and 5.8c). TEM micrographs reveal completely dense microcrystalline structures characterized by small micro domains and without clear boundaries. These microstructures are promoted by the high metallic ion bombardment of the growing films due to highly ionized MPPMS plasma. High metallic ion bombardment increases the adatom mobility in the growth surface and

induces the densification of the coatings. Thus, MPPMS technology can prevent the typical long columnar grain growth with clear grain boundaries attributed to the films grown by conventional dcMS technique. This is known as a key parameter to ensure a good corrosion response of sputtered films.

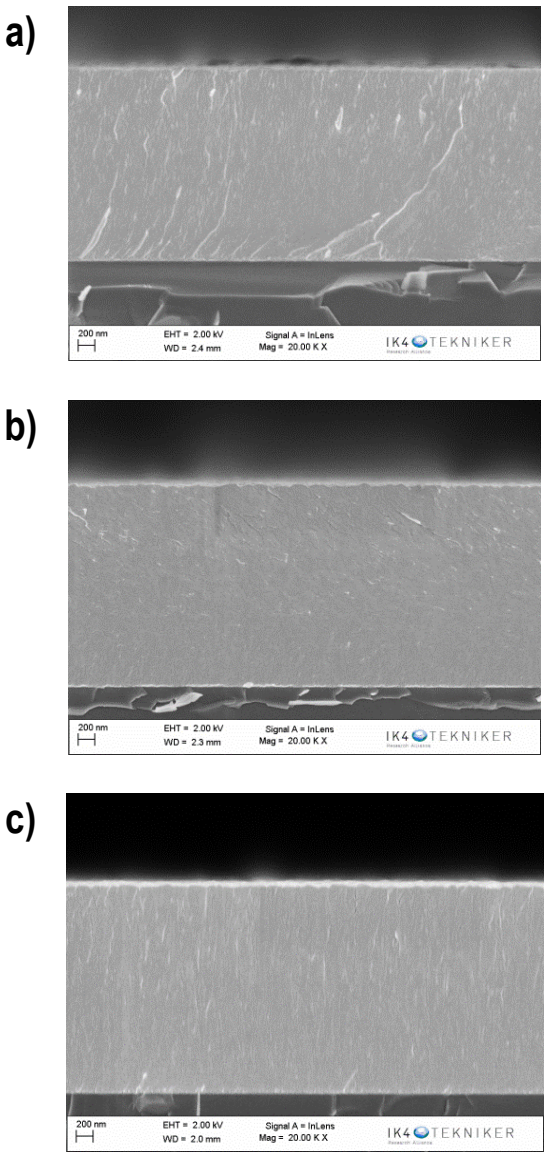


**Fig 5. 7: Cross-sectional SEM micrographs of a) TaN monolayer, b) TaN multilayer_1, and c), TaN multilayer_2 films**

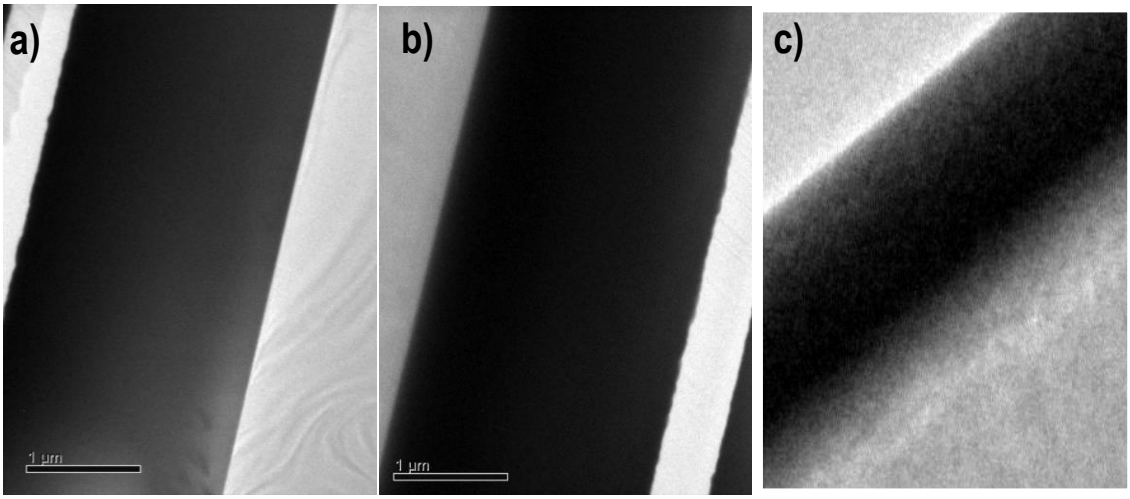


**Fig 5. 8 Cross sectional TEM micrographs a) TaN monolayer, b) TaN multilayer_1, and c), TaN multilayer_2 films**

TEM micrographs taken with a higher magnification from selected areas in Fig. 5.8a-5.8c are shown in Fig. 5.9a-5.9b, respectively, with their corresponding Fast Fourier transform (FTT) to analyse the differences between monolayer and multilayer films (Fig 5.9c and 5.9d). No clear multilayer structure is observed, likely due to the similar composition of nanolayers deposited alternatively by pulse 996 and 200, which hardly can give any contrast to easily detect the interfaces along the film. Nevertheless, the micrographs and FTTs reveal a different microstructure development. Both samples show nano-crystalline TaN structures with small domain sizes of 3-4 nm and <3nm for TaN monolayer and TaN multilayer_2 films, respectively. FTT pattern of TaN monolayer film shown in Fig 5.9c reveals a homogeneous and ordered microstructure which exhibits a diffuse spot pattern that matches well with a face-centered-cubic (fcc) structure and confirms the small size of the microdomains. The FTT pattern of TaN multilayer_2 (Fig 5.9d) evidences a more disordered and heterogeneous microstructure characterized by elongated diffraction maximums implying that crystal domains are oriented at random as typically observed in polycrystalline materials. The FTT image of TaN multilayer_2

exhibits spots that form either 90 or 120 degrees, suggesting the coexistence of hexagonal and cubic TaN crystal phases.

Even though the multilayer structure is not clearly detected, the microstructure modification induced by the multi pulse MPPMS technique application is observed. In this study, a slight variation of nitrogen content is observed between TaN monolayer and TaN multilayer films. SEM analysis also reveals a more pronounced columnar growth suppression during multi pulse MPP technique depositions along with a tendency for developing a heterogeneous microstructure. The crystal structure is also modified during multilayer film deposition which will eventually influence the final properties of the growing films.

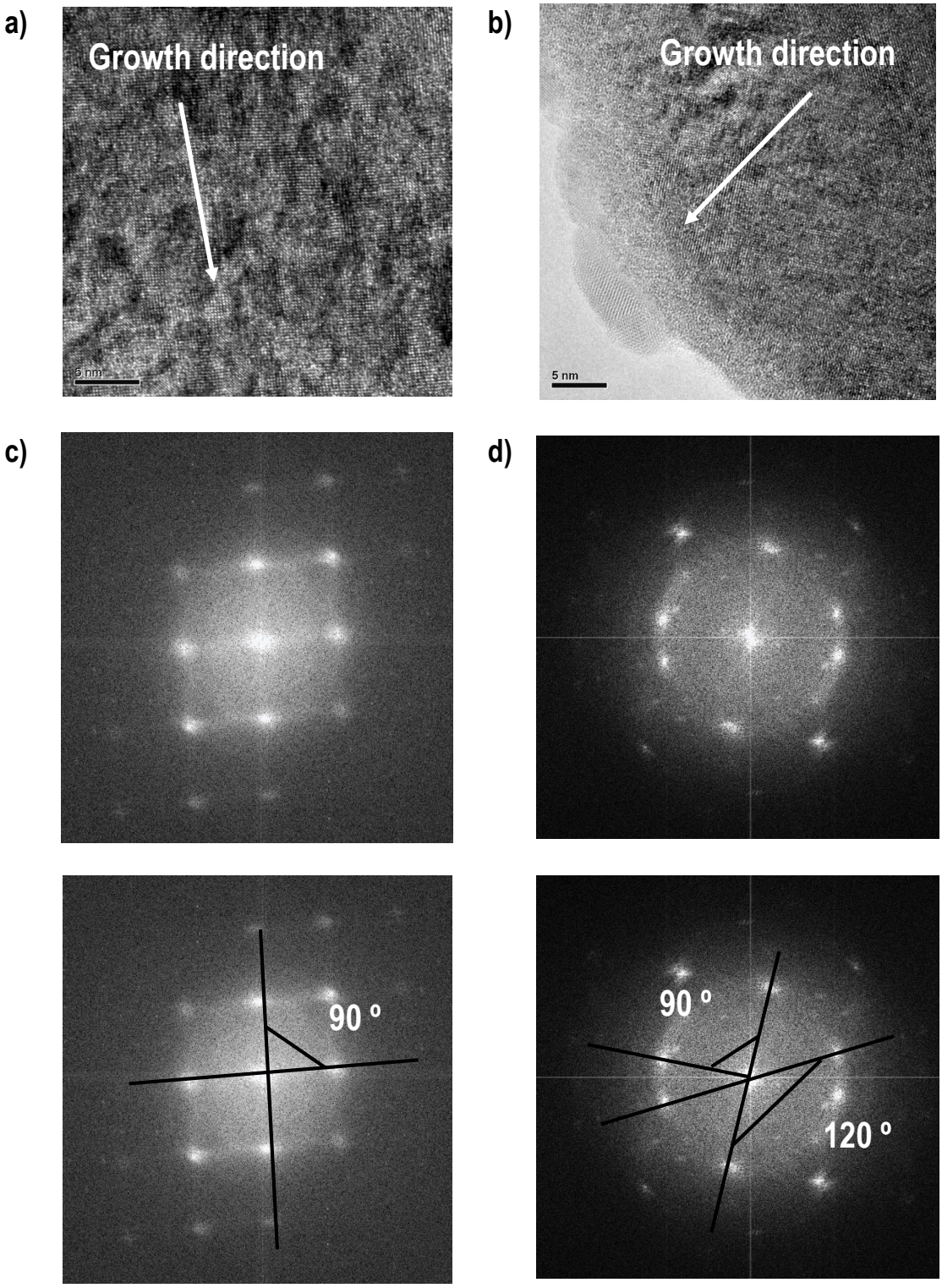


**Fig 5. 9: Cross-sectional TEM micrographs a) TaN monolayer and b) TaN multilayer_2 films and corresponding FTTs for c) TaN monolayer and d)TaN multilayer_2 films at high magnification**

### 3.3.2 Hardness measurements

Table 5.4 shows the hardness values for TaN films deposited during different processes calculating using the method of Oliver and Pharr [82]. The hardness decreases from 16.7 GPa for TaN monolayer film deposited by pulse 1 to 15.81 and 15.27 GPa for TaN multilayer 1 and 2 films, respectively. No significant difference arise from hardness data and surprisingly TaN monolayer film exhibit the highest hardness. It has been documented in the literature that a heterogeneous multilayer film, i.e. made from different materials, can exhibit improved mechanical properties compared to a monolayer structure film [83, 84]. In general, the hardness of multilayer films increases as the bilayer period decreases to an optimized value around 3-10 nm [85]. Contrary to the films studied in the literature, TaN multilayer films analyzed in this study exhibit much larger bilayer periods than the ones known to influence the hardness and their composition is based on a unique material. Thus, the general rule may not be applicable in this case. The slight decrease in hardness observed for TaN multilayer films may be induced by softer nanolayer grown by pulse 2 due to the lower peak current density registered during this plasma discharge. Lower peak current density means lower ion bombardment towards the substrate which is known to reduce the hardness of the growing films [86].

### 3.3.3 Corrosion resistance evolution

Electrochemical Impedance Spectroscopy (EIS) measurements were registered at open circuit potential ($E_{oc}$) after 4 h, 24 h and 168 h of immersion in the PBS+albumin electrolyte in order to assess the corrosion resistance evolution with time in the simulated body fluid for each material. A sinusoidal AC perturbation of 10 mV was applied to the electrode at a frequency range from 100 kHz to 10 mHz with an

amplitude of 10 mV. The interpretation of the Impedance experimental data was based on the equivalent circuit modeling using Autolab software. All potential are referred to Ag/AgCl electrode (0.207 vs SHE). Fig. 5.10 shows the Bode plots for Ti-cp and different TaN coatings.

Ti-cp exhibited a capacitive behavior and elevated polarization resistance, both increasing with immersion time. This is represented by a shift to -90º phase angles when immersion time reaches 168 hours [87]. The enhancement of polarization resistance with time for Ti-cp is due to the formation of a dense and protective $TiO_2$ layer on the top of its surface [88].

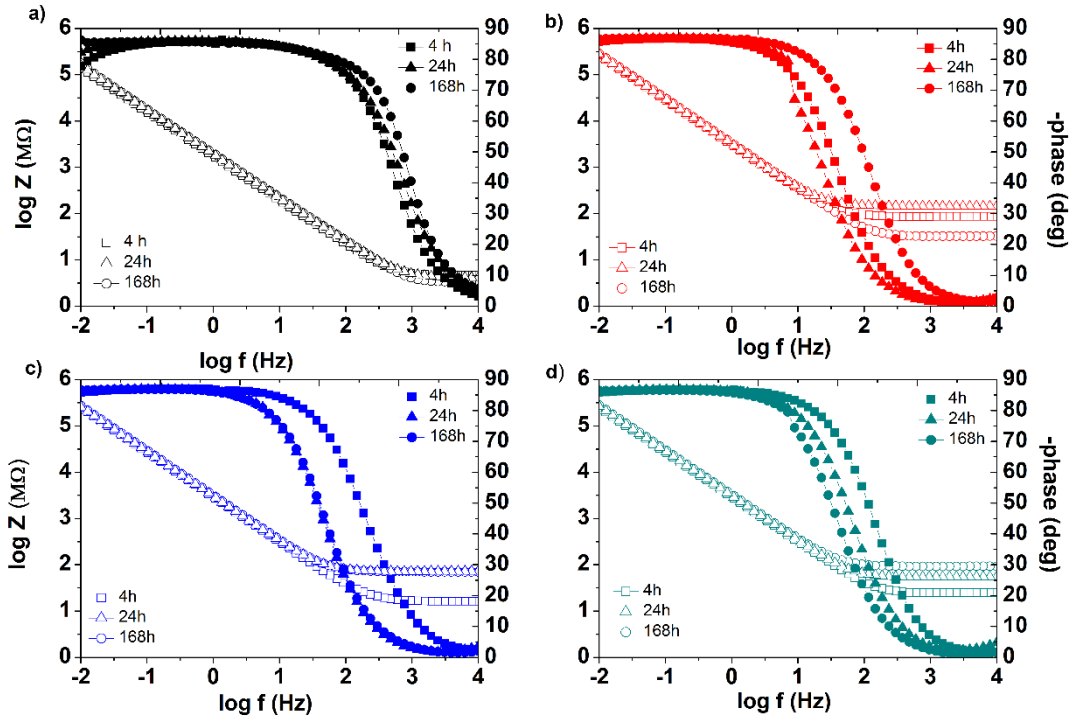


**Fig 5. 10: Bode plots obtained from EIS data at different immersion times for a) Ti-cp, b)TaN monolayer, c)TaN multilayer_1 and d)TaN multilayer_2**

For TaN coatings, impedance diagrams show even higher capacitive behavior and polarization resistance values than for the bare Ti-cp. The phase angle is already -90º for all coatings at 4 h of immersion which is an indicative of a faster oxide film

formation on the top of their surfaces. Such a high polarization resistance for TaN coatings is based on the formation of an impervious stable and firmly adherent film of tantalum pentoxide ($Ta_2O_5$) on the coating surface [89]. The similar behavior observed between TaN monolayer and TaN multilayer coatings is due to the fact that the topmost layer is exactly the same for all of them and it is well known that electrochemical response of the materials is highly dependent on surface characteristics.

For Ti-cp substrate, the best fitting was obtained by the utilization of Randles equivalent circuit shown in Fig 5.11 at all immersion times [87]. When Randles is applied to model an uncoated metal, the CPE and R are defined by double layer capacitance and charge transfer resistance, respectively, as shown in Fig 5.11 a).

The Bode Plots of TaN films are characterized by a unique constant time at all immersion times indicating the absence of substrate contribution in the electrochemical response of these coatings. After different equivalent circuit simulations with all experimental data registered, the best fitting was obtained by using a unique couple of CPE and R representing the coating capacitance and coating resistance, respectively, i.e. the previously mentioned Randles Circuit (Fig 5.11 b).

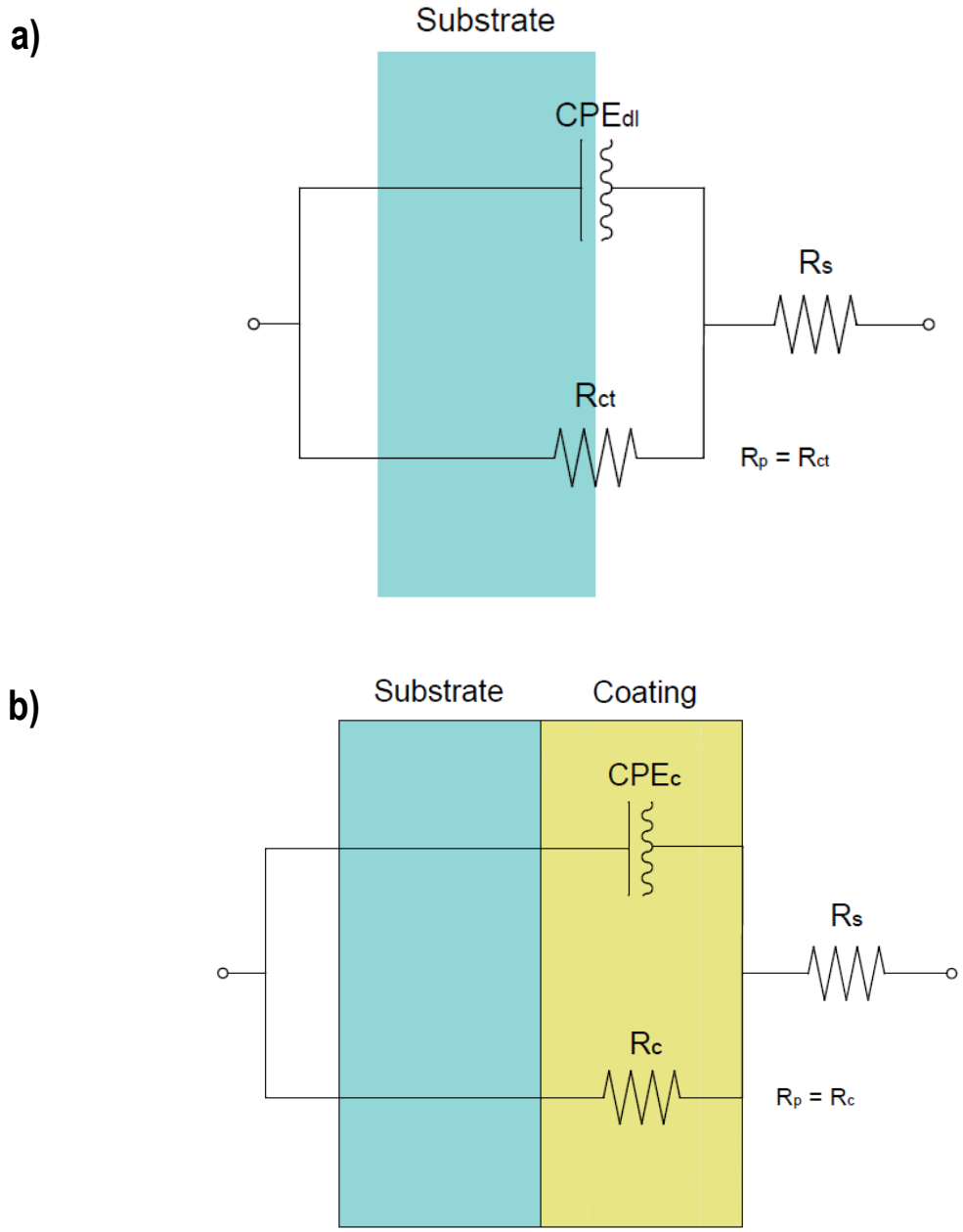


**Fig 5. 11: Randles circuit applied for EIS data modeling**

This suggests that the contribution of the substrate trough the coating pores is either negligible or difficult to detect for the immersion times analyzed. The possible reasons for this can be i) the inhibition of the electrolyte penetration towards the substrate promoted by extremely dense and low-defect TaN film microstructure

developed by MPPMS technology as shown in Fig 5.8, ii) and/or the high polarization resistance of Ti-cp which prevents the quantification of its contribution trough the coating pores. Thus, experimental parameters obtained after fitting processes are displayed in Table 5.5.

| | Time | OCP (V) | $R_s$ ($\Omega cm^2$) | $Y_0$-$CPE_{dl}$ ($\mu Fcm^{-2}$) | n | $R_{ct}=R_p$ ($M\Omega cm^2$) |
|---|---|---|---|---|---|---|
| Ti-cp | 4 h | -0.466 | 4.48 | 64.90 | 0.96 | 0.97 |
| | 24h | -0.407 | 4.08 | 55.00 | 0.96 | 3.15 |
| | 168 h | -0.445 | 3.13 | 54.20 | 0.96 | 17.36 |
| | **Time** | **OCP (V)** | **$R_s$ ($\Omega cm^2$)** | **$Y_0$-$CPE_c$ ($\mu Fcm^{-2}$)** | **n** | **$R_c=R_p$ ($M\Omega cm^2$)** |
| TaN monolayer | 4 h | -0.297 | 86.10 | 3.92 | 0.97 | 9.35 |
| | 24h | -0.299 | 143.30 | 4.030 | 0.97 | 8.40 |
| | 168 h | -0.394 | 32.20 | 36.80 | 0.97 | 17.85 |
| TaN multilayer_1 | 4 h | -0.294 | 16.24 | 41.30 | 0.97 | 10.35 |
| | 24h | -0.352 | 71.30 | 41.50 | 0.97 | 8.90 |
| | 168 h | -0.379 | 70.40 | 38.80 | 0.97 | 20.28 |
| TaN multilayer_2 | 4 h | -0.284 | 24.21 | 41.63 | 0.97 | 8.55 |
| | 24h | -0.274 | 53.90 | 39.90 | 0.97 | 10.13 |
| | 168 h | -0.392 | 92.00 | 36.36 | 0.97 | 21.31 |

**Table 5. 5 EIS data of Ti-cp and TaN coatings obtained by equivalent circuit modelling using Randles circuit at different immersion times**

The polarization resistance ($R_p$) of both Ti-cp substrate and TaN coatings increases with immersion time. It is expected that the protective oxides layers, i.e. $TiO_2$ and $Ta_2O_5$, continuously grow as the time increases up to a steady-state, further enhancing the polarization resistance as it is observed in Fig 5.12.

The low values of Y0-CPE element as well as n values close to 1 are indicative of an almost perfect capacitors.

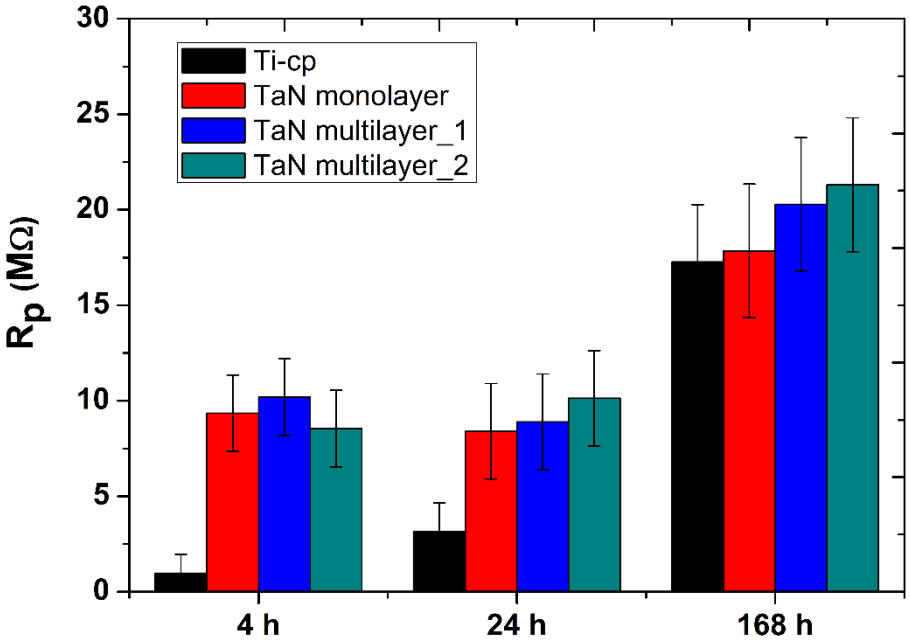


**Fig 5. 12: Evolution of corrosion resistance with time**

TaN films exhibit better response than the bare substrate and all of them are characterized by excellent barrier properties represented by $R_p$ values in the MΩ range in simulated body fluid environment at all immersion times. The measurements registered at short immersion times are related to growth kinetics of the protective oxide film rather than to oxide stability. After 168 h, very similar $R_p$ values are obtained for both Ti-cp and TaN films. Even if slightly higher values are observed for TaN multilayer_2 film, if standard deviation is considered, all TaN films exhibited the same excellent electrochemical behaviour. In fact, these results should be expected, since the topmost layer of all TaN films, both monolayer and multilayer ones, is the same in terms of composition and properties. Therefore, the growth of very similar tantalum oxide surface barrier layer, responsible for the extraordinary inertness and chemical stability of TaN films, occurs.

Potentiodynamic polarization was carried out after 192 h of immersion in PBS+abumin electrolyte (Fig 5.13). The potential range was varied from $E_{oc}$– 0.2 V to $E_{oc}$ + 1.2 V with a scan rate of 0.5 mV/s.

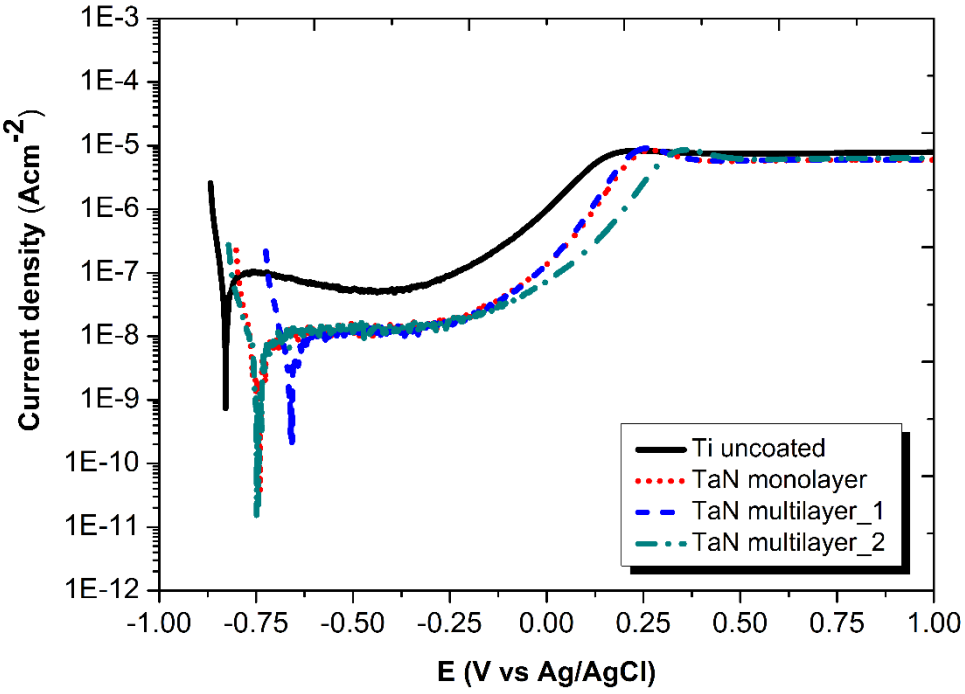


**Fig 5. 13: Potentiodynamic polarization curves obtained for uncoated Ti-cp and TaN films after 192 h of immersion in PBS+albumin solution**

TaN coated Ti samples exhibit higher corrosion potentials ($E_{corr}$) than the uncoated Ti-cp, indicating the more passive character of TaN. The corrosion current density of Ti-cp was one order of magnitude higher than the TaN coated samples, confirming the enhancement of corrosion resistance of Ti-cp substrate by the application of any of $TaN_x$ films (monolayer or multilayer structure films). At potentials around 0.1-0.2 V, the corrosion current value of all tested samples stops at 10 μA $cm^{-2}$ and remains stable up to the end of the test (1 V). These low corrosion currents along the whole polarization test are an indicative of passive behaviour of both Ti-cp and TaN

coatings. The very similar passive features of all TaN films confirm the comparable corrosion resistance of monolayer TaN and multilayer TaN coatings.

### 3.3.4. Tribocorrosion performance

The tribocorrosion performance of Ti-cp and TaN coatings was evaluated following the procedure described in section 3.2. The evolution of the open circuit potential ($E_{oc}$) of Ti-cp and TaN coatings was monitored before, during and after sliding process (Wear test 1) in PBS+albumin electrolyte and it is shown in Fig 5.14.

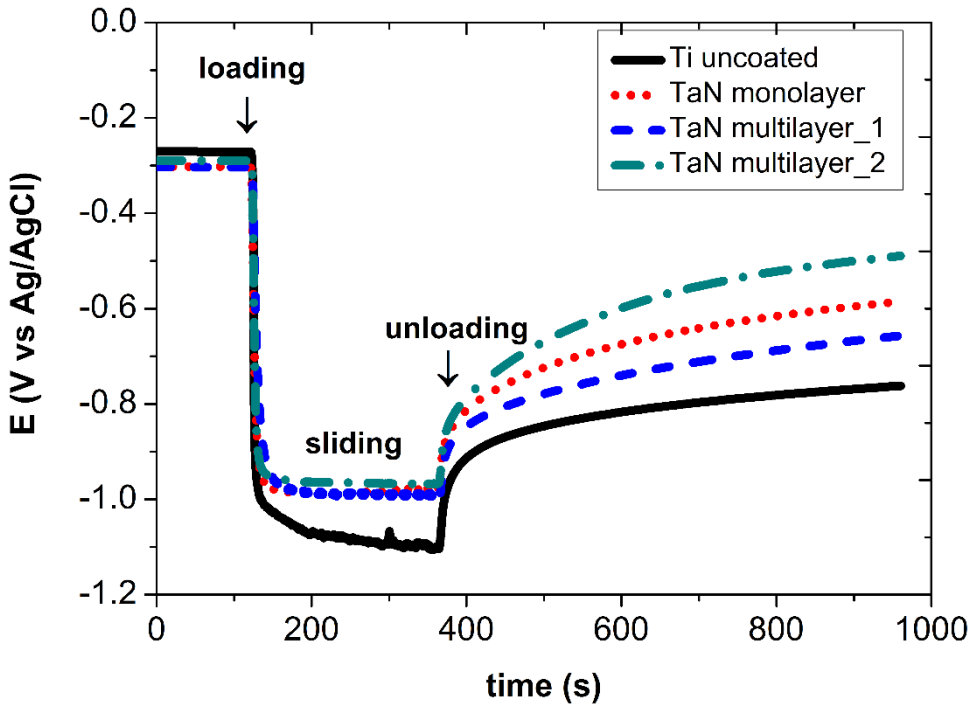


**Fig 5. 14: Evolution of open circuit potential (Eoc) before, during and after sliding**

Before the wear tests were carried out, the Ti-cp potential was slightly higher than the potentials of TaN coatings. Once the sliding starts, the potentials of both Ti-cp and TaN coatings decreased to a more negative values indicating the total or partial removal of their passive oxide surface layer. The potential of Ti-cp decreased from -

0.27 V to -1.07 V once the load is applied and kept decreasing as the number of cycles increased. This fact indicates that the active area (wear track size) exposed to the corrosive environment due to the elimination of surface protective layer continuously grows, negatively affecting both the electrochemical and tribological response of the substrate material. After 400 cycles, the alumina ball was unloaded and the potential raised to more positive values although it did not reach the highly stable initial value. The potential evolution of TaN coatings differed from the substrate one. The potential also decreased when the load was applied, but in these cases, the potentials were not as low as for Ti-cp. Anyhow, the removal of the protective passive layer also occurred in coated surfaces. The achieved values of the potential during sliding were similar for all coatings, varying from -0.96 V to -0.98 V for TaN multilayer_2 and the other ones, respectively. During sliding all potentials remained stable indicating that the active surface area of the TaN coatings exposed to the electrolyte was also constant in size during the wear test. Once the alumina ball was removed, the potentials of coated samples increased to more positive values faster than the substrate potential. After 10 minutes, an almost constant potential was reached in all coated samples indicating that the surface repassivation phenomena occurred on the wear track area. The potential values registered 10 minutes after the end of the sliding were around -0.62 V for TaN monolayer, -0.7 V for TaN multilayer_1 and -0.5 V for TaN multilayer_2 coatings. Hence, the re-passivation phenomena of the worn surface occurs faster for the latter coating.

Fig 5.15 and Fig 5.16 show the Nyquist and Bode plots, respectively, before and during sliding (Wear test 2) for Ti-cp and TaN coatings. The high difference between the electrochemical response of the samples before and during sliding, confirms the great influence of tribological processes on the electrochemical response of the materials. It must be considered that the higher the diameter of the semi-circle in the Nyquist diagram and the broader the range of frequencies showing phase angles

values near to -90º in Bode diagram, the higher the polarization resistance of the material will be [90, 91].

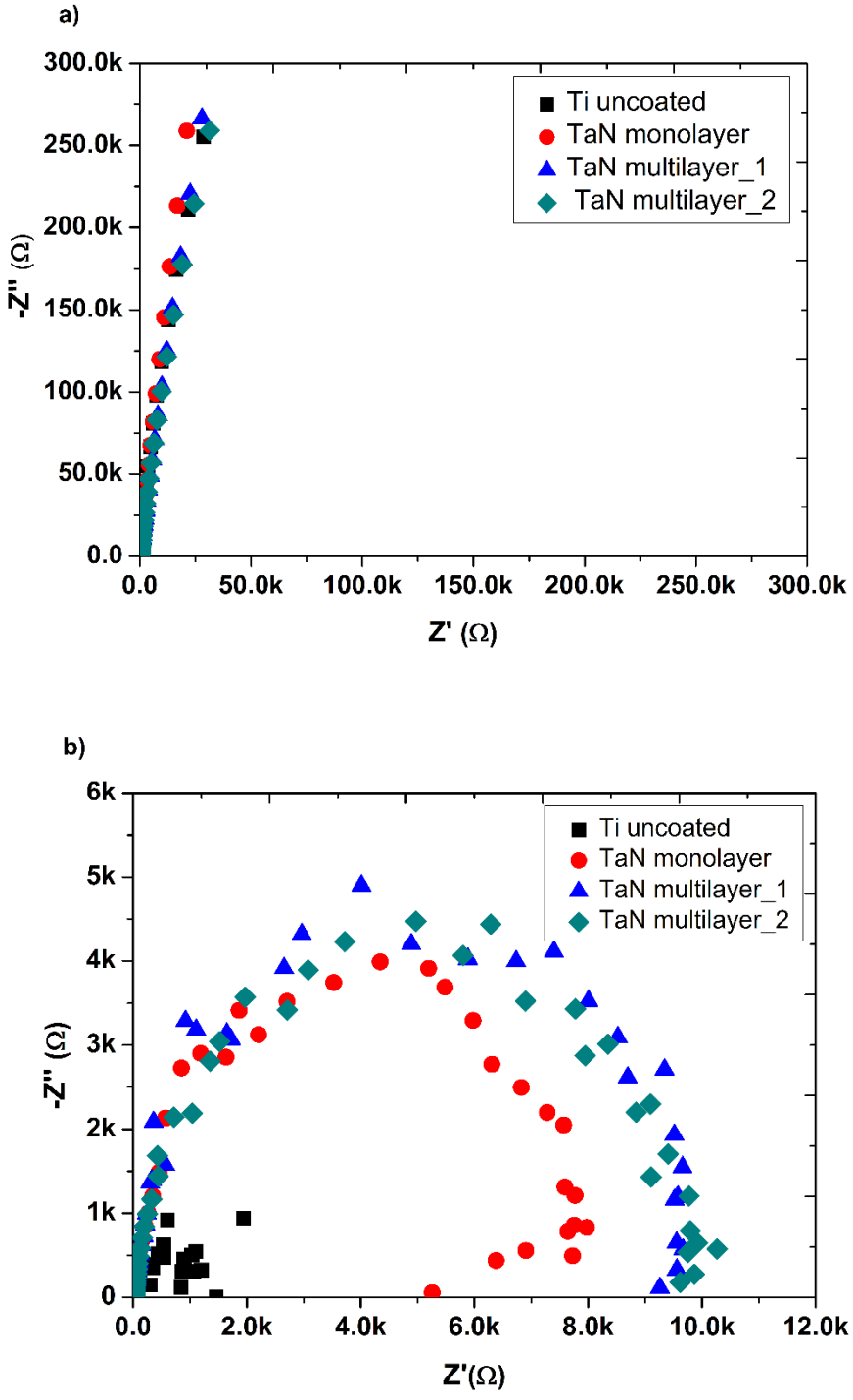


**Fig 5. 15: Nyquist plots obtained from EIS data a) before and b) during sliding**

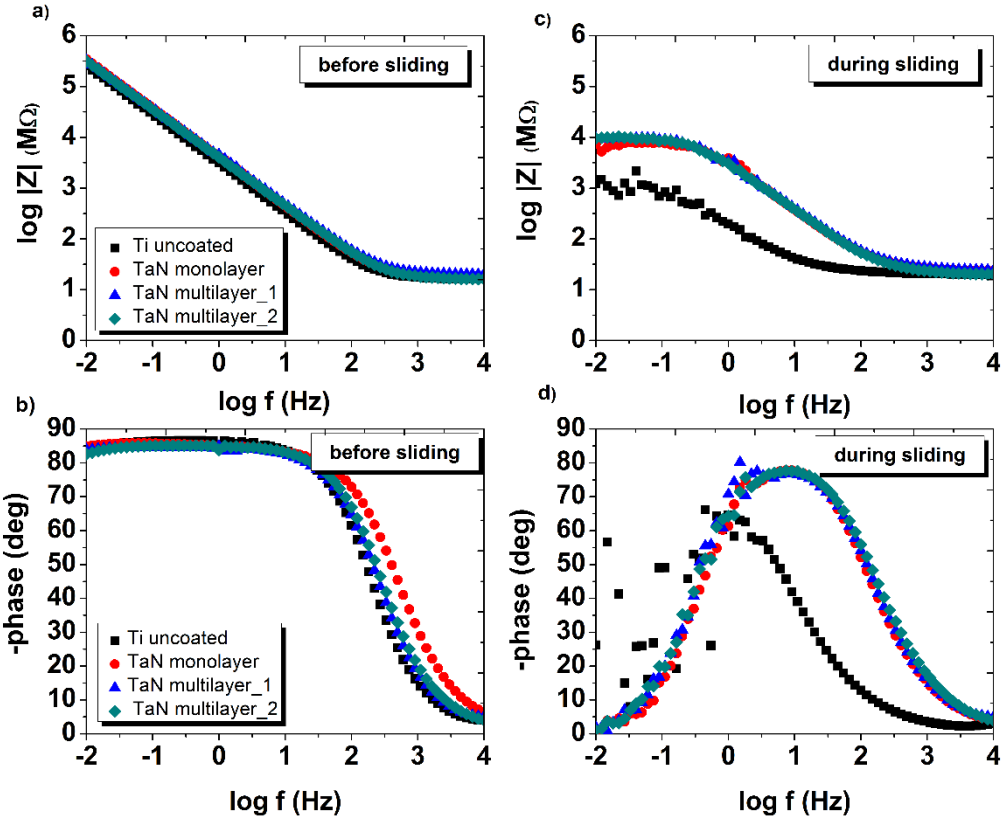


**Fig 5. 16 Bode plots obtained from EIS data before a), b) and during c), d) sliding**

Experimental data obtained before and during sliding of both Ti-cp and TaN coatings were fitted using the simple Randles circuit (Fig 5.11) already explained in previous section 3.3.3. This data is shown in Table 5.6.

| | Time | OCP (V) | $R_s$ (Ω) | $Y_0$-$CPE_{dl}$ (μF $cm^{-2}$ ) | n | $R_{ct}=R_p$ (kΩ $cm^2$ ) |
|---|---|---|---|---|---|---|
| **Ti-cp** | before | -0.27 | 16.57 | 59.55 | 0.96 | 5470 |
| | during | -1.07 | 20.61 | 1278 | 0.79 | 1.22 |
| | **Time** | **OCP (V)** | **$R_s$ (Ω)** | **$Y_0$-$CPE_c$ (μF $cm^{-2}$)** | **n** | **$R_c=R_p$ (kΩ $cm^2$)** |
| **TaN monolayer** | before | -0.30 | 10.30 | 37.08 | 0.95 | 19870 |
| | during | -0.98 | 15.97 | 56.85 | 0.90 | 7.56 |
| **TaN multilayer_1** | before | -0.28 | 20.36 | 41.72 | 0.93 | 20360 |
| | during | -0.97 | 25.44 | 57.74 | 0.92 | 10.03 |
| **TaN multilayer_2** | before | -0.29 | 17.88 | 43.05 | 0.95 | 16530 |
| | during | -0.96 | 21.06 | 60.40 | 0.91 | 10.07 |

**Table 5. 6: EIS data of Ti-cp and TaN coatings before and during sliding obtained by equivalent circuit modeling using Randles Circuit**

In both coated and uncoated surfaces, polarization resistance considerably decreases as a consequence of the wear process. Before sliding, Ti-cp and TaN coatings exhibit passive behavior characterized by extremely high polarization resistances in the range of the MΩ and pure capacitive behaviors with phase angle very close to -90˚ throughout the entire range of frequencies. No remarkable improvements could be observed by the application of the TaN coatings, since Ti-cp electrochemical response was already good enough in PBS+albumin media. However, during sliding, the worn surface area of all samples was maintained in an active state along the whole test due to the specific load and rotational speed deliberately selected for preventing the repassivation phenomena to occur on the worn surface during sliding and hence, enabling the comparison between different materials. This active behavior was clearly represented by the narrowing of the maximum amplitude and the phase angle shift towards lower values at low-medium frequencies during sliding in Bode plots (Fig 5.15). Moreover, higher capacitance (CPE) and lower polarization resistance ($R_p$) values were observed during sliding for both Ti-cp and TaN coatings, an additional indicative of the active state of their wear tracks. Nevertheless, the polarization resistance of the TaN coated samples was still

one order of magnitude higher than Ti-cp. The much bigger active area of Ti-cp compared to TaN coatings exposed to the corrosive media due to the wear processes was responsible for this behavior, since the total polarization resistance of the materials was the sum of the resistance inside the wear track (active area) plus the resistance outside the wear track (passive area).

Friction coefficients measured during the second sliding process of 2600 cycles for all surfaces are displayed in Fig. 5.17.

The deposition of all TaN coatings reduced friction coefficient of the bare substrate, i.e. 0.58, as it was expected considering the poor mechanical properties of Ti-cp. Contrary to electrochemical response, the tribological response between TaN films is rather different. The TaN multilayer_2 film, characterized by lowest hardness value exhibited a coefficient of friction around 0.4, while TaN monolayer and TaN multilayer_1 coatings showed similar friction coefficients of 0.25.

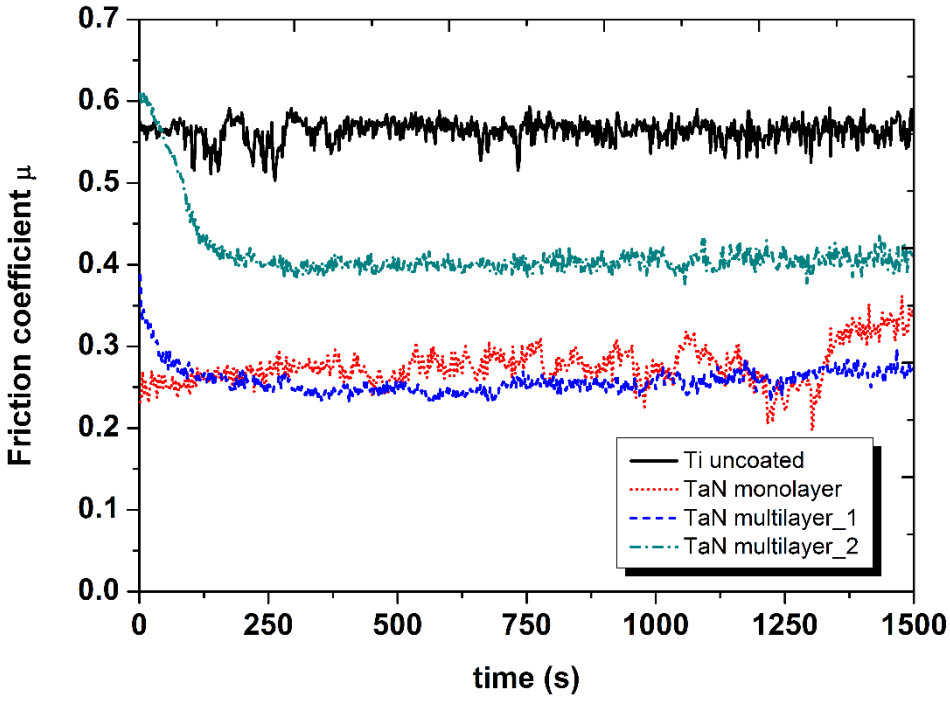


**Fig 5. 17: Friction coefficient monitored during Wear test 2 (2600 cycles)**

Table 5.7 shows the measured width and depth of the wear tracks calculated from confocal inspection of the wear tracks cross section. The TaN multilayer_2 wear scar is deeper than the other two coatings. The presence of a greater contact area during sliding increases the friction coefficient of this film.

| | Depth (µm) | Width (µm) |
|---|---|---|
| **Ti uncoated** | 13.310 | 1360.00 |
| **TaN monolayer** | 0.450 | 160.35 |
| **TaN multilayer_1** | 0.380 | 167.99 |
| **TaN multilayer_2** | 0.520 | 160.66 |

**Table 5. 7: Depth and width of the wear track of Ti-cp and TaN coatings after tribocorrosion tests**

The wear track for Ti-cp was 10 times deeper and wider than for TaN coatings, confirming the enhancement of tribological response of Ti-cp by the application of these particular TaN protective coatings. The big difference between the wear tracks can be observed in Fig 5.18, where the tracks of TaN coatings are barely appreciable while Ti-cp wear scar is huge. The wear depth of multilayer TaN_2 was deeper compared to the wear track of the other TaN coatings and small evidences of abrasive scars were observed. The lower hardness and higher coefficient of friction of this coating were responsible for this behavior which after all, lead to worse tribological response of TaN multilayer_2 coating.

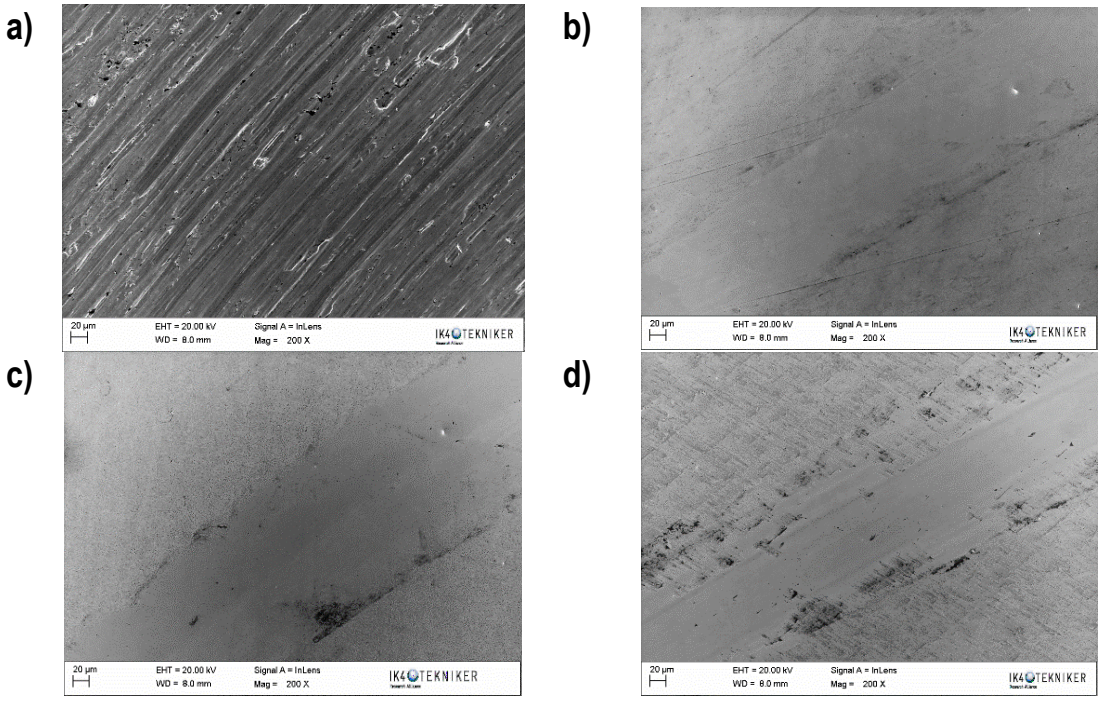


**Fig 5. 18: SEM images of wear tracks after tribocorrosion tests for a) Ti-cp, b) TaN monolayer, c) TaN multilayer_1 and d) TaN multilayer_2**

The total material loss of each material after tribocorrosion tests is calculated from measured wear tracks (Table 5.7) using equations [5.12], [5.13] and [5.14]. The width and depth of the wear track correspond to parameter a and b, respectively, already defined in Section 3.2. The total material loss after tribocorrosion for each tested sample is shown in Table 5.8.

| | a (mm) | b ($x10^{-3}$ mm) | r (mm) | $W_{tr}$ ($x10^{-3}$ $mm^3$) |
|---|---|---|---|---|
| **Ti uncoated** | 1.360 | 13.31 | 5 | 464.45 |
| **TaN monolayer** | 0.160 | 0.45 | 5 | 1.97 |
| **TaN multilayer_1** | 0.167 | 0.38 | 5 | 1.55 |
| **TaN multilayer_2** | 0.160 | 0.52 | 5 | 2.00 |

**Table 5. 8: Total material loss measured after tribocorrosion tests for Ti-cp and TaN coatings**

Fig 5.19 exhibits the comparison between the total material loss due to tribocorrosion processes of Ti-cp and TaN coatings. The differences of tribocorrosion damage are strong between the coated and uncoated surfaces. All tested TaN coatings reduced the total material loss of Ti-cp due to tribocorrosion phenomena in ~ 90%. Comparing separately the TaN coatings performance, the material loss after tribocorrosion is almost equal for all tested coated samples. TaN multilayer_1 might exhibit a slightly better tribocorrosion resistance than TaN monolayer and TaN_multilayer 2.

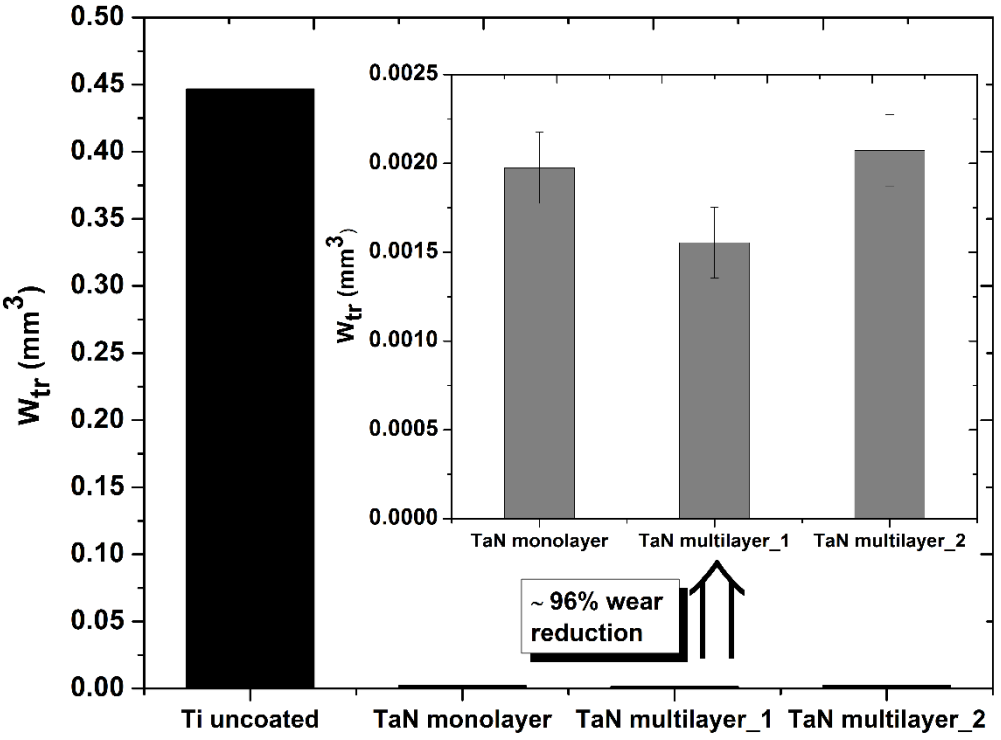


**Fig 5. 19: Determined total material loss (Wtr) from wear tracks volume after tribocorrosion tests**

In a simplified approach, it was considered that the total material loss due to tribocorrosion is occasioned by the sum of two different degradation mechanisms; namely, electrochemical corrosion and mechanical process. This approach does not take into account the synergistic factors that influence on the pure electrochemical or mechanical degradation. Then, the corrosion contribution ($W_c$) to the total material

loss ($W_{tr}$) could be determined by the equation [5.16] accurately described in Section 3.2.

$$W_c = i_{act} A_{act} \frac{M}{nFd} N t_{lat} \quad [5.16]$$

While $i_{act}$, $A_{act}$, N and $t_{lat}$ are obtained from the experimental EIS measurements and testing conditions; M, d and n are intrinsic properties of Ti-cp and TaN coatings.

From testing conditions, N and $t_{lat}$ are obtained. The total number of cycles, N, is the sum of the cycles performed during Wear test 1 and Wear test 2; i.e. 3000 and $t_{lat}$, the period between two successive cycles, is 0.6 seconds.

$A_{act}$ and $i_{act}$ are calculated from measurements registered during EIS analysis and using the equations [5.9], [5.10] and [5.11].

$$A_{act} = a \times 2\pi r$$

$$i_{act} = \frac{B}{r_{act}} = B \times \frac{r_{pass} - R_{ps}(A_0 - A_{act})}{A_{act} R_{ps} r_{pass}}$$

The calculations are shown in Table 5.9, considering B and $A_0$ constants for all tested samples.

B = 0.024 V; $A_0$ = 2.54 $cm^2$

| | $A_{act}$ ($cm^2$) | $R_p$ (Ω) | $R_{ps}$ (Ω) | $R_{pass}$ (Ω) | $r_{pass}$ (Ω $cm^2$) | $r_{act}$ (Ω $cm^2$) | $i_{act}$ (A $cm^{-2}$) |
|---|---|---|---|---|---|---|---|
| **Ti uncoated** | 4,30E-01 | 5,36E+06 | 1280 | 6,45E+06 | 1,36E+07 | 5,5E+02 | 4,3E-05 |
| **TaN monolayer** | 5,04E-02 | 1,99E+07 | 7560 | 2,03E+07 | 5,06E+07 | 3,8E+02 | 6,3E-05 |
| **TaN multilayer_1** | 5,28E-02 | 2,04E+07 | 10000 | 2,08E+07 | 5,18E+07 | 5,3E+02 | 4,5E-05 |
| **TaN multilayer_2** | 5,05E-02 | 8,42E+06 | 10070 | 8,59E+06 | 2,14E+07 | 5,1E+02 | 4,7E-05 |

**Table 5. 9: Experimental parameters obtained during testing to calculate material loss due to corrosion mechanism**

The intrinsic parameters for Ti-cp and TaN coatings are summarized in Table 5.10. **M** and **d** are molecular weight and density of the tested materials, while n is the number of the electrons involved in the anodic reaction occurring on the sample surface.

For Ti-cp the anodic reaction is:

$$Ti + 2\,H_2O \rightarrow TiO_2 + 2H^+ + 2e^- \quad [5.18]$$

For TaN the anodic reaction is:

$$2\,TaN + 5H_2O \rightarrow Ta_2O_5 + N_2 + 5H^+ + 5e^- \quad [5.19]$$

| Material | M (g mol$^{-1}$) | d (g cm$^{-3}$) | n |
|---|---|---|---|
| **Ti-cp** | 47.9 | 4.5 | 2 |
| **TaN** | 147.56 | 14.3 | 5 |

**Table 5. 10: Intrinsic parameters of tested materials**

The mechanical contribution to the total material loss ($W_m$) could be obtained by subtracting the material loss due to electrochemical effect ($W_c$) to the total material loss ($W_{tr}$). The detailed contribution from each degradation mechanism to the total material loss is shown in Table 5.11.

| | $W_{tr}$ (x10$^{-3}$ mm$^3$) | $W_c$ (x10$^{-5}$ mm$^3$) | $W_m$ (x10$^{-3}$ mm$^3$) |
|---|---|---|---|
| Ti uncoated | 464.45 | 185.84 | 462.6 |
| TaN monolayer | 1.97 | 12.21 | 1.85 |
| TaN multilayer_1 | 1.55 | 9.2 | 1.46 |
| TaN multilayer_2 | 2.00 | 9.16 | 1.98 |

**Table 5. 11: Total material loss (Wtr), material loss caused by electrochemical corrosion (Wc) and material loss caused by mechanical degradation (Wm) after tribocorrosion tests**

The main contribution to the total material loss for Ti-cp and TaN coatings was due to the mechanical effect rather than electrochemical corrosion degradation. Nevertheless, the action of the wear process also compromised the good electrochemical performance of the materials since the corrosion resistance was three orders of magnitude lower when sliding process took place (Table 5.6). It is difficult to make a comparative evaluation of TaN films, since they show similar results after tribocorrosion. The main difference among them is caused by mechanical degradation processes, where TaN multilayer_1 exhibits lower material loss compared to the other TaN films. Multilayer structure of TaN multilayer_1 and lower coefficient of friction (Fig 5.17) shown by this film compared to TaN_multilayer 2 film, might lead to a slightly better tribocorrosion performance of TaN multilayer_1 coating.

In fact, more severe wear tests (loads higher than 3N) are needed to induce greater degradation of TaN coatings. These tests would give more information about significant differences among TaN film performance. But higher loads could not be applied on this study due to the complete degradation of Ti-cp. The wear track and total materials loss was not measurable at higher loads and hence it was impossible to compare with TaN coatings.

## 4. Conclusions

Three different TaN coatings were deposited by MPPMS technology to protect pure titanium (Ti-cp) substrates against tribocorrosion phenomena in simulated body fluids. Two different multilayer TaN films characterized by different bilayer periods were developed by alternatively switching two different MPP pulses within one overall

deposition process. A monolayer TaN film was also deposited by the application of a single MPP pulse.

The microstructural analysis of the TaN films revealed extremely dense microstructures and suppression of columnar growth for all deposited samples confirming the importance of highly ionized plasmas developed during MPPMS discharges on the densification of the films. TEM micrographs and FTT patterns evidenced the transformation from predominant cubic crystal phase in TaN monolayer film to a mixture of cubic and hexagonal phases in TaN multilayer films.

The polarization resistance of Ti-cp and TaN coatings in the absence of sliding was incredibly high (~MΩ) and increased with time. TaN coatings exhibited comparable electrochemical responses and slightly enhanced the Ti-cp resistance. The topmost layer of monolayer TaN and multilayer TaN films is exactly the same, leading to the growth of similar surface barrier tantalum oxides which are responsible for the similar polarization resistance values exhibited by TaN coatings.

During sliding processes, the polarization resistance of Ti-cp decreased up to 1 kΩ $cm^2$ and TaN coatings exhibit one order of magnitude higher resistance values than Ti-cp. This is attributed to the higher wear track of Ti-cp during sliding compared to TaN coated Ti-cp, since the total polarization resistance is the sum of polarization resistance outside the wear track (passive material) and inside the wear track (active material where passive film is broken).

The coefficient of friction of Ti-cp was reduced from 0.58 to 0.25 by TaN monolayer and TaN multilayer_1 coating application. The wear rate of Ti-cp was considerably reduced and total material loss caused by tribocorrosion decrease in 90 % by the application of any of TaN coatings developed in this study. More severe tribocorrosion tests need to be applied in order to observe significant differences between monolayer and multilayer TaN films.

In order to accurately compare TaN coated Ti-cp (monolayer and multilayer structure films) with uncoated Ti-cp performance, electrochemical and mechanical features measured in this work during tribocorrosion testing are summarized in the following table 5.12.

| **Electrochemical properties** | | | | |
|---|---|---|---|---|
| **Samples** | **Time** | **Polarization resistance (kΩ cm²)** | | |
| **Ti-cp** | before sliding | 5470 | | |
| | during sliding | 1.22 | | |
| **TaN monolayer** | before sliding | 19870 | | |
| | during sliding | 7.56 | | |
| **TaN multilayer_1** | before sliding | 20360 | | |
| | during sliding | 10.03 | | |
| **TaN multilayer_2** | before sliding | 16530 | | |
| | during sliding | 10.07 | | |
| **Mechanical properties** | | | | |
| | **Friction coefficient** | **Wear** | | **$W_{tr}$ (x $10^{-3}$ $mm^3$)** |
| | | **Depth (μm)** | **Width (μm)** | |
| **Ti-cp** | 0.58 | 13.310 | 1360.00 | 464.45 |
| **TaN monolayer** | 0.25 | 0.450 | 160.35 | 1.97 |
| **TaN multilayer_1** | 0.25 | 0.380 | 167.99 | 1.55 |
| **TaN multilayer_2** | 0.4 | 0.520 | 160.66 | 2.00 |

**Table 5. 12 Electrochemical and mechanical features measured for TaN coatings and uncoated Ti-cp during tribocorrosion testing**

# 5. References

[1] N. R. Patel, P. P. Gohil, A review on biomaterials: Scope, Applications & Human Anatomy Significance, International Journal of Emerging Technologies and Advanced Engineering 2 (2012)

[2] J.B. Park, R.S. Lakes, Biomaterials: An Introduction, Springer, New York, 2007.

[3] H. Hermawan, D. Ramdan, J. R. P. Djuansjah (2011). Metals for Biomedical Applications, Biomedical Engineering - From Theory to Applications, Prof. Reza Fazel (Ed.), ISBN: 978-953-307-637-9, InTech, Available from: http://www.intechopen.com/books/biomedical-engineering-from-theory-toapplications/metals-for-biomedical-applications

[4] A. Arsiwala, P. Desai, V. Patravale, Recent advances in micro/nanoscale biomedical implants, Journal of Controlled Release 189 (2014) 25–45

[5] Q. Chen, G. A. Thouas, Metallic implant biomaterials, Materials Science and Engineering R 87 (2015) 1–57

[6] M. Niinomi, M. Nakai, J. Hieda, Development of new metallic alloys for biomedical applications, Acta Biomaterialia 8 (2012) 3888- 3903

[7] M. Niinomi, Recent metallic materials for biomedical applications. Metal Mater Trans A 33 (2002) 477–86.

[8] K. Wang, The use of titanium for medical applications in the USA. Mater Sci A 213 (1997) 134

[9] A.D. Mazzocca, J.P. De Angelis, A.E. Caputo, B.D. Browner, J.W. Mast, M.W. Mendes, Principles of internal fixation, in: B.D. Browner (Ed.), Skeletal Trauma, W.B. Saunders Company, Philadelphia, 2008.

[10] Metallic materials, J.R. Davies (Ed.), Handbook of Materials for Medical Devices, ASM International, Materials Park, Ohio, 2003, pp. 21–50.

[11] S.S.M. Tavares, F.B. Mainier, F. Zimmerman, R. Freitas, C.M.I. Ajus, Characterization of prematurely failed stainless steel orthopedic implants, Eng. Fail. Anal. 17 (2010) 1246–1253.

[12] U.K. Mudali, T.M. Sridhar, B. Raj, Corrosion of bio implants, Sadhana 28 (2003) 601–637.

[13] U.K. Mudali, T.M. Sridhar, N. Eliaz, B. Raj, Failures of Stainless Steel Orthopedic Devices - Causes and Remedies, Corros. Rev. 21 (2003) 231–267.

[14] A.F. Kamath, P.B. Voleti, T.W.B. Kim, J.P. Garino, G.-C. Lee, Impaction Bone Grafting With Proximal and Distal Femoral Arthroplasty, J. Arthroplast. 26 (2011) 1520–1526.

[15] IARC, On the Evalution of Carcinogenic Risks to Humans: Surgical Implants and Other Foreign Bodies, IARC, Lyon, 1999.

[16] M. Geetha, A.K. Singh, R. Asokamani, A.K. Gogia, Ti based biomaterials, the ultimate choice for orthopaedic implants – A review, Progress in Materials Science 54 (2009) 397–425.

[17] R.S. Kirby, S.R. Heard, P. Miller, I. Eardley, S. Holmes, J. Valve, J. Urol. 148 (1992) 1192–1195.

[18] K. Machara, K. Doi, T. Matsushita, Y. Susaki, Application of Vanadium-Free Titanium Alloys to Artificial Hip Joints, Mater. Trans. 43 (2002) 2936–2942.

[19] R.J. Narayan, C. Boehlert, Advanced Processing of biomaterials, Mat. Sci. Eng. C 28 (2008) 321-322

[20] M. Niinomi, Biologically and Mechanically Biocompatible Titanium Alloys, Mater. Trans. 49 (2008) 2170–2178.

[21] M. Niinomi, Recent metallic materials for biomedical applications Metall. Mater. Trans. A 33 (2002) 477–486.

[22] D.A. Basketter, G. Briaticovangosa, W. Kaestner,C. Lally , W.J. Bontinck, Nickel, cobalt and chromium in consumer products: a role in allergic contactdermatitis. Contact Dermatitis 28 (1993) 15–25.

[23] P.J. Uggowitzer, W-F. Bähre, M.O. Speidel, Metal injection moulding of nickel free stainless steels. Adv Powder Metall Part Mater 3 (1997) 113–21

[24] S.J. Stohs, D. Bagchi, Oxidative mechanisms in the toxicity of metal-ions. Free Radic Biol Med 18 (1995) 321–36.

[25] S.S. Tower, Arthroprosthetic Cobaltism: Neurological and Cardiac Manifestations in Two Patients with Metal-on-Metal Arthroplasty, J. Bone Joint Surg. Am. 92A (2010) 2847–2851.

[26] J. Alvarado, Biomechanics of Hip and Knee Prostheses, in: Applications of Engineering Mechanics in Medicine, GED – University of Puerto Rico Mayaguez, 2003.

[27] J.J. Ramsden, D.M. Allen, D.J. Stephenson, J.R. Alcock, G.N. Peggs, G. Fuller, G. Goch, The Design and Manufacture of Biomedical Surfaces, CIRP Ann. Manuf. Technol. 56 (2007) 687–711.

[28] Y. Li, C. Yang, H. Zhao, S. Qu, X. Li, Y. Li, New Developments of Ti-Based Alloys for Biomedical Applications, Materials 7 (2014) 1709-1800

[29] S. Nag, R. Banerjee, H.L. Fraser, Microstructural evolution and strengthening mechanisms in Ti–Nb–Zr–Ta, Ti–Mo–Zr–Fe and Ti–15Mo biocompatible alloys, Mater Sci Eng C 25 (2005) 357–62.

[30] E. Eisenbarth, D. Velten, M. Muller, R. Thull, J. Breme, Biocompatibility of beta-stabilizing elements of titanium alloys, Biomaterials 25 (2004) 5705–13.

[31] G. Lutjering, J.C. Williams, Titanium, Springer, Berlin, 2007.

[32] A.J. Hart, P.D. Quinn, B. Sampson, A. Sandson, K.D. Atkinson, J.A. Skinner,J.J. Powell, J.F.W. Mosselmans, The chemical form of metallic debris in tissues surrounding metal-on-metal hips with unexplained failure, Acta Biomater. 6 (2010) 4439–4446.

[33] A. Sargeant, T. Goswami, Hip implants – Paper VI – Ion concentrations, Mater. Des. 28 (2007) 155–171.

[34] T. Schmitz, F. Warmuth, E. Werner, C. Hertl, J. Groll, U. Gbureck, C. Moseke,

PhysicalandchemicalcharacterizationofAg-dopedTicoatingsproducedby magnetron sputtering of modular targets, Mater. Sci. Eng. C 44 (2014) 126–131.

[35] J. Hesketh, Q. Meng, D. Dowson, A. Neville, Biotribocorrosion of metal-on-metal hip replacements: How surface degradation can influence metal ion formation, Tribol. Int. 65 (2013) 128–137.

[36] P.J. Uggowitzer, R. Magdowski, M.O. Speidel, Nickel free high nitrogen austenitic steels. ISIJ 36 (1996) 901–8.

[37] A. Chiba, K. Kumagai, H. Takeda, N. Nomura, Mechanical properties of forged low Ni and C-containing Co–Cr–Mo biomedical implant alloy, Mater Sci Forum 475–479 (2005) 2317–22.

[38] M. Niinomi, T. Hattori, K. Morikawa, T. Kasuga, A. Suzuki, H. Fukui, S. Niwa, Development of low rigidity b-type titanium alloy for biomedical applications. Mater Trans 43 (2002) 2970–7.

[39] M. Niinomi, Recent research and development in titanium alloys for biomedical applications and healthcare goods, Sci Tech Adv Mater 4 (2003) 445–54.

[40] B. D. Ulery, L. S. Nair, C. T. Laurencin, Biomedical Applications of Biodegradable Polymers, J Polym Sci B Polym Phys. 49 (2011) 832–864.

[41] X. Liu, P. K. Chu, C. Ding, Surface modification of titanium, titanium alloys, and related materials for biomedical applications, Materials Science and Engineering R 47 (2004) 49–121

[42] M.F. Montemor, Functional and smart coatings for corrosion protection: A review of recent advances, Surf. Coat. Technol. 258 (2014) 17–37

[43] R. J. K.Wood, Tribo-corrosion of coatings: a review, Journal of Physics D 40 (2007) 5502–5521.

[44] S. A. Alves, R. Bayón, A. Igartua, V. Saénz de Viteri, L. A. Rocha, Tribocorrosion behaviour of anodic titanium oxide films produced by plasma electrolytic oxidation for dental implants, Lubrication Science 26 (2013)

[45] A.P. Serro, C. Completo, R. Colaço, F. dos Santos, C. Lobato da Silva, J.M.S. Cabral, H. Araújo, E. Pires, B. Saramago, A comparative study of titanium nitrides, TiN, TiNbN and TiCN, as coatings for biomedical applications, Surface & Coatings Technology 203 (2009) 3701–3707

[46] R. P. van Hove, I. N. Sierevelt, B. J. van Royen, P. A. Nolte, Titanium-Nitride Coating of Orthopaedic Implants: A Review of the Literature, BioMed Research International 2015 (2015) 485975

[47] R. Bayón, A.Igartua, J.J.González, U.Ruiz de Gopegui, Influence of the carbón content on the corrosion and tribocorrosion performance of Ti DLC coatings for biomedical alloys, Tribology International 88 (2015) 115–125

[48] M. Abdel-Hady Gepreel, M. Niinomi, Biocompatibility of Ti-alloys for long-term implantation, J. Mech. Behav. Biomed.Mater. 20 (2013) 407–415,

[49] L.S. Kubie, G. M. Shults. Studies on the relationship of the chemical constituents of blood and cerebrospinal fluid. J Exp Med 42 (1925) 565-91.

[50] G. Manivasagan, D. Dhinasekaran, A. Rajamanickan, Biomedical Implants: Corrosion and its prevention – A review, Recent Patents on Corrosion Resistance, 2 (2010) 40-54

[51] T. Hanawa, Metal ion release from metal implants, Materials Science and Engineering C 24 (2004) 745–752

[52] B. Kasemo, J. Lausmaa, Surface science aspects on inorganic biomaterials. CRC. Crit Rev Biocompat 2 (1986) 335-30.

[53] S. Cao, S. G. Maldonado, S. Mischler, Tribocorrosion of passive metals in the mixed lubrication regime: theoretical model and application to metal-on-metal artificial hip joints, Wear 324-325 (2015) 55–63

[54] P.A. Dearnley, A brief review of test methodologies for surface engineered biomedical implant alloys. Surf Coat Technol 98 (2005) 483-90.

[55] T. Hanawa, Reconstruction and regeneration of surface oxide film on metallic materials in biological environments. Corrosion Rev 21 (2003) 161-81.

[56] T. Hanawa, S. Hiromoto, A. Yamamoto, D. Kuroda, K. Asami, XPS Characterization of the Surface Oxide Film of 316L Stainless Steel Samples that were Located in Quasi-Biological Environments, Mater. Trans. 43 (2002) 3088.

[57] D.C. Smith, R.M. Pilliar, J.B. Metson, N.S. McIntyre, Dental implant materials. II. Preparative procedures and surface spectroscopic studies, J. Biomed. Mater. Res. 25 (1991) 1069.

[58] T. Hanawa, S. Hiromoto, K. Asami, Characterization of the surface oxide film of a Co–Cr–Mo alloy after being located in quasi-biological environments using XPS, Appl. Surf. Sci. 183 (2001) 68.

[59] E.J. Kelly, Electrochemical Behavior of Titanium, Mod. Aspect Electrochem. 14 (1982) 319.

[60] I. Pais, M. Feher, E. Farkas, Z. Szabo, I. Cornides, Titanium as a new trace element, Commun. Soil Sci. Plant Anal. 8 (1977) 407–410.

[61] T. Hanawa, M. Ota, Calcium phosphate naturally formed on titanium in electrolyte solution, Biomaterials 12 (1991) 767.

[62] A. H. Hussein, M. A.-H. Gepreel, M. K. Gouda, A. M. Hefnawy, S. H. Kandil, Biocompatibility of new Ti–Nb–Ta base alloys, Materials Science and Engineering C 61 (2016) 574–578

[63] Y. Ikarashi, K. Toyoda, E. Kobayashi, H. Doi, T. Yoneyama, H. Hamanaka, T. Tsuchiya, Improved Biocompatibility of Titanium–Zirconium (Ti–Zr) Alloy: Tissue Reaction and Sensitization to Ti–Zr Alloy Compared with Pure Ti and Zr in Rat Implantation Study, Mat. Trans. 46 (2005) 2260 - 2267

[64] M. T.Mathew, P. Srinivasa Pai, R. Pourzal, A. Fischer, M. A.Wimmer, Significance of Tribocorrosion in Biomedical Applications: Overview and Current Status, Advances in Tribology Volume 2009 (2009) 250986

[65] S. Mischler, S. Debaud, and D. Landolt, Wear-accelerated corrosion of passive metals in tribocorrosion systems, Journal of the Electrochemical Society 145 (1998) 750–758,

[66] J.-P. Celis, P. Ponthiaux, F. Wenger, "Tribo-corrosion of materials: interplay between chemical, electrochemical, and mechanical reactivity of surfaces," Wear 261 (2006) 939–946

[67] S. Mischler, "Triboelectrochemical techniques and interpretation methods in tribocorrosion: a comparative evaluation," Tribology International 41 (2008) 573–583

[68] Bio-Tribocorrosion in Biomaterials and Medical Implants, Edited by Yu Yan, Published by Woodhead Publishing Limited 2013

[69] Anna Igual Muñoz, Leandre Casabán Julián, Tribocorrosion behavior of CoCrMo alloy for hip prosthesis as a function of loads: A comparison between two testing systems, Electrochimica Acta 55 (2010) 5428–5439

[70] M.T. Mathew, M.J. Runa, M. Laurent, J.J. Jacobs, L.A. Rochab, M.A. Wimmer, Tribocorrosion behavior of CoCrMo alloy for hip prosthesis as a function of loads: A comparison between two testing systems, Wear 271 (2011) 1210– 1219

[71] M P Licausi, A Igual Muñoz and V Amigo Borras, Tribocorrosion mechanisms of Ti6Al4V biomedical alloys in artificial saliva with different pHs, J. Phys. D: Appl. Phys. 46 (2013) 404003

[72] R. Chistyakov, B. Abraham, W.D. Sproul, , 49th Annual SVC Technical Conference, Washington, DC, April 23–27, 2006, 88–91.

[73] J. Lin, W.D. Sproul, J.J. Moore, R. Chistyakov, B. Abraham, Structurally laminated CrN films deposited by multi pulse modulated pulsed power magnetron sputtering, Surf. Coat. Technol. 206 (2011) 1780–1786

[74] M. E. Launey, R. O. Ritchie, On the Fracture Toughness of Advanced Materials, Adv. Mater. 21 (2009) 2103.

[75] D.M. Marulanda, J.J. Olaya, U. Piratoba, A. Mariño, E. Camps, The effect of bilayer period and degree of unbalancing on magnetron sputtered Cr/CrN nano-multilayer wear and corrosion, Thin Solid Films 519 (2011) 1886–1893

[76] C. Valero Vidal, A. Igual Muñoz, Electrochemical characterisation of biomedical alloys for surgical implants in simulated body fluids, Corrosion Science 50 (2008) 1954–1961

[77] S. Virtanen, I. Milosˇev, E. Gomez-Barrena, R. Trebsˇe, J. Salo, Y.T. Konttinen, Special modes of corrosion under physiological and simulated physiological conditions, Acta Biomaterialia 4 (2008) 468–476

[78] B. Alemon, M. Flores, W. Ramirez, J. C. Huegel, E. Broitman, Tribocorrosion behavior and ions release of CoCrMo alloy coated with a TiAlVCN/CNx multilayer in simulated body fluid plus bovine serum albumin, Tribology International 81 (2015) 159-168

[79] N. Diomidis, J.-P. Celis, P. Ponthiaux and F. Wenger, A methodology for the assessment of the tribocorrosion of passivating metallic materials, *Lubrication Science* **21** (2009) 53–67

[80] J.-P. Celis, P. Ponthiaux (Eds.), Testing Tribocorrosion of Passivating Materials Supporting Research and Industrial Innovation: Handbook, Maney Publishing, UK, ISBN: 978-1-907975-20-2 2012, pp. 150–183.

[81] N. Diomidis, J.-P. Celis, P. Ponthiaux, F. Wenger, Tribocorrosion of stainless steel in sulfuric acid: Identification of corrosion–wear components and effect of contact area, Wear 269 (2010)93-103

[82] W.C.Oliver and G.M. Pharr, An improved technique for determining hardness and elastic modulus using load and displacement sensing indentation experiments, J. Mater. Res. Vol 7 (1992)

[83] P.C. Yashar, W.D. Sproul, Nanometer scale multilayered hard coatings, Vacuum 55 (1999) 179

[84] H. Holleck, V. Schier, Multilayer PVD coatings for wear protection, Surf. Coat. Technol 76-77 (1995) 328

[85] M. Stueber, H. Holleck, H. Leiste, K. Seemann, S. Ulrich, C. Ziebert, Concepts for the design of advanced nanoscale PVD multilayer protective thin films, J. Alloys Compd 483 (2009) 321

[86] J.Lin, W.D. Sproul, J. J. Moore, Z.L. Wu, S.L. Lee, Effect of negative substrate bias voltage on the structure and properties of CrN films deposited by modulated pulsed power (MPP) magnetron sputtering, J. Phys. D: Appl. Phys. 44 (2011) 425305

[87]D. Loveday, P. Peterson, B.Rodgers—Gamry Instruments, JCT CoatingsTech, (2004) EIS Part I, pp. 46-52

[88] R. Narayanan, S.K. Seshadri, Point defect model and corrosion of anodic oxide coatings on Ti–6Al–4V, Corrosion Science 50 (2008) 1521–1529

[89] M. Schutze, R. Bender, K.G. Schutze, Corrosion Resistance of High Performance Materials", Wiley VCH, pp. 3-83

[90] V.M.C.A. Oliveira, C. Aguiar, A.M. Vazquez, A. Robin, M.J.R. Barboza, Improving corrosion resistance of Ti-6Al-4V alloy through plasma-assisted PVD deposited nitride coatings, Corrosion Science 88 (2014) 317–327

[91] M. Moisel, A.F.L. Mele, W. Müller, Biomaterial Interface Investigated by Electrochemical Impedance Spectroscopy, Adv. Eng. Mater. 10 (2008) B33–B46.

# CHAPTER 6

# TANTALUM BASED FILMS FOR BIPOLAR PLATE PROTECTION IN PEMFC

# 1. Introduction

Fuel cells have gained much attention during the last decade owing to the great concern on petroleum based energy resources depletion and environmental pollution and climate change.

Fuel cells are electrochemical devices that convert chemical energy of a fuel directly into electrical energy while enabling high efficiencies and low emissions [1]. Polymer electrolyte membrane fuel cells (PEMFC) are one of the most promising candidates as the next generation power sources using hydrogen as fuel to generate green electricity for stationary and transportation applications. PEMFC remarkable features are low operating temperature, high power density, efficiencies up to 60% and easy up-scaling [2-3]. PEMFC are particularly suited to substitute internal combustion engines of passenger vehicles. In fact, major car companies have already manufactured prototype cars that meet consumer requirements with respect to driving speed, acceleration and driving range. This objective has been reached due to advances in both fuel cell components and systems level [4].

The basic operational processes of a PEMFC [5] are illustrated in Fig 6.1 and described below:

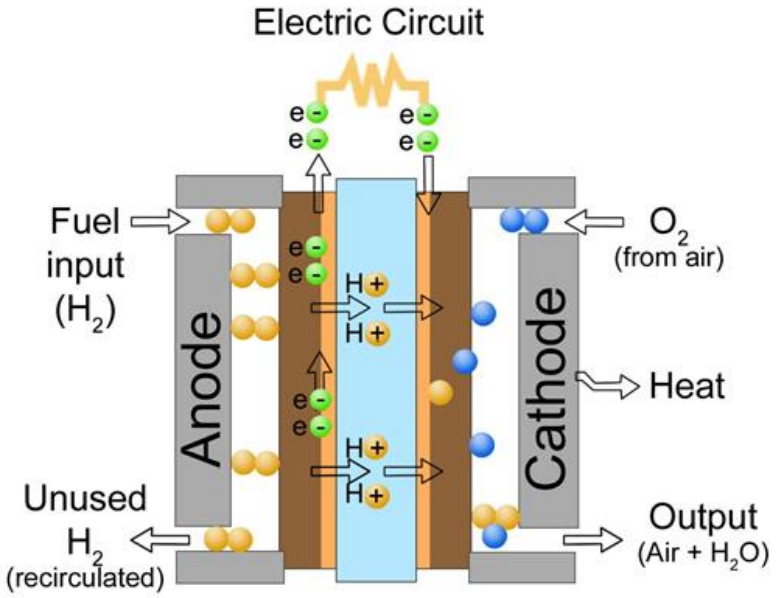


**Fig 6. 1: A schematic representation of operation principle of a PEMFC (taken from [6])**

1. Hydrogen ($H_2$) is delivered through the gas-flow plate to the anode where it reacts electrochemically to form hydrogen ions and electrons following the next equation:

$$H_2 \rightarrow 2H^+ + 2e^- \qquad [6.1]$$

2. The hydrogen ions migrate through the electrolyte or proton conducting membrane while the electrons are conducted through an external electrical circuit down to the cathode. At the cathode, the electrons and hydrogen ions re-combine with oxygen ($O_2$) outwardly supplied from gas-flow stream to form water, per the following equation:

$$\frac{1}{2}O_2 + 2H^+ + 2e^- \rightarrow H_2O \qquad [6.2]$$

3. The global reaction within a fuel cell generates water, heat and electrical work as follows:

$$H_2 + \frac{1}{2}O_2 \rightarrow H_2O + W_{ele} + Q_{heat} \qquad [6.3]$$

The theoretical voltage at open circuit of hydrogen –oxygen fuel cell is 1.23 V at 298 K. Under loading conditions, the fuel cell voltage varies between 0.5 and 1 V, delivering a current density up to 1.5 A $cm^{-2}$.

In spite of the great interest and important research and development currently in progress, there are still two main barriers preventing the widespread commercialization of PEMFC: the durability and cost of fuel cell components and the optimization of the system layout and balance of plant.

In this thesis, the improvement of one of the components of the PEMFC is addressed. In section 2 of this chapter the different PEMFC components will be described with special emphasize on bipolar plates. Section 3 describes bipolar plate requirements and limitations, which are the scope of this chapter. The experimental work carried out on $TaN_x$ coating solution for BPPs durability enhancement is explained in Section 4. In section 5, a bilayer Ta based coating solution is exhibited.

## 2. PEMFC components

A schematic representation of fuel cell components is given in Fig 6.2.

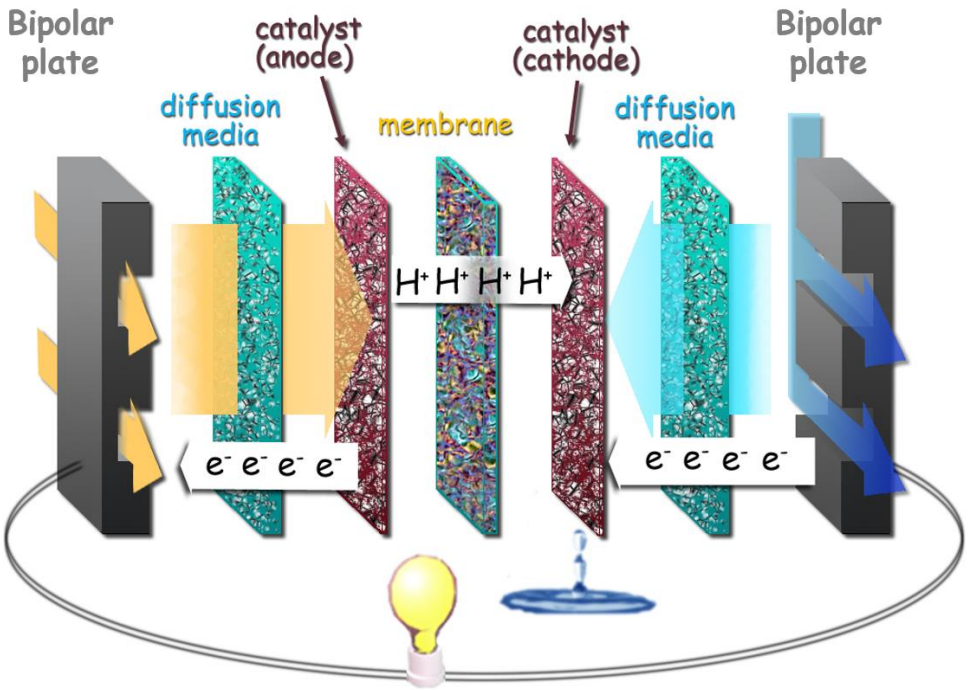


**Fig 6. 2: Cross sectional overview of PEMFC components (taken from [7])**

The membrane electrode assembly (MEA) is the core of the PEMFC. It consists of the polymer electrolyte membrane (also called proton exchange membrane) and two catalyst electrode layers. The gas diffusion media and the bipolar plate completed the stack.

The ***polymer electrolyte membrane*** conducts only positively charged hydrogen ions and blocks the electrons penetration. It is the key component of a fuel cell since it allows only the penetration of the necessary ions from the anode to the cathode.

The thickness of the membrane is around 10-100 μm. The accepted commercial standard for membranes is made of a Polytetrafluoroethylene (PTFE) backbone with a perfluorovinylether side chain that ends with a sulfonic acid group. One of the most common and commercially used PEM membrane is Nafion membrane manufactured by DuPont.

The ***catalyst electrode layers (CL)*** are where the hydrogen oxidation reaction (HOR) and oxygen reduction reaction (ORR) take place at anode side and cathode side, respectively. CL is usually very thin (less than 10 μm) and includes several materials that are key components to the electrochemical reaction: carbon support with Pt catalyst particles dispersed on the carbon surface and the ionomer. Platinum (Pt) and Pt alloys are popular catalysts for both HOR and ORR. On the anode side, the platinum catalyst enables hydrogen molecules to be split into protons and electrons. On the cathode side, the platinum catalyst enables oxygen reduction by reacting with the protons generated by the anode, producing water. Thus, catalyst layer is one of the most costly components of a PEMFC.

The ***gas diffusion media*** is composed of the gas diffusion layer (GDL) and micro-porous layer (MPL). The diffusion media plays multiple roles: it electrically connects the bipolar plate with the electrodes (anode and cathode), acts as passage for reactant transport and heat/water removal, adds mechanical support to the MEA and protects the catalyst layer from degradation by corrosion or erosion. Carbon and graphite papers as woven structures are being used as GDL. PTFE coatings are commonly applied for hydrophobicity property incorporation. The MPL mainly consists of carbon powder with a PTFE emulsion.

The ***bipolar plates (BPP)*** provide mechanical support over diffusion media and conductive passage for both heat and electron transport. They incorporate gas-flow channels which enable the supply and distribution of hydrogen fuel and oxygen

reactant for electrochemical reaction and by-product water removal. Furthermore, each individual MEA generates less than 1 V which is insufficient voltage for most applications. To solve this problem, multiple cells are connected in series to deliver the required output voltage and are sandwiched between two bipolar plates to separate one from another. Manufacturing of BPP contributes considerably to the total fuel cell stack cost.

## 3. Corrosion phenomena in bipolar plates

One important component in a PEMFC stack is the bipolar plate (BPP) which accounts for about 80% of the total weight and about 30% total stack cost [8-9] . This multi-functional component provides the electrical connection from cell to cell, distributes gases and removes heat from the active areas. Therefore, the bipolar plate material must be chemically stable, highly electrical and thermal conductive; have low contact resistance to the backing, good mechanical strength, low gas permeability and inexpensive massive production.

BPPs have traditionally been fabricated from graphite due to its excellent corrosion resistance, high thermal and electrical conductivity and availability. However, it is not suitable for transportation applications because it exhibits poor mechanical properties, high manufacturing costs and difficult machinability. In contrast, metal bipolar plates are suitable options due to their good mechanical strength, high electrical conductivity, low gas permeability, low cost, and easy manufacturing.

In terms of durability, carbon-polymer composite materials are preferable. However, metallic materials can be manufactured in a very thin plate shape, leading to a considerable increase in volumetric power density. Major car manufacturers are using metallic BPPs in their latest generation fuel cell electric vehicles (FCEV) and

high power density shown by these new FECV is ascribed to metallic BPPs incorporation [10-11].

Nevertheless, there is an important concern related to the utilization of metallic BPPs: corrosion phenomena in the aggressive environment of a PEMFC which leads to an accelerated degradation of the fuel cell and service lifetime reduction [12]. At the anode side, corrosion leads to the release of metal ions from the BPP that can poisoned the membrane, increase the resistance of the catalyst electrode layer and membrane and reduce the PEM fuel cell efficiency [13-14]. At the cathode side, the main problem arise from the build-up of an oxide layer that even though it's true that protects the BPP against corrosion, it has lower conductivity than the metal itself promoting an increase in the interfacial contact resistance with the GDL. Recent studies have revealed that a huge amount of total power losses during fuel cell operation are due to high contact resistance between the BPP and the GDL [15].

Particularly, stainless steel (SS) is considered one of the most promising candidates for transport applications. Nevertheless, chemical stability of SS in humid and acidic conditions of a fuel cell must be improved. At the cathode side, the protective passive film formed on its surface does not completely prevent release of metallic ions leading to membrane poisoning, which reduces the efficiency of the fuel cell. This same passive film significantly increases ICR between the BPP and the gas diffusion layer (GDL), compromising the conductivity of the BPP. In order to improve SS performance many attempts have been performed applying different surface treatments on different types of SS, many of them related with the deposition of transition metal nitrides. The U.S. Department of Energy (DoE) has established several targets for year 2020 with respect to bipolar plate requirements [16]. The important and challenging targets for bipolar plates are i) corrosion currents < 1 μA

$cm^{-2}$, ii) contact resistance < 10 mΩ $cm^2$ at compaction pressure of 140 N $cm^{-2}$ while iii) cost is kept below 3 $ $kW^{-1}$.

# 4. Protective films for stainless steel bipolar plates

## 4.1. Introduction

The literature on transition metal nitride coatings for stainless steel BPP performance improvement is extensive. O. Lavigne et al [17] deposited two thin (100 nm) chromium nitride PVD coatings on SS316L bipolar plates. The first coating (coating 1) was a mixture of $Cr_2N$ and Cr, the second (coating 2) a single phase CrN. The electrolyte used was an aqueous solution containing 0.07 M of $Na_2SO_4$ to limit ohmic drop with the addition of a small amount of $H_2SO_4$ (to adjust the pH to about 4). The electrolyte was either purged with $H_2$ and samples polarized to +0.05 $V_{SHE}$ or purged with air and samples polarized to +0.85 $V_{SHE}$ at 60 ºC to simulate anode and cathode side environment, respectively. In the simulated anodic environment, the corrosion currents of both coatings were very low (~ $10^{-8}$ A $cm^{-2}$). In the simulated cathodic environment, corrosion currents were in the range of ~$10^{-7}$ A $cm^{-2}$ and ~$10^{-6}$ A $cm^{-2}$ for coating 1 and coating 2, respectively, after 25 h of polarization. The ICR values after polarization tests at 140 N $cm^{-2}$ compaction pressure were 30 mΩ $cm^2$ and 10 mΩ $cm^2$ for coating 1 and coating 2, respectively.

S.H. Lee et al. [18] investigated the corrosion and electrical characteristics of CrN and TiN coatings deposited by cathode arc ion plating on SS316L substrate. A 0.1 M $H_2SO_4$ solution with 2 ppm $F^-$ at 80 °C was purged continuously with hydrogen gas and air to simulate anodic and cathodic PEMFC environment. While TiN coating was dissolved during corrosion testing and showed a corrosion current of 29 μA $cm^{-2}$ at 0.6 $V_{SCE}$, CrN exhibited lower corrosion currents of 6 μA $cm^{-2}$ at cathode potential. In

comparison to uncoated SS316L, CrN- and TiN-coated SS316L exhibit lower ICR value. H. Sun et al. [19] tested 1 μm TiN coating deposited on SS316L by closed field unbalanced magnetron sputter ion plating (CFUBMSIP) at higher cathodic potential of 1 $V_{SHE.}$ Under these simulated conditions, the corrosion current registered was 11 μA $cm^{-2}$, slightly higher than US DoE target of 1 μA $cm^{-2}$. The ICR value measured after corrosion testing increased up to 230 mΩ $cm^2$.

Wang et al. [20] prepared a molybdenum nitride (Mo-N) diffusion coating on the surface of SS304 by a plasma surface diffusion alloying method. The coating was tested electrochemically in 0.05 M $H_2SO_4$ + 2 ppm $F^-$ solution at 70 ºC and ICR measurements were taken before and after polarization. The corrosion currents of Mo-N coated 304SS were around 1 μA $cm^{-2}$ at both -0.1 $V_{SCE}$ anodic potential and +0.6 $V_{SCE}$ cathodic potential, reducing the corrosion current density of uncoated SS304 by nearly one order of magnitude. ICR values measured after polarization at 140 N $cm^{-2}$ compaction pressure were 27.26 mΩ $cm^2$ and 100.98 mΩ $cm^2$ for coated- and uncoated-SS304.

C. Choe et al. [21] used inductively coupled plasma assisted reactive magnetron sputtering to deposited $TaN_x$ coatings at various $N_2$ flow rates. The electrochemical properties of the samples were investigated in a 0.05 M $H_2SO_4$ + 0.2 ppm HF solution at 80 ºC and polarized to -0.1 $V_{SCE}$ ($H_2$ bubbling) and +0.6 $V_{SCE}$ (air bubbling) to mimic anode and cathode potential, respectively. $TaN_x$ coated samples exhibited excellent corrosion resistance that satisfied the DoE requirement with a lowest current density value of 0.3 μA $cm^{-2}$ (at 0.6 V, cathodic condition) and 0.01 μA $cm^{-2}$ (at - 0.1 V, anodic condition). Lowest ICR value of 11 mΩ $cm^2$ was obtained at highest $N_2$ flow rate.

However, the coating materials, deposition techniques and more importantly, testing parameters are so diverse that making conclusions and establishing a tendency becomes rather complicated. The US Department of Energy (DoE) has

recommended to evaluate electrochemical ex-situ performance of bipolar plates in pH 3 environment at potentials not exceeding 0.8 $V_{SHE}$ [8]. Kumagai et al. [22] investigated the electrochemical behaviour and contact resistance of different austenitic stainless steels as a function of pH after polarization tests and cell operation. It was found that pH variation altered the type of oxide and oxide layer thickness grown on SS surfaces which led to completely different ICR values after corrosion testing. S. Lædre et al. [23] studied the effect of pH and presence of small amounts of fluorides and halides on the performance of SS316L in PEMFC. They demonstrated the difference on iron oxide thickness in terms of solution acidity. Acidity was not inversely proportional to iron oxide thickness and hence to the ICR measured value after polarization. Lowering the pH to simulate accelerated tests may not have the expected influence and it was suggested to use a pH value close to the real pH in operating fuel cell. Hinds and Brightman have shown that during start-up/shut down of a PEMFC, cathodic potential as high as 1.4 $V_{SHE}$ are delivered [24]. A. Orsi and co-workers [25] studied the effect of corrosion testing variables (applied potential, pH and test duration) and compared these ex-situ testing with those from in-situ fuel testing. They concluded that ex-situ test parameters that best mimic the real operational conditions in a fuel cell were 1.4 $V_{SHE}$ cathodic potential and 1 mM $H_2SO_4$ solution (pH 3).

The aim of this study was to investigate the performance of $TaN_x$ coatings deposited on SS316L by MPPMS as a function of $N_2$-to-Ar ratio. The utilization of MPPMS for the deposition of protective coatings for bipolar plates in PEMFC has never been reported. The correlation between the nitrogen content and microstructure of $TaN_x$ films with electrochemical and electrical properties was analysed thoroughly. The relationship between the oxides formed on the top of $TaN_x$ coatings and ICR values after polarization is investigated. Although passive films protect the SS316L substrate from corrosion, they also increase the interfacial contact resistance

between the bipolar plate and the gas diffusion layer [23, 26]. The objective is to correlate the composition and thickness of the oxide layers grown on top of each $TaN_x$ coating with corresponding ICR value. C. Choe et al. have tested $TaN_x$ coatings at different $N_2$ flow rates but only up to 0.84 $V_{SHE}$ cathodic potential during 10 minutes. H. Yu et al. [27] examined the corrosion resistance of Ta coated SS316L under 0.8 $V_{SHE}$ cathodic potential but they didn't give any information about ICR values. During this study, the electrochemical testing was carried out under different applied potentials (up to 1.4 $V_{SHE}$), pH values and test durations (up to 180 min) in order to mimic the real operational conditions of a PEMFC.

## 4.2 Experimental development of $TaN_X$ films by MPPMS to protect SS bipolar plates in cathode side of PEMFC

### 4.2.1 $TaN_X$ film deposition

The high corrosion resistance of $TaN_X$ (different Ta/N atomic ratio) and multilayer TaN films observed in previous chapters 4 and 5, encourages the evaluation of these films as protective coatings for stainless steel BPP in cathodic side of PEMFC environment. Since the composition of the coating defines the composition of the barrier surface oxide film and therefore, the electrochemical and electrical features of the coating, the development of $TaN_x$ films deposited at different $N_2$-to-Ar ratios (0, 0.25, 0.625, and 1) is proposed.

The $TaN_x$ films were deposited in the MIDAS 450 sputtering system (described in Chapter 3) under the same process parameters defined in Chapter 4, section 3.1.

SS316L thin coupons (35 x 35 x 0.1 mm) and silicon wafers were used as substrates.

The same MPPMS pulse 996 was used for all depositions. Pulse characteristics were already shown in Chapter 4. The pulse shape is shown in Fig 6.3.

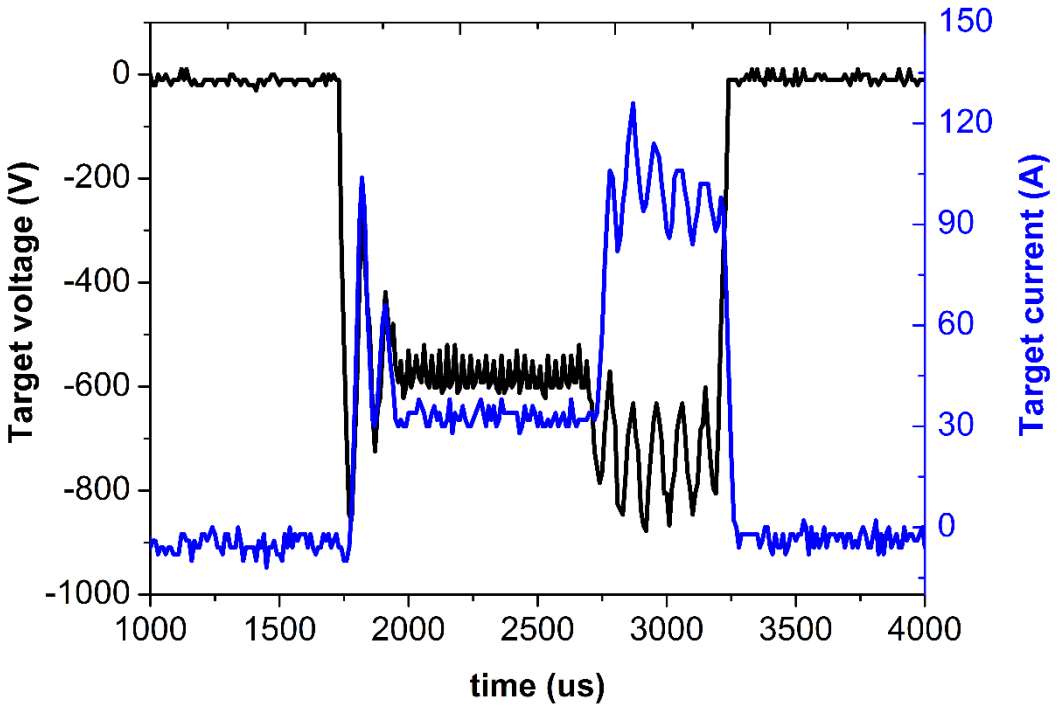


**Fig 6. 3: Voltage-current characteristics of pulse 996 applied during TaNx coating deposition**

Table 6.1 exhibits the the peak target voltaje and current values during each film deposition process and the thickness and composition of each $TaN_x$ film, already measured in Chapter 4.

| | $N_2$/Ar ratio | Peak target voltage (V) | Peak target current (A) | Thickness (µm) | Ta (at. %) | N (at. %) |
|---|---|---|---|---|---|---|
| Ta | 0 | 720 | 85 | 2.6 | 100 | 0 |
| TaN_0.25 | 0.25 | 740 | 93 | 2.5 | 90 | 10 |
| TaN_0.625 | 0.625 | 700 | 75 | 2.3 | 75 | 25 |
| TaN_1 | 1 | 700 | 66 | 2.1 | 55 | 45 |

**Table 6. 1: Pulsing parameters of MPPMS discharge during TaNx deposition**

### 4.2.2 $TaN_X$ film characterization equipment in PEMFC simulated environment

To simulate the cathodic side of a real PEMFC electrochemical environment, a three-electrode cell setup (described in Chapter 3) was used. In order to simulate the pH on the bipolar plates during fuel cell operation, polarization tests were carried out for in 1 mM $H_2SO_4$ and lower concentrated electrolytes to achieve 3 and 6 pH values, respectively. The electrolyte was heated (80 ºC) and bubbled with nitrogen gas for 20 min to reduce the concentration of dissolved oxygen prior to the introduction of the samples. During the electrochemical testing, the nitrogen gas bubbler was positioned above the surface of the electrolyte in order to maintain the nitrogen levels. The reference electrode, $Hg/Hg_2SO_4/K_2SO_4$ (0.64 V vs SHE), was connected to the electrolyte cell by a salt bridge. All standard potentials are referred to standard hydrogen electrode potentials (SHE). The simulated PEMFC electrochemical set-up can be seen in Fig 6.4.

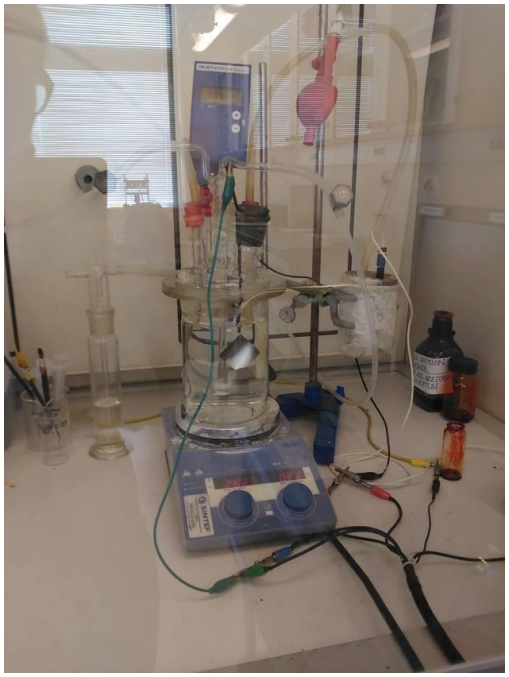

**Fig 6. 4: Electrochemical set-up for ex-situ testing of TaNx coated SS316L in PEMFC environment**

Interfacial contact resistance (ICR) measurements were conducted before and after each electrochemical test. The coated and uncoated SS316L coupons were placed between two gold coated copper plates as illustrated in Fig 6.5. A Freudenberg I2C6 gas diffusion layer (GDL) was located between the coupon and the top plate. A spring loaded gold pin was positioned on the centre of the bottom plate. A constant current was applied (2A) and voltage difference between the pin and the top plate was measured at different compaction pressures from 34-530 N $cm^{-2}$. The total interfacial contact resistance ($R_T$) is calculated from this experiment. The $R_T$ is the sum of the interfacial contact resistances between i) the top gold plate and the GDL ($R_{gold/GDL}$) , iii) the GDL and the coated/uncoated sample ($R_{GDL/sample}$) and the iii) sample and gold pin ($R_{sample/pin}$). The $R_{sample/pin}$ is considered negligible and $R_{gold/GDL}$ is known from previous testing. Thus, $R_{GDL/sample}$ can be calculated from the following equation:

$$R_{GDL/sample} = R_T - R_{gold/GDL} \quad [6.4]$$

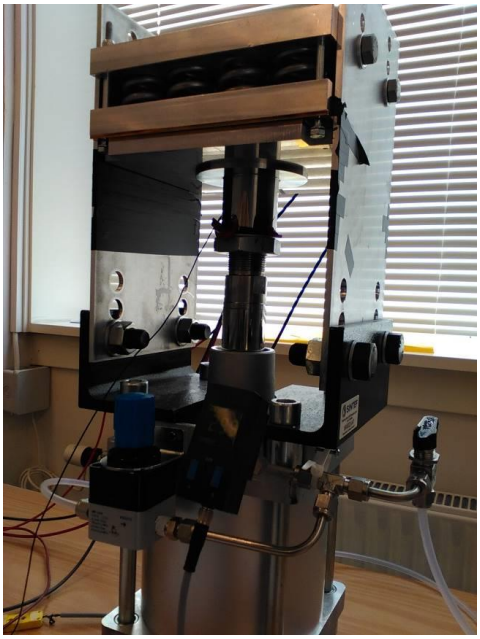

**Fig 6. 5: Experimental set-up for ICR measurement between $TaN_x$ coated SS316L samples and GDL**

### 4.2.3 $TaN_x$ film performance in PEMFC environment

The microstructural characterization of $TaN_x$ films was already accomplished in Chapter 4, since the films are deposited under the same MPPMS pulse shape and process parameters. For simplicity purposes, the cross-sectional microstructure images of $TaN_X$ films are shown in Fig 6.6. As demonstrated in chapter 4, the suppression of columnar growth is restricted to TaN_0.25 characterized by 10 at. % of nitrogen and corresponding to the higher peak current density during MPPMS discharge [28]. The great density and smooth surface exhibited by TaN_0.25 were important factors contributing to the presentation of the best corrosion resistance of all evaluated films in NaCl 0.06 M. The microstructure of $TaN_x$ films correlation with their performance in PEMFC is investigated.

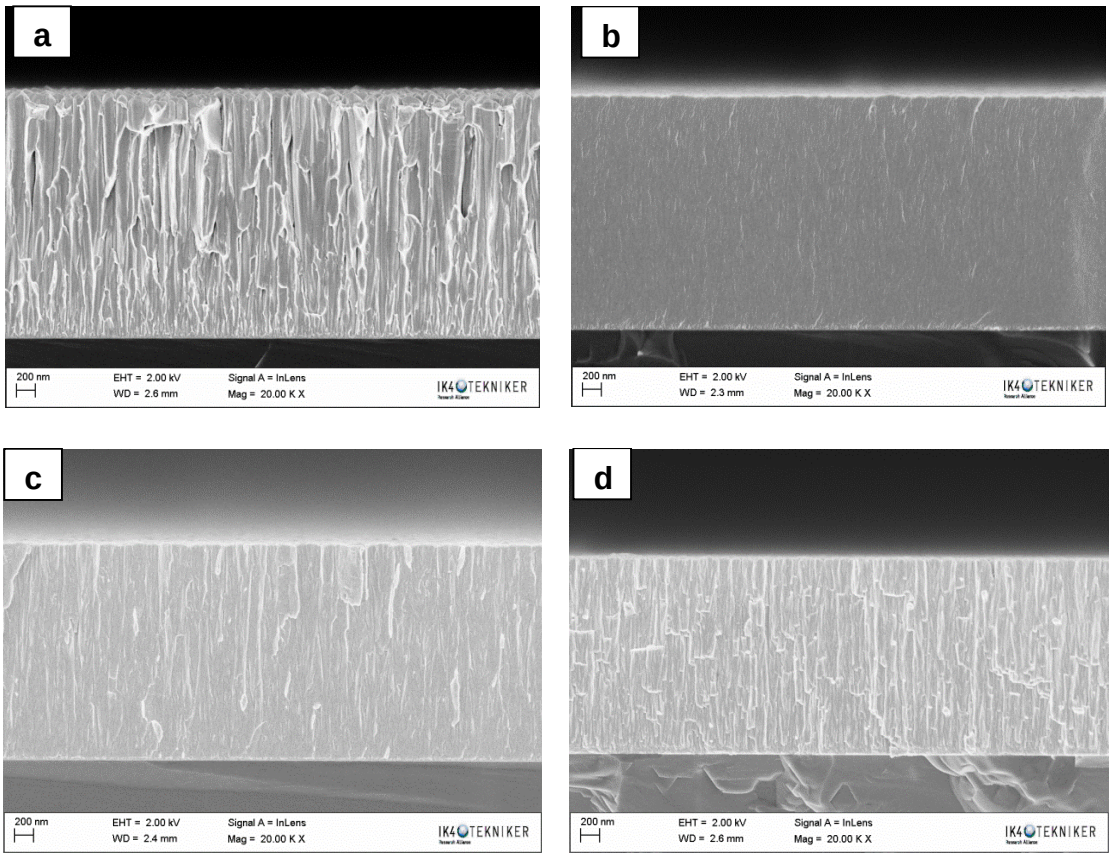


**Fig 6. 6: Cross-sectional SEM micrographs of a) Ta, b)TaN_0.25, c) TaN_0.625 and d) TaN_1 coatings**

The composition of the $TaN_x$ films under different $N_2$-to-Ar ratios was previously analized in Chapter 4 and illustrated in Table 6.1. The composition of $TaN_x$ films differs considerably, which will promote different oxide based layers growth after polarization. Hence, distinguished behaviours are expected from each $TaN_x$ coating. The correlation between electrochemical and interfacial contact resistance characteristics with $TaN_x$ coating composition will be investigated in the following sections.

*4.2.3.1 Potentiodynamic measurements at different pH values.*

Potentiodynamic scans were conducted from - 0.2 to + 1.6 $V_{SHE}$ at scan rate of 1 mV $s^{-1}$ in pH 3 and pH 6 electrolytes. Fig 6.7 shows the potentiodynamic polarization behaviour of $TaN_x$ coated and non-, coated AISI 316L in electrolytes with different pH values. In pH 3 electrolyte (Fig 6.8.a), all $TaN_x$ coatings exhibited current densities of 1 µA $cm^2$ up to 1.6 $V_{SHE}$ (much higher than recommended DOE targets), demonstrating a better performance than non-coated SS316L. The most corrosion resistant coating is TaN_0.25, showing the highest corrosion potential and the lowest current density in comparison to the other coatings and non-coated SS316L. In fact, the denser microstructure is observed for TaN_0.25 coating.

In pH 6 electrolyte (Fig 6.8.b), the lowest corrosion potential was observed for non-coated SS316L. But current density started to abruptly increase at potentials higher than 1.2 $V_{SHE}$, suggesting a high corrosion of non-coated sample. The current density of $TaN_x$ coatings remained stable about 1 µA $cm^{-2}$ up to 1.5 $V_{SHE}$.

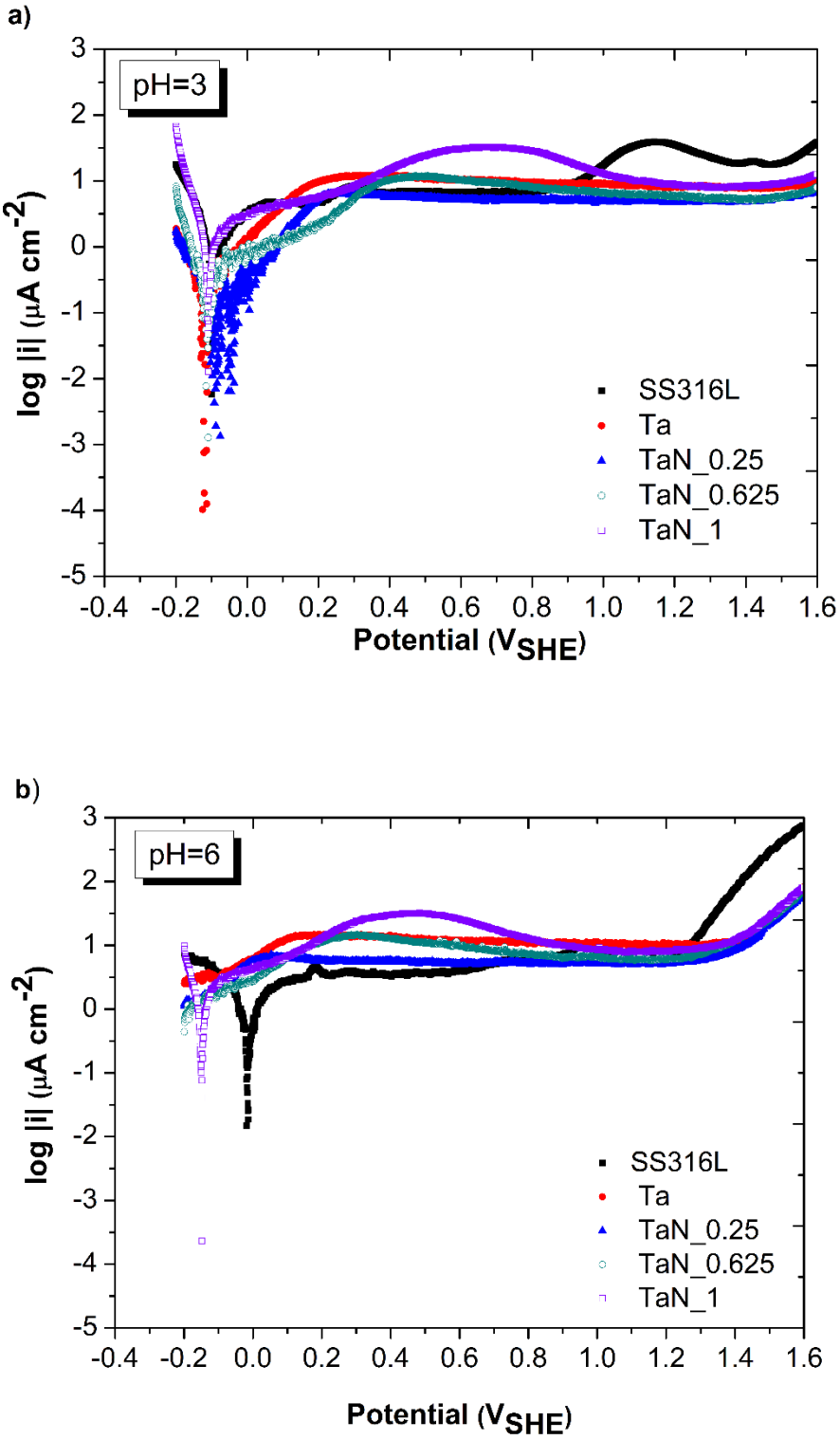


**Fig 6. 7: Current-potential relation during potentiodynamic measurements at a) pH 3 and b) pH 6**

*4.2.3.2 Potentiostatic measurements with different variable parameters*

**Variable parameter: Applied potential**

Potentiostatic measurements were taken after polarization for 5 minutes at 1 $V_{SHE}$ and 1.4 $V_{SHE}$ in pH 3 electrolyte and are shown in Fig 6.8 and Fig 6.9, respectively. The application of potentials as high as 1.4 $V_{SHE}$ is justified due to the fact that several studies have measured potentials above 1.4 $V_{SHE}$ in the fuel cell cathode during start-up/shut down periods [24, 29]. After 5 minutes electrochemical testing, no significant difference is observed on current density values polarized either at 1 $V_{SHE}$ or 1.4 $V_{SHE}$. TaN_0.25 and TaN_0.625 exhibited corrosion currents slightly higher than 1 μA $cm^{-2}$, the established DoE target for corrosion current for bipolar plates. Corrosion current of metallic Ta is around 4 μA $cm^{-2}$ while TaN_1 and non-coated SS316L showed current densities of 10 μA $cm^{-2}$. It is important to mention that the corrosion current limits established by US DoE were supposed to be measured at 0.8 $V_{SHE}$. All $TaN_x$ coatings most likely would have registered much lower current values if they had been polarized at potentials lower than 1 $V_{SHE,}$ as observed for TiN coated SS [25] and non-coated SS316L. [26].

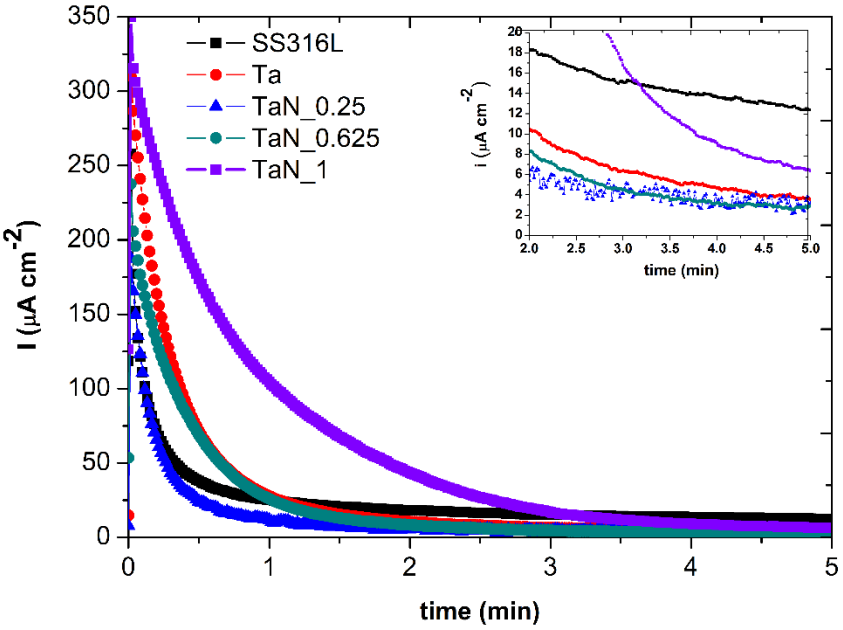


**Fig 6. 8: Potentiostatic tests (5 min) at 1 $V_{SHE}$ in pH 3 electrolyte of $TaN_x$ ($N_2$-to-Ar ratio 0, 0.25, 0.625 and 1) coated on SS316L and non-coated SS316L**

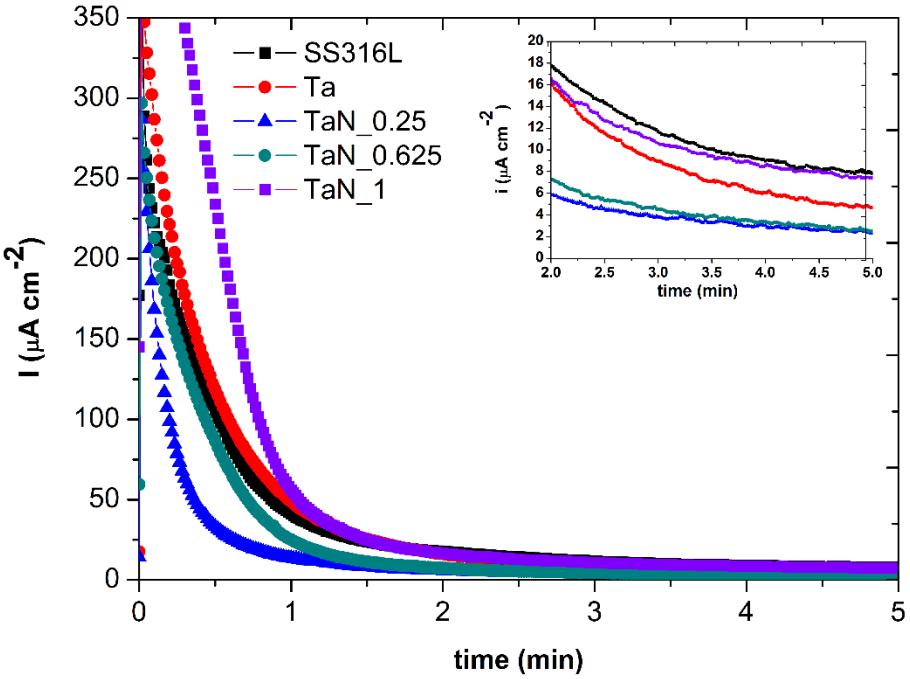


**Fig 6. 9: Potentiostatic tests (5 min) at 1.4 $V_{SHE}$ in pH 3 electrolyte of $TaN_x$ ($N_2$-to-Ar ratio 0, 0.25, 0.625 and 1) coated on SS316L and non-coated SS316L**

The contact resistance measurements performed before and after potentiostatic tests for two different applied potentials are presented in Fig 6.10. It is clearly observed that when $TaN_x$ coatings are polarized at higher potentials (i.e. 1.4 $V_{SHE}$), the ICR values increase abruptly. This rise in ICR value is probably related to the thickening of the oxide layer on the coating surface when higher potentials are applied [26]. This increase is particularly important for nitride $TaN_x$ coatings, reaching values between 248 mΩ $cm^2$ – 401 mΩ $cm^2$, much higher than the ICR value exhibited from non-coated SS316L (96 mΩ $cm^2$) and exceeding the DoE targets for ICR after polarization (< 10 mΩ $cm^2$) considerably. Analysing the corrosion currents and ICR values together, it can be concluded that the increased passivity, i.e. lower corrosion currents obtained for TaN_0.25 and TaN_0.625, gave rise to much higher contact resistance values after polarization tests than the ones recommended by US DoE.

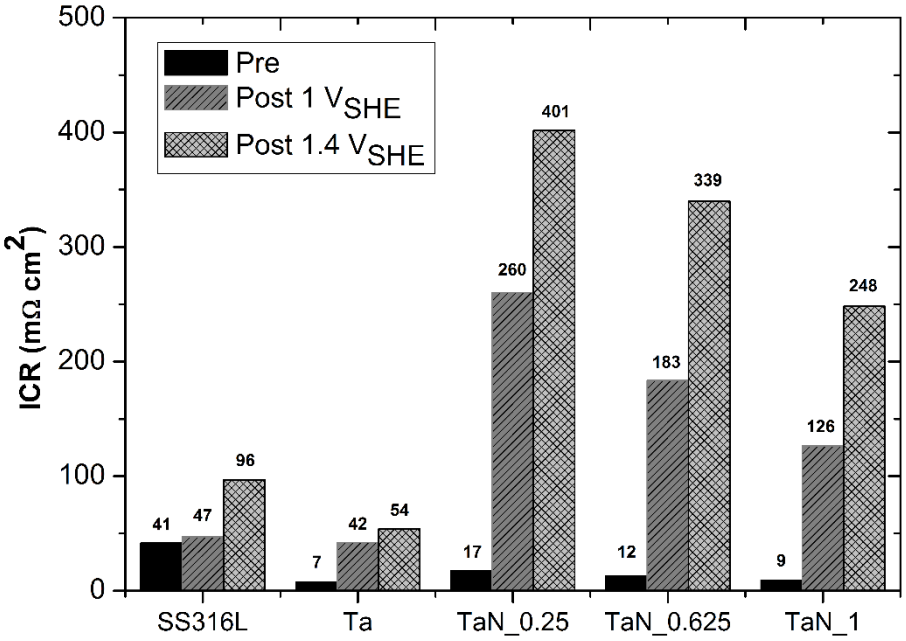


**Fig 6. 10: 11 ICR at 140 N $cm^{-2}$ before and after polarization tests in pH 3 electrolyte (5 min) at different potentials for $TaN_x$ coated- and non-coated SS316L**

The behaviour of metallic Ta film is different from the behaviour of nitride films and it exhibited lower ICR than the non-coated SS316L. The ICR value after polarization at 1.4 $V_{SHE}$ is 54 mΩ $cm^2$, much lower than ICR values for nitride films, while Ta film still showed an excellent corrosion resistance in PEMFC environment (corrosion currents around 4 µA $cm^{-2}$ at 1.4 $V_{SHE}$). The much lower ICR value after polarization observed for Ta film compared with nitride $TaN_x$ films suggests that its oxide film composition must be different, indicating the great importance of oxide composition, besides the thickness, on interfacial contact resistance.

## Variable parameter: pH of the electrolyte

The effect of pH variation on corrosion resistance and electrical properties of the $TaN_x$ films was investigated. Potentiostatic measurements were carried out at 1.4 $V_{SHE}$ for 5 minutes in pH 6 electrolyte (Fig 6.11) for comparison with results obtained in pH 3 (Fig 6.9).

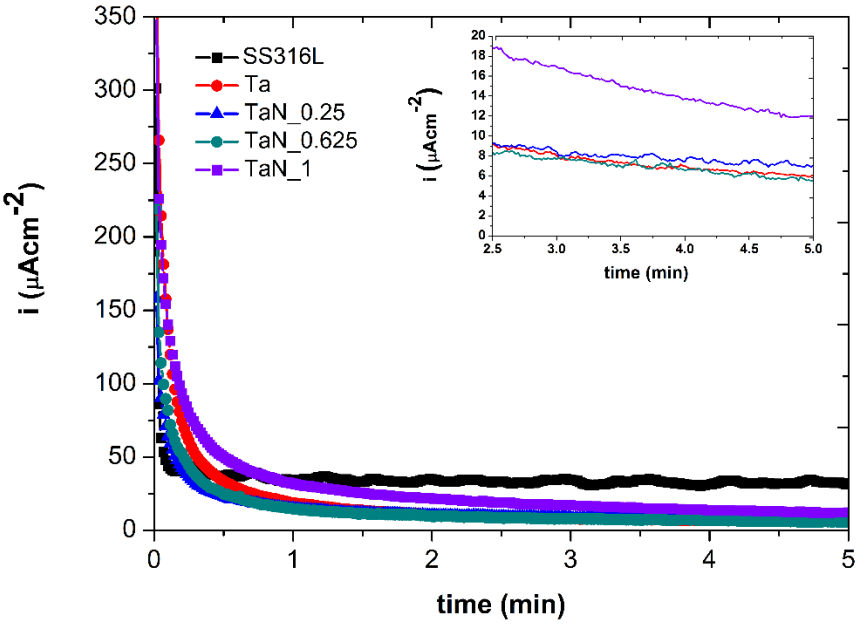


**Fig 6. 11: Potentiostatic tests (5 min) at 1.4 $V_{SHE}$ in pH 6 electrolyte of $TaN_x$ ($N_2$-to-Ar ratio 0, 0.25, 0.625 and 1) coated SS316L and non-coated SS316L.**

The current densities observed are very similar to the ones recorded at pH 3. The lowest currents, values between 6-8 μA $cm^{-2}$, are registered for Ta, TaN_0.25 and TaN_0.625, confirming the tendency observed in more acidic electrolyte. The corrosion resistance of $TaN_x$ films does not seem to be affected by the pH, for the values selected for this study.

ICR values measured before and after polarization at 1.4 $V_{SHE}$ for 5 minutes in electrolytes with different pH are plotted in Fig 6.12. Again, the contact resistance values measured after potentiostatic tests in pH 6 electrolyte, follow the trend observed in previous tests.

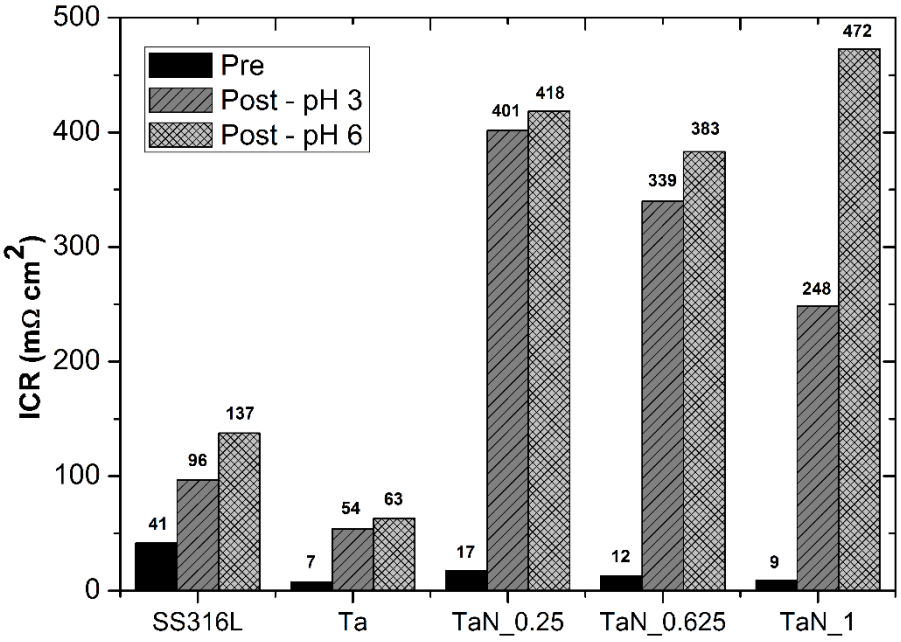


**Fig 6. 12: 11 ICR at 140 N cm-2 before and after polarization tests at 1.4 $V_{SHE}$ (5 min) in varying pH electrolytes (3 and 6) for TaNx coated- and non-coated SS316L**

Nitride $TaN_x$ coatings exhibited highest ICR values (between 383-472 mΩ $cm^2$) while metallic Ta showed lowest value of 63 mΩ $cm^2$, reducing the contact resistance of the uncoated SS316L by half. All tested samples presented lower ICR values when

exposed to lower pH electrolyte. The passive oxide layer of $TaN_x$ coatings may dissolve when exposed to low pH electrolyte which would lead to ICR decrease, as it has been demonstrated for TiN coating elsewhere [25]. Further tests in lower pH electrolytes are needed to extend this behaviour to $TaN_x$ coatings.

**Variable parameter: polarization test duration**

Potentiostatic measurements at 1.4 $V_{SHE}$ in pH 3 electrolyte recorded for 180 min are shown in Fig 6.13.

A huge decrease of the current density is observed for all tested samples, i.e. $TaN_x$ coatings and uncoated SS316L, during the first minute of polarization test. The fast decay of the current density has been already explained and related to the passive oxide formation on nitride coatings [25, 30] and uncoated SS316L [22, 31]. The oxide formation process seems to be fast, reaching an almost steady-state after 20 minutes of polarization. Ta, TaN_0.25 and TaN_0.625 exhibited current density values around 1 μA $cm^{-2}$ at 1.4 $V_{SHE}$ after 180 minutes. These three coatings are excellent alternatives to protect SS316L from corrosion degradation and considerably exceed the established DoE targets for corrosion which required current densities lower than 1 μA $cm^{-2}$ but at much lower potentials (0.8 $V_{SHE}$).

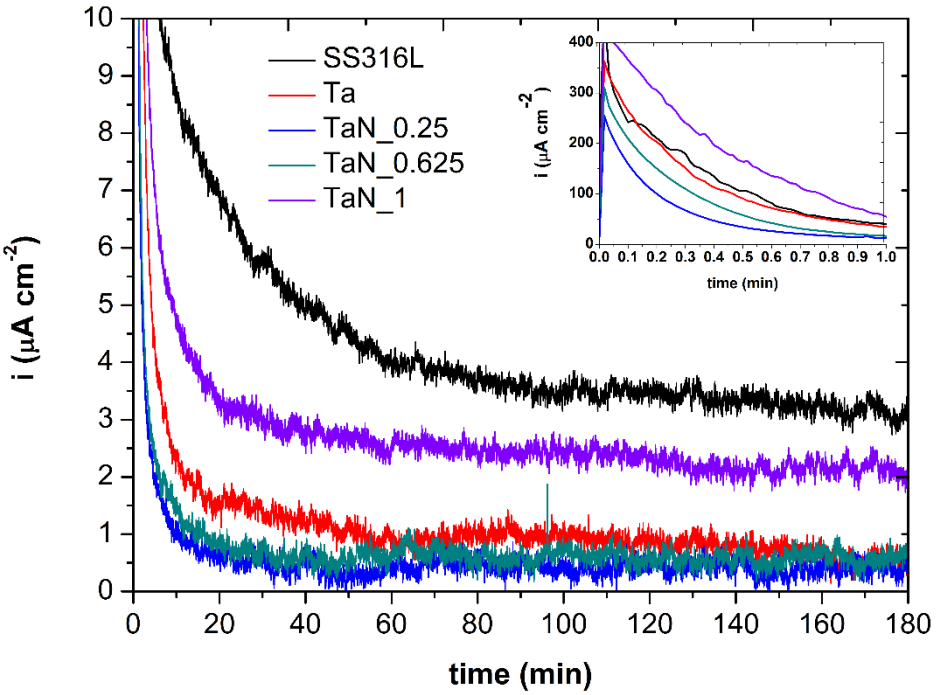


**Fig 6. 13: Potentiostatic tests at 1.4 $V_{SHE}$ for 180 min in pH 3 electrolyte for $TaN_x$ coated and non-coated SS316L**

ICR values measured before and after polarization tests at 1.4$V_{SHE}$ in pH 3 electrolyte for 180 minutes are shown in Fig 6.14. ICR values obtained after 180 minutes of polarization at 1.4 $V_{SHE}$ confirmed the trend already observed for ICR values after shorter polarization testing (Fig 6.11). The ICR for nitride coatings substantially increases up to 538 mΩ $cm^2$ for TaN_1. SS316L contact resistance also rises up to 278 mΩ $cm^2$. The metallic Ta coating (82 mΩ $cm^2$) is the only one capable to keep ICR lower than non-coated SS316L after polarization.

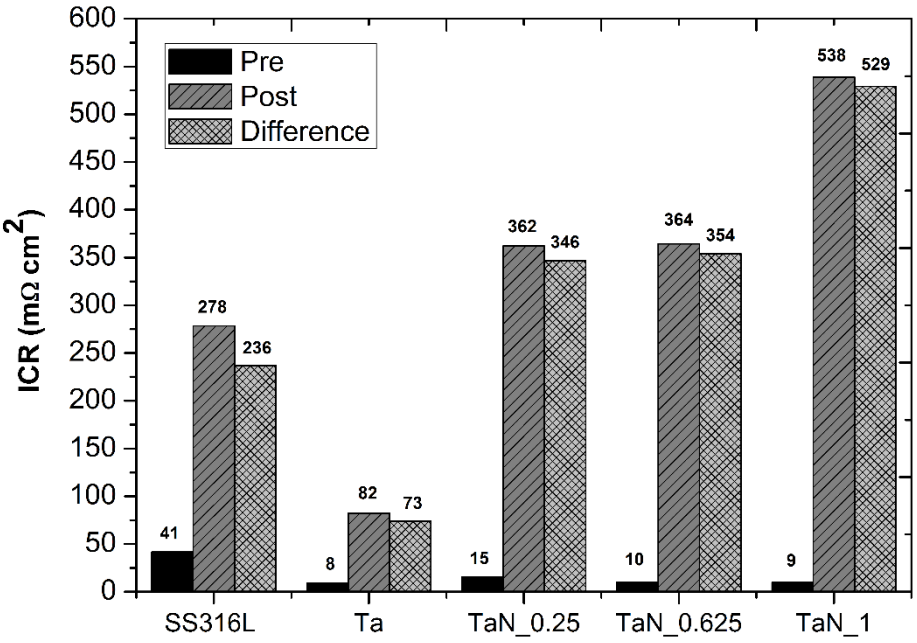


**Fig 6. 14: ICR measurements at 140 N cm$^{-2}$ for pre- and post-potentiostatic tests (1.4 $V_{SHE}$, 180 min, pH 3 electrolyte) for $TaN_x$ coated and non-coated SS316L**

When comparing the ICR values measured after 1.4 $V_{SHE}$ after 5 minutes shown in Figure 6.10 and the ICR measured after 180 minutes at 1.4 $V_{SHE}$ it can be seen that most of the ICR increase has occurred already after 5 minutes. During the polarization, dissolution and built up of oxide layer thickness will occur at the same time. This means that when the dissolution and the oxide layer build up has the same rate, the oxide layer thickness and probably the ICR has reached a steady state. For SS316L, Ta and TaN_1 apparently the ICR is increasing slightly after 5 minutes polarization, for TaN_0.25 and TaN_0.625 the oxide layer has probably reached a steady state thickness already after 5 minutes. For TaN_0.25 the ICR is even higher after 5 minutes compared to after 180 minutes, experimental discrepancy most be the reason for that.

*4.2.3.3 AES measurements for barrier oxide features analysis*

In order to explain the different behaviours of $TaN_x$ coatings in terms of interfacial contact resistances values after polarization, AES analysis were performed before and after corrosion tests at $1.4V_{SHE}$ in pH 3 electrolyte during 3 hours. Fig 6.15 shows the atomic composition spectra of the first 30 nm of each $TaN_x$ coating, since the oxide layer grown on the coating surface after polarization is known to strongly increase the ICR [25, 32, and 33].

Before polarization, metallic Ta already exhibited a spontaneously grown thin tantalum oxide of approximately 10 nm. Nitride $TaN_x$ coatings did not show such affinity for oxide layer formation in contact with atmosphere. In spite of different compositions observed before polarization, ICR values for all $TaN_x$ are low and below 20 $m\Omega\ cm^2$.

After polarization, the increase of ICR from 8 to 82 $m\Omega cm^2$ in Ta coating is due to the thickening of tantalum oxide layer which is characterized by a high dielectric constant. The passive film formed on $TaN_x$ coatings is an oxynitride tantalum layer rather than pure tantalum oxide. The much higher ICR shown by TaN_1, 538 $m\Omega\ cm^2$, can be related to the much thicker oxynitride layer formation compared to the other coatings. However, the passive layer grown on top of TaN_0.25 and TaN_0.625 is thinner than the pure tantalum oxide formed on top of metallic Ta which does not correspond with higher ICR values shown by nitride $TaN_x$ coatings. The nitride $TaN_x$ coatings behaviour after polarization seems to be dominated by the composition of the oxynitride layer rather than by its thickness.

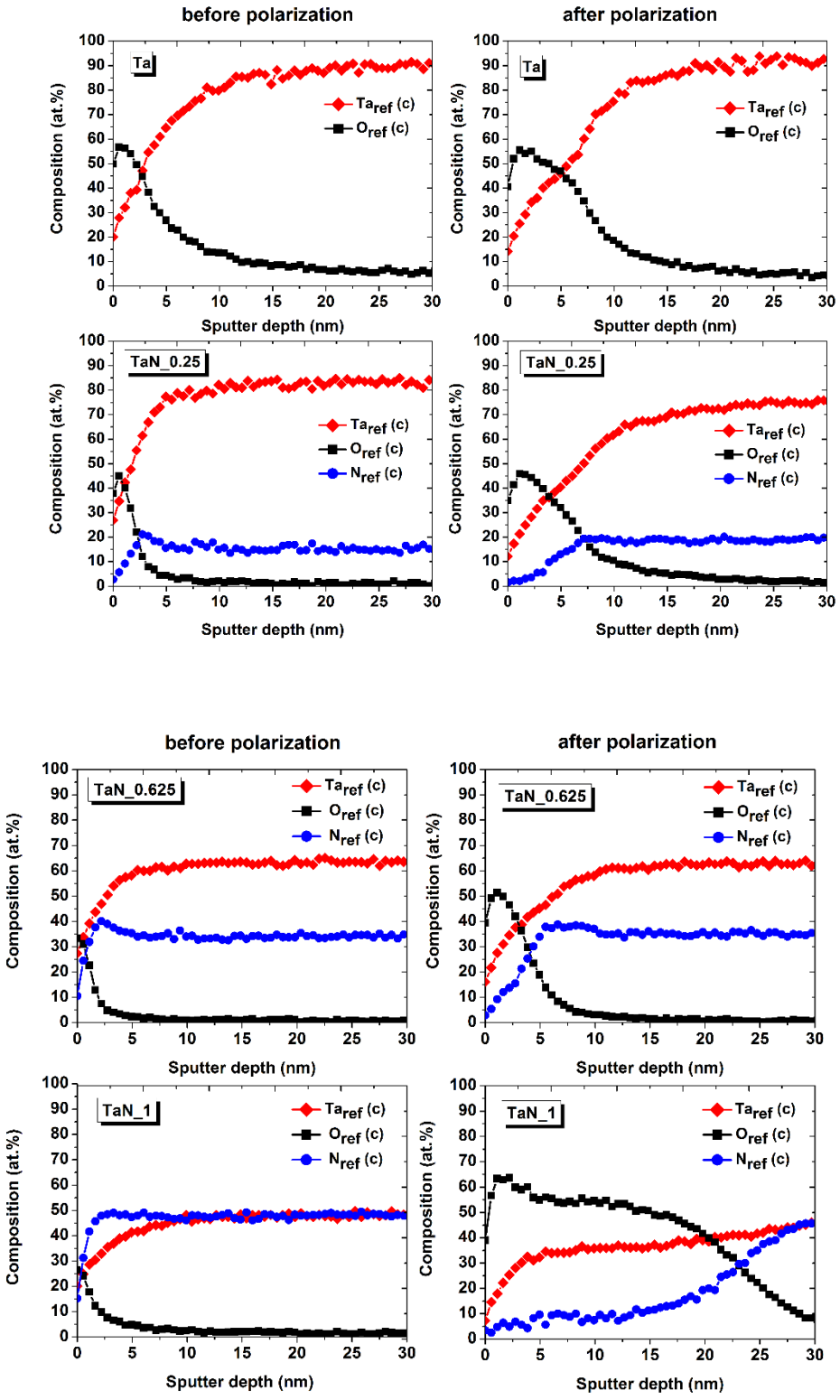


**Fig 6. 15: AES results showing the change in barrier layer thickness and composition before and after polarization for each $TaN_x$ coating**

The literature concerning the electrical properties of tantalum oxynitride thin films is, at present, quite limited, but an extensive study recently published by D. Cristea and co-workers [34] may help to correlate the tantalum oxynitride passive characteristics with ICR values obtained on this study. Tantalum oxynitride ($Ta_xN_yO_z$) thin films with electrical resistivity's varying from $5.29x10^{-4}$ Ω cm up to $1.93x10^{6}$ Ω cm were grown in [34] by (N+O)/Ta ratio variation. Main conclusions arising from that study are that resistivity of the films grows with increasing (N+O)/Ta ratio and that oxygen content is the prevalent contributor to the rise in resistivity. The thickness and average composition of oxynitride and oxide tantalum layers grown on top of nitride $TaN_x$ and metallic Ta coatings after polarization, respectively, are plotted in Table 6.2.

| | Oxynitride layer thickness (nm) | Ta (at. %) | N (at. %) | O (at. %) | (N+O)/Ta | O/Ta |
|---|---|---|---|---|---|---|
| **Ta** | 15 | 60 | 0 | 40 | 0.66 | 0.66 |
| **TaN_0.25** | 10 | 50 | 15 | 35 | 1.00 | 0.70 |
| **TaN_0.625** | 8 | 45 | 30 | 25 | 1.22 | 0.55 |
| **TaN_1** | 25 | 40 | 15 | 45 | 1.50 | 1.12 |

**Table 6. 2: Passive oxynitride layer thickness and composition of $TaN_x$ coatings after polarization at 1.4 $V_{SHE}$ for 180 min in pH 3 electrolyte**

The quantification is based on sensitivity factors provided by the instrument manufacturer. As described in the introduction, thicknesses assume the same sputtering rate as for a $SiO_2$ standard. Sputtering of a complete coating thickness for one of the samples gave a film thickness that is close to that suggested by the SEM observations which suggests that the absolute values are reasonably reliable. For the thinnest oxynitride layers, thickness values may be expected to show some variation due to small differences in handling and exposure to the atmosphere before analysis.

These thin oxynitride layers are acting as dielectrics between the sample and the GDL during conductivity measurements and are responsible for the abrupt rise in ICR. It seems that when (N+O)/Ta is above 1 (non-metallic/metallic atomic ratio above 1) the resistivity abruptly increases, while below this threshold the ICR increase is not such significant, as observed for metallic Ta film. This assumption is based on similar conclusions from [34]. Much higher oxygen content on oxynitride film of TaN_1, along with larger thickness, is responsible for the much higher ICR compared with other nitride coatings.

Assuming that in real fuel cell operation conditions, peak voltages as high as $1.4V_{SHE}$ are delivered, none of these $TaN_x$ coatings seems suitable due to the high ICR values shown after polarization at $1.4V_{SHE}$ in ex-situ testing. Nitride $TaN_x$ coatings are definitely rejected as protective candidates as a consequence of abrupt rise in ICR readily after a few minutes polarized at 1 $V_{SHE}$. New strategies to block the dielectric thin tantalum oxide layer on top of metallic Ta are under investigations, since this coating has exhibited promising behaviour in terms of corrosion resistance but needs to exhibit lower ICR values after polarization. An alternative bi-layer coating based on Ta is investigated in the following section.

## 4.3 Experimental development of bi-layer Ta_ITO coating to protect SS bipolar plates in cathode side of PEMFC

A new bi-layer coating solution based on Tantalum and ITO layers was deposited on SS316L in order to try to reduce the ICR rise observed for pure Ta after electrochemical tests. This ICR rise is devoted to the formation of insulating tantalum oxide barrier film on top of Ta during polarization. In order to block the growth of

insulating oxides that compromise the conductivity of the BPPs, the deposition of a conductive oxide layer; specifically, indium-tin-oxide (ITO), on top of Ta is addressed.

Indium Tin Oxide (ITO) is a tin-doped indium oxide ($In_2O_3$:Sn) and n-type semiconductor which exhibits high optical transmittance in the visible region, high electrical conductivity and good chemical stability. These properties have led to the use of ITO films as transparent electrodes in manifold devices for different applications.

In this thesis, the electrical properties of the ITO exclusively are significant, since the purpose of this film deposition is to hinder the formation on non-conductive oxides when the BPP is subjected to potentials as high as 1.4 $V_{SHE}$ during fuel cell operation.

### 4.3.1. Ta_ITO film deposition

The bi-layer Ta-ITO film was deposited by successive sputtering of metallic Ta and ceramic ITO ($In_2O_3$: $SnO_2$, 90:10 wt. %) targets by MPPMS on SS316L coupons and silicon wafers.

Prior to film deposition the substrates were sputter etched in Ar+$H_2$ atmosphere to eliminate the oxides on top of SS316L surface. The substrate temperature was 350 ºC. The Ta film was deposited under the same process parameters employed in section 4.2 for pure Ta film development (Table 6.1). ITO film was grown using MPPMS 996 pulse shown in Fig 6.3. For comparative purposes, the process and pulsing parameters used during Ta and ITO layer deposition are summarized in Table 6.3.

| | $P_{av}$ (kW) | $V_p$ (V) | $I_p$ (A) | $P_p$ (kW) | F (Hz) | Ar (sccm) | $O_2$ (sccm) | P (Pa) | $V_b$ (V) | Thickness (nm) |
|---|---|---|---|---|---|---|---|---|---|---|
| **Ta** | 4 | 720 | 85 | 61.2 | 150 | 125 | 0 | 0.7 | - 50 | 2600 |
| **ITO** | 1.5 | 612 | 21 | 13 | 135 | 75 | 3 | 0.4 | 0 | 300 |

**Table 6. 3 Deposition parameters during Ta and ITO layers growth**

### 4.3.2. Ta_ITO film performance in PEMFC environment

The cross-sectional SEM micrograph of Ta_ITO coating is plotted in Fig 6.16. The interface between metallic Ta layer and ITO layer on top is clearly observed by a color change which is indicated by the red arrow in the image. The ITO growth mode clearly follows the well-packed columnar structure of metallic Ta underneath.

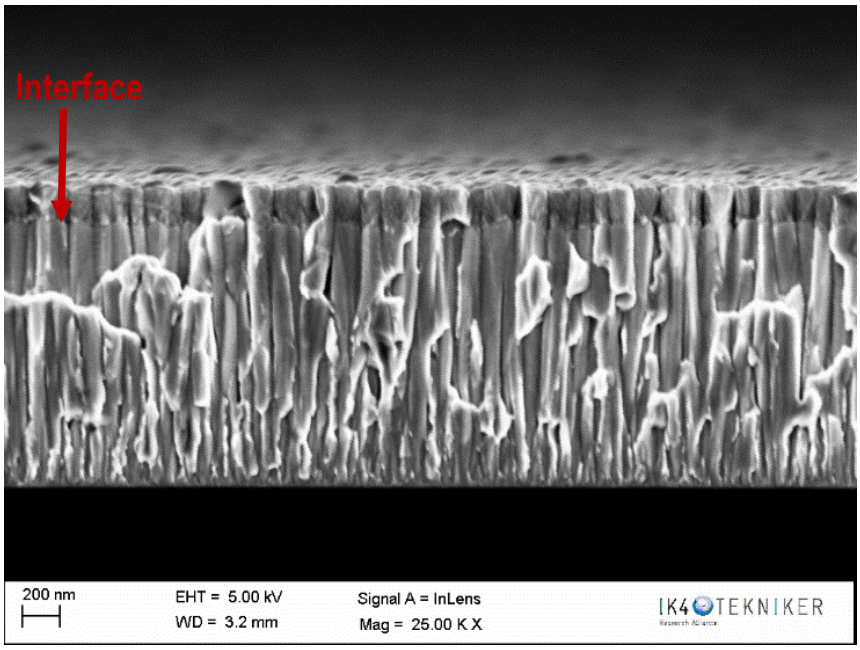


**Fig 6. 16: Cross-sectional micrograph of bi-layer Ta_ITO coating**

The Ta_ITO coated SS316L coupons were polarized at 1.4 $V_{SHE}$ during 5 and 180 minutes in pH 3 electrolyte. The Ta_ITO coating performance is compared with metallic Ta film. The evolution of corrosion current with time during polarization at 1.4 $V_{SHE}$ is monitored and shown in Fig 6.17. Corrosion current of Ta_ITO coating is slightly higher than for pure Ta, but remains low and constant around 5 µA $cm^{-2}$ after 180 minutes polarization.

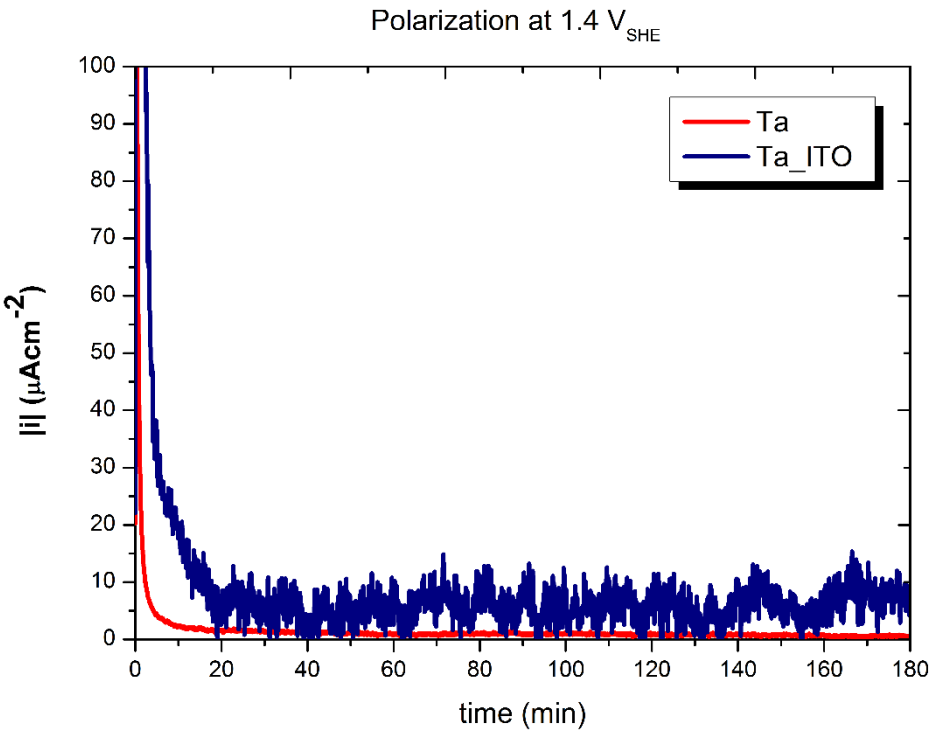


**Fig 6. 17: Potentiostatic tests at 1.4 $V_{SHE}$ for 180 min in pH 3 electrolyte for metallic Ta and Ta_ITO films**

ICR measurements were taken before and after polarization at 1.4 $V_{SHE}$ during 5 and 180 minutes at different compaction forces. Fig 6.18 shows the ICR value at 140 N $cm^{-2}$ compaction force (compaction force applied in PEMFC) for Ta and Ta_ITO films before and after polarization tests. The deposition of a thin ITO layer on top of metallic Ta reduces the ICR from 82 mΩ $cm^2$ to 29 mΩ $cm^2$ after 180 minutes polarization at 1.4 $V_{SHE}$, demonstrating the suitability of this approach to somehow prevent the formation on non-conductive barrier layer on coating surface. It is true that the DoE

target establishes an ICR value of 10 mΩ $cm^2$, but it should be noticed that this targeted value corresponds to a measurement taken after 60 minutes polarization at 0.8 $V_{SHE}$. It has been previously confirmed that increasing applied potential during electrochemical testing, substantially increases the ICR measured after tests. Hence, lower ICR value is expected for Ta_ITO film polarized at 0.8$V_{SHE}$ that could meet the requirements established by DoE target.

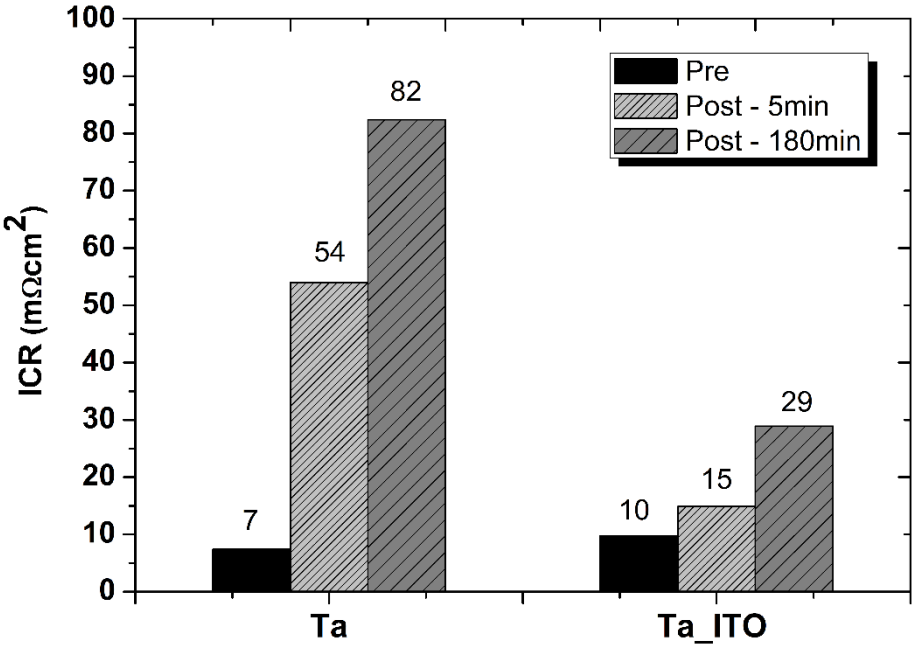


**Fig 6. 18: ICR values at 140 N $cm^{-2}$ measured for Ta and Ta_ITO films before and after polarization tests at 1.4 $V_{SHE}$ during 5 and 180 minutes**

## 4.4. Conclusions

Tantalum based coatings have been evaluated as potential candidates to enhance SS316L bipolar plates performance and durability in PEMFC.

Electrochemical and ICR measurements were performed to study the effect of $TaN_X$ coating composition (different Ta/N atomic ratio) on corrosion rate and contact resistance of $TaN_x$ coated SS316L BPP in PEMFC simulated environment. The effect of applied potential, pH of the electrolyte and time on $TaN_x$ coated SS316L performance was also investigated.

Corrosion currents measured for all $TaN_x$ coatings are low (1-10 μA $cm^{-2}$) for all tested conditions. Applied potential and pH of the electrolyte do not alter the excellent corrosion resistance of $TaN_x$ films even at potentials as high as 1.4 $V_{SHE}$. Corrosion currents measured at 1.4 $V_{SHE}$ for 180 min in pH 3 electrolyte for Ta, TaN_0.25 and TaN_0.625 are lower than 1 μA $cm^{-2}$, satisfying the DOE target for corrosion resistance even at such high potentials. Best performance is exhibited from TaN_0.25, the film characterized with denser microstructure and hence, lower defect content.

ICR measurements revealed strong influence of testing conditions on all $TaN_x$ coatings and non-coated SS316L. Overall, ICR considerably increases with increasing applied potential and slightly increases with increasing pH. ICRs measured after long tests did not show significant rise compared with shorter tests, indicating that barrier oxide layer build-up occurs at the beginning of the tests and reaches a steady state rapidly. ICR measurements manifested completely different behaviours for each $TaN_x$ coating. AES analysis showed the difference in both composition and thickness of the barrier oxide layer grown on top of $TaN_x$ films depending on coating composition. Metallic Ta film showed much lower ICR (82 mΩ

$cm^2$) than nitride $TaN_x$ films (362-538 $m\Omega cm^2$) after polarization at 1.4 $V_{SHE}$ for 180 min in pH 3 electrolyte. Composition of barrier oxide films is responsible for this behaviour. When non-metallic/metallic atomic ratio ((N+O)/Ta) in top barrier film is above 1, ICR abruptly increases, as observed for nitride $TaN_x$ films. (N+O)/Ta atomic ratio is below 1 in tantalum oxide grown on metallic Ta surface and hence, such rise in ICR is not detected. ICR increase observed for metallic Ta is due to thickening of oxide layer. However, neither the metallic Ta can satisfy the DoE targets in terms of ICR which is established at 10 $m\Omega\ cm^2$ after 0.8 $V_{SHE}$ polarization during 60 min.

In order to try to reduce the ICR, the deposition of a conductive indium-tin-oxide (ITO) layer on top of metallic Ta to prevent insulating tantalum oxide layer growth during polarization is proposed. The ICR measured for this bilayer Ta_ITO film after polarization at 1.4 $V_{SHE}$ (180 min) is three times lower than for pure metallic Ta, strongly enhancing the performance of Ta_ITO coated SS316L. Moreover, the corrosion current of Ta_ITO remains low during polarization at potentials as high as 1.4 $V_{SHE}$. To sum it up, the corrosion current and ICR values measured for each evaluated coating under different testing conditions are shown in Table 6.4

| Samples | Testing conditions | | | Coating properties | |
|---|---|---|---|---|---|
| | Electrolyte pH | Applied potential ($V_{SHE}$) | Test duration (min) | $I_{corr}$ ($\mu A\ cm^{-2}$) | ICR after ($m\Omega\ cm^2$) |
| SS316L | 3 | 1 | 5 | ~ 15 | 47 |
| | 3 | 1.4 | 5 | ~ 11 | 96 |
| | 6 | 1.4 | 5 | ~ 30 | 137 |
| | 3 | 1.4 | 180 | ~ 4 | 278 |
| Ta | 3 | 1 | 5 | ~ 5 | 42 |
| | 3 | 1.4 | 5 | ~ 7 | 54 |
| | 6 | 1.4 | 5 | ~ 8 | 63 |
| | 3 | 1.4 | 180 | ~ 1 | 82 |
| TaN_0.25 | 3 | 1 | 5 | ~ 3 | 260 |
| | 3 | 1.4 | 5 | ~ 4 | 401 |
| | 6 | 1.4 | 5 | ~ 8 | 418 |
| | 3 | 1.4 | 180 | ~ 0.5 | 362 |
| TaN_0.625 | 3 | 1 | 5 | ~ 3 | 183 |
| | 3 | 1.4 | 5 | ~ 4 | 339 |
| | 6 | 1.4 | 5 | ~ 8 | 383 |
| | 3 | 1.4 | 180 | ~ 0.5 | 364 |
| TaN_1 | 3 | 1 | 5 | ~ 12 | 126 |
| | 3 | 1.4 | 5 | ~ 10 | 248 |
| | 6 | 1.4 | 5 | ~ 15 | 472 |
| | 3 | 1.4 | 180 | ~ 3 | 538 |
| Ta_ITO | 3 | 1.4 | 5 | ~ 60 | 15 |
| | 3 | 1.4 | 180 | ~ 5 | 29 |

**Table 6. 4 Corrosion current and ICR measured for different $TaN_x$ and Ta_ITO films in PEMFC simulated environment.**

# 6. References

[1] D. Papageorgopoulos, DOE fuel cell technology program overview and introduction to the 2010 fuel cell pre-solicitation workshop in DOE fuel cell pre-solicitation workshop. Department of Energy, Lakewood, Colorado; 2010.

[2] Y. Wang, K. S. Chen, J. Mishler, S. Chan Cho, X. Cordobes Adroher, A review of polymer electrolyte membrane fuel cells: Technology, applications, and needs on fundamental research, Applied Energy 88 (2011) 981–1007

[3] O. Z. Sharaf, M. F. Orhan, An overview of fuel cell technology: Fundamentals and applications, Renewable and Sustainable Energy Reviews 32 (2014) 810–853

[4] G. Janssen, F. A. de Brujin, In book: Encyclopedia of Sustainability, Edition: 1, Chapter: PEM Fuel Cell Materials: Costs, Performance and Durability, Publisher: Springer, Editors: R.A. Meyers, pp.7694 – 7730 (2012). DOI: 10.1007/978-1-4614-5785-5_9

[5] Polymer electrolyte membrane fuel cells. Helsinki University of Technology. http://tfy.tkk.fi/aes/AES/projects/renew/fuelcell/pem_index.html

[6] http://www.spinam.eu/fc.html

[7] http://www2.lbl.gov/publicinfo/newscenter/features/2008/apr/eet-fuel-cell-modeling.html

[8] R. Taherian, A review of composite and metallic bipolar plates in proton exchange membrane fuel cell: Materials, fabrication, and material selection, Journal of Power Sources 265 (2014) 370-390

[9] Y. Hung, Materials Science and Engineering 2010, Stony Brook University.

[10] H. Morikawa, H. Kikushi, N. Saito, Development and advances of a V-flow FC stack for FCX clarity. SAE Int J Engines 2 (2009) 955–959

[11] R. Shimoi, T. Aoyama T, A. Iiyama, Development of fuel cell stack durability based on actual vehicle test data: current status and future work. SAE Int J Engines 2 (2009) 960–970

[12] F.A. de Bruijn, R.C. Makkus, R.K.A.M. Mallant, G.J.M. Janssen, Chapter Five - Materials for state-of-the-art PEM fuel cells, and their suitability for operation above 100 ºC. In: Zhao T, Kreuer KD, Nguyen T (eds) Advances in fuel cells. Elsevier, The Netherlands

[13] R.A. Antunes, M.C. L. Oliveira, G. Ett, V. Ett, Corrosion of metal bipolar plates for PEM fuel cells: A review, Int J Hydrogen Energy 35 (2010) 3632-3647

[14] S. Karimi, N. Fraser, B. Roberts, F. R. Foulkes, A Review of Metallic Bipolar Plates for Proton Exchange Membrane Fuel Cells: Materials and Fabrication Methods, Advances in Materials Science and Engineering 2012 (2012), ID 828070

[15] L. Zhang, Y. Liu, H. Song, S. Wang, Y. Zhou, S. J. Hu, Estimation of contact resistance in proton exchange membrane fuel cells, Journal of Power Sources 162 (2006) 1165-1171

[16] U.S.D.o. Energy, Hydrogen, Fuel Cells & Technologies Program. In: Multi-year research, development and demonstration Plan. D.O. Energy. p. 29 [Chapter 3.4.4], http://www1.eere.energy.gov/hydrogenandfuelcells/mypp/; 2012.

[17] O. Lavigne, C. Alemany-Dumont, B. Normand, S. Berthon-Fabry, R. Metkemeijer. Thin chromium nitride PVD coatings on stainless steel for conductive component as bipolar plates of PEM fuel cells: Ex-situ and in-situ performances evaluation. Int J Hydrogen Energy 37 (2012) 10789-97

[18] S.H. Lee, N. Kakati, J. Maiti, S.H. Jee, D.J. Kalita, Y.S. Yoon. Corrosion and electrical properties of CrN- and TiN-coated 316L stainless steel used as bipolar plates for polymer electrolyte membrane fuel cells Thin Solid Films 529 (2013) 374e379.

[19] H. Sun, K. Cooke, G. Eitzinger, P. Hamilton, B. Pollet. Development of PVD coatings for PEMFC metallic bipolar plates. Thin Solid Films 528 (2013) 199–204.

[20] L. Wang, J. Sun, P. Li, J. Sun, Y. Lv, B. Jing, S. Li, S. Ji, Z. Wen. Molybdenum nitride modified AISI 304 stainless steel bipolar plate for proton exchange membrane fuel cell. Int J Hydrogen Energy 37 (2012) 5876-5883

[21] C. Choe, H. Choi, W. Hong, J-J. Lee. Tantalum nitride coated AISI 316L as bipolar plate for polymer electrolyte membrane fuel cell. Int J Hydrogen Energy 37 (2012) 405-411

[22] Kumagai M, Myung ST, Kuwata S, Asaishi R, Yashiro H. Corrosion behavior of austenitic stainless steels as a function of pH for use as bipolar plates in polymer electrolyte membrane fuel cells. Electrochim Acta 2008; 53:4205-12.

[23] S. Lædre, O.E. Kongstein, A. Oedegaard, F. Seland, H. Karoliussen. The effect of pH and halides on the corrosion process of stainless steel bipolar plates for proton exchange membrane fuel cells Int. J. Hydrogen Energy 37 (2012) 18537-18546.

[24] G. Hinds, E. Brightman. In situ mapping of electrode potential in a PEM fuel cell. Electrochemistry Communications 17 (2012) 26–29.

[25] A. Orsi, O.E. Kongstein, P.J. Hamilton, A. Oedegaard, I.H. Svenum, K. Cooke. An investigation of the typical corrosion parameters used to test polymer electrolyte fuel cell bipolar plate

coatings, with titanium nitride coated stainless steel as a case study. Journal of Power Sources 285 (2015) 530-537

[26] D.D. Papadias, R. K. Ahluwalia, J.K. Thomson, H. M. Meywer III, M.P. Brady, H. Wang, J. A. Turner, R. Mukundan, R. Borup, Degradation of SS316L bipolar plates in simulated fuel cell environment: Corrosion rate, barrier film formation kinetics and contact resistance, Journal of Power Sources 273 (2015) 1237-1249

[27] H. Yu, L. Yang, L. Zhu, X. Jian, Z. Wang, L. Jiang, Anticorrosion properties of Ta-coated 316L stainless steel as bipolar plate material in proton exchange membrane fuel cells, Journal of Power Sources 191 (2009) 495–500

[28] Y.P. Purandare, A.P. Ehiasarian, M.M. Stack, P.Eh. Hovsepian, CrN/NbN coatings deposited by HIPIMS: A preliminary study of erosion-corrosion performance Surf. Coat. Technol., 204 (2010) 1158-1162

[29] G. Hinds, E. Brightman, Towards more representative test methods for corrosion resistance of PEMFC metallic bipolar plates, Int. J. Hydrogen Energy 40 (2015) 2785-2791

[30] M.P. Brady, B. Yang, H. Wang, J.A. Turner, K.L. More, M. Wilson, and F. Garzon, The Formation of Protective Nitride Surfaces for PEM Fuel Cell Metallic Bipolar Plates, JOM (2006) 50-57

[31] D. Hamm, C.-O.A. Olsson, D. Landolt, Effect of chromium content and sweep rate on passive film growth on iron–chromium alloys studied by EQCM and XPS, Corrosion Science 44 (2002) 1009–1025

[32] J. Xu, H.J. Huang, Z. Li, S. Xu, H. Tao, P. Munroe, Z-Han. Xie, Corrosion behaviour of a ZrCN coated Ti alloy with potential application as a bipolar plate for proton exchange membrane fuel cell, Journal of Alloys and Compounds 663 (2016) 718-730.

[33] A.S. Gago, S.A. Ansar, B. Saruhan, U. Schulz, P. Lettenmeier, N.A. Cañas, P. Gazdzicki, T. MOrawietz, R. Hiesgen, J. Arnold, K.A. Friedrich, Protective coatings on stainless steel bipolar plates for proton exchange membrane (PEM) electrolysers, Journal of Power Sources 307 (2016) 815-825

[34] D. Cristea, A. Crisan, N. Cretu, J. Borges, C. Lopes, L. Cunha, V. Ion, M. Dinescu, N.P. Barradas, E. Alves, M. Apreutesei, D. Munteanu, Structure dependent resistivity and dielectric characteristics of tantalum oxynitride thin films produced by magnetron sputtering, Applied Surface Science 354 (2015) 298-305

# CHAPTER 7

# GENERAL CONCLUSIONS & PERSPECTIVES

# 1. Overall conclusions

The main objective in this work has been the development of high density corrosion-resistant $TaN_x$ thin films by new emerging modulated pulsed power magnetron sputtering (MPPMS) technique to be applied for the protection of metallic substrates in applications exposed to harsh environments. The in-depth study about $TaN_x$ films electrochemical performance in different corrosive environments accomplished in this thesis, allows a better understanding of this promising and rather unexplored material, which has turned into a reliable coating solution to stand up to corrosion phenomena. The utilization of MPPMS for the deposition of $TaN_x$ has enabled the development of columnar-free and low defect microstructure films owing excellent corrosion resistance, overcoming the main drawback of conventional dc-sputtered films.

The main conclusion arising from this work is the great importance of $TaN_x$ film composition and crystal structure on the subsequent type of surface barrier oxide layer growth, since this surface layer eventually determines the corrosion resistance of the whole film. Additionally, it was found that the microstructure of the films is a key feature for the enhancement of electrochemical behaviour of $TaN_x$ coatings. MPPMS application has allowed the development of improved microstructure $TaN_x$ films with refined properties.

In existing literature, there was a lack of information regarding TaN electrochemical performance despite of the excellent corrosion resistance and inertness of metal tantalum (Ta). This work has demonstrated the potential of $TaN_x$ films deposited by MPPMS for the protection of metallic substrates in corrosion facing applications. MPPMS application for the growth of these films allows the deposition of tailored and enhanced $TaN_x$ coatings compared to those films grown by conventional DCMS.

$TaN_x$ film properties are highly dependent on nitrogen content on the film, due to the huge complexity of Ta-N system that exhibits many different crystal phases. This work presents a detailed study on the influence of nitrogen on $TaN_x$ film microstructure and properties. $TaN_x$ films with nitrogen contents of 0, 10, 25 and 45 at. % on the film were grown by MPPMS at high deposition rates (~ 20 nm $min^{-1}$), confirming the industrial viability of this technique. Different crystal phases were detected depending on $TaN_x$ composition that were responsible for the exhibition of different properties. It was found that suppression of columnar growth was restricted to $TaN_x$ films containing 10 at. % of nitrogen (TaN_0.25). TaN_0.625 film (25 at. % of nitrogen) exhibited the highest hardness, related to the presence of super-hard $Ta_4N$ phase. Excellent corrosion resistance in NaCl 0.06 M was observed for $TaN_x$ coatings containing less than 30 at. % of nitrogen in the film and characterized by the presence of α-Ta crystal phase. The extremely stable and impervious tantalum oxide layer growth on top of $TaN_x$ films was responsible for the outstanding corrosion resistance showed by these films. The TaN_1 film, containing 45 at. % of nitrogen, did not exhibit such a high corrosion resistance, likely due to the formation of an oxynitride tantalum barrier layer instead of greatly protective pure tantalum oxide.

The second part of the thesis is related to the evaluation of $TaN_x$ films for the protection of metallic substrate in real applications facing corrosion; i.e. pure titanium (Ti-cp) in biomedical implants and SS316L bipolar plates in PEMFC.

Multilayer and monolayer TaN films were grown on Ti-cp for tribocorrosion resistance enhancement. Ti-cp exhibits excellent corrosion resistance but suffers from poor mechanical properties that compromise its service lifetime as an implant material. It was found that the corrosion resistance in PBS, in the absence of wear processes, of uncoated Ti-cp and TaN coated Ti-cp was comparable. TaN films slightly increased the Ti-cp corrosion resistance, and all TaN films regardless of

microstructure type, exhibited similar polarization values. This comparable electrochemical behaviour was due to the same topmost layer in all TaN films which gave rise to the formation of similar surface barrier tantalum oxide layer, confirming the great importance of this layer in corrosion resistance exhibited by the whole films. However, during simultaneous application of corrosion and wear processes, the performance enhancement of TaN coated Ti-cp was noticeable. Polarization resistance of uncoated Ti-cp during sliding processes was one order of magnitude lower than the one shown by TaN coated Ti-cp. Friction coefficient and wear tracks measured for Ti-cp were much higher than for TaN coated Ti-cp which led to huge differences in total material loss due to tribocorrosion. The benefits of multilayer structure in TaN films were not accurately measurable in this study, where all TaN films showed comparable performances.

$TaN_x$ films with different nitrogen contents (0, 10, 25, and 45 at. % of nitrogen) were grown on SS316L for performance and durability enhancement of BPP in PEMFC simulated environment. The corrosion resistance trend previously exhibited by $TaN_x$ films in NaCl 0.06 M, was reproduced in $H_2SO_4$ electrolyte. $TaN_x$ films with less than 30 at. % of nitrogen in the film met the requirements established by DoE targets ($i_{corr}$ < 1 μA $cm^{-2}$, ICR < 10 mΩ $cm^2$ after polarization at 0.8 $V_{SHE}$ during 1 hour) in terms of corrosion resistance. $TaN_x$ films were stable even up to 1.4 $V_{SHE,}$ guaranteeing an adequate corrosion protection of SS316L even during start-up/shut down of PEMFC. However, the ICR measurements after polarization were too high for nitride $TaN_x$ films (~400 mΩ $cm^2$) and high for metallic Ta (82 mΩ $cm^2$). AES analysis revealed that even if surface barrier oxide formed was thin, it was sufficient to considerably decrease the conductivity of the whole TaN film due to the high dielectric constant of tantalum oxide. As an attempt to block the growth of insulating surface tantalum oxide layer during polarization, a bi-layer film consisting of tantalum and conductive indium-tin-oxide (ITO) layers was deposited on SS316L. Corrosion resistance of Ta_ITO film

remained low while ICR value after polarization at 1.4 $V_{SHE}$ was 29 mΩ $cm^2$. It can be expected that Ta_ITO film would exhibit lower ICR after polarization at 0.8 $V_{SHE}$, reaching the DoE targets of < 10 mΩ $cm^2$ established for 2020. Further and more in-depth evaluation is needed, but Ta_ITO coating exhibited promising performance for the protection of SS316L bipolar plates in PEMFC.

All the objectives presented in the introduction have been achieved, and this thesis has contributed to gain an in-depth knowledge about TaN thin films electrochemical performance, which have turned into promising coating candidates for harsh environments. MPPMS technique has shown its potential to deposited, at high rates, high density microstructure $TaN_x$ films owing excellent corrosion resistance.

## 2. Future perspectives

The $TaN_x$ thin films deposited by MPPMS within this thesis have demonstrated a great capacity to protect uncoated metallic substrates from electrochemical degradation in several simulated harsh environments. Promising performance is, hence, expected when $TaN_x$ films are applied to real metallic components in investigated applications, but this hypothesis requires a verification under real operation conditions and standards.

The $TaN_x$ films should be deposited on real Ti-cp implants in order to analize if the $TaN_x$ performance is comparable in flat and curved samples. $TaN_x$ films show promising features for Ti-cp dental implants durability enhancement. However, for $TaN_x$ films to be considered suitable for commercialization as protective coating in dental implants, the following ISO standards need to be fulfilled:

- Citotoxicity: ISO 10993-5
- Biocompatibility: ISO 7405:2008
- Surface Waste: EN – 1484 Determination of total organic carbon (TOC)

IK4-Tekniker is currently working with two Spanish companies for the assessment of industrial viability and production of TaN based protective films for Ti-cp dental implants.

Additionally, if the benefits of multilayer TaN thin films want to be further analysed, higher loads during tribocorrosion testing need to be applied to cause significant degradation on TaN films that would facilitate the evaluation and ranking of different microstructure films in terms of Ti-cp longer protection.

Equivalently, $TaN_x$ films should be applied on real bipolar plates for PEMFC, since these components incorporate gas flow fields to distribute $H_2$ and $O_2$ gases. The complete coverage of the bipolar plate surface must be ensured to guarantee a long-term protection. Furthermore, a more exhaustive study on promising Ta_ITO film has to be accomplished. It exhibited promising results both in corrosion resistance and ICR measurements, but a more in-depth understanding of Ta_ITO performance is essential for a complete assessment of this new coating. For that purpose, ex-situ and in-situ tests in PEMFC must be performed before any consideration for commercialization.